



Dublin City University
Ollscoil Chathair Bhaile Átha Cliath

**Preparation and characterization of
novel hierarchical nanoparticle
assemblies for biomedical applications**

Fadwa El Haddassi, MSc

Thesis submitted for the Degree of
Doctor of Philosophy

Supervisors:
Dr. Kieran Nolan
Dr. Dermot Brougham (University College Dublin)

School of Chemical Sciences

2016

I hereby certify that this material, which I now submit for assessment on the programme of study leading to the award of Doctor of Philosophy is entirely my own work, that I have exercised reasonable care to ensure that the work is original, and does not to the best of my knowledge breach any law of copyright, and has not been taken from the work of others save and to the extent that such work has been cited and acknowledged within the text of my work.

Signed: _____ ID No.: _____ Date: _____

This thesis is dedicated to my beloved parents.

“May the wind always be at your back and the sun upon your face. And may the wings of destiny carry you aloft to dance with the stars”

- George Jung

Acknowledgments

I would like to thank my supervisor Dr. Dermot Brougham (UCD) for all his advice, patience and encouragement through my time in his group. I sincerely appreciate all the opportunities and the financial support he has made available to me during my PhD.

I would like to thank all my lab colleagues and friends past and present, Dr. Lionel Maurizi, Mr. Bing Wu, Dr. Jose Hierrezuelo, Ms. Sarah Martyn, Ms Orla Carron, Cara Moloney, Patricia Monks and all the others who have made my time in the XG-36 lab memorable.

Part of my work has benefited from the collaboration I was a part of, and I would like to thank Dr. Paolo Gasco and his co-workers in Nanovector (Torino, Italia) with special thanks to Mr. Francesco Barbero and Miss Claudia Musicanti. I would also like to thank all the partners involved in the European Project UNION.

I would like to thank all the technical staff in DCU for all their patience, support and advices. In particular I would like to thank Mr. Vincent Hooper for all his expertise on the ICP and also Ms. Aisling McCarthy for all her help on the FESEM.

On a personal note I would like to thank all my friends back in Italy and here in Dublin who stayed by my side in difficult and happy moments. I would especially like to thank Xiaoyun He, Elena Bobbi, Zeliha Ates, Tushar Borase, Bing Bing (again), Antonis Kapetanakis, Fernando Salles, Saltuk Hanay, Rahul Dina, Teresa Lauria and all the others that I did not mention. Thank you guys for everything and for cheering me up when I needed.

I would like to thank my parents, sisters, Khalid and my little babies Karima e Asyia that have always been there for me and supported me and encouraged me during my whole academic career. I love you so much guys!

Finally I would like to thank Yassine for his patience and unconditional love that he showed to me in the last few years. I cannot wait to start our new adventure together!!

Table of Contents

Title page	I
Declaration	II
Acknowledgments	IV
Table of Contents	V
List of Abbreviations	XI
List of Figures	XV
List of Tables	XXII
Abstract	XXV
CHAPTER 1 - Introduction to Nuclear Magnetic resonance and Magnetic Nanoparticle Assemblies	1
1.1 Introduction	2
1.2 The basics of NMR Spectroscopy	3
1.2.1 Spin	3
1.3 Magnetism and magnetic materials	6
1.4 Superparamagnetism in nanoparticles	10
1.5 Applications of nanoparticle and nanoparticle assemblies in biomedicine	13
1.5.1 Drug Delivery	14
1.5.2 Magnetic fluid hyperthermia therapy	15
1.5.3 Magnetic Resonance Imaging	17
1.6 Study of magnetic properties of nanoparticle and nanoparticle clusters by NMRD	19
1.7 Interparticle interactions	21
1.8 Synthetic strategies for Magnetic Nanoparticle assemblies	23
1.8.1 Evaporation-induced self-assembly (EISA)	25
1.8.2 Layer-by-layer (LBL) assembly	26
1.8.3 Self-assembly by Competitive Stabilizer Desorption	27
1.9 Surface modification of magnetic nanoparticles and nanoparticle assemblies	29
1.10 Thesis Overview	31
CHAPTER 2 - Experimental section	33
2.1 Introduction	34
2.2 Dynamic Light Scattering	34
2.2.1 Theory	34
2.2.2 Experimental set up	37

2.2.3 Practical limitations.....	38
2.3 Zeta potential.....	38
2.3.1 Theory.....	38
2.3.2 Experimental set up	41
2.3.3 Practical considerations	41
2.4 Fast Field –Cycling NMR.....	41
2.4.1 Theory.....	41
2.4.1.1 Pre-polarised sequence.....	42
2.4.1.2 Non polarized sequence.....	43
2.4.1.3 Non-polarized Carr–Purcell–Meiboom–Gill sequence.....	43
2.4.2 Experimental set up	44
2.4.3 Practical limitations.....	45
2.5 Inductively Coupled Plasma Atomic Emission Spectroscopy	45
2.5.1 Theory.....	45
2.5.2 Experimental set up	46
2.6 Transmission Electron Microscopy.....	47
2.6.1 Theory.....	47
2.6.2 Experimental set up	48
2.6.3 Practical limitations.....	49
2.7 Field Emission Scanning Electron Microscopy	49
2.7.1 Theory.....	49
2.7.2 Experimental set up	51
2.7.3 Practical limitations.....	51
2.8 Magnetic fluid hyperthermia	51
2.8.1 Theory.....	51
2.8.2 Experimental set up	52
2.8.3 Practical limitations.....	52
2.9 Attenuated Total Reflectance – Infrared Spectroscopy.....	53
2.9.1 Theory.....	53
2.9.2 Experimental set up	54
2.9.3 Practical limitations.....	54
 CHAPTER 3 - Preparation of novel stable suspensions of size-controlled hybrid magnetic nanoclusters.....	 55
3.1 Introduction	56
3.2 Materials and methods.....	57
3.2.1 Materials	57

3.2.2	Synthesis of iron oxide nanoparticles	57
3.2.3	Synthesis of cobalt ferrite nanoparticles.....	58
3.2.4	Nanoparticle stabilization with oleic acid	58
3.2.5	NPC assembly experiments	59
3.2.5.1	Controlled assembly nanoparticles from single component nanoparticle suspensions	59
3.2.5.2	Controlled assembly nanoparticles from multi component nanoparticle suspensions	59
3.3	Results and discussion	59
3.3.1	Size and stability of the primary nanoparticles.....	59
3.3.2	Controlled assembly nanoparticles from single component nanoparticle suspensions	61
3.3.3	Reproducibility of single nanoparticle type assembly.....	62
3.3.4	Kinetics and mechanism of the nanoparticle assembly by Water Interface Competitive Stabilizer Desorption approach.....	63
3.3.5	Optimization of NP assembly conditions	66
3.3.5.1	Iron concentration.....	66
3.3.5.2	Oleic acid concentration.....	68
3.3.6	Study of hybrid CoFeO -FeO NP assembly from mixed-metallic oxide co-suspensions	70
3.3.7	Reproducibility of nanoparticle co-assembly.....	72
3.3.8	NP assembly using different ratios of CoFeO:FeO nanoparticles	72
3.3.9	FESEM analysis of CoFeO:FeO hybrid assemblies	73
3.3.10	Scale up of WI-CSD for CoFeO-FeO hybrid assemblies	74
3.3.11	Effect of the binary NPC composition on Nuclear Magnetic Resonance Properties.....	76
3.4	Conclusions.....	79
CHAPTER 4 - Competitive stabilizer desorption method development.....		81
4.1	Introduction	82
4.2	Materials and methods.....	83
4.2.1	Materials	83
4.2.2	Synthesis and stabilization of 8 nm iron oxide nanoparticles	83
4.2.3	SI-CSD.....	83
4.2.4	Synthesis and stabilization of 12.3 nm iron oxide nanoparticles.....	84
4.2.5	Flow assembly	84
4.2.6	Characterization	84
4.3	Results and discussion	85

4.3.1 SI-CSD method.....	85
4.3.1.1 Iron oxide NP clustering by SI-CSD.....	85
4.3.1.2 Effect of methanol in the clustering process.....	88
4.3.1.3 NP assembly blocking in SI-CSD.....	89
4.3.1.4 Comparison of NPC suspensions prepared with SI-CSD and WI-CSD method.....	91
4.3.2 Effect of primary NP size on assembly by WI-CSD.....	94
4.3.3 Flow assembly.....	98
4.3.3.1 Device development.....	98
4.3.3.2 Reproducibility of nanoparticle assembly.....	99
4.3.3.3 Effect of the tube length on nanoparticle assembly.....	101
4.3.3.4 Effect of flow rate on nanoparticle assembly.....	103
4.3.4 Nanoparticle assembly experiments monitored with DLS Probe.....	104
4.3.4.1 Comparison of data generated by Zetasizer Nano and by DLS probe.....	104
4.3.4.2 Investigating the spatial distribution of clusters during assembly.....	106
4.3.4.3 Effect of magnetic field on nanoparticle assembly.....	107
4.3.4.4 Effect of attenuation of magnetic field on NP clustering by WI-CSD.....	108
4.4 Conclusion.....	111
CHAPTER 5 - Transfer of stabilized suspensions of magnetic nanoparticle assemblies of controlled size from an organic to aqueous medium.....	112
5.1 Introduction.....	113
5.2 Materials and methods.....	116
5.2.1 Materials.....	116
5.2.2 OA-NP and OA-NPC synthesis.....	116
5.2.3 Phase transfer of OA-NPCs.....	116
5.2.3.1 Preparation of P123-NPCs.....	116
5.2.3.2 Preparation of DTAB-NPCs.....	117
5.2.4 Characterization.....	118
5.3 Results and discussion.....	118
5.3.1 Synthesis of OA-NPCs.....	118
5.3.2 Phase transfer of NPCs.....	119
5.3.2.1 Preparation of P123-NPCs.....	119
5.3.2.2 Preparation of DTAB-NPCs.....	123
5.3.3 Reproducibility and colloidal stability.....	124
5.3.4 Phase transfer optimization.....	126

5.3.4.1 Effect of P123 concentration.....	126
5.3.4.2 Effect of DTAB concentration.....	128
5.3.4.3 Effect of the NPC concentration on P123-NPC preparation.....	129
5.3.4.4 Effect of the NPC concentration on DTAB-NPC preparation.....	131
5.3.5 Scale up.....	132
5.3.6 Effect of nanoparticle cluster encapsulation on Nuclear Magnetic Resonance Properties.....	133
5.3.6.1 Relaxometric properties of P123-NPC suspensions	133
5.3.6.2 Relaxometric properties of DTAB-NPC suspensions	136
5.3.6.3 Comparison of P123-NPC and DTAB-NPC magnetic properties	138
5.3.7 Magnetic fluid hyperthermia	139
5.3.8 Biotesting.....	142
5.4 Conclusions.....	143
CHAPTER 6 - Preparation and characterization of size controlled lipid stabilized magnetic nanoparticle and nanoparticle clusters.....	145
6.1 Introduction	146
6.2 Materials and methods.....	149
6.2.1 Materials	149
6.2.2 Synthesis of iron oxide nanoparticle	149
6.2.3 Synthesis of iron oxide nanoparticle clusters	149
6.2.4 Lipid encapsulation of magnetic nanoparticles and nanoparticle clusters	150
6.2.4.1 Preparation of aqueous suspensions of LNPs.....	150
6.2.4.2 Preparation of aqueous suspensions of LNPA.....	150
6.2.4.3 Formation of aqueous suspensions of LNPC.....	150
6.2.5 LNP drug loading.....	151
6.2.6 Magnetic chromatography.....	151
6.2.7 Characterization	152
6.3 Results and discussion	152
6.3.1 Primary characterization of LNP suspensions.....	152
6.3.2 Primary characterization of LNPA suspensions.....	156
6.3.3 Primary characterization of LNPC suspensions	158
6.3.4 Magnetoliposome stability	161
6.3.5 Nuclear magnetic resonance relaxometry.....	162
6.3.6 Magnetic chromatography of lipidic magnetic nanostructure suspensions	165
6.3.6.1 Magnetic chromatography of LNP suspensions.....	165

6.3.6.2 Magnetic chromatography of LNPA suspensions.....	166
6.3.6.3 Magnetic chromatography of LNPC suspensions.....	167
6.3.7 Effect of magnetic chromatography on lipidic magnetic nanostructure magnetic properties.....	168
6.3.7.1 Effect of magnetic chromatography on LNP magnetic properties .	168
6.3.7.2 Effect of magnetic chromatography on LNPA magnetic properties.....	170
6.3.7.3 Effect of magnetic chromatography on LNPC magnetic properties	173
6.3.7.4 Comparison of the magnetic properties of initial and filtered lipidic nanostructures	176
6.3.8 Magnetic Fluid Hyperthermia	177
6.3.9 Drug loading and release experiments	179
6.3.9.1 Stability of drug loaded LNPs.....	180
6.3.9.2 Device development and drug release experiments.....	181
6.3.10 Biotesting.....	182
6.4 Conclusion.....	184
Thesis conclusions	186
References.....	189
Appendix.....	195

List of Abbreviations

Abbreviation	Description	Unit
B_{acq}	Acquisition Field	$s^{-1} T^{-1}$
t_{acq}	Acquisition Time	s
NPC*	Activated NPC	-
AC	Alternating Current	-
ΔE_{anis}	Anisotropy energy	GHz
BA	Benzyl Alcohol	-
T_B	Blocking temperature	K
k_B	Boltzman constant	$kgm^2s^{-2}K^{-1}$
$CoFe_2O_4$	Cobalt ferrite	-
H_c	Coercivity field	$s^{-1}T^{-1}$
CSD	Competitive Stabiliser Desorption	-
d_{TEM}	Core diameter	nm
d_{crit}	Critical diameter	nm
T_C	Curie temperature	K
d_p	Depth of penetration	mm
d	Diameter	nm
D	Diffusion coefficient	$cm^2 \cdot s^{-1}$
DTAB	Dodecyltrimethylammonium bromide	-
DLS	Dyanamic Light Scattering	-
EDLY	Echo Delay	ns
τ_{exp}	Exponential time	hr
FFC	Fast Field Cycling	-
OA	Oleic Acid	-

Abbreviation	Description	Unit
FE-STEM	Field Emission – Scanning TEM	-
FID	Free Induction Decay	-
γ	Gyromagnetic ratio	$\text{rad}\cdot\text{s}^{-1}\cdot\text{T}^{-1}$
hr	Hour	-
HPPS	High Performance Particle Sizer	-
d_{hyd}	Hydrodynamic diameter	nm
t_0	Induction time	h
ICP-AES	Atomic Emission Spectroscopy	-
K	Kelvin	-
ω_L	Larmor frequency	MHz
$\gamma\text{-Fe}_2\text{O}_3$	Maghemite	-
H	Magnetic field strength	A/m
B_0	Magnetic flux density	$\text{s}^{-1}\cdot\text{T}^{-1}$
μ_0	Magnetic permeability in vacuum	$\text{N}\cdot\text{A}^2$
MRI	Magnetic Resonance Imaging	-
χ	Magnetic susceptibility	$\text{emuOe}^{-1}\text{ g}^{-1}$
M_{xy}	Manetization in xy plane	-
M_z	Manetization in z axes	-
Fe_3O_4	Magnetite	-
NMR	Nuclear Magnetic Resonance	-
NMRD	Nuclear Magnetic Relaxation Dispersion	-
NP	Nanoparticle	-

Abbreviation	Description	Unit
NPC	Nanoparticle Cluster	-
τ_N	Neel correlation time	ns
NP/S	Non-Polarized Sequence	-
NPCPMG	Non-Polarized Carr-Purcell-Meiboom-Gill	
$R_{i,obs}$	Observed relaxation rate	s^{-1}
PC	Phosphatidylcholine	-
P123	Poly(ethylene glycol)-block-poly(propylene glycol)-block-poly(ethylene glycol) 123	-
B_{POL}	Polarization field	T
t_{POL}	Polarization time	s
PDI	Polydispersity Index	-
τ_{pow}	Power time	h
PP/S	Pre-Polarized Sequence	-
$P(x)$	Probability distribution	%
S	Quantised spin magnitude	s
s	Quantised spin angular momentum	-
RF	Radio Frequency	-
r	Radius	nm
\hbar	Planks constant	m^3kgs^{-1}
B_{RLX}	Relaxation field	Tesla
M_0	Sample magnetisation	emu/g
T_1	Spin-lattice relaxation time	s^{-1}
R_1	Spin-lattice relaxation rate	s^{-1}
r_1	Spin-lattice relaxivity	$mM^{-1}s^{-1}$

Abbreviation	Description	Unit
T_2	Spin-spin relaxation time	s^{-1}
R_2	Spin-spin relaxation rate	s^{-1}
r_2	Spin-spin relaxivity	$mM^{-1}s^{-1}$
Σ	Standard deviation	nm
SPM	Superparamagnetic	-
T	Temperature	K
d_{TEM}	TEM	nm
THF	Tetrahydrofuran	-
τ_D	Translational diffusion time of protons	s
TEM	Transmission Electron Microscopy	-
K_{eff}	Uniaxial anisotropy constant	GHz
H	Viscosity	cP
V	Volume	nm^3

List of Figures

CHAPTER 1

Figure 1-1 Energy levels for a nucleus with spin quantum number of $\frac{1}{2}$. p. 3

Figure 1-2 Precession of the nucleus spin around the magnetic field B_0 . p. 4

Figure 1- 3 Spin-lattice relaxation process. p. 5

Figure 1-4 Spin-spin relaxation process. p. 5

Figure 1-5 Exponential decay of the exponential recovery of the longitudinal and transversal magnetization. p. 6

Figure 1-6 Atom dipole configuration for a diamagnetic material. p. 7

Figure 1-7 Atom dipole configuration for a paramagnetic material in presence and absence of an external magnetic field. p. 7

Figure 1-8 Alignment of atomic dipoles within domains in ferromagnetic materials. p. 8

Figure 1-9 Magnetization as function of magnetic field for a ferromagnetic material. p. 8

Figure 1- 10 Spin magnetic moment configuration for Fe^{2+} and Fe^{3+} . p. 10

Figure 1- 11 Coercivity as a function of particle diameter. p. 11

Figure 1- 12 Energy as a plot of the angle between the magnetization and the easy axis for a single domain particle. p. 12

Figure 1-13 Applications of magnetic nanoparticles in biomedicine. p. 14

Figure 1-14 Relaxation curve for superparamagnetic nanocrystals. p. 19

Figure 1-15 Effect of the anisotropy energy on the relaxivity. p. 20

Figure 1-16 Effect of the SPM NP size on the relaxivity. p. 20

Figure 1-17 Effect of the Néel correlation time on the relaxivity. p. 21

Figure 1-18 Interparticle interactions. p. 22

Figure 1-19 Strategies used for the preparation of colloidal nanoparticle assemblies. p. 24

Figure 1-20 Evaporation induced self-assembly of nanoparticles. p. 25

Figure 1-21 Layer-By-Layer nanoparticle assembly. p. 27

Figure 1-22 Competitive stabilizer desorption approach. p. 28

CHAPTER 2

Figure 2-1 Optical setup for dynamic light scattering. p. 34

Figure 2-2 Intensity fluctuations for large and small particles. p. 34

Figure 2-3 Correlogram of small and large iron oxide nanoparticles. p. 36

Figure 2-4 Size distribution by intensity of magnetite clusters. p. 37

Figure 2-5 Electrical double layer of a negative charged particle. p. 39

Figure 2-6 Light scattering in the Zeta potential measurements. p. 40

Figure 2-7 Plot phase versus time and Zeta potential distribution. p. 40

Figure 2-8 Prepolarised sequence (PP/S) in NMRD. p. 42

Figure 2-9 Non-polarised sequence (NP/S) in NMRD. p. 43

Figure 2-10 CPMG sequence in NMR. p. 44

Figure 2-11 Typical ICP-AES standard calibration curve. p. 46

Figure 2-12 Transmission electron microscope. p. 47

Figure 2-13 Field emission scanning microscope. p. 50

Figure 2-14 Interaction between the primary electron beam and the sample in FESEM.
p.50

Figure 2-15 MagneTherm. p. 52

Figure 2-16 Total internal reflectance in an ATR-IR system. p. 53

CHAPTER 3

Figure 3-1 TEM image of oleic acid-stabilized iron oxide and cobalt ferrite nanoparticles.
p. 60

Figure 3-2 Size distribution by intensity plot of cobalt ferrite nanoparticles. p. 60

Figure 3-3 Size distribution by intensity plot of iron ferrite nanoparticles. p. 61

Figure 3-4 Assembly data by DLS of FeO cluster formation. p. 61

Figure 3-5 Scattering intensity distribution of assembling FeO and CoFeO NPCs. p. 62

Figure 3-6 FeO NPs and CoFeO NPs assembly in chloroform. p. 63

Figure 3-7 Stages of typical assembly data by DLS of FeO cluster formation. p. 64

Figure 3-8 Water Interface Competitive Stabilizer Desorption mechanism. p. 65

Figure 3-9 Kinetics of particle assembly for suspensions phase transferred at different Fe concentrations. p. 67

Figure 3-10 Effect of the nanoparticle concentration on assembly. p. 68

Figure 3-11 Kinetic curves for oleic acid stabilised FeO and CoFeO NPs using different OA concentrations. p. 69

Figure 3-12 DLS data of FeO and CoFeO NP assembly. p. 70

Figure 3-13 DLS data of co-clustering experiments. p. 71

Figure 3-14 Intensity weighted size distribution and correlation function of CoFeO-FeO NPs co-clustering over time. p. 71

Figure 3-15 Reproducibility studies for co-clustering experiments. p. 71

Figure 3-16 Effect of co-suspension ratio on the assembly process. p. 73

Figure 3-17 Size distribution and correlation function of 107 nm CoFeO:FeO. p. 73

Figure 3-18 Bright- and dark -field FSTEM images of CoFeO:FeO (1:1) NPCs. p. 74

Figure 3-19 Glass flat bottom vessels used in scale-up experiments. p. 75

Figure 3-20 Scale up of CSD method. p. 75

Figure 3- 21 NMRD profiles of clusters made from co-suspensions of CoFeO:FeO. p. 77

Figure 3-22 NMRD $r_{\text{Co-NPCs}} = 0.5r_{\text{FeNPCs}} + 0.5r_{\text{CoNPCs}}$ simulation curve. p. 78

Figure 3-23 Relaxivity of CoFeO-FeO clusters prepared using different CoFeO:FeO ratios. p. 79

CHAPTER 4

Figure 4-1 DLS data for OA-FeO NP assembly by SI-CSD approach. p. 86

Figure 4-2 Size distribution by intensity of clustering of FeO NPs in chloroform over CN-modified silica as a function of time. p. 86

Figure 4-3 Stages of a typical assembly experiment performed with SI-CSD approach. p. 87

Figure 4-4 Dark-field FESEM image of NPCs prepared by SI-CSD. p. 88

Figure 4-5 DLS data for NPC assembly by SI-CSD at different experimental conditions. p. 89

Figure 4-7 Kinetics of particle assembly using SI- and WI-CSD approach. p. 91

Figure 4-8 NMRD profiles of NPC suspensions prepared with SI-CSD and with WI-CSD method. p. 92

Figure 4-9 FESEM image of 12-NPs. p. 95

Figure 4-10 Reproducibility study of 12-NPs assembly. p. 96

Figure 4-11 Effect of iron and OA content on the assembly using 12-NPs. p. 97

Figure 4-12 Clustering curves of 12-NPs using different content of OA. p. 97

Figure 4-13 Flow assembly device. p. 98

Figure 4-14 Size distribution by intensity of FeO NPs and NPCs produced by flow assembly. p. 99

Figure 4-15 Size distribution by intensity of different FeO NPC suspensions produced by flow assembly at similar experimental conditions. p. 101

Figure 4-16 Effect of tube length on NPC size. p. 102

Figure 4-17 Effect of flow rate on NPC size. p. 103

Figure 4-18 DLS probe system. p. 105

Figure 4-19 Size distribution by intensity of measurements performed with DLS probe and Zetasizer Nano. p. 105

Figure 4- 20 DLS data of NP clustered with WI-CSD approach measured using two different laser positions. p. 106

Figure 4- 21 DLS data of NP clustered with WI-CSD approach under the effect of a magnetic field. p. 108

Figure 4-22 Monitoring of hydrodynamic diameter DLS data of NP clustered with WI-CSD approach under the effect of a magnetic field of different strengths. p. 109

CHAPTER 5

Figure 5-1 Oleic acid stabilized iron oxide nanoparticle coated with P123 following phase transfer. p. 114

Figure 5-2 Oleic acid stabilized iron oxide nanoparticle coated with DTAB following phase transfer. p. 114

Figure 5-3 NPC phase transfer by DTAB coating. p. 117

Figure 5-4 Phase transfer of nanoparticle clusters before and after coating with P123. p.120

Figure 5-5 Z-potential distribution of FeO NPCs@P123 suspension. p. 120

Figure 5-6 FESEM image of a typical aqueous FeO NPC@P123 suspension. p. 121

Figure 5-7 ATR-IR spectra of FeO NPC@P123 suspension. p. 122

Figure 5-8 Z-potential distribution of FeO NPCs@DTAB suspension. p. 123

Figure 5-9 FESEM image of aqueous DTAB-NPC suspension. p. 124

Figure 5-10 Stability of FeO NPCs@P123 suspension. p. 124

Figure 5-11 Effect of P123 content of NPC phase transfer. p. 127

Figure 5-12 Effect of Fe content of NPC phase transfer. p. 130

Figure 5-13 NMRD profile of P123-NPCs. p. 133

Figure 5-14 Effect of P123-NPC size on relaxivity. p. 135

Figure 5-15 r_1 , r_2 and r_2/r_1 ratio as function of P123-NPCs size. p. 136

Figure 5-16 NMRD profile of DTAB-NPCs. p. 136

Figure 5-17 Effect of DTAB-NPC size on relaxivity. p. 137

Figure 5-18 r_1 , r_2 and r_2/r_1 ratio as function of DTAB-NPCs size. p. 138

Figure 5-19 Temperature–time curves of suspensions of P123-NPC and DTAB-NPCs. p. 140

Figure 5-20 SAR values of P123-NPCs and DTAB-NPCs as function of cluster size. p.140

Figure 5-21 Biototoxicity studies of P123-NPCs and DTAB-NPCs. p. 142

CHAPTER 6

Figure 6-1 Solid lipid nanoparticle, lipidic nanocomposite and their potential applications. p. 147

Figure 6-2 LNP structure and drug release after magnetic field application. p. 148

Figure 6-3 Magnetic chromatography. p. 152

Figure 6-4 ATR-IR spectra of LNPs. p. 153

Figure 6-5 Schematic representation of NPs encapsulated in lipids. p. 154

Figure 6-6 Size distribution by intensity of LNPs. p. 155

Figure 6-7 FESEM images of LNPs. p. 156

Figure 6-8 ATR-IR spectra of LNPAs. p. 156

Figure 6-9 Size distribution by intensity of LNPAs. p. 158

Figure 6-10 ATR-IR spectra of LNPCs. p. 158

Figure 6-11 Size distribution by intensity of LNPCs. p. 160

Figure 6-12 Colloidal stability study of LNPs, LNPAs and LNPCs. p. 162

Figure 6-13 NMRD profiles of LNPs. p. 163

Figure 6-14 NMRD profiles and stability of LNPs, LNPAs and LNPCs. p. 164

Figure 6-15 Effect of magnetic chromatography on LNPs magnetic properties and size distribution. p. 169

Figure 6-16 NMRD profiles of LNPAs of different size. p. 171

Figure 6-17 Effect of LNPA size on spin-lattice relaxivity. p. 171

Figure 6-18 Effect of LNPA size and magnetic filtration on spin-spin relaxivity. p. 172

Figure 6-19 NMRD profiles of LNPAs of different size. p. 174

Figure 6-20 Effect of LNPA size on spin-lattice relaxivity. p. 175

Figure 6-21 Effect of LNPC size on spin-lattice and spin-spin relaxivity values. p. 176

Figure 6-22 Temperature–time curves of LNPs, LNPA and LNPCs. p. 178

Figure 6-23 Schematic representation of LNP, LNPA and LNPC magnetic moments. p. 179

Figure 6-24 LNP, LNPA and LNPC drug loading. p. 180

Figure 6-25 Structure of the device used in drug delivery studies. p. 181

Figure 6-26 Drug release experiments. p. 182

Figure 6-27 Cell viability of THP-1 cells after 24 and 72 hour incubation with lipidic nanocomposite loaded with dexamethasone and/or DiO dye. p. 183

Figure 6-28 Cell viability of HepG2 cells after 24 hour incubation with lipidic nanocomposite loaded with dexamethasone and/or DiO dye. p. 183

List of Tables

CHAPTER 1

Table 1-1 Saturation magnetization and Curie temperature of ferromagnetic materials. p.10

Table 1-2 Single domain size limit D_{crit} . p. 11

Table 1-3 Commercial SPIO agents. p. 18

CHAPTER 2

Table 2-1 FFC NMR acquisition parameter ranges. p. 44

Table 2-2 Frequency and magnetic field strength ranges used in MFH measurements. p.52

CHAPTER 3

Table 3-1 Parameters extracted from the exponential fitting of assemblies conducted with different NP concentration. p. 67

Table 3-2 Parameters extracted from the exponential fitting for the FeO NP assembly with different amount of OA. p. 69

Table 3-3 Parameters extracted from the exponential fitting for the CoFeO NP assembly with different concentration of OA. p. 69

Table 3-4 DLS data from before and after the NMRD experiment of CoFeO-FeO clusters assembled using different CoFeO:FeO molar ratios. p. 76

CHAPTER 4

Table 4-1 Hydrodynamic diameter and PDI for clusters made by SI- and WI-CSD. p. 92

Table 4-2 NMRD data of suspensions of nanoparticle clusters prepared by WI- and SI-CSD approach. p. 93

Table 4-3 Parameters extracted from the exponential fitting of assembly experiments performed adding different amounts of oleic acid. p. 97

Table 4-4 Reproducibility study of flow assembly experiment. p. 100

Table 4-5 Stability study of flow assembly experiment. p. 101

Table 4-6 Dependence of size distribution on tube length. p. 102

Table 4-7 Dependence of size distribution on flow rate. p. 103

CHAPTER 5

Table 5-1 Surfactant/Fe mole ration in phase transfer with P123. p. 117

Table 5-2 Surfactant/Fe mole ration in phase transfer with DTAB. p. 117

Table 5-3 Hydrodynamic diameter and PDI values for NPCs prepared by WI-CSD. p. 119

Table 5-4 ATR-IR analysis of P123-NPCs. p. 122

Table 5-5 Stability of P123-NPCs. p. 125

Table 5-6 Stability of P123- and DTAB-NPCs in PBS. p. 125

Table 5-7 Effect of P123/Fe molar ratio on the phase transfer process. p. 128

Table 5-8 Effect of DTAB/Fe molar ratio on the phase transfer process. p. 129

Table 5-9 Effect of Fe concentration on phase transfer using P123. p. 130

Table 5-10 Effect of Fe concentration on phase transfer using DTAB. p. 131

Table 5-11 Phase transfer scale up. p. 132

Table 5-12 Spin-lattice and spin-spin relaxivity of P123-NPCs. p. 133

Table 5-13 Spin-lattice and spin-spin relaxivity of DTAB-NPCs. p. 137

Table 5-14 Comparison of magnetic properties of P123- and DTAB-NPCs. p. 139

CHAPTER 6

Table 6- 1 Infrared band assignments for LNPs. p. 154

Table 6-2 DLS data at 25 °C of LNP suspensions prepared with different formulations. p. 155

Table 6-3 Infrared band assignments for unloaded SLNs and LNPA. p. 157

Table 6-4 DLS data at 25 °C of LNPA suspensions in water prepared with different formulations. p. 157

Table 6-5 Infrared band assignments for uncoated NPCs and LNPCs. p. 159

Table 6-6 DLS data at 25 °C of LNPC suspensions prepared with different formulations. p. 159

Table 6-7 Stability of lipidic nanocomposite in water and PBS. p. 161

Table 6-8 Stability of LNPs. p. 163

Table 6-9 Stability of LNPAs and LNPCs. p. 164

Table 6-10 Effect of magnetic chromatography on LNP size. p. 165

Table 6-11 Effect of magnetic chromatography on LNPA size. p. 167

Table 6-12 Effect of magnetic chromatography on LNPC size. p. 168

Table 6-13 DLS and NMRD data of aqueous LNP suspensions before and after magnetic chromatography. p. 169

Table 6-14 DLS data of suspensions of LNPAs before and after magnetic chromatography. p. 170

Table 6-15 DLS data of suspensions of LNPAs before and after magnetic chromatography. p. 173

Table 6-16 DLS data of suspensions of LNPCs before and after magnetic chromatography. p. 174

Table 6-17 Effect of magnetic chromatography on lipidic nanocomposite relaxivity. p. 176

Table 6-18 Stability studies. p. 180

Table 6-19 DLS data, iron, dye and drug content in the lipidic nanocomposite suspensions. p. 183

Abstract - “Preparation and characterization of novel hierarchical nanoparticle assemblies for biomedical applications” by Fadwa El Haddassi

The biomedical applications of iron oxide nanoparticle clusters (FeO NPCs) are particularly dependent on the ability to control cluster size, architecture and surface composition, as these properties largely determine biodistribution and the extent of contrast enhancement. This highlights the need for methods to assemble FeO NPs into assemblies of controlled size. Our group recently developed a method for producing stable NPC suspensions with good control over the size by a novel process, competitive stabilizer desorption. CSD allows production of stable CHCl_3 suspensions of monodisperse, oleic acid stabilized, NPCs with sizes ranging from 40–500 nm. In CSD a substrate competes with the NP surface for the stabilizing oleic acid ligand, resulting in destabilization of NP suspensions by the gradual removal of the surface ligand. In the first part the optimization of an improved version of CSD using a $\text{CHCl}_3:\text{H}_2\text{O}$ interface as the competitive substrate, is reported. The details of the mechanistic study that permitted the scale-up are presented in detail. The robust CSD process has been applied to the assembly of different types of NPs and combinations of more than one NP type (including FeO and metal ferrite NPs), different types of substrates, NP size and finally in presence of external solicitation such as magnetic field. The development of a novel flow set-up that ideally allows the production of large quantities of NPC is also presented. The second part of the thesis presents novel methods for the transfer of nanoparticle assemblies from organic to aqueous media has been also developed which can be used to transfer clusters of controlled size in large quantities. It is shown that the final NPCs have good colloidal stability and very narrow size distributions. Assessment over the biotoxicity of these materials was also undertaken in order to study their behavior in biological systems.

CHAPTER 1

Introduction to Nuclear Magnetic resonance and Magnetic Nanoparticle Assemblies

1.1 Introduction

In the last decades significant progress has been achieved in the preparation of nanoparticles (NPs) of controlled compositions, sizes and shapes. It has been shown that such nanoparticles can be used as 'blocks' for building novel nanoparticle clusters (NPCs) that can assume the properties of the single NP and also generate new combined properties that arise from the nanoparticle-nanoparticle interactions within the nanostructure. This includes distinctive mechanical, magnetic, electronic, and optical properties. The controlled clustering of the NPs into defined geometric configurations opened a new research area in nanotechnology and as a result much interest has been paid to the nanoparticle nanostructures, either by direct NPC growth in solution or by NP assembly methods ^[1]. Self-assembly has emerged as a powerful technique for controlling the morphology and properties of inorganic nanoparticle assemblies. These techniques rely on energetically cheap and low cost processes, and provide access to a large selection of composite materials from inorganic, organic and even biological starting components ^[2].

Magnetic nanoparticles are of considerable interest both because of fundamental scientific interest and for applications in different research areas such as catalysis, data storage, biomedicine, and separation ^[3]. For example, small superparamagnetic iron oxide NPs (typically <30 nm) are very attractive for a wide range of biomedical applications since their agglomeration (resulting from strong magnetic interaction) can be avoided. Upon increase of the NP size the magnetic moment increases, but the resulting nanoparticle suspension becomes unstable because of the superparamagnetic-ferromagnetic transition. Much effort has therefore been addressed on the preparation of magnetic NP assemblies that provides an attractive strategy to controllably increase magnetization while retaining the superparamagnetic behaviour of the resulting material. Hence, the research of a possible way to control and optimize the magnetic properties of these nanostructures of biomedical interest is extremely important.

The main theme of this project is the use of nanomaterials for biomedical applications, and in particular for developing image contrast in magnetic resonance imaging (MRI). Therefore the knowledge of the basics of NMR spectroscopy and magnetism in materials are crucial for the understanding of the concepts reported. These concepts are reported in the entrance of this chapter.

1.2 The basics of NMR Spectroscopy

Nuclear Magnetic Resonance (NMR) spectroscopy is a powerful and theoretically complex analytical tool that gives information about the chemical environment of specific nuclei. The principles and physical background of this technique will be described briefly in the following paragraphs.

1.2.1 Spin

The spin is a fundamental property of nature like electrical charge or mass and protons, electrons and neutrons possess spin. A nucleus of spin I will have $2I+1$ possible orientations and a nucleus like ^1H with spin $1/2$ will have 2 possible orientations (α and β). In the absence of an external magnetic field (B_0), these orientations are of equal energy. If a magnetic field is applied, then the energy levels split. To each level is assigned a magnetic quantum number, m (Figure 1-1).

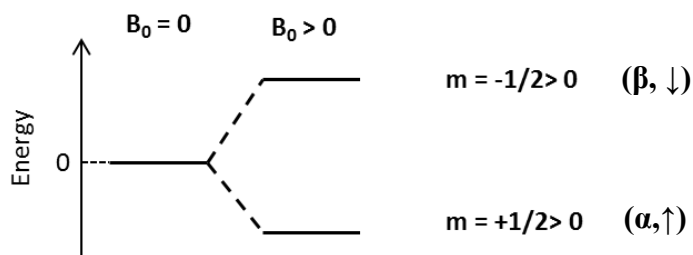


Figure 1- 1 Energy levels for a nucleus with spin quantum number of $1/2$.

When the nucleus is placed in a magnetic field, the initial populations of the energy levels are determined by thermodynamics, as described by the Boltzmann distribution described by Equation 1-1:

$$\frac{N_{\alpha}}{N_{\beta}} = e^{\frac{\Delta E}{T k_B}} \quad \text{Equation 1-1}$$

where ΔE is the energy difference between the spin states; k is Boltzmann's constant, 1.3805×10^{-23} J/Kelvin; and T is the temperature in Kelvin. At room temperature, the number of spins in the lower energy level, N_{α} , slightly outnumbers the number in the upper level, N_{β} . The nucleus has a positive charge and is spinning. This generates a small magnetic field so that the nucleus possesses a magnetic moment $\mu = \gamma I$, where γ is the gyromagnetic ratio. The difference in energy ΔE between the state α and β is given by the Equation 1-2:

$$\Delta E = \frac{\gamma \hbar B_0}{2\pi} \quad \text{Equation 1-2}$$

where \hbar is the Planks constant and B_0 is the applied magnetic field.

According to the classical physics the nucleus of spin in a magnetic field can be represented by a vector model where the angular momentum vector precesses around the magnetic field axis, z (Figure 1-2), with a frequency ω_L :

$$\omega_L = \gamma B_0 \quad \text{Equation 1-3}$$

called Larmor frequency which is proportional to B_0 and to the nuclear magnetic moment.

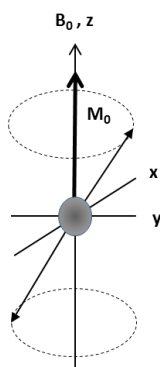


Figure 1- 2 Precession of the nucleus spin around the magnetic field B_0 .

At equilibrium, the net magnetization vector lies along the direction of the applied magnetic field B_0 and is called the equilibrium magnetization M_0 which is the vector sum of all the z-components of all proton magnetic moments. Applying a RF pulse with a frequency equal to the energy difference between the spin states, a transition between the spin states is induced (Figure 1-3, 1-4). The time constant which describes how M_Z returns to its equilibrium value is called longitudinal or spin-lattice relaxation time T_1 . The equation governing this behavior as a function of the time t after its displacement is reported in Equation 1-4:

$$M_z(t) = M_0(1 - e^{-t/T_1}) \quad \text{Equation 1-4}$$

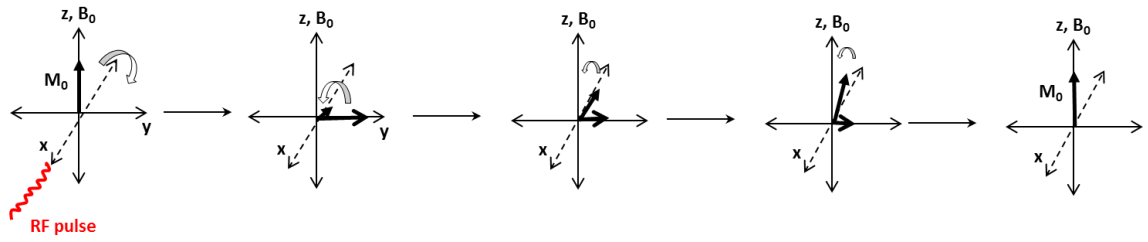


Figure 1- 3 Schematic representation of the spin-lattice relaxation process.

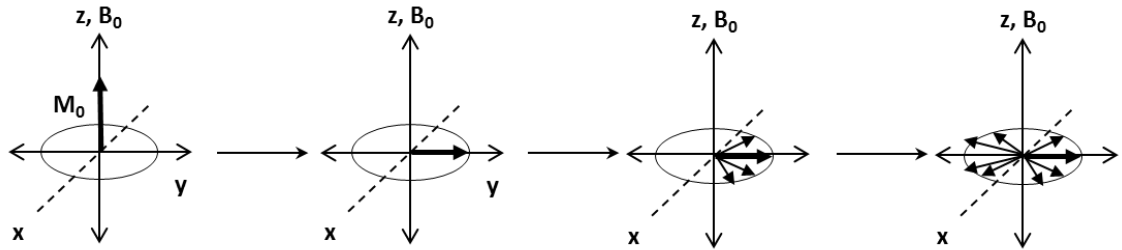


Figure 1- 4 Schematic representation of the spin-spin relaxation process.

Basically the spin-lattice relaxation mechanisms allow nuclear spins to exchange energy with their surroundings, the lattice, allowing the spin populations to equilibrate. In addition to the rotation, the net magnetization starts to dephase (Figure 1-4) because each of the spin packets making it up is experiencing a slightly different magnetic field and rotates at its own Larmor frequency. The time constant which describes the return to equilibrium of the transverse magnetization, M_{xy} , is called the transverse or spin-spin relaxation time, T_2 (Figure 1-5). The M_{xy} decay to B_0 over time is described by the Equation 1-5.

$$M_{xy}(t) = M_{xy}(0)e^{-t/T_2} \quad \text{Equation 1-5}$$

The decoherence can arise due to magnetic field inhomogeneity which is not a true "relaxation" process; it is random and dependent on the location of the molecule in the magnetic field. The corresponding transverse relaxation time constant is thus T_2^* , which is usually much smaller than T_2 . The relation between T_2^* and T_2 is given by the Equation 1-6:

$$\frac{1}{T_2^*} = \frac{1}{T_2} + \frac{1}{T_{inhom}} = \frac{1}{T_2} + \gamma\Delta B_0 \quad \text{Equation 1-6}$$

Where ΔB_0 the difference in strength of the locally varying field.

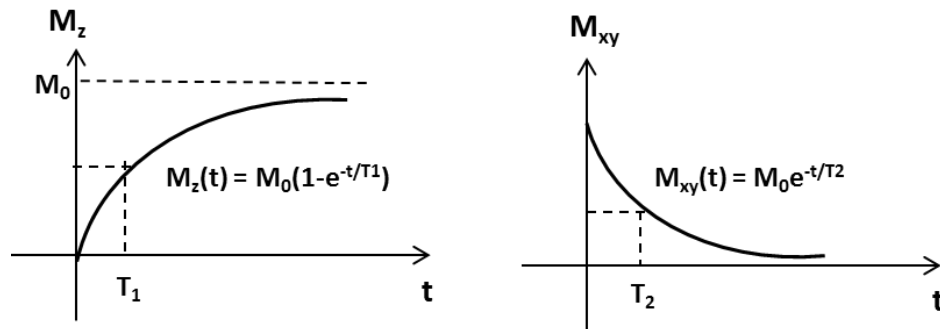


Figure 1- 5 Exponential decay of the exponential recovery of the (left) longitudinal and (right) transversal magnetization component M_z and M_{xy} .

1.3 Magnetism and magnetic materials

The magnetic materials can be classified based on how they to respond in presence of an applied magnetic field. The susceptibility (χ) indicates whether the material is attracted into or repelled out of the external magnetic field (H) and it is given by the Equation 1-7:

$$\chi = \frac{M}{H} \quad \text{Equation 1-7}$$

Where M is the net magnetization of the material.

The magnetic behaviour of materials can be classified into five major groups: diamagnetism, paramagnetism, ferromagnetism, antiferromagnetism and ferrimagnetism.

Diamagnetic materials are composed by atoms that have no net moments because all the orbital shells are filled and no unpaired electrons are present ^[4]. However when exposed to a magnetic field a negative magnetization is generated so that the susceptibility is negative (Figure 1-6). Diamagnetism is due to the change of the orbital electron motion in presence of a magnetic field that generates a really small induced magnetic moment oriented in the opposite direction of H . This phenomenon persists just in presence of an applied field.

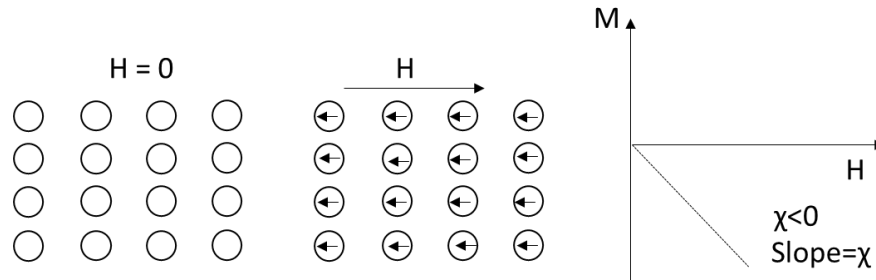


Figure 1- 6 (Left) Schematic representation of the atom dipole configuration for a diamagnetic material in presence and absence of an external magnetic field. (Right) Magnetization as a function of the applied magnetic field for a diamagnetic material.

Paramagnetic materials are formed by atoms that possess a permanent dipole moment due to unpaired electrons in partially filled orbitals [4]. In the absence of an external magnetic field, the magnetic moments are free to rotate and assume random orientations so that the material do not exhibit a net magnetic moment (Figure 1-7). Paramagnetism occurs when the magnetic dipoles align with an external field without interacting with adjacent magnetic moments. The magnetic susceptibility for these materials is positive and it is proportional to the applied magnetic field. Once the external field is removed, the magnetic moments resume random orientations so that the net magnetization is lost.

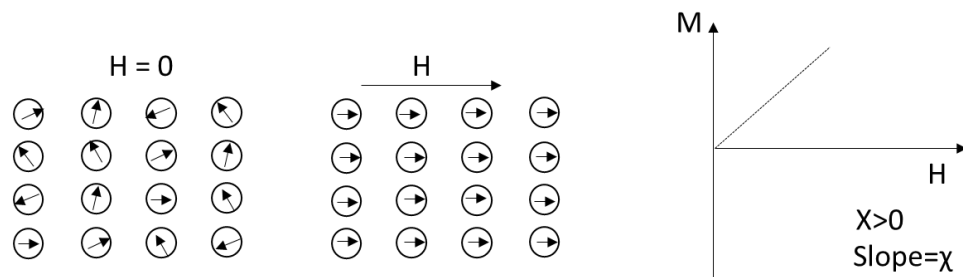


Figure 1- 7 (Left) Schematic representation of the atom dipole configuration for a paramagnetic material in presence and absence of an external magnetic field. (Right) Magnetization as a function of the applied magnetic field for a paramagnetic material.

Ferromagnetic materials have a permanent magnetic moment even in absence of an external field. This is due to the coupling of orderly arrays of unpaired electrons spins of large groups of atoms that form microscopic and spontaneously magnetized magnetic domains. In absence of the external magnetic field the domains are randomly orientated; a high applied field reorient the domains to face the same direction so that the material has a net magnetization (Figure 1-8).

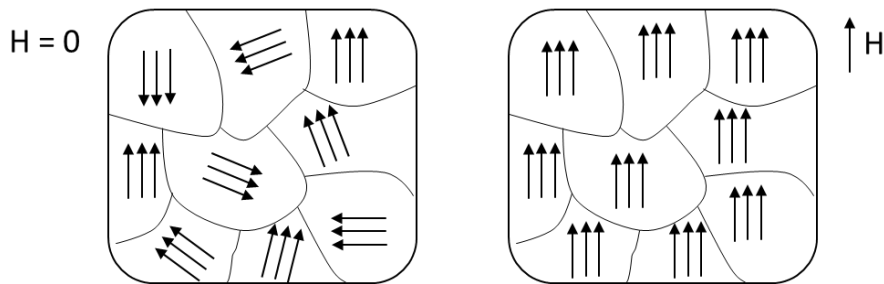


Figure 1- 8 (Left) Schematic representation of the mutual alignment of atomic dipoles within domains in ferromagnetic materials.

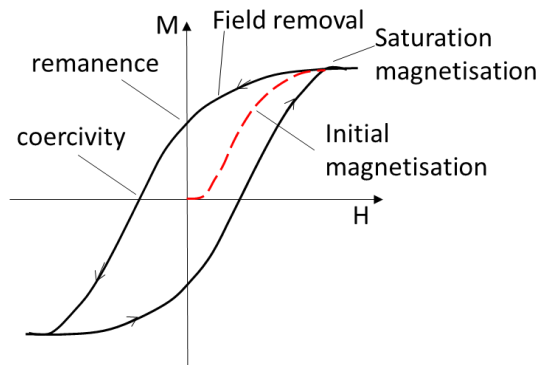


Figure 1- 9 Magnetization as function of magnetic field for a ferromagnetic material which is subjected to forward and reverse saturation.

Saturation of the magnetisations is achieved until all the macroscopic specimen becomes a single domain which is aligned with the applied field. From the saturation point as the field is reduced the process by which the domains change is reversed and a hysteresis effect is produced (Figure 1-9). At zero field, there exists a residual magnetization that is called remanence; the material remains magnetized in the absence of H field. To reduce the residual magnetization an H field (called coercivity) of magnitude in a direction opposite to that of the original external field must be applied. Upon increasing of the applied field in this reverse direction, saturation is ultimately achieved once again completing the symmetrical hysteresis loop. The hysteresis for ferromagnetic materials depends on several parameters including particle size, shape, domain structure (single or multi-domain) and temperature [5]. Even though electronic exchange forces in ferromagnets are very large, thermal energy eventually overcomes the exchange and produces a randomizing effect. This occurs at the Curie temperature and the saturation magnetization decreases to zero. Below the Curie temperature, the magnetic moments are ordered while above it, disordered. Ferromagnetism is displayed by the transition metals iron (ferrite), cobalt, nickel and some of the rare earth metals such as gadolinium.

Antiferromagnetism is due to coupling of adjacent atoms or ions spin moments. Unlike ferromagnetic materials, in presence of an external magnetic field the magnetic moments align spontaneously antiparallel to the neighbouring moments resulting in a net moment of zero. The magnetic susceptibility reaches a maximum value at a critical temperature known as Neel temperature above which the antiferromagnetic material become paramagnetic. Manganese oxide (MnO) is one material that displays this magnetic behaviour ^[6]. As in case of the antiferromagnetism, the ferrimagnetism arises from the presence of populations of atoms of opposing magnetic moments however in the latter case an unequal and spontaneous and spontaneous net magnetization remains in absence of an external magnetic field.

Similarly to antiferromagnetism, ferromagnetism arises from the antiparallel spin-coupling interactions between atoms or ions with the exception that the net magnetization is due to the incomplete cancellation of the opposing spin moments which have an unequal magnitude. An example of ferromagnetic materials are metal oxides such as iron oxides, maghemite ($\gamma\text{-Fe}_2\text{O}_3$) and magnetite (Fe_3O_4), and cobalt ferrite (CoFe_2O_4). In iron oxides the position of iron ions is responsible for the net magnetization of the crystal which is formed by two ferromagnetic sublattices, a tetrahedral (A) octahedral (B) site. The schematic representation of the distribution of the magnetic moments in the crystal structure of iron oxide of formula $[\text{Fe}^{3+}]_A[\text{Fe}^{2+}\text{Fe}^{3+}]_B\text{O}_4$ is shown in Figure 1-10. At the Curie temperature, the magnetic moments in site A and B are in opposite directions so that the resulting material is ferrimagnetic. Maghemite and magnetite has a similar inverse spinel structure with a cubic unit cell but they differ in the iron ions arrangement within the crystal. For instance in maghemite the trivalent iron cations occupy both tetrahedral A-sites and octahedral B-sites while cation vacancies are confined to octahedral sites so that the global positive charge is increased ^[7]. The magnetic moments of these ions are opposite in direction and unequal so that the resulting material has ferromagnetic properties below the Curie temperature.

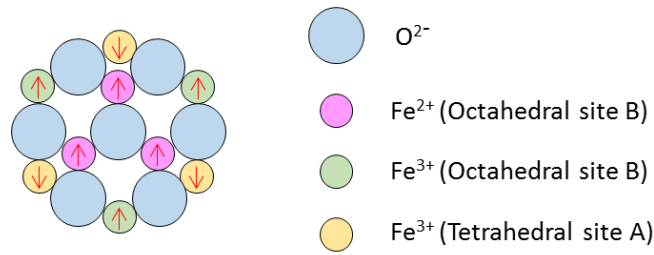


Figure 1- 10 Schematic representation of the spin magnetic moment configuration for Fe^{2+} and Fe^{3+} [8].

For ferromagnetism, antiferromagnetism, and ferrimagnetism, the atomic thermal motions oppose the coupling forces between the adjacent atomic dipole moments, causing some magnetic moment misalignment, even in presence of an external field. This results in a decrease in the saturation magnetization with increasing of the temperature until it drops to zero at what it is called Curie temperature (T_c). Above this temperature both ferrimagnetic and ferromagnetic materials become paramagnetic. The temperature dependence of paramagnetic materials can be determined by the Curie Law given by the Equation 1-8:

$$\chi = \frac{C}{T} \quad \text{Equation 1-8}$$

where C is the Curie constant which is characteristic to a given material (Table 1-1).

Material	M_s (KA/m)	T_c ($^{\circ}C$)
Magnetite	585	470
Maghemite	590	414
Cobalt ferrite	520	422

Table 1- 1 The saturation magnetization (M_s) and Curie temperature (T_c) of ferromagnetic materials.

1.4 Superparamagnetism in nanoparticles

The magnetic properties of the nanoparticles (NPs) are strictly correlated to their size, shape and composition and temperature [9]. When the size is below a certain critical diameter (D_{crit}), each nanoparticle becomes a single magnetic domain and behave like a

single magnet responsive to an external magnetic field. These materials are called superparamagnetic NPs and their critical diameter is given by the Equation 1-9:

$$D_{crit} = 18 \frac{(AK_{eff})^{1/2}}{\mu_0 M_s^2} \quad \text{Equation 1-9}$$

where A is the exchange constant, K_{eff} is the uniaxial anisotropy constant, μ_0 is the constant of permeability and M_s is the saturation magnetization.

Within a crystal domains are separated by domain walls which have characteristic width and their motion is a primary means reversing magnetization. The dependence of coercivity on particle diameter is similar to the one shown in Figure 1-11. As the particle size decreases toward D_{crit} value, the formation of domain walls become energetically unfavourable so that single domain particles are formed resulting in larger coercivities. A further decrease of the particle size below the single domain size limit the transition from ferromagnetic to the superparamagnetic state occurs. As the particle continues to decrease below the superparamagnetic size limit D_{spm} the particles are considered as giant magnetic moments which are not interacting with each other and can spontaneously fluctuate between two energetically equal magnetisation directions since the thermal energy ($k_b T$) is larger than the anisotropy energy.

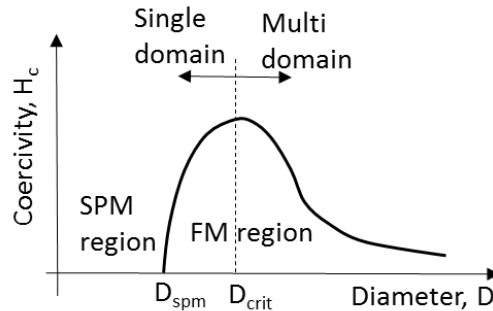


Figure 1- 11 Coercivity (H_c) as a function of particle diameter (D). D_{crit} is the single domain size limit while D_{spm} is the superparamagnetic size limit. FM stands for ferromagnetic region.

Material	D_{crit} (nm)
Co	70
Fe	14
Fe_3O_4	128
γ - Fe_2O_4	166
Ni	55

Table 1- 2 The single domain size limit D_{crit} for some materials ^[9].

The anisotropy energy (E_a) is the energy barrier required for the flip of the magnetization from parallel or anti-parallel configuration respect the easy axis which is the direction favoured by the magnetocrystalline anisotropy (Figure 1-12). It can be described by the Equation 1-10:

$$\Delta E_a(\vartheta) = K_{eff}V\sin^2\vartheta \quad \text{Equation 1-10}$$

Where K_{eff} is the anisotropy constant, V the volume of the crystal and θ is the angle between the magnetization vector and the easy axis. The anisotropy energy is proportional to the crystal volume increases thus very rapidly as crystal radius increases. The magnetic energy increases with the tilt angle between the magnetization vector and the directions that minimize the anisotropy energy ^[10].

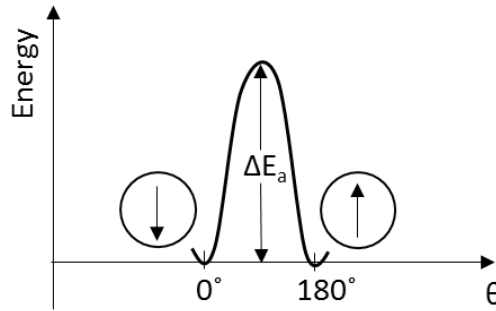


Figure 1- 12 Energy as a plot of the angle θ , which is the angle between the magnetization and the easy axis for a single domain particle.

The fluctuations of the magnetization between parallel and anti-parallel configuration are characterized by the Néel relaxation time τ_N which is given by the Néel-Brown expression (Equation 1-11) where $\tau_0 \sim 10^{-9}$, k_B is the Boltzmann constant and T is the absolute temperature.

$$\tau_N = \tau_0 \exp\left(\frac{K_{eff}V}{k_B T}\right) \quad \text{Equation 1-11}$$

With increasing of the temperature, the thermal energy is larger than the anisotropy barrier so that the rate of fluctuations is higher. The fluctuation rate decreases to a point so-called blocking temperature (T_B) where the magnetic moments are static and below at

this temperature the superparamagnetic behaviour disappears. T_B is given by the Equation 1-12.

$$T_B = \frac{K_{eff}V}{25k_B} \quad \text{Equation 1-12}$$

In the case of superparamagnetic NPs, the magnetization is not fixed overtime and tends to go back to the equilibrium by two processes once the external magnetic field is switched off so that the net magnetization is no longer retained. The first is the Néel relaxation time τ_N , and the second is the Brownian relaxation time which controls the rotation of the particle. The overall magnetic relaxation rate τ of the colloidal particle is defined by the Equation 1-13:

$$\frac{1}{\tau} = \frac{1}{\tau_N} + \frac{1}{\tau_B} \quad \text{Equation 1-13}$$

$$\tau_B = \frac{3V\eta}{Tk_B} \quad \text{Equation 1-14}$$

where τ_B is the Brownian relaxation time; V is the volume of the crystal and η is the viscosity of the medium (Equation 1-14). For large particles, τ_B is longer than τ_N because the Brownian relaxation time depends from the crystal volume and Néel relaxation is an exponential function of the volume.

1.5 Applications of nanoparticle and nanoparticle assemblies in biomedicine

Both superparamagnetic NPs and NP assemblies have been widely exploited in biology for diagnostic and therapeutic applications, opening up great interest in material science field for their potential in bringing antitumor biomedicine into a new era ^[11]. Those materials can be used as cellular targeting nanostructure in drug delivery, therapeutic agents and contrast agents for imaging (Figure 1-13). Several studies have shown that it is possible to visualize the behaviour of NPs in metabolic pathways and to control their response to external stimuli, including heat (RF pulses) and magnetic field to name a few. This improvement could lead to optimized and personalized therapy maximizing the efficiency of therapeutic agents and decreasing the dose injected to the patient ^[12]. In the

next few sections some of the main applications of the NPs and NPCs in biomedicine will be reported.

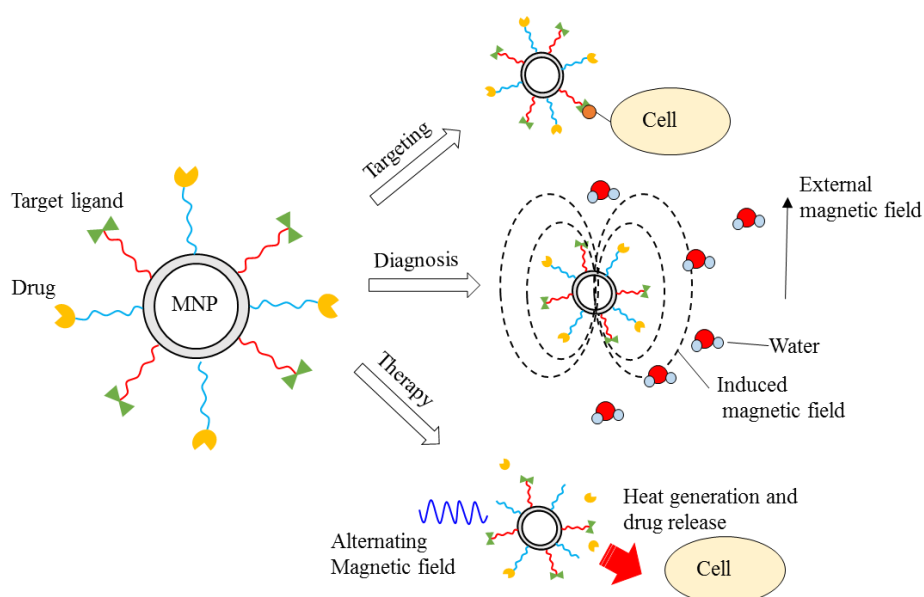


Figure 1- 13 Schematic representation of applications of magnetic nanoparticles in biomedicine.

1.5.1 Drug Delivery

Nano-systems that incorporate therapeutic agents, molecular targeting, and diagnostic imaging properties are becoming the next generation of multifunctional nanomedicine. The primary limitations of most chemotherapeutic agents is their low non-specificity and thus potential side effects to healthy cells. To overcome this problem, magnetic drug targeting technique utilizes the attraction of magnetic NPs or NPCs carriers to an external magnetic field in order to increase the specific delivery ^[13]. In general, this process is based on the attachment of a cytotoxic drug to the biocompatible magnetic NP or NPC carrier and after intravenous injection of these structures as colloidal suspension, a magnetic field gradient is applied to conduct the magnetic material to the pathological site and release of the therapeutic agent. However, there are many parameters that complicate the execution of this approach. Variables such as the physical properties like the stability of the drug-loaded magnetic NPs or NPCs, the field strength, the blood flow rate and many other elements that play a role in determining the effectiveness of this method of drug delivery. Among the many nanostructures, polymeric micelles, self-assembled nanoparticles from amphiphilic block copolymers, provide a core-shell configuration wherein the hydrophobic core works as a natural carrier environment for

hydrophobic drugs and the hydrophilic shell allows particle stabilization in aqueous medium ^[14]. Nasongkla and co-workers ^[15] reported the development of multifunctional polymeric micelles with cancer-targeting capability for controlled drug delivery and efficient magnetic resonance imaging (MRI) contrast characteristics. These micelles are composed of three components: (1) a chemotherapeutic agent doxorubicin (DOXO) that is released from polymeric micelles because it is pH responsive; (2) a cRGD ligand that can target $\alpha_v\beta_3$ integrins on tumor endothelial cells and subsequently induce receptor-mediated endocytosis for cell uptake; and (3) a SPM NPC of iron oxide NPs that is placed in the micelle core. In vitro MRI and cytotoxicity studies demonstrated the ultrasensitive MRI imaging and $\alpha_v\beta_3$ -specific cytotoxic response of these robust and stable polymeric micelles in the physiological environment.

1.5.2 Magnetic fluid hyperthermia therapy

Hyperthermia has been utilized in treatment of malignant tumours exposing cancer cells to high temperatures, typically 41–46 °C ^[16]. Based on the nature of magnetic NPs, hyperthermia therapy combined with MRI technique ^[17] would generate heat by alternating a magnetic field to kill tumour cells as long as the imaging displays the position of the magnetic particles. This approach decreases efficiently undesired damage to healthy cells with an increase also of the efficiency of the therapy. The mechanisms behind hyperthermia are strongly correlated to the magnetic NP/NPC properties and particularly to their magnetic state, being superparamagnetic or ferromagnetic monodomain or multidomain, and to their size. Several advantages have been pointed out for 8-20 nm iron oxide NPs because of their high stability in colloidal suspension, their properties as biocompatible MRI contrast agents, and a comprehensive theoretical description of their magnetic behaviour dominated by Neel and Brown relaxation mechanism predicting an optimum diameter for heat generation with all the other properties being fixed ^[18]. Magnetic NPCs synthesized embedded in a polymer or organic coating have been proposed as efficient mediators for hyperthermia in cancer treatment. Dutz et al ^[19] reported a method to prepare water-based suspensions of multicore nanoparticles by coating of assembled nanomagnets with a carboxymethyl dextran shell. The peculiar structure of such nanosized clusters have been shown theoretically and experimentally to influence their magnetic properties. However, the relationship between magneto-structural properties and heating efficiency is still not clear.

The parameter determining the heating of the magnetic nanostructures in a medium is called specific absorption rate (SAR) that is the rate at which electromagnetic energy is absorbed by a unit mass of medium. The SAR is expressed in calories per kilogram (W/Kg) and is proportional to the rate of the temperature increase $\Delta T / \Delta t$ as described by the Equation 1-15:

$$SAR = 4.1868 \frac{P}{m_c} = C_e \frac{\Delta T}{\Delta t} \quad \text{Equation 1- 15}$$

where P is the electromagnetic wave power absorbed by the biological material, m_c is its mass and C_e its specific heat capacity; the temperature increase ΔT is expressed in °C and the exposure time Δt is expressed in seconds. For a given SPM material, the SAR is mainly determined by the volume ratio of the nanocrystal ^[10] and it is reduced by increasing the NP/NPC size distribution ^[18]. The SAR of a magnetic material depends on several parameters including particle composition, particle size distribution shape, frequency and the amplitude of the applied magnetic field ^[20]. Typically monodispersed Fe₃O₄ NPs with core size in the range 5-19 nm gives SAR in the range of 60-2000 W/g ^[21]. Guardia et al. ^[22] reported recently a one-pot synthesis of 19 nm PEG-stabilized cube shaped iron oxide NPs that showed SAR values in clinical conditions up to 2452 W/g at a frequency of 520 kHz with cell mortality of about 50% after 1 hour of treatment at 43°C. Very high SAR values were measured recently using various nanoparticle assemblies ^[23] ^[24] with the maximal value of 960 W/g at a frequency of 410 kHz and moderate magnetic field amplitude (10 kA/m) in bacterial magnetosomes ^[23]. Recently Bazzi et al. ^[25] produced flowerlike assembly of 11 nm maghemite NPs that have a heating efficiency comparable to that of magnetosome chains extracted from bacteria and to 19 nm cubic maghemite nanoparticles synthesized by Guardia ^[22].

Magnetic nanoparticles can generate heat as a result of two mechanisms: the Néel relaxation and rotational Brownian motion ^[26]. In the first mechanism the heat is generated by the rotation of the magnetic moments which rotates at the characteristic relaxation time τ_N described by the Equation 1-1. The maximum output of heating through Néel relaxation is given by the Equation 1-16.

$$\nu_N = \frac{1}{2\pi\tau_N} \quad \text{Equation 1- 16}$$

The second mechanism generates heat by the rotation of the whole particle of volume V_B under the effect of a magnetic field ^[20]; the characteristic time of Brownian relaxation time τ_B is described by the Equation 1-17.

$$\tau_B = \frac{3\eta V_B}{Tk_B} \quad \text{Equation 1- 17}$$

1.5.3 Magnetic Resonance Imaging

Magnetic resonance imaging (MRI) is a non-invasive imaging technique, based on NMR, for visualizing with excellent anatomical detail and soft tissue contrast ^[27] by using contrast agents. MRI contrast agents are substance generally classified as positive/negative agents or T_1/T_2 agents. Positive contrast agents or T_1 -agents, reduce the spin-lattice relaxation time of the ^1H magnetisation of the surrounding molecules of water giving an enhancement of the local MRI signal (bright spot) under T_1 -weighted conditions. Negative contrast agents or T_2 -agents, reduce the spin-spin relaxation time giving a reduction of the local signal intensity. Upon accumulation in tissues, single magnetic NPs provide MR contrast enhancement by shortening both the longitudinal and transverse relaxation of surrounding protons. However, T_1 shortening processes require a close interaction between protons and T_1 -agents which can be hindered by the thickness of the coating on the NP surface. The effect of MNP on T_2 shortening is caused by the large susceptibility difference between the NPs and surrounding medium resulting in microscopic magnetic field gradients. Diffusion of protons through these field gradients leads to dephasing of the proton magnetic moments and thus decreased transverse relaxation times of protons ^[28].

In MRI two pulse sequences are commonly used: the spin-echo and the inversion-recovery sequence. By adjusting the parameters of these pulse sequences is possible to enhance T_1 and/or T_2 , tailoring the sensitivity of the MRI signal. Over the last decades, many scientists have focused on developing novel MRI contrast agents based on monodisperse magnetic NPs, with enhanced relaxation properties and biocompatibility ^[29] ^[30]. Both SPM magnetite (Fe_3O_4) or maghemite ($\gamma\text{-Fe}_2\text{O}_3$) NPs and iron oxide based NPCs received great attention as a nanoparticle contrast agent in the last two decades because their low toxicity ^[31]. These SPM nanocrystal agents induce strong enhancement of the T_1 - relaxation rate of water, but their dominant effect is on T_2/T_2^* relaxation due to

the large magnetic moment of the nanoparticles. The relaxation enhancement observed with iron based contrast agents are similar to the ones observed with gadolinium agents, but, with generally stronger effects on transverse relaxation. Table 1-3 reports some of the iron oxide based MRI contrast agents commercially available with their relative features. Besides iron oxides, various bimetallic ferrite nanoparticles, such as CoFe_2O_4 , MnFe_2O_4 ,^[32] NiFe_2O_4 ,^[33] have been tested as T_2 contrast media.

Trade name	Relaxivity ($\text{mM}^{-1}\text{s}^{-1}$)	Coating agent	d_{hyd} (nm)
Ferumoxtran-10	$r_1 = 9.9$ $r_2 = 65$	dextran T10-T1	15-30
Ferumoxytol	$r_1 = 15$ $r_2 = 89$	carboxymethyl-dextran	30
Resovist	$r_1 = 10.7$ $r_2 = 38$	carboxydextran	21

Table 1- 3 SPIO agents available in the market. The relaxivity values are measured at 1.5 T.

The analytical method used to assess the contrast efficiency involves measuring the ^1H relaxation time T_1 , T_2 of the suspending medium as a function of the concentration of the contrast agent. The relaxivity values r_1 , r_2 quantify the relaxation enhancement per millimolar concentration of the magnetic metal in the suspension, and are used as a measure of the efficiency of an agent *in vitro*:

$$r_i = \frac{R_{i,\text{obs}} - R_{i,\text{dipolar}}}{[M]} \quad \text{Equation 1- 18}$$

$R_{i,\text{obs}}$ is the reciprocal of the relaxation time measured ($1/T_{1,2}$) at a given concentration of the magnetic metal M , $R_{i,\text{dipolar}}$ is the rate of pure solvent. Normally the observation of a linear dependence of $R_{i,\text{obs}}$ on concentration confirms stability of the agent across the concentration range and the relaxivity value r_i (units $\text{s}^{-1}\text{mM}^{-1}$) can be extracted as the slope.

1.6 Study of magnetic properties of nanoparticle and nanoparticle clusters by NMRD

The field dependence on the longitudinal relaxation rate is an interesting tool to control the reproducibility and optimize the parameters of magnetic NP and NPC synthesis. Nuclear Magnetic Resonance Dispersion (NMRD) profiles are commonly used for investigating the field dependence of the relaxation behavior of magnetic colloidal suspensions in function of the applied magnetic field B_0 (from 0.01 up to 40 MHz). The fitting of the NMRD profiles by the accepted superparamagnetic nanoparticles theory (SPM theory) developed by Muller and co-workers^{[34] [35]} provides information about the nature of the NPs and NPCs, namely their specific magnetic properties, size, their anisotropy energy and their Néel relaxation time.

In SPM theory the low frequency ^1H relaxation is controlled by random fluctuations of the magnetic moments of the NPs, called Néel relaxation process, so that the reorientation of the moment (Equation 1-11), τ_N is fast, when compared to the translational diffusion coefficient of the solvent, $\tau_D = d_p^2/4D$, where d is the particle diameter and D is the diffusion coefficient. At high frequency the magnetic moments are locked to the given magnetic field B_0 and the overall relaxation is fully controlled by diffusion of the solvent molecules, giving rise to the Brownian relaxation process. At intermediate frequencies the relaxation is obtained by interpolation of the Néel and Brownian relaxation weighted by the Langevin function, which gives the fraction of spins locked at the magnetic field B_0 . All the relaxation processes described above are represented in Figure 1-14.

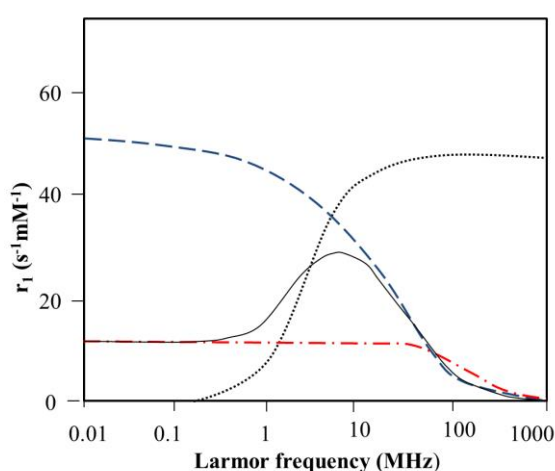


Figure 1- 14 Representation of relaxation curve (solid black line) for superparamagnetic nanocrystals and the contributing relaxation curves, Néel (red) and Brownian (blue) relaxation^[10]. Langevin function (---) is also reported.

Finally because to the high sensitivity of r_1 to the aggregation state of magnetic nanomaterials, the NMRD technique can give informations about the magnetic parameters; the magnetic anisotropy energy, saturation magnetisation, Néel correlation time and the diameter of the suspended nanomagnets. This makes it a powerful tool for the characterization of colloidal magnetic materials. Informations about the characteristic magnetic anisotropy and size of the NPs (or NPCs) are given by the position and depth of the minimum in the mid-frequency range. The depth of the minimum increases for smaller particles. The effect of the anisotropy energy on the relaxivity is shown in Figure 1-15.

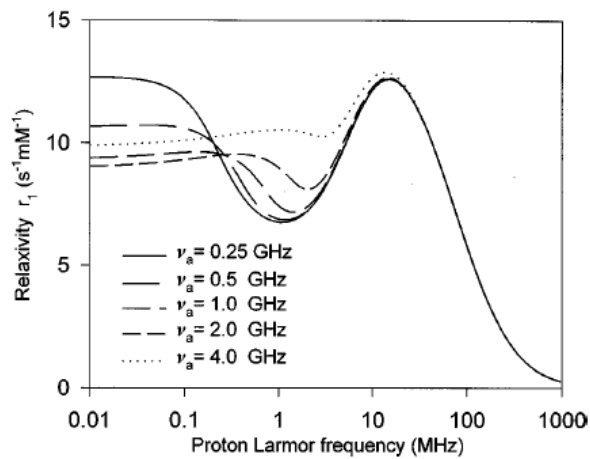


Figure 1- 15 NMRD curve simulations showing the effect of the anisotropy energy on the relaxivity response of 4.5 nm NPs, $\tau_N = 20$ ns, $M_s = 2.07 \times 10^5$ A/m, $D_{H_2O} = 3.4 \times 10^{-9}$ m²/s at T= 310 K [36].

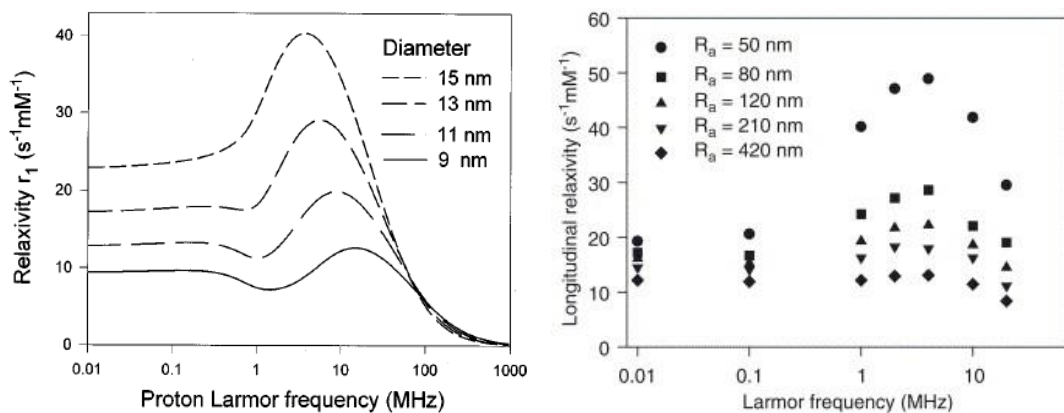


Figure 1- 16 (Left) NMRD curve simulations showing the effect of the SPM NP size on the relaxivity; $\tau_N = 20$ ns, $M_s = 2.07 \times 10^5$ A/m, $\Delta E_{anis} = 1$ GHz, $D_{H_2O} = 3.4 \times 10^{-9}$ m²/s at T= 310 K [36]. (Right) Experimental NMRD profiles showing the effect of ferrite NPC size on the relaxivity at 310 K [37].

The position and the amplitude of the r_1 maximum is dependent on the particle or NPC size and a shift to lower frequencies is expected with increasing of the size. The global amplitude of the r_1 curves is scaled according to the saturation magnetisation (M_s) of the nanostructure. Simulated and experimental NMRD curves demonstrating the effect of size on the relaxivity for NPs and NPCs is shown in Figure 1-16.

Finally since the relaxation response at low frequencies is mainly caused by the fluctuations of the particle magnetic moment, informations about the Néel correlation time τ_N which is described by the Equation 1-11 can be extracted from this portion of the NMRD profile. The effect of τ_N on the relaxivity is shown in Figure 1-17.

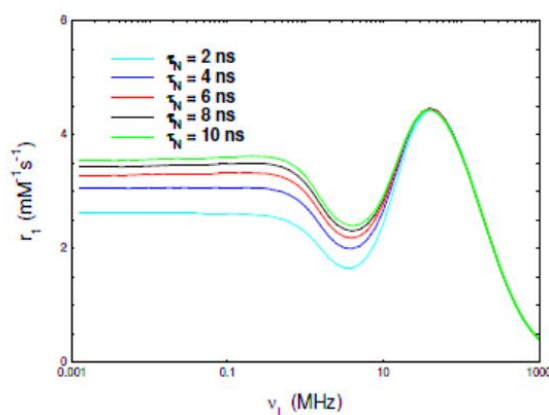


Figure 1- 17 NMRD curve simulations showing the effect of the Néel correlation time (τ_N) on the relaxivity for SPM NPs of 6 nm; $M_s=40$ emu/g, $\Delta E_{anis}= 2$ GHz, $D_{H_2O}= 4.02 \times 10^{-5}$ cm²/s [38].

Having defined the attractive functional properties of magnetic NPs and NPCs, the following sections will focus on strategies for the production and surface functionalization of colloidal NPCs.

1.7 Interparticle interactions

Stable nanoparticle suspensions are normally formed from pre-formed, and usually coated. NPs that are stabilized through electrostatic and/or steric interactions that dominate at short distances. Upon application of a stimulus (*e.g.* addition of a solvent), the repulsive forces between the NPs can be reduced and/or the attractive terms of the total interaction potential can increase leading to spontaneous assembly of the NPs in

order to reduce their surface area to volume ratio. The changes to the total interactions that drive the clustering process are typically solvophobic, electrostatic, Van der Waals (VdW) and/or magnetic. The total interaction potential (Φ_{tot}) can be considered as the sum of the contribution of each interaction (Equation 1-19).

$$\Phi_{tot} = \Phi_{ligand} + \Phi_{elect} + \Phi_{VdW} + \Phi_{magn} \quad \text{Equation 1- 19}$$

So for instance, in non-aqueous suspensions for MNPs, the interaction potential is mainly dominated by the Van der Waals-, ligand- and the magnetic- terms. Controlled assembly is commonly achieved through modification of the short-range ligand interactions, involving both ligand-ligand and solvent-ligand interactions, and which can include steric, osmotic, elastic, solvophilic, solvophobic and depletion terms ^[39]. In aqueous suspensions the electrostatic interactions can be tuned by altering the NP surface charge density through the pH or by controlling the salt concentration in suspension. The interaction potential for sterically stabilized MNPs in non-aqueous media, as a function of the surface-to-surface interparticle distance (d_{ss}) is illustrated in Figure 1-18. The ligand coated NPs do not “stick” to each other as long as the potential interaction is positive.

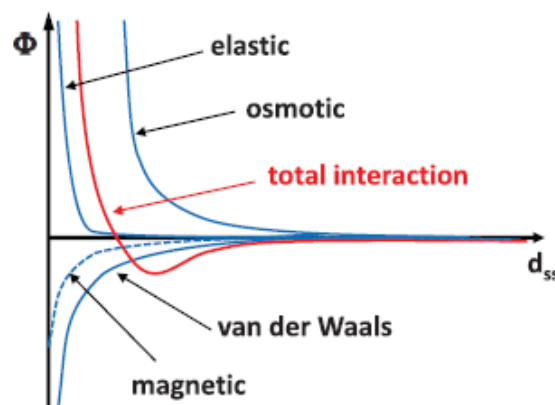


Figure 1- 18 Interaction potential for sterically stabilized NPs as function of the surface-to-surface interparticle distance ^[39].

1.8 Synthetic strategies for Magnetic Nanoparticle assemblies

Colloidal NPs are inorganic nanocrystals stabilized by a layer of organic ligands and dispersed in a solution. Their synthesis typically involves the reaction of a specific inorganic precursors in organic solvents at high temperatures ^[40]. Many type of NPs important in the nanotechnology, such as semiconductor and metal oxide NPs, can be easily prepared through various modified versions of the thermolytic method. By heating up the reaction solution to a certain temperature (typically 150–320 °C), the precursors are chemically transformed into active atomic or molecular species to form NPs ^[41]. Even though the reaction mechanism is not fully understood yet, in case of the formation of monodisperse NPs is believed to occur in two distinct phases; nucleation and growth. In order to produce NPs with narrow size distribution these two phase need to be separated. This can be achieved by using two nucleation strategies, homogenous or heterogeneous nucleation. In case of the homogeneous nucleation, a single nucleation event generated typically by heat is followed by a slow controlled growth phase. For instance, the precursor mixed with the organic solvent decomposes and generates metal ions at the reflux temperature of the solvent. When the concentration of metal ions exceeds the saturation limit, a single homogenous nucleation event occurs so that the growth of the particle starts and monodisperse NPs are formed resulting into the decrease of the global energy of the system because of the NP lower surface area to volume ratio. In the case of the heterogeneous nucleation, the nucleation phase is physically separated from the growth phase, namely pre-formed nanocrystals (or “seeds”) are introduced into a fresh solution reaction for the deposition of “new” metal ions onto the seed surfaces leading to the growth to larger monodisperse NPs. The NP size can be controlled by playing with several parameters such as by stopping the reaction at different growth stages, by changing the temperature, ligand concentrations or by changing the inorganic precursor:solvent ratio. Shaped nanoparticles can also be synthesized by modulating other parameters such as taking advantage of the selective cohesion of certain ligands to specific crystalline faces to kinetically control the growth rates along different crystalline directions ^[42]. The formation of complex NP architectures typically implicates different and more complicated reaction pathways. As shown in Figure 1-19, there are basically two strategies for NPC preparation: (i) one-step synthetic procedures which include the NP synthesis and their aggregation into clusters in a single step; and (ii) multi-step processes which first produce NPs of particular surface functionality, shape and size, and then assemble them into NPCs of designed arrangements in distinct steps.

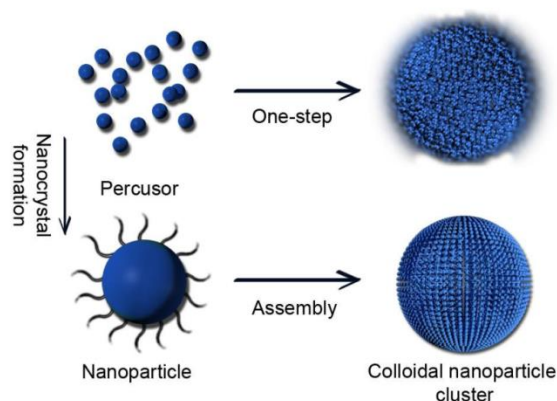


Figure 1- 19 Schematic illustration of the strategies used for the preparation of colloidal nanoparticle assemblies ^[1].

NPCs can be produced through a number of different one-step techniques, including solvothermal, ^[43] thermolysis, ^[44] and microwave ^[45] methods. Each of these techniques involves two growth stages in which primary nanoparticles first nucleate and grow in a supersaturated solution and then assembled into larger structures. On the other hand the multi-step approach can be highly attractive for the preparation of secondary structure nanomaterials with various arrangement and programmable properties. Several example of multi-step approaches can be found in literature, wherein the assembly step is driven by modulation of the colloidal interactions including polymer mediated assembly, layer-by-layer assembly, ^[46] interfacial tension ^[47] and evaporation induced self-assembly ^[48]. One-step synthesis of NPCs are more time-saving than those involving multiple steps and the NPCs produced by these methods often have narrower size distributions ^[49], which is very important for example in biomedical applications or in the crystals for optical applications. However, the literature only contains a limited number of examples for successful preparation of NPC structures because controlling the NP clustering process is even more challenging than that of simple isolated NPs. The key issue is to identify the critical conditions avoiding the formation of uncontrolled aggregations with random configurations. Considering the variety of NPs that has been prepared in the last decade, and the many possibilities to arrange them, multi-steps approaches are advantageous for preparing materials with tailored properties, as they may limit the number of determinant factors.

A more detailed review of the colloidal assembly methods for the production of NPC suspensions is beyond the goal of this thesis, so only some example of assembly methods that use pre-formed NPs are described in the following sections including a detailed description of the competitive stabilizer desorption (CSD) approach which is used throughout this thesis.

1.8.1 Evaporation-induced self-assembly (EISA)

This approach involves slow evaporation of the solvent from the uniform size oxide nanoparticle dispersion in presence of block-copolymers or eumulsifier which act as structure directing templates ^[50] (Figure 1-20). In this case self-assembly is governed by the balance of attractive forces (such as covalent or hydrogen bonding, electrostatic attraction between oppositely charged ligands, depletion forces or dipole–dipole interactions) and repulsive forces (such as steric forces and electrostatic repulsion between ligands of like charge) ^[3]. The resulting clusters included a variety of architectures, such as chains, sheets, vesicles, three-dimensional (3D) crystals or more complex 3D architectures of controlled size.

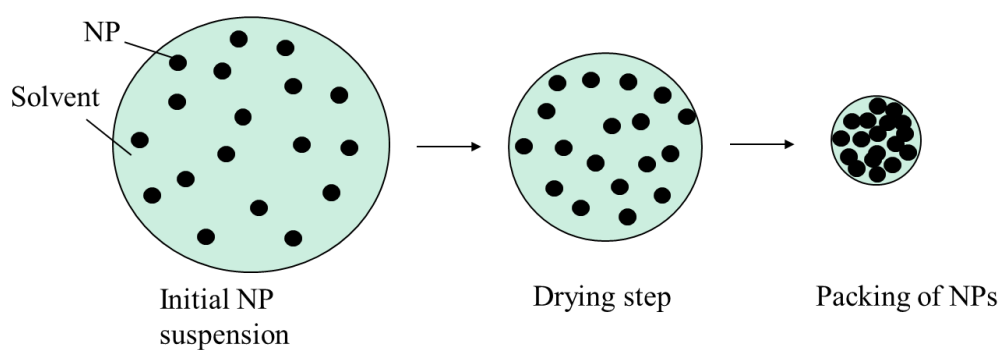


Figure 1- 20 Schematic illustration of the evaporation induced self-assembly of nanoparticles ^[51]. The drying step refers to the evaporation of the solvent to induce NP assembly.

In a typical oil-un-water emulsion evaporation process, a nonpolar suspension of pre-formed NPs is mixed with an aqueous solution containing the emulsifier (e.g. SDS, DTAB or CTAB) leading to the formation of oil droplets of few micrometers. The evaporation of the oil phase leads to the packing of the NPs into NPCs that do not tend to break up in water because of their hydrophobic nature. Therefore, the NP assembly

process is driven by the hydrophobic interactions of the ligands attached to the NP surface. This relatively simple approach was used by Bai and co-workers^[52] for the synthesis of Fe₃O₄ and other metal oxide NPCs of controlled size, shape and narrow size distribution. The same group showed that it is possible to control the assembly process by changing the experimental conditions including the NP concentration, emulsion composition and reaction temperature which affects the solvent evaporation rate. Typically well-ordered NP structures are obtained with slow evaporation rates at room temperature, while at higher temperatures multi-domain polydisperse NPCs are produced^[53].

The EISA method can be combined with the application of an external magnetic field to assemble nanoparticle superlattices or during the entire duration of the self-assembly process^[54]. The induced dipolar attraction during the first stage of solvent evaporation-mediated self-assembly process was demonstrated to be responsible to assemble the oleate stabilised γ -Fe₂O₃ nanocubes into micrometre-sized structures with both translational and orientational order. This approach gives the possibility to tune the interactions of magnetic dipolar particles by the field and thus control of the clustering process extending the material potential applications.

1.8.2 Layer-by-layer (LBL) assembly

The layer-by-layer assembly technique is used as a route for the creation of various NP shells by sequential adsorption of NPs and polyelectrolyte onto the surface of submicrometer beads (e.g silica or polystyrene)^[55]. In a typical process, beads are first primed with layers of polyelectrolyte film to provide a uniform charge surface that ensures the deposition of NPs of opposite charge (Figure 1-21). The nanostructures are finally centrifuged and washed several times to remove unabsorbed species, and used for the next cycle of adsorption of polyelectrolytes. This process is repeated until the desired number of NP layers is obtained. The limitation of LBL method is that it is limited to hydrophilic NPs because the process relies on electrostatic interactions.

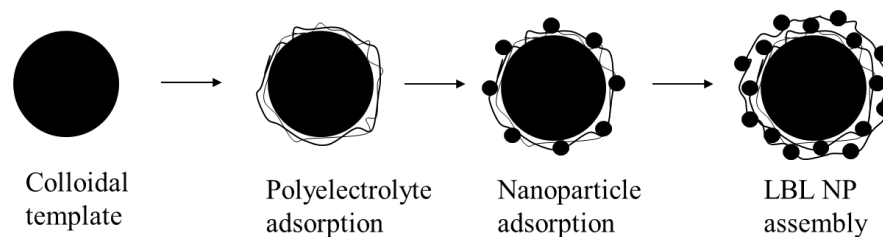


Figure 1- 21 Schematic illustration of the LBL assembly of nanoparticles^[56].

Caruso and co-workers^[56] reported a method for the sequential electrostatic adsorption of 25 nm silica NPs and poly(diallyldimethylammonium chloride) (PDADMAC) onto negatively charged 640 nm polystyrene (PS) beads which acts as a template. The thickness of the silica-PDADMAC multilayers were ranging from 10 to 100 nm. Using the same strategy, the same group showed an approach for the preparation of monodisperse submicrometer-sized hollow silica or iron oxide spheres^[57] by the removal of the solid template core by calcination or chemical extraction. The advantage of this approach is that the size and shape of the hollow spheres can be controlled by changing the dimension of the template and moreover the method can be used to form a wide range of NPs (including TiO₂ and ZrO₂) to form inorganic and hybrid nanocomposites that can be used for biomedical applications.

1.8.3 Self-assembly by Competitive Stabilizer Desorption

Recently, two processes for the controlled growth of NPCs *in situ* through Competitive Stabiliser Desorption (CSD) were developed by our group. The first approach is called Silica CSD (SI-CSD)^[58] and uses non-aqueous (heptane, chloroform) suspensions of oleic acid stabilised iron oxide NPs exposed to a polar cyanopropyl-modified silica layer, which is responsible of the partial and continuous depletion of the fatty acid ligands from the NP surface. As the ligand coverage is gradually reduced, the NPs become active interacting with other active NPs or NPCs in the suspension, in an ongoing controlled clustering process. This is possible because of the high affinity between the carboxylate groups of the fatty acid with the cyano group of the silica beads. Interestingly, the process is gradual and the monodispersity is maintained throughout the clustering. Initially small NPCs are formed through an $N \rightarrow N+1$ assembly between two activated primary NPs

from the suspension. With the continuous depletion of the ligands, it is suggested that the clustering take place between NP assemblies because of further oleic acid desorption, giving stable larger clusters (Figure 1-22). It was shown that the process can be stopped at any time simply by the removal of the suspension from the silica layer, allowing in this way the preparation of NPCs of specific size in the range from 20 to 400 nm with the same size dispersity of the original NP suspension. Moreover, the SI-CSD approach allows external interventions during the assembly experiment such as the interruption of the NPC growth by the removal of the competitor or the addition of a new NP type to produce hybrid NPCs. For instance, the addition of 2-3 nm gold NPs results in decorated magnetic iron oxide NPCs over the size range from 20 to 150 nm. This method adds both plasmonic and chemical functionalities to the clusters without affecting the superparamagnetic properties of the isolated iron oxide NPs.

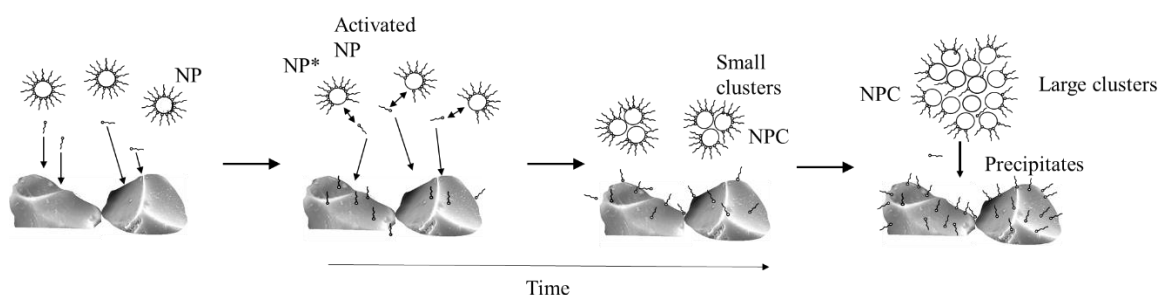


Figure 1- 22 Schematic illustration of the mechanism of CSD method ^[59].

There also some limitations of the SI-CSD approach that have to be taken in account. Firstly, it is really difficult to avoid disturbing the silica layer while the introduction of the NP suspension; silica particles mix easily with the suspending medium, which drastically alters the kinetics of assembly the sample. Moreover, the variability of the surface of the silica exposed to the suspension limits the reproducibility of the experiment. Secondly, the concentration of the NP suspension visibly decrease over time because the formation of NPCs on the silica layer. Thirdly, the cyano-modified silica is expensive, not reusable and slightly different from one supplier to another. Finally, in order to get a good monodispersity at the end of the experiment, low concentration ($< 1.5 \text{ mM [Fe]}$) NP suspensions are required. Hence, the silica CSD process is difficult to reproduce and it is not optimal from an economic point of view.

We therefore reported another method for producing stable non-aqueous suspensions of size-controlled FeO NPCs by a process based on the CSD principle that use in this case a liquid-liquid interface as the competitive layer. For instance, after placing water onto a suspension of oleic acid-stabilized FeO NPs (in chloroform) controlled particle assembly in the organic phase starts because of the free fatty acid accumulation to the liquid-liquid interface. Unlike the silica CSD approach, the water CSD permits the synthesis of size-controlled NPC over a really wide range (up to 600 nm) with excellent monodispersity both in organic solvent and in water after phase transfer of using a polymer. Moreover, it is a process that has been successfully scaled up making it a good candidate for biomedical applications.

The conditions for competitive stabilizer desorption leading to controlled cluster growth could, in principle, be identified for a wide range of NPs that are stabilized by many surfactants and that are dispersed in many solvents. The key step in adapting the process for any given stabilized NP suspension is identifying appropriate substrates and reaction conditions for competitive desorption. This method has the potential to address the two main problems in the production of NPCs. Firstly, it produces stable suspensions of monodispersed NPCs. Secondly, not only it is possible to get a very tight control over the NPC size but it is also possible to stop the process at any time and then restart it for further derivatization.

1.9 Surface modification of magnetic nanoparticles and nanoparticle assemblies

In the last decade it has been shown that nanocrystals can be either synthesized in aqueous or in organic medium. However, some materials need to be synthesized in organic solvents in order to have better control over the crystallinity, shape, size and polydispersity^[60]. This involves their surface coating with hydrophobic ligands and their further stabilization with surfactants with hydrophilic properties so that they can be used for biomedical applications. Several nanoparticle coating approaches can be found in literature that involve two strategies. One strategy is the ligand exchange with shorter ligand chains as was used by Caruso and co-worker for the phase transfer of gold nanoparticles from toluene to water^[61]. Alternatively, the nanocrystal surface chemistry can be modified by the formation of surfactants bilayers with the surfactant hydrophobic chain portion chain exposed to the aqueous phase. Wang et al^[62] presented a general

surface modification method that allows the transfer of oleic stabilized iron oxide and silver NPs from hexane to water by the coating with α -cyclodextrin which is penetrated by the hydrophobic tails of the first layer and its hydrophilic surface is pointing toward the water. Sastry's group^[63] reported the transfer dodecylamine (DDA)-capped colloidal gold particles dispersed in an organic solvent into water containing cetyltrimethylammonium bromide (CTAB) forming stable CTAB-DDA-Au complexes at a very high concentration of NPs and over a wide range of pH.

Many groups have used Pluronic polymer for NP phase transfer^[64]. Pluronic 127 has been used to form an intercalating structure with the hydrophobic capping molecules on oleic acid stabilised iron oxide NPs synthesized by the co-precipitation. In this case, the second layer of polymer molecules is coupled with the first layer of capping molecules through the hydrophobic interaction between the polypropylene oxide block (PPO) and the oleic acid chain, whilst the other two polyethylene blocks (PEO) of the polymer molecules renders the particles to be dispersible in aqueous phase.

The surface of pre-formed NPC surface can be modified as in the case of primary NPs, however the Van der Waals interactions between the ligands capping the NPs are generally weak and can be easily disturbed following mechanical forces or by changing the chemical environment leading to either the NPC desegregation or to the formation of large aggregates in suspension. In addition it is necessary to link functional surfactants to the NPC surface minimizing the change of the NPC hydrodynamic diameter in order to keep unaltered the physical properties of the clusters for their application. To the best of our knowledge no attempts were made so far for the phase transfer of pre-formed NPCs to water without changing their size and size distribution. This was a further motivation for us to develop methods for the phase transfer of pre-formed NPCs dispersed in organic medium to the aqueous phase by their encapsulation with low molecular weight amphiphilic surfactants and lipids with small change in the NPC size. The approaches used are described in details in Chapter 5 and Chapter 6.

1.10 Thesis Overview

Chapter 1 reports an introduction to theory of Nuclear Magnetic Resonance technique and the principles of magnetism in materials including proton relaxation and fast field-cycling NMR (FFC-NMR) also known as nuclear magnetic relaxation dispersion (NMRD) and the classification of magnetic nanoparticle based on their magnetic properties are reported. In the second part prospective applications of superparamagnetic nanoparticles (SPM NPs) in the fields of biomedicine and recently developed strategies for magnetic nanoparticle assembly and their surface modification are presented.

Chapter 2 describes briefly the principles, experimental conditions and practical consideration of the main analytical techniques used throughout this thesis work. dynamic light scattering (DLS), fast field cycling nuclear magnetic resonance spectroscopy (FFC-NMR), attenuated total reflectance infrared spectroscopy (ATR-IR), inductively coupled plasma atomic emission (ICP-AES), transmission electron microscopy (TEM) and magnetic fluid hyperthermia (MFH) are described.

Chapter 3 presents the synthesis of hydride and iron oxide based nanoparticle clusters (NPCs) of controlled size in organic medium by competitive stabiliser desorption method (CSD). The kinetics of the NP assembly process was investigated by varying some parameters such as the NP and ligand concentration and NP type. The effect of the cluster composition on the magnetic properties of the clusters was investigated. The method was successfully scaled up by a factor of 250 and reproducibility and size control ranging from 50 to 400 nm was achieved.

Chapter 4 presents the optimization of the CSD approach by using different experimental conditions including changing competitive substrate type (solid) and particle size. The insight into the kinetics of the CSD performed with liquid and solid competitive substrates is reported. The development of a novel flow system that allows to synthesize NPCs in flow is presented; the effect of parameters that affects the assembly process including the flow rate and tube length were investigated. This system would open a new pathway towards the production of size-controlled nanocomposite materials at larger scale. A new DLS probe was for the first time used for investigating over the NP assembly process under the application of a magnetic field.

In Chapter 5 the phase transfer from organic medium to water of pre-formed iron oxide NPCs, synthesized with CSD approach. Low molecular weight surfactants, Pluronic[®] and dodecyltrimethylammonium bromide, were used for the cluster coating and the effect of the cluster and surfactant concentration on the resulting size of the clusters in water was investigated. In the second part of Chapter 5, the magnetic properties of the clusters dispersed in organic and in aqueous medium were compared and the role of the nature of the cluster coating and cluster size determining the magnetic resonance properties was investigated. MFH analysis of the aqueous suspensions was undertaken and an increase of the heating efficiency was found with increasing of the cluster size. Finally the effect of the coating on the cell viability revealing that at certain iron concentration Pluronic[®] coated clusters were more suitable for biomedical applications.

Chapter 6 presents a method for the encapsulation of magnetic iron-oxide nanoparticles and nanoparticle clusters (synthesized by CSD method) into lipid vesicles. The resulting magnetoliposomes, lipid nanoparticles (LNPs), lipid nanoparticles aggregates (LNPA) and lipid nanoparticle clusters (LNPCs) are characterized and compared in terms of their physical and magnetic properties. The magnetoliposomes morphology was assessed by DLS, ATR-IR and FESEM while their magnetic properties were evaluated by NMRD technique. Magnetic chromatography technique was used as a mean for particle size selection; we demonstrated that magnetic filtration had an effect in most cases on the resulting magnetoliposomes size distribution and magnetic properties and specifically an increase in the spin-spin relaxivity response of LNPA and LNPCs of hydrodynamic size below 200 nm was observed. This may be attributed to an increase of the internal order in NPCs or to an alteration of the surface chemistry.

Chapter 2

Experimental section

2.1 Introduction

This chapter reports the description of the main experimental techniques used during the project work. Some details about the principles, experimental set up and eventually limitations are reported for each technique.

2.2 Dynamic Light Scattering

2.2.1 Theory

Dynamic Light Scattering (DLS) is a technique that measures the rate at which sub-micron size particles are diffusing due to Brownian motion. Brownian motion is the random movement of particles due to the bombardment by the solvent molecules that surround them. The DLS instrument set up is illustrated in Figure 2-1. A cuvette containing the suspension is illuminated by light generated by a laser light. The scattered light signal is collected with one of two detectors, either at a 90° (right-) or 173° (backscatter) scattering angle. The provision of both detectors allows more flexibility in choosing measurement conditions. The rate at which the intensity of the light fluctuates is measured. The obtained optical signal shows random changes due to the randomly changing of the position of the particles. The rate at which these intensity fluctuations occur depends on the size of the particles. Figure 2-2 schematically illustrates typical intensity fluctuations arising from a dispersion of large particles and a dispersion of small particles. The small particles cause the intensity to fluctuate more rapidly than the large ones.

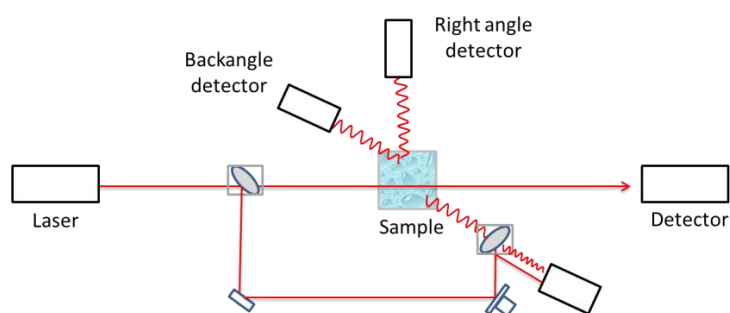


Figure 2- 1 Optical setup for dynamic light scattering (DLS) nanoparticle size analyzer.

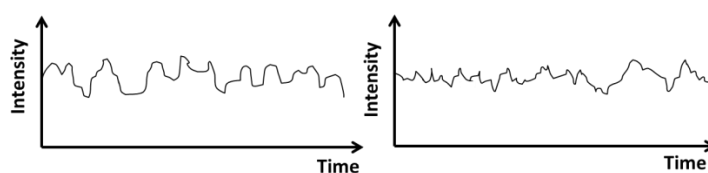


Figure 2- 2 Intensity fluctuations for large and small particles.

The fluctuations are quantified via a second order correlation function given by Equation 2-1:

$$g^2(\tau) = \frac{\langle I(t)I(t+\tau) \rangle}{\langle I(t) \rangle^2} \quad \text{Equation 2- 1}$$

where $I(t)$ is the intensity of the scattered light at time t , and the brackets indicate averaging over all t and the delay τ , that is, the amount that a duplicate intensity trace is shifted from the original before the averaging is performed. For a large number of monodisperse particles in Brownian motion, the correlation function G is an exponential decaying function of the correlator time delay τ (Equation 2-2).

$$G(\tau) = A(1 + \beta e^{-2\Gamma\tau}) \quad \text{Equation 2- 2}$$

where A is the baseline of the correlation function, β is the intercept and r is the decay rate, which is equal to:

$$\Gamma = q^2 D \quad \text{Equation 2- 3}$$

$$q = \frac{4\pi\eta}{\lambda} \sin(\theta / 2) \quad \text{Equation 2- 4}$$

where D is the translational diffusion coefficient, q is the magnitude of the scattering vector, η is the refractive index of the solvent, λ is the wavelength of the incident light and θ is the scattering angle. A typical correlation function for a monodisperse sample is shown in Figure 2-3.

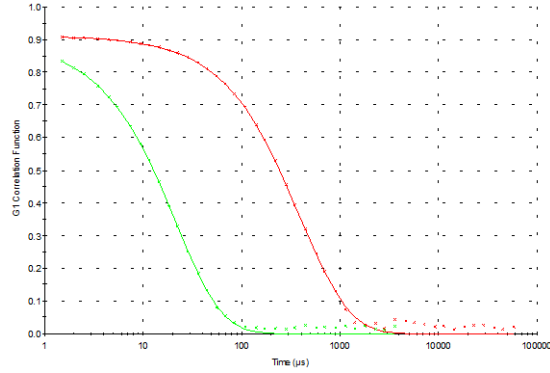


Figure 2- 3 A typical correlogram from a sample containing (-) small iron oxide nanoparticles in which the correlation of the signal decays more rapidly and (-) a correlogram of 262 nm nanoparticle.

The size of the particle is related to the time dependence of scattered light intensity and it can be calculated using the Stokes-Einstein equation (Equation 2-5):

$$d_{hyd} = \frac{kT}{3\pi D\eta} \quad \text{Equation 2- 5}$$

where d_{hyd} is the hydrodynamic diameter of the particle, k is the Boltzmann constant, T is the absolute temperature, D is the translational diffusion constant and η is the viscosity. The translational diffusion coefficient gives information about the velocity of the Brownian motion and it depends not only on the size of the particle core but also on any structure on the surface particle, as well as the concentration and the nature of ions in the medium.

For polydisperse samples, two methods are normally used for the extraction of the translational diffusion coefficient: cumulants^[65] and distribution analysis^[66]. The first approach, cumulants analysis, applies a natural log to the correlation coefficient and a polynomial function as shown in Equation 2-6.

$$\frac{1}{2} \ln G(\tau) = a_0 + a_1\tau + a_2\tau^2 + a_3\tau^3 + \dots \quad \text{Equation 2- 6}$$

The diffusion coefficient is given by the value a_1 which can be converted to hydrodynamic diameter keeping in account of the viscosity of the solvent and the instrument constants

^[67]. The values a_2 and a_3 give information about the skewness and kurtosis of the size distribution. Size is obtained from the correlation function by using various algorithms. The width of the distribution is given by $2a_2/a_1^2$ and it is known as polydispersity index (PDI). The PDI is a dimensionless parameter and it is in the range 0-1, such that smaller values (<0.1) indicate really monodisperse particles while higher values (> 0.3) indicate that the sample has a very broad size distribution.

The second approach, distribution analysis, obtains the translational diffusion coefficient by fitting an exponential model to the experimental data reported in Equation 2-7:

$$G(\tau) = B + \sum e^{-2q^2 D \tau} \quad \text{Equation 2-7}$$

Where B is the baseline and q is the scattering vector (Equation 2-4). The hydrodynamic diameter is then calculated the Stokes-Equation described in Equation 2-5.

The size distribution by intensity are obtained from correlation function analysis using the Multiple Narrow Modes algorithm which is based on the non-negative least squares fit ^[68]. The size distributions by intensity reported in this thesis were obtained with the commercially available software Malvern Instruments version 7.11. The intensity size distribution of a typical suspension of NPCs is shown in Figure 2-4.

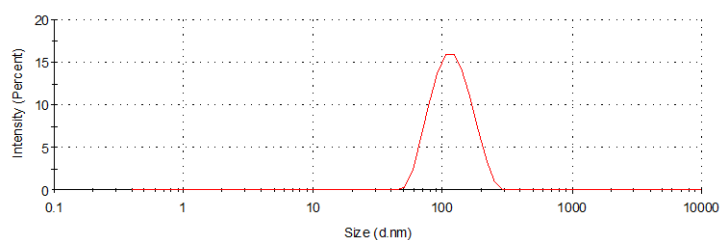


Figure 2- 4 Size distribution by intensity of magnetite clusters of $d_{\text{hyd}}=110$ nm, PDI = 0.095.

2.2.2 Experimental set up

DLS measurements were carried out on either a Zetasizer Nano ZS (Malvern Instruments; Worcestershire UK) or a High Performance Particle Sizer (HPPS). The sample was contained in a 12.5 x 12.5 x 45 mm sizing cuvette. Aqueous sample were placed in PE cuvettes, while samples in organic solvent were placed in quartz cuvettes. The temperature was kept at 25 °C in all cases and a thermal equilibration time of ~5 minutes

was required before each DLS measurement. These machines use a He-Ne laser with λ 633 nm and detect the back scattering information at 7° and the forward scattering at 173° .

2.2.3 Practical limitations

As any other particle sizing technique, DLS has advantages and disadvantages. Measuring with DLS high concentrated solutions may spoil measured correlation function. This is caused by effect called multiple scattering. With multiple scattering, the randomness of the interaction tends to be averaged out by the large number of scattering events, so that the final path of the radiation appears to be a deterministic distribution of intensity. On the other hand DLS is a rapid, non-invasive technique and its time (10^{-7} – 10^3 sec) and length (10^{-9} - 10^{-6} m) range are quite wide if compared with other techniques [69]. DLS is therefore also suitable for diffusional studies of polymers and large biomolecules.

2.3 Zeta potential

2.3.1 Theory

Particles dispersed in polar solvents can carry a characteristic surface charge also known as Zeta potential. The magnitude of the zeta potential gives an indication of the potential stability of the colloidal system as particle large negative or positive zeta potential will end to repel each other and there is no tendency to form aggregates in suspension. Particles with zeta potentials more positive than +30 mV or more negative than -30 mV are normally considered stable. The theory behind the zeta potential and its measurements is described below.

In a given solvent, the particle are surrounded by two layers the first is a “fixed layer” (called Stern Layer) which is formed by oppositely charged ions strongly bound to the particle surface and then a second layer which, known as the diffuse double layer, where a little number of ions of opposite charge are placed (Figure 2-5). The combination of these two layers is known as the ‘Electrical Double Layer’. The point at which the dispersion medium meets with the stationary fluid attached to the particle is called slipping plane and that defines the zeta potential of the particle.

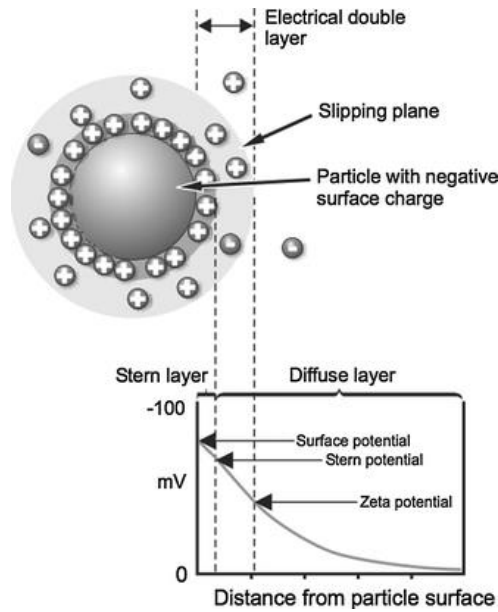


Figure 2- 5 Schematic representation of the electrical double layer of a negative charged particle [70].

When an electric field is applied, the particles move towards the electrode of the opposite polarity. The direction and velocity of the motion is a function of particle charge, the suspending solvent, and the electric field strength. The Zeta potential is determined through the particle electrophoretic velocity (U_E) which is described by the Henry equation (Equation 2-8):

$$U_E = \frac{2\varepsilon Z F(k a)}{3\eta} \quad \text{Equation 2- 8}$$

where ε is the dielectric constant, Z is the Zeta potential, η is the viscosity of the dispersing medium and $F(ka)$ is the Henry's function which depends on k , Debye length (the thickness of the electrical double layer) and on a (the particle radius).

The Zetasizer Nano ZS instrument uses laser Doppler electrophoresis to measure the Zeta potential of particles in suspensions. A He-Ne laser (λ 633 nm) beam passes through the sample placed within the cell in presence of an electrical field applied at an angle of 17° relative to the incident beam (Figure 2-6). The scattered light from the particles in motion is shifted with a frequency, ΔF , given by the Equation 2-9:

$$\Delta F = \frac{2v \sin(\theta/2)}{\lambda} \quad \text{Equation 2- 9}$$

where v is the particle velocity, λ is the laser wavelength and θ is the scattering angle. Hence, the phase change (ΔF) in light scattered by the particles in motion is proportional to their electrophoretic mobility

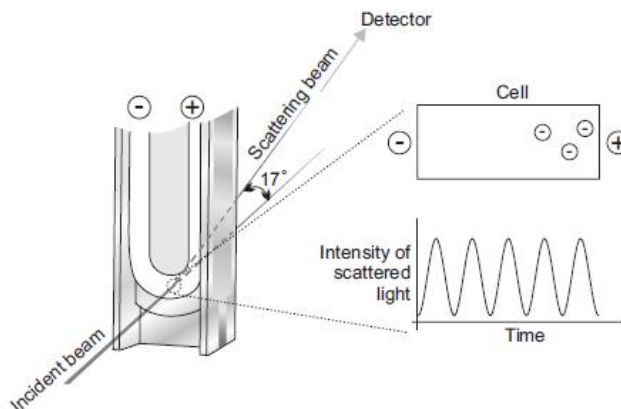


Figure 2- 6 Schematic representation of light scattering in the Zeta cell following the application of an electric field to the particle suspension [71].

Malvern Instruments software (Worcestershire, UK) provide the phase change as function of time, known as phase plot, and the zeta potential distribution at every analysis. An example of phase plot and zeta potential distribution of NP suspension is shown in Figure 2-7. In the first part of the phase plot low voltages are applied and the phase oscillations contain information about the mobility of the particles while in the latter part higher voltages are applied and the data obtained here gives information about the particle surface.

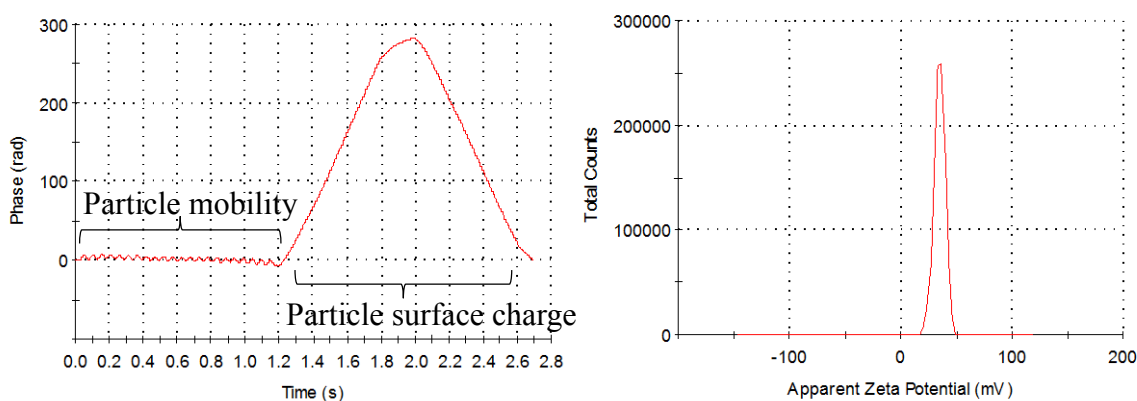


Figure 2- 7 (Left) Plot phase versus time and (right) Zeta potential distribution of a suspension of 3-aminopropyltriethoxysilane stabilized- iron oxide NPs (17 nm, +34.3 mV).

2.3.2 Experimental set up

The Zeta potential of NP and NPC suspensions was measured using the same Zetasizer Nano ZS instrument (Malvern, Worcestershire, UK) used for particle sizing measurements. The aqueous suspension was contained in disposable cuvette for zeta potential measurements. The sample temperature was kept at 25 °C and a thermal equilibration time of ~5 minutes was required before each measurement.

2.3.3 Practical considerations

As for particle sizing measurements, the measurement of Zeta potential is strictly dependent on the particle concentration. The minimum and maximum concentration required will depend on different factors including particle size, polydispersity of particle size distribution and also on refractive index ^[72]. The larger the particle size is, the more scattered light and so lower is the concentration necessary for the measurement. However the optimal concentration required for a successful zeta potential measurement has to be determined experimentally. Another parameter that needs to be taken in account is the pH of the particle dispersion.

2.4 Fast Field –Cycling NMR

2.4.1 Theory

Fast Field-Cycling relaxometry technique measures the frequency (or magnetic field) dependence of relaxation times, T_1 and T_2 ^[73]. It is a tool for measuring nuclear relaxation rates from very low magnetic fields of c. 2.5 G (0.01 MHz ¹H Larmor frequency) up to 1 T (about 45 MHz proton Larmor frequency) continuously. The plot of the spin-relaxation rate R_1 ($= 1/T_1$) as a function of magnetic field is known as Nuclear Magnetic Resonance Dispersion (NMRD) profile.

The field dependence of the relaxation rates have been shown to be useful in determining the presence of binding between macromolecules or between a small paramagnetic complex and a macromolecule, as well as for studying the mechanisms responsible for electron relaxation ^[73]. The two field-cycling sequences commonly employed to measure the spin-relaxation time (T_1) are described below.

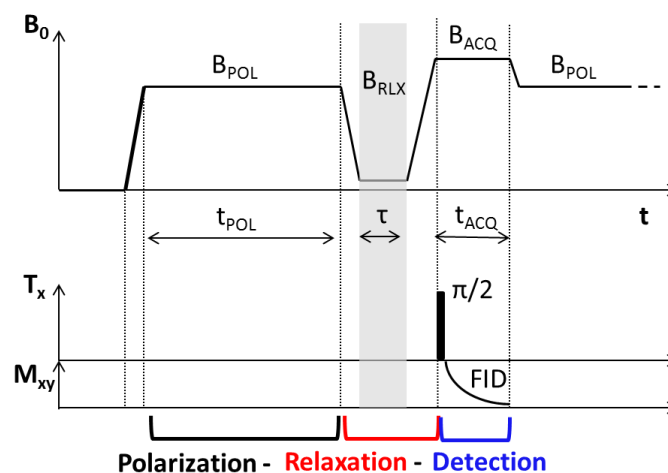


Figure 2- 8 Schematic representation of the external flux density B_0 ; the transmitter output T_x and the magnetization M_{xy} in the intervals τ for prepolarised sequence (PP/S) is used at low field. The shaded section indicates the variable relaxation interval τ [73].

2.4.1.1 Pre-polarised sequence

Figure 2-8 schematically shows the field cycle experiment known as the prepolarised sequence (PP/S) for ν_L below ~ 6 MHz [73]. The ^1H magnetization is polarized in the polarization field, B_p (normally 10- 14 MHz) which amplify the equilibrium magnetization giving a better signal-noise ratio. The polarization time t_{POL} has to be at least 4 times T_1 of the material analyzed in order to reach saturation of the magnetization. The magnetic flux density is then switched down to the selected relaxation field, B_{RLX} ; at which the spin-relaxation process is observed. The magnetization remaining after the relaxation interval τ is finally detected in the xy plane with the aid of a 90° RF pulse switching the magnetic flux density to a fixed detection field, B_{ACQ} . After having recorded the signal, the flux density is switched back to the polarization flux density. After a relaxation period of a couple of (high-field) spin-lattice relaxation times, the whole cycle begins again. Incrementing the relaxation interval τ thus permits one to record the relaxation curve for a given relaxation flux density B_{RLX} : The spin-lattice relaxation dispersion is then scanned point by point by stepping B_{RLX} through the desired magnetic field range. Normally, the signal intensity is measured at 16 τ -values, ranging from 1 ms to approximately 5 times T_1 . The value of T_1 is extracted by least squares fitting of the exponential decay function at each relaxation field (AcqNMR, v.2.1.0.60, Stelar; Mede, Italy). Finally, all the magnetic recovery curves of all the samples studied in this report were mono-exponential, and the fitting errors in T_1 were reasonably small ($< 1\%$).

2.4.1.2 Non polarized sequence

When the relaxation field approaches the polarization one, the magnetization evolution takes place between similar initial and final values, increasing the error in the measurement ^[74]. Figure 2-9 schematically shows the field cycle for high relaxation fields (> 6 MHz), called the non-polarised sequence (NP/S). This sequence starts the cycle without any polarization field this means that the magnetization growth from an initial zero value. The cycle is repeated periodically for different relaxation intervals τ and different relaxation flux densities B_{RLX} while all other intervals and flux densities remain constant.

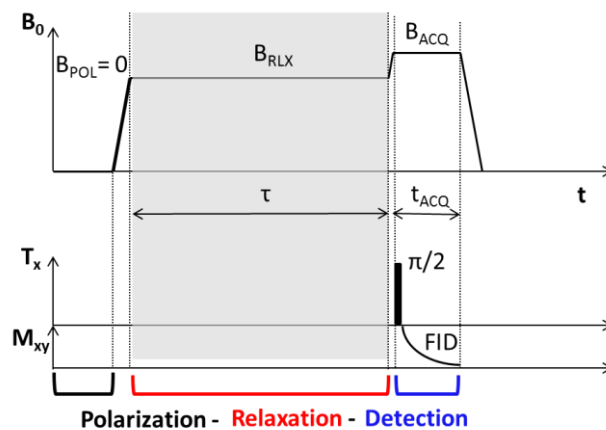


Figure 2- 9 Schematic representation of the external flux density B_0 ; the transmitter output T_x and the magnetization M_{xy} in the diverse field-cycling time intervals for non-polarised sequence (NP/S) used for high fields. The relaxation interval τ is indicated in the shaded section ^[73].

2.4.1.3 Non-polarized Carr–Purcell–Meiboom–Gill sequence

In order to measure spin-spin relaxation time T_2 at a fix magnetic field (normally at 16.3 and 60 MHz), a non-polarized Carr–Purcell–Meiboom–Gill sequence (NPCPMG) was used. This technique applies a 90° pulse followed by a series of 180° pulses to refocus inhomogeneous broadening of the nuclear spins (Figure 2-10). The magnetization is first rotated to the xy plane by a 90° pulse so that the spins diphase by two processes, T_2 and T_2^* . The 180° pulses are separated by an echo delay τ . The number of echoes which can be acquired is directly related to T_2 processes. The echo tops will diminish in intensity due to coherence losses between spins, which is the homogenous T_2 process, as the 180°

pulses refocus the inhomogeneous T_2^* due to the varying magnetic field experienced by the sample.

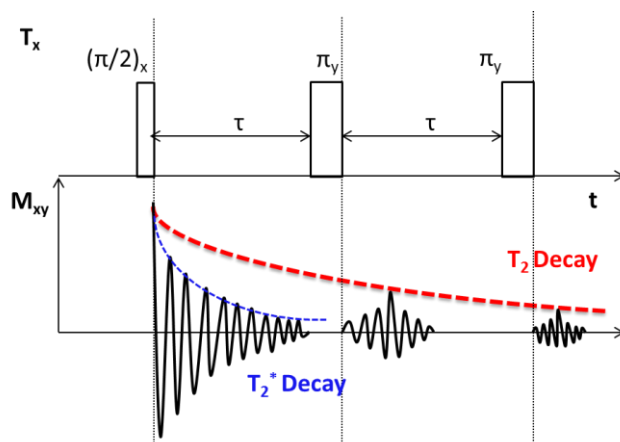


Figure 2- 10 Schematic representation of a CPMG sequence performed at a fixed external field B_0 ; top graph shows RF pulse sequence with the echo delay constant (τ); bottom shows the free induction decay and the resultant T_2 delay.

2.4.2 Experimental set up

NMRD experiments from 0.01 up to 40 MHz were performed on a Spinmaster FFC-2000 Fast Field-Cycling NMR Relaxometer (Stelar, Mede, Italy) while the measurements at 60 MHz have been done on a Bruker WP80 variable field electromagnet. Sample volume of 0.5 - 1 mL and concentration of metal in the range of 2-3 mM were used for the analysis. The temperature was kept at 25 °C in all cases and a thermal equilibration time of ~15 minutes was required before each field-cycling experiment. In Table 2-1 the acquisition parameter ranges used for the NMRD characterization of the samples are reported.

B_{POL}	10 – 14 MHz
t_{POL}	0.2 – 0.5 s
B_{ACQ}	9.25 MHz
Switching time	0.0015 - 0.003 s
TAU delay	0.001 s
Block size	512 – 1024
90° Pulse duration	6 – 7 μ s

Table 2- 1 FFC NMR acquisition parameter ranges utilized for the characterization of the samples discussed in this report.

2.4.3 Practical limitations

The NMRD technique presents some limitations that can be related basically to two FFC parameters. The first is the field switching time that is the time required for the switch from B_{ACQ} to the B_{RLX} . Since the field switching time is < 3 ms, the T_1 must be several times longer than this or significant relaxation will occur during the time that the field is stabilizing. For magnetic nanoparticle suspensions this problem can be resolved by diluting the sample lengthening the relaxation process. The second critical parameter is the relaxation period τ that defines the upper applicable magnetic field (40 MHz). At higher magnetic field, the current through the magnet coil is high generating more heat that can be dissipated by the cooling system, which would damage the magnet. A resolution of this problem is to measure T_1 at high fields with a Bruker WP80 variable field magnet. With this instrument is possible to measure T_1 from 20 – 80 MHz using an Aperiodic-Pulse-Sequence Saturation Recovery (APSR/S) pulse sequence.

2.5 Inductively Coupled Plasma Atomic Emission Spectroscopy

2.5.1 Theory

Inductively Coupled Plasma Atomic Emission Spectroscopy (ICP-AES) is an emission spectrophotometric technique, exploiting the fact that excited electrons emit energy at a given wavelength as they return to ground state. The fundamental characteristic of this process is that each element emits energy at specific wavelengths peculiar to its chemical character. Although each element emits energy at multiple wavelengths, in the ICP-AES technique it is most common to select a single wavelength (or a very few) for a given element. The intensity of the energy emitted at the chosen wavelength is proportional to the amount (concentration) of that element in the analyzed sample. Thus, by determining which wavelengths are emitted by a sample and by determining their intensities, the analyst can quantify the elemental composition of the given sample relative to a reference standard. The ICP-AES systems consist basically of three main components: the sample introduction system, the torch assembly, and the spectrometer. The fluid sample is pumped into the nebulizer via the peristaltic pump. The nebulizer generates an aerosol mist and injects humidified Ar gas into the chamber along with the sample and the finest particles are subsequently swept into the torch assembly and finally in the plasma. Light emitted from the plasma is focused through a lens and passed through an entrance slit into the spectrometer where the diffraction grating sequentially moves each wavelength into

the detector. Depending on the wavelength chosen by the user, the grating sequentially moves to the specified wavelengths, and the energy intensity at each wavelength is measured to provide a quantitative result that can be compared to a reference standard.

2.5.2 Experimental set up

In this report the iron and cobalt concentrations were determined by Liberty 220 ICP Emission Spectrometer (Varian Inc, Agilent Technologies, Santa Clara, USA) at the millimolar level. A 998 ± 2 mg/L iron ($\text{Fe}(\text{NO}_3)_3$ in 1M Nitric, Merck Chemicals, Darmstadt, Germany) and 999 ± 1 mg/L cobalt standard (Co^{+2} in 1 wt. % HNO_3 , Sigma Aldrich UK) were used to make up the calibration curve. The curve ranged from 0.05 to 10 mg/L Fe and Co and a linear fit was used to calculate the metal concentrations of the samples. Typical calibration curves for Fe and Co determination are presented in Figure 2-11. In all cases $R^2 > 0.998$

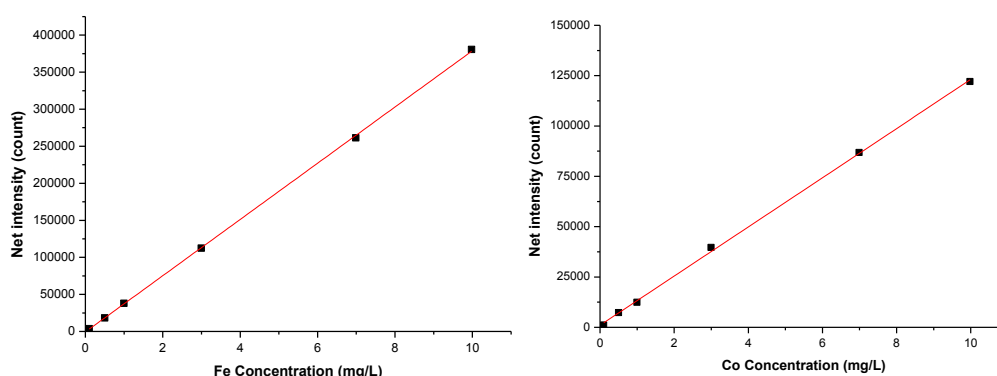


Figure 2- 11 Typical ICP-AES standard calibration curve for: (left) iron using standards of known Fe concentration on the range of 0.1 – 10 mg/L; $y = 37961x - 685.84$, $R^2 = 0.9998$; (right) cobalt using standards of known Co concentration on the range of 0.1 – 10 mg/L; $y = 12415x + 712.23$; $R^2 = 0.999$.

Before the analysis, the samples were digested method described by Meledandri et al. [75]. Typically a volume of 50 - 100 μL was placed into a conical flask to let the sample dry. 1.5 mL of concentrated HCl (36%) and of MilliQ water were added to the flask. This was heated until the volume of the solution was reduced to ~ 200 μL . 3 mL of deionized water was added to the flask and the solution was heated to boiling. After cooling down, the solution was quantitatively transferred to a volumetric flask and made up to the mark with 1 M nitric acid.

2.6 Transmission Electron Microscopy

2.6.1 Theory

The transmission electron microscopy (TEM) technique that uses an electron beam to determine the positions of atoms within materials to form larger and detailed images of micro- and nanomaterials ^[76] with higher resolution than those obtained from a light microscope. deBroglie (Equation 2-10) stated that since the wavelength λ of an electron beam, with mass m , is a function of the accelerating voltage used then by increasing the voltage, the electron velocity v will increase as will resolution. By increasing the accelerating voltage, a shorter wavelength is obtained.

$$\lambda = \frac{h}{mv} \quad \text{Equation 2- 10}$$

A schematic representation of the transmission emission microscope is reported in Figure 2-12.

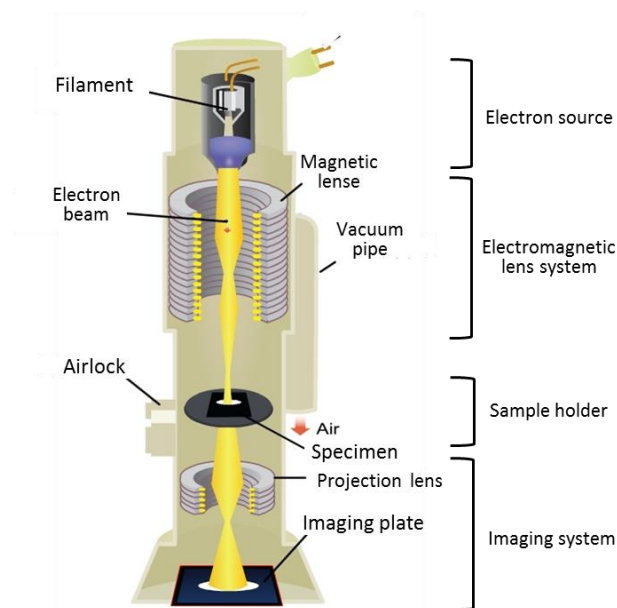


Figure 2- 12 Schematic of a transmission electron microscope.

In TEM the source of illumination is a beam of electrons of very short wavelength (1 nm), emitted from a tungsten filament (cathode) at the top of a cylindrical column of about 2 m high. The electrons beam is accelerated by a voltage in the anode of the filament and a small emission current is then applied to achieve the release of electrons. The magnetic coils placed at specific intervals in the column acts as an electromagnetic condenser lens

system. The electron beams are passes through the specimen and focus onto the specimen to illuminate only the area being examined. Finally, projector lenses further magnify the image coming from the intermediate lens and projects it on to the phosphorescent screen. A film camera is located beneath the phosphorescent screen to capture the image. The whole optical system of the microscope is enclosed in vacuum so that the collision of electrons with air molecules and hence the scattering of electrons are avoided.

2.6.2 Experimental set up

NP and NPC dispersions are diluted to a metal concentration range of 0.2 – 1 mM. One drop of diluted dispersion was spotted on 3.05mm diameter copper grid carbon coated for extra stability and to render the sample conductive. The grids were supplied by Agar scientific and used as supplied. The machines used were a Tecnai G2 12 BioTwin (FEI, Oregon, USA), acceleration voltage 120kV equipped with a Megaview III camera (Olympus, SIS, Münster, Germany) and a Tecnai G2 20 (FEI, Oregon, USA), acceleration voltage 20kV equipped with an Eagle 4k CCD camera (FEI, Oregon, USA). The images were typically collected using a 20 kV voltage. The grids were placed in a topography grid holder and measured at an angle of 0° tilt with respect to the beam.

The statistical analysis of the samples was performed on images using Image J (National Institute of Health, US government). The size distributions were fitted to a log-normal size distribution and the mean particle size and standard deviations were derived from the log-normal distribution function shown in Equation 2-11:

$$P(x) = \frac{1}{\sqrt{2\pi}\sigma x} e^{-\frac{(\ln x - \mu)^2}{2\sigma^2}} \quad x > 0 \quad \text{Equation 2- 11}$$

P(x) is the probability density of the distribution, $x = D/D_p$ is the reduced diameter, D_p is the median diameter, D is the particle diameter, and μ and σ are the mean and standard deviation of $\ln x$, respectively. Once values for μ and σ were obtained, the mean particle diameter and standard deviation were calculated using Equations 2-12 and 2-13, respectively:

$$D_{TEM} = D_p (e^{\mu + \sigma^2/2}) \quad \text{Equation 2- 12}$$

$$\sigma_{TEM} = D_p \sqrt{(e^{\sigma^2} - 1)e^{2\mu + \sigma^2}}$$
 Equation 2- 13

2.6.3 Practical limitations

Some practical considerations have to be taken in account for TEM analysis of suspensions., the sample drying process seems to be a critical issue for NPC suspensions in particular. The assemblies dry deposited onto the grid seem to lose the structure adopted in solution that is inferred by the low PDI values from DLS. The resolution to this problem can be the optimization of the concentration spotted onto the grid. The second limitation arises from the composition of the material and its interaction with the electrons. As mentioned in the theory, nanoparticles with materials made with high atomic number elements appear darker while those with lower atomic number appear brighter in the TEM image. This raises two issues; if two materials made with elements of similar atomic numbers, it may be hard to distinguish between the two materials. Furthermore, there is a limit to the different in contrast that can be recorded. Finally, TEM relies of the transmission of electrons through a sample to form an image; this limits the thickness of a sample. Because of trying to have a thin layer of sample on the grid, the sample preparation process can be time consuming.

2.7 Field Emission Scanning Electron Microscopy

2.7.1 Theory

FESEM is a versatile analytical technique used to investigate the topology of nanostructures and compared to the traditional SEM microscope it offers advantages including high magnification, large depth of focus and great resolution^[77]. A schematic representation of the field emission scanning microscope is reported in Figure 2-13. The electron beam source is placed on the top of the instrument and it is a thin and sharp tungsten needle that functions as a cathode in front of a primary and secondary anode. The voltage between cathode and anode is in the order of magnitude of 0.5 to 30 kV. The electrons liberated (known as primary electrons) from the field emission source are accelerated in a high electrical field gradient then focused and finally deflected by electronic lenses to produce a narrow scan that hit the sample placed within the high vacuum column (10^{-8} Torr). As a result secondary electrons are emitted from each section

of the sample and are caught by a detector, which generates an electronic signal. The angle and velocity of these secondary electrons gives information about the surface structure of the specimen. Finally, the resulting electron signal is amplified and converted to a scan-image.

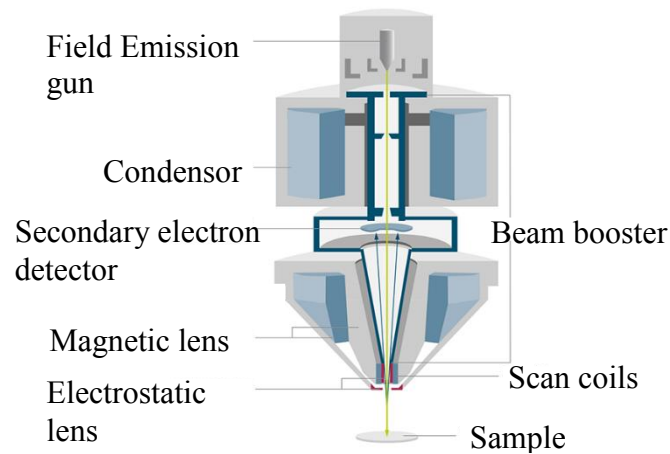


Figure 2- 13 Schematic representation of a field emission scanning microscope [78].

When the primary electron beam hits the sample, two electron beam interaction process occur. Secondary electrons (SE) and backscattered electrons (BSE) are generated (Figure 2-14). Three main categories of secondary electrons (SE1, SE2, SE3) are ejected from the outer atomic shell of the sample analyzed and they differ in energy. BS electrons are generated by elastic scattering deeper in the sample and they have higher energy than SEs (> 50 eV). Depending on the information required by the user, there are two image modes that are commonly used; the secondary electron (SE) and the backscattered electron (BSE) image mode. The SE mode provides good surface information while the second is normally used to display compositional differences (material contrast) in the specimen.

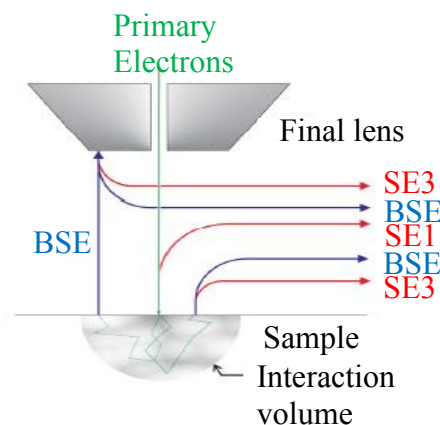


Figure 2- 14 Schematic representation of the interaction between the primary electron beam and the sample [79].

2.7.2 Experimental set up

The NP size and morphology were obtained using a Hitachi S5500 Field-Emission SEM (at an accelerating voltage of 20 kV). The sample was normally diluted to approximately 0.1-1 mM (iron content) in order to avoid any aggregation, and 5 μL of this was placed first onto a Formvar coated 400 mesh Copper grid (Agar Scientific, Essex, UK) allowing the solvent to evaporate under a watch glass prior imaging. Statistical analysis of the samples was performed as in the case of TEM characterization.

2.7.3 Practical limitations

The same practical considerations described for the preparation of the sample in TEM analysis are valid also for FESEM analysis.

2.8 Magnetic fluid hyperthermia

2.8.1 Theory

Magnetic fluid hyperthermia is based on the application of an AC magnetic field onto magnetic nanoparticles which generates a quantity of heat that is determined by the type of particles, frequency and magnetic field strength applied^[80]. The phenomenon beyond the generation of heating by the magnetic nanoparticles is described in detailed in Chapter 1. Figure 2-15 reports the schematic representation of the instrument set up used in MFH. The frequency and strength of the externally applied AC magnetic field used to generate the heating used in clinical trials are 100 kHz and 0-18 KA/m as variable field strength^[81]. Experimentally, the value of the heating efficiency of the magnetic particles is achieved by recording the temperature-time curve from which the specific absorption rate (SAR) is calculated using the Equation 2-14:

$$SAR = \Delta T / \Delta t \times C / m \quad \text{Equation 2- 14}$$

where $\Delta T / \Delta t$ is the increase of temperature in the period of time of measurement (normally $\Delta t = 10\text{-}20$ minutes); C is the heat capacity of the solvent (4.186 J/g °C for water) and m is the mass of the magnetic material suspended in the medium.

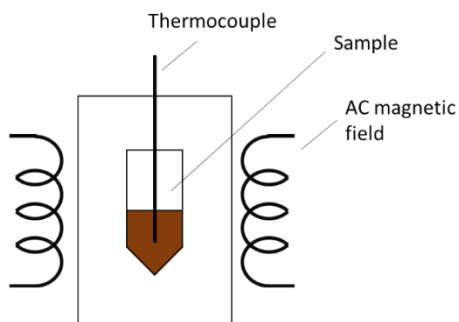


Figure 2- 15 Schematic representation of a magneTherm.

2.8.2 Experimental set up

All MFH experiments were performed on a MagneTherm™ (Nanotherics Ltd; Newcastle, UK) which have a frequency-adjustable magnetic field in the range 110-1000 kHz. Typically a sample volume of 0.-1 mL and concentration of metal in the range of 0.5-3 mM were used. A thermal equilibration time of ~20 minutes was required before the starting of each experiment. The Table 2-1 report all the acquisition parameter ranges used for the MFH characterization of the samples reported in the following chapters.

Frequency (kHz)	Max Magnetic field (mT)	Max Magnetic field (KA/m)
110.0	25	19.9
335	17	13.5
474	11	8.7
523	20	15.9
739	16	12.7

Table 2- 2 Frequency and magnetic field strength ranges used in MFH measurements.

2.8.3 Practical limitations

In hyperthermia measurements there are always some inaccuracies due to heat loss during the measurements that might occur in different ways such as conduction, convection or evaporating of the sample ^[82]. Another source of error can be related to the spatial inhomogeneity of the temperature in the sample which makes the location of the thermocouple within the sample really important. Finally, a further source of uncertainty can be the delay of heating when it takes some time for the heating curve to take off after

the heating process and most importantly inhomogeneity of the magnetic field within the sample [82].

2.9 Attenuated Total Reflectance – Infrared Spectroscopy

2.9.1 Theory

ATR-IR spectroscopy is a non-destructive analytical fingerprinting technique that can be used to identify and quantify liquid or solid substances. An infrared beam is transmitted into a crystal of relatively high refractive index. Immediately after the crystal/sample interface, an electromagnetic field (E) constituted in the sample generating an evanescent wave which has the same frequency of the incoming light but decays exponentially with distance from the crystal surface (z) [83] (Equation 2-15). The depth of penetration d_p of the evanescent wave is proportional to the wavelength λ , the incident angle θ and the refractive index of the sample (η_p) and of the crystal (η_c) as it is shown in Equation 2-16. The resulting reflected IR radiation has a lower energy than the original original beam because of its partially absorption by the sample at a specific wavelength. The attenuated reflected beam is finally measured by the detector and it is plotted as function of $1/\lambda$. A schematic representation of the total internal reflectance in an ATR-IR system is reported in Figure 2-16.

$$E = E_0 e^{\frac{-z}{d_p}} \quad \text{Equation 2- 15}$$

$$d_p = \frac{\lambda}{2\pi\eta_c \left(\sin^2 \theta - \left(\frac{\eta_s}{\eta_c} \right)^2 \right)^{1/2}} \quad \text{Equation 2- 16}$$

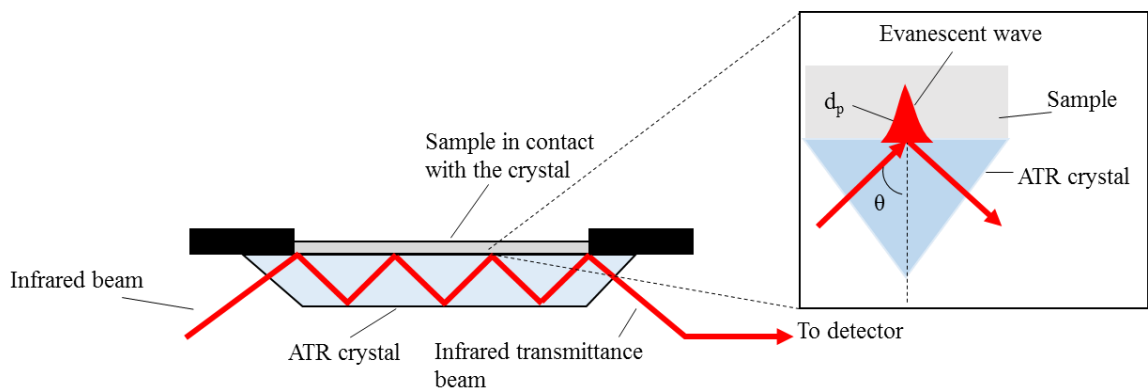


Figure 2- 16 Schematic representation of total internal reflectance in an ATR-IR system.

2.9.2 Experimental set up

The ATR-IR instrument used in this thesis was a Spectrum100 FT-IR (Pelkin Elmer, Massachusetts, USA) equipped with a ZnSe crystal ($n = 2.38$)^[84]. For solid samples, a spatula tip of material was placed on the crystal, and the pressure gauge was set to ~50. In case of liquid samples, a drop of the substance was placed on the crystal allowing the solvent to evaporate before starting the measurement of the spectrum. In both cases a blank test was done prior the analysis of the sample in order to make sure that the crystal surface was clean from any contamination.

2.9.3 Practical limitations

Two limitations can be related to the experimental set up described above. Firstly, the ZnSe crystal has a working pH range of 5-9 and it scratches quite easily and so care must be taken when cleaning the crystal. A solution for overcoming this is to replace it with a diamond crystal. Secondly, the path length of the IR beam is dependent on d_p and consequently on λ as it is shown by Equation 2-16 while in traditional IR technique the path depends only on the thickness of the sample. Therefore the resulting spectrum is wavelength depend and must be corrected with an algorithm included in the commercial ATR-IR software.

CHAPTER 3

Preparation of novel stable suspensions of size-controlled hybrid magnetic nanoclusters

3.1 Introduction

The process recently developed by our group is a CSD approach that uses a liquid-liquid interface as the competitor for oleic acid in the place of the silica. This approach is called WI-CSD, Water Interface Competitive Stabilizer Desorption. By careful addition of water onto the chloroform suspension, a stable, reproducible interface is formed. Due to the gradual depletion of the oleic acid, controlled particle assembly takes place in the organic phase^[85]. The mechanism will be described and discussed in details.

The aim of this work is to improve WI-CSD by controlling the NPC size and polydispersity and by tailoring the magnetic properties of the resulting suspensions by changing the nature of the NPs in the clusters. The control of both the size and the magnetic properties of the NPCs could be useful for passive physical targeting and for magnetic-mediated hyperthermia and possibly MRI applications.

An important current research direction in nanomaterial synthesis is the development from single-component NPs and NPCs to hybrid nanostructures with discrete domains of different materials arranged in controlled fashion. Thus, not only can new functionalities can be integrated but it is possible to provide entirely novel properties arising from the coupling between the different components. Progress in nanomaterial synthesis has made it possible to uniformly mix nanoscale components in hybrid materials^[86]. Recently, by co-assembling different NPs with specific size ratios, precisely ordered three-dimensional binary superlattices have been created on a surface^[87]. However few assembly experiments between different colloid NPs have been reported and none using mixtures of NPs without expensive polymers to modulate the interaction potentials. As mentioned before, the silica CSD approach can be used to produce multifunctional hybrid nanostructures with another shell of the second NP type^[88]. Because of the limitations arising from the silica substrate mentioned above, we preferred to use the WI-CSD approach for co-assembly to produce hybrid NPCs.

Cobalt ferrite, CoFe_2O_4 , nanomaterials have shown promise for biological applications because of their chemical stability, high magnetocrystalline anisotropy and coercivity^[89]. Therefore, doping nanomaterials with cobalt could be advantageous to produce NPCs with tuned magnetic properties. However, only few papers report data on the effect of cobalt incorporation in ferrite NPCs on their magnetic response^[90].

A current challenge is the synthesis of cobalt ferrite doped superparamagnetic iron oxide NPCs with desired size and composition. To date, there has been report a small number of works on the effect of cobalt ferrite NPs incorporation in iron oxide NPCs on their magnetic response, size control and composition. Herein we describe the generalisation of the CSD method for cluster assembly to include the preparation of single component clusters (FeO or CoFeO NPCs) and also clusters made starting from co-suspensions of different types of NPs like cobalt ferrite:iron oxide (CoFeO:FeO) clusters. This has opened a new pathway to size-controlled hybrid nanomaterials and has provided further insight into the mechanism of assembly.

3.2 Materials and methods

3.2.1 Materials

Iron (III) acetylacetonate, Fe(III)(acac)₃ (purity ≥ 99.9 %), cobalt(II) acetylacetonate, Co(II)(acac)₂ (purity ≥ 99.0 %), benzyl alcohol (BA ≥ 99.0 %), CHCl₃ (≥ 99.0 %), oleic acid (OA, ≥ 99.0 %) were purchased from Sigma Aldrich ltd Ireland.

3.2.2 Synthesis of iron oxide nanoparticles

A modified protocol ^[91] was used for the preparation of iron oxide NPs. This approach is a free surfactant thermal decomposition of the inorganic iron precursor, iron(III) acetylacetonate. In a typical experiment iron (III) (acac)₃ (1 g, 2 mmol) was weighted into a glass vials, then transferred to the 3-neck round-bottomed flask. 20 mL of benzyl alcohol was added, and the system was degassed by purging nitrogen through the flask for 15 minutes prior the start of the reaction. The flask was simultaneously attached to a nitrogen flow, a water cooled condenser and a high-temperature (>200 °C) thermometer. The reaction was started by turning on the heating mantle to its highest setting and the N₂ flow was reduced. In all cases, the reaction reached its reflux temperature (200 °C) in 15 minutes. The reaction was carried out without stirring. During the reflux, a colour change from red to black was observed, which suggests the formation of iron oxide NPs. After 7 hours, the NP suspension was allowed to cool naturally to room temperature (~ 21 °C), while still under N₂ atmosphere. The resulting NPs are known as benzyl alcohol stabilised iron-oxide NPs (BA-NPs). The suspension was then stored in the absence of O₂. Throughout this thesis iron oxide NPs will be referred to as FeO NPs.

3.2.3 Synthesis of cobalt ferrite nanoparticles

A similar synthetic route has been used for cobalt ferrite nanoparticle preparation. In this case precursors cobalt(II) acetylacetonate (0.33 g, 97 %) and iron(III) acetylacetonate (0.667 g) mixed in a molar ratio of 2:1, were used as precursors. Throughout this chapter cobalt ferrite NPs will be referred to as CoFeO NPs.

3.2.4 Nanoparticle stabilization with oleic acid

The NP suspension produced by the reaction described above was shaken using a vortex mixer until the NPs precipitated was homogenous distributed throughout the solvent (approximately 1 minute). Consecutively 1.5 mL of the concentrated NP suspension was placed into a 1.5 mL Eppendorf centrifuge tube and centrifuged at 13200 rpm for 5 minutes. The resultant supernatant was removed. The centrifuge tube was filled twice with 1.5 mL of acetone and finally centrifuged at 13200 rpm for 5 minutes. Oleic Acid solution was prepared in chloroform at a concentration of 10 mg ligand per mL chloroform. A pre-calculated quantity of this stock solution was added to the washed BA-NPs. This quantity is equivalent to a ligand excess needed to form a monolayer on the surface of the nanoparticles. To do this it is necessarily to use in the calculation the core size obtained from TEM for each type of NPs. In the case of FeO NPs the core size founded is 8.2 nm (and a footprint of 38 \AA^2); for CoFeO has a core size of 7.34 nm. After shaking, this mixture was transferred to a glass vial and the final volume was made up to 1.5 mL using chloroform. The dispersion was shaken overnight to allow for the complete surface coating of the nanoparticles. The stabilised nanoparticles were centrifuged for 10 minutes at 13,200 rpm in order to remove aggregates. This concentrated stabilised dark brown NP solution; the FeO suspension is typically in the concentration range of ~ 108 - 111 mM of Fe, while the CoFeO suspension has a concentration of iron of ~ 115 mM and cobalt of ~ 64 mM.

3.2.5 NPC assembly experiments

3.2.5.1 Controlled assembly nanoparticles from single component nanoparticle suspensions

For the assembly experiment, a volume (20-50 μL) of the concentrated stabilised NP suspension and 1.4 mL of chloroform were mixed (for approximately 1 minute) into a 1.5 mL EppendorfTM tube and then centrifuged for 10 minutes at 13200 rpm. After the removal of eventual aggregates, a volume of 1.2 mL of the NPs solution was placed in a standard glass cuvette (1 cm^3) and then an amount of 0.6 mL of MilliQ water was carefully dripped down the side of the cuvette to the ferric solution, taking care not to agitate the cuvette. The average hydrodynamic diameter of the growing clusters in suspension was continuously monitored by Dynamic Light Scattering (MalvernTM NanoZS) at 25°C. Typically the concentration of the suspension before the beginning of the assembly process was of $\sim 1.8\text{-}2$ mM [Fe].

3.2.5.2 Controlled assembly nanoparticles from multi component nanoparticle suspensions

The cobalt ferrite dispersion was diluted to 1.8 mM Fe, and then dilute dispersion was combined with the 2 mM iron-oxide dispersion to produce a broad range of [FeO]:[CoFeO] ratios: 1:1, 1:2, 1:6, 1:8. A volume of 1.2 mL of nanoparticle co-suspension was placed in the glass cuvette with 600 μL of water on top, as described above, and the average hydrodynamic diameter growth was continuously monitored by DLS.

3.3 Results and discussion

3.3.1 Size and stability of the primary nanoparticles

The core size of the iron oxide and cobalt ferrite nanoparticles were measured using TEM. The procedure used for the sample preparation is described in detail in Chapter 2. According to the TEM images (Figure 3-1) both types of NPs seem to be uniform with quasi-spherical shape. More than 1000 particles have been counted in both cases. From these measurements, particle size distributions were fitted to a log-normal size

distribution function shown in Equation 2-11 and the mean particle size and standard deviations were derived by the Equation 2-12 and Equation 2-13. The CoFeO and FeO core size found are 7.34 and 8.2 nm respectively. The R^2 value was found to be greater than 0.99 for both type of NPs and standard deviations of 1.75 nm and 1.20 nm for CoFeO and FeO respectively were calculated.

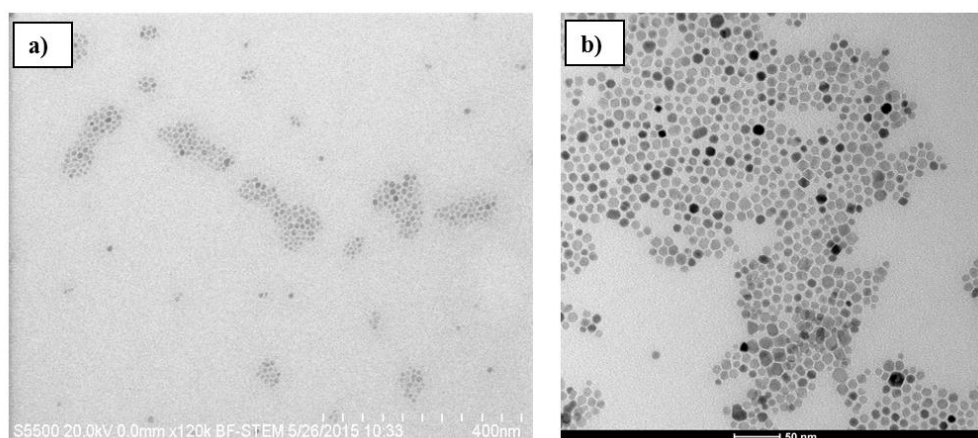


Figure 3- 1 a) TEM image of oleic acid-stabilized iron oxide nanoparticles dispersed in chloroform. The hydrodynamic size is 15 nm, PDI=0.08. b) TEM image of oleic-stabilized cobalt ferrite nanoparticles dispersed in chloroform. The hydrodynamic size is 13 nm, PDI = 0.11. 1250 FeO NPs and 1450 CoFeO NPs were counted.

The hydrodynamic size of both FeO and CoFeO primary nanoparticles in chloroform was measured by DLS. In Figure 3-2 and Figure 3-3 typical intensity weighted hydrodynamic size distributions are shown. The results of DLS measurements show that both suspensions were monodisperse; the analysis indicated the presence of unimodal size distributions with hydrodynamic diameter of 13 nm and low PDI values (< 0.11) with no evidence of agglomerates before cluster growth. The suspensions obtained were stable, by DLS, for periods of months.

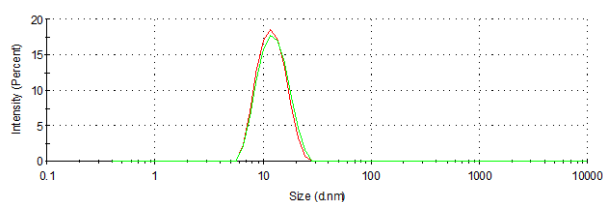


Figure 3- 2 Size distribution by intensity plot for two suspensions of cobalt ferrite nanoparticles dispersed in chloroform at day 1, $d_{\text{hyd}} = 13$ nm, PDI = 0.102 (red line) and day 65 $d_{\text{hyd}} = 13.68$ nm, PDI = 0.11 (green line).

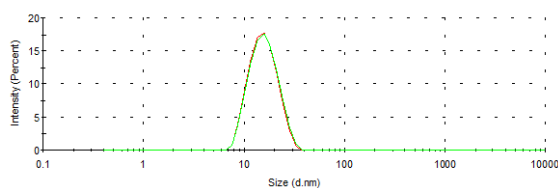


Figure 3- 3 Size distribution by intensity plot for two suspensions of iron ferrite nanoparticles in chloroform at day 1 $d_{\text{hyd}} = 14.6$ nm, PDI = 0.076 (red line) and day 72 $d_{\text{hyd}} = 14.8$ nm, PDI = 0.08 (green line).

3.3.2 Controlled assembly nanoparticles from single component nanoparticle suspensions

Typical assembly data obtained by DLS for the formation of iron oxide and cobalt ferrite clusters are shown in Figure 3-4, in which the hydrodynamic size (d_{hyd}) of the NPCs is plotted as a function of time starting from oleic acid-stabilised primary nanoparticles (FeO, $d_{\text{hyd}}=15$ nm; CoFeO, $d_{\text{hyd}}= 13$ nm). The PDI values were also plotted as a function of time. Note that the suspensions were phase transferred to chloroform using the same equivalents of OA (i.e. 0.75 excess).

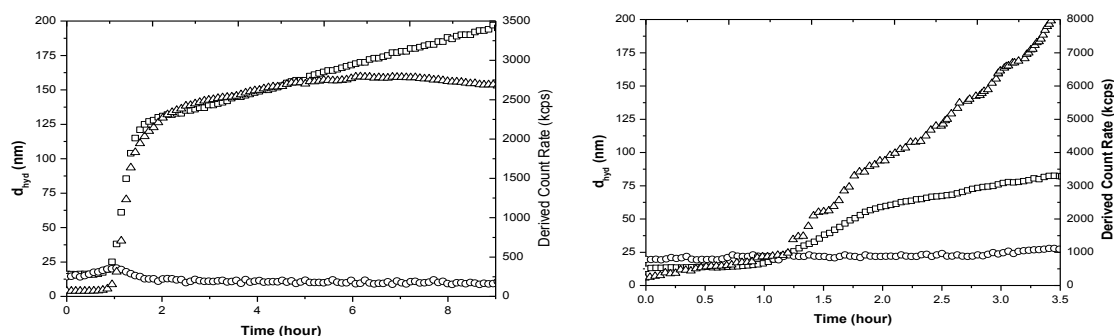


Figure 3- 4 (Left, a) Typical assembly data by DLS of FeO cluster formation starting from of OA stabilised FeO dispersed in chloroform (1.2 mL, ~ 2 mM [Fe]) over time by WI-CSD. D_{hyd} (nm) (\square), $\text{PDI} \times 100$ (\circ) (left hand axis) and derived count rate (kcps) (Δ). (Right, b) NP assembly of OA stabilised CoFeO NPs dispersed in chloroform (1.2 mL, ~ 1.85 mM [M]) over time by water CSD. D_{hyd} (nm) (\square) $\text{PDI} \times 100$ (\circ) and derived count rate (kcps) (Δ) are reported. Note that all experiments are performed under the same conditions unless stated otherwise.

Figure 3-4 (a) shows the DLS data of FeO NPCs growth over time. The primary NPs used in this experiment have hydrodynamic diameter of 15 nm and a PDI of 0.08. The gradual increase of intensity of the backscattered photons up to 9 hours indicates the gradual increase in the number of larger particles in suspension. During all the process of

assembly there is a unimodal size distribution as it is possible to see from PDI values which remain low (0.08 – 0.15). Typical assembly data obtained by DLS for the formation of CoFeO NPCs from 13 nm (PDI 0.17) CoFeO primary nanoparticles are also shown in Figure 3-4 (b).

Compared to FeO NPs, under similar conditions CoFeO NPs seem to have a slower assembly rate even though they have similar induction time (~1 hour). This could be related to a higher amount of OA transferred, higher free energy for ligand adsorption^[92] or differences in the nature of the NP* species formed in the initial stages of the assembly process (reducing reactive in this case). Finally, FeO NPs show lower PDI values (0.065-0.1) than CoFeO (0.1-0.12) over the whole assembly process.

The particle size distributions were obtained from correlation function analysis and were unimodal for both type of NPCs. The particle peak distributions of assembling NPC suspensions shifted to larger diameters over time, as is shown in Figure 3-5.

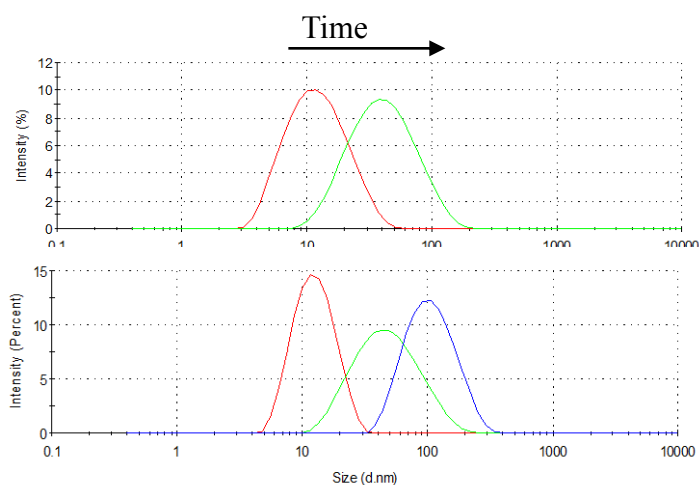


Figure 3- 5 Scattering intensity distribution of assembling FeO (a) and CoFeO (b) NPCs in chloroform by water CSD as a function of time.

3.3.3 Reproducibility of single nanoparticle type assembly

To achieve controlled assembly of binary clusters it was felt that strong control over single component assembly was required. Hence reproducibility tests were conducted for both FeO and CoFeO nanoparticles. Both primary nanoparticles of FeO and CoFeO from two different syntheses were stabilised with oleic acid, keeping the same total concentration of metal and of ligand (~2 mM [M], 0.75 excess of OA). At this point the nanoparticles were suspended in chloroform and assembled under the same experimental

conditions. The DLS results are shown in Figure 3-6. The difference of hydrodynamic diameter between the two experiments is low (less than 5 %). This confirms that both FeO and CoFeO nanocluster hydrodynamic size and the rate of assembly can be reproduced when care is taken. In the case of FeO the reproducibility is verified in the size range of 20-200 nm (over 4 hours), while in the case of the CoFeO NPCs this range is limited to 15-90 nm (over 4 hours). In addition the PDI values were excellent in the case of FeO NP assemblies (0.07-0.85) throughout the whole process, while in the case of CoFeO NP assemblies a slightly reduced of monodispersity ($0.12 < \text{PDI} < 0.19$) is observed.

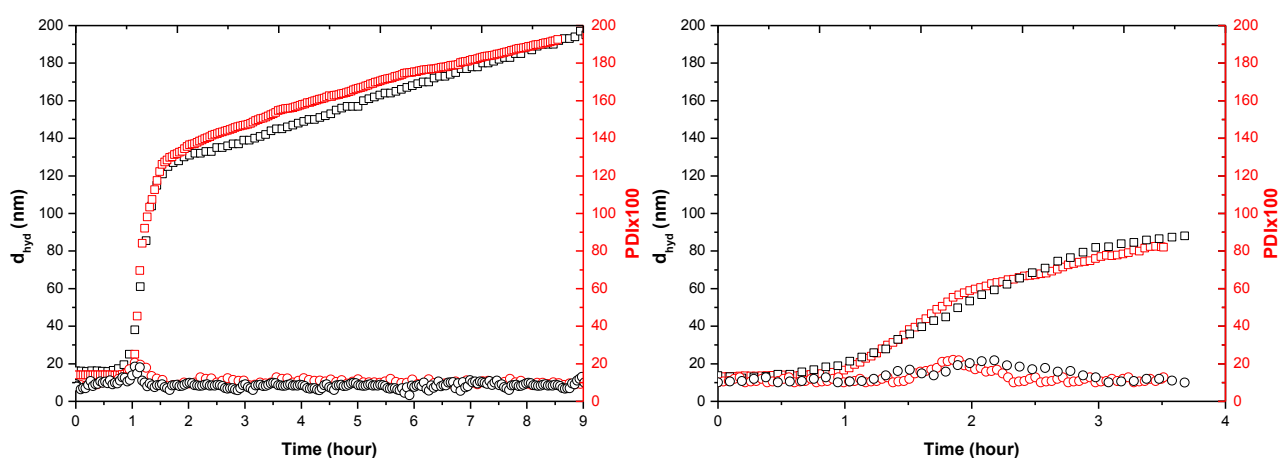


Figure 3- 6 (Left) FeO NPs (2.2 mM [Fe]) assembly in chloroform over time by WI-CSD. (closed square) d_{hyd} (nm), (empty square) PDI*100. (Right) CoFeO NPs assembly in chloroform. (closed square) d_{hyd} (nm), (empty square) PDI*100.

3.3.4 Kinetics and mechanism of the nanoparticle assembly by Water Interface Competitive Stabilizer Desorption approach

In order to analysis the kinetics of the NP assembly process, the assembly curves were fitted using three mathematical models that can be related to three distinct stages of the assembly as shown in Figure 3-7; i.e. an initial exponential, subsequent intermediate and later linear assembly stages.

The early stage (stage I) was fitted with an exponential function given by the Equation 3-1:

$$y = y_0 + Ae^{\frac{-t_0}{\tau_{\text{exp}}}}$$
Equation 3- 1

where y_0 is the y offset, A is the amplitude, t_0 is the time offset and τ_{exp} is the characteristic time related to the exponential assembly stage.

The later stage (stage II) was fitted using the power function described by the Equation 3-2:

$$y = A|t - t_0|^{\tau_p}$$
Equation 3- 2

where A is the amplitude, t_0 is the time offset and τ_p is the characteristic power associated with the intermediate assembly stage.

The assembly in the third and last stage (stage III) is slower if compared to stage I and it was fitted to the linear function given by the Equation 3-3:

$$y = mt + c$$
Equation 3- 3

where m is the slope and c is the intercept of the straight line.

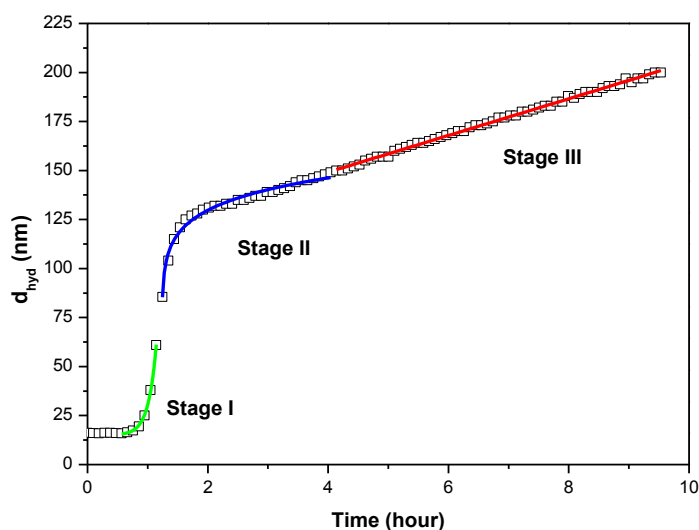


Figure 3- 7 The stages of typical assembly data by DLS of FeO cluster formation starting from of OA stabilised FeO dispersed in chloroform (1.2 mL, ~2 mM [Fe]) over time. The curve was fitted using three mathematical models; (green line) exponential fit, Equation 3-1 (blue line) power fit, Equation 3-2, and (red line) linear fit, Equation 3-3.

The transition from the exponential to linear assembly stage can be explained as follows. Upon addition of the water layer onto the equilibrium between bound and unbound OA is perturbed, so that unbound OA diffuse towards the water/suspension interface. At this point the OA bound to the NP surface desorbed to reestablish the equilibrium creating activated NPs (NP*). At the end of the induction period sufficient NPs* are formed for small NPCs to appear and an exponential acceleration of the assembly occurs (stage I). The assembly process is here dominated by NP* to NP* collisions. Subsequently, in stage II the kinetics of the assembly can be expressed as $NPC_n^* + NP^* \rightarrow NPC_{n+1}$. At later stage (stage III) the OA desorption occurs from the NPC surface generating activated NPCs (NPC*) which assemble further through collisions with other NPC* resulting in an acceleration of the assembly rate. In this kinetic phase the OA adsorption to the interface is reduced (as it is partially complete) leading to gradual assembly of moderate rate which is linear. A schematic representation of the assembly process by WI-CSD method is shown in Figure 3-8.

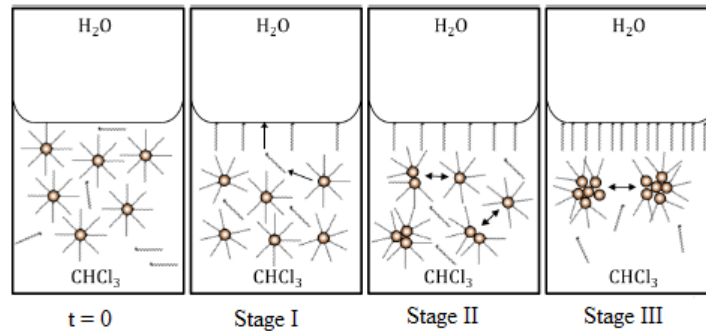


Figure 3- 8 Schematic representation of Water Interface Competitive Stabilizer Desorption mechanism ^[85].

Irreversible (and controlled) assembly of NP*, following collision, arises from the reduction in interparticle repulsion ^[59] due to gradual depletion of OA from the NP surface. Two repulsive interactions, the osmotic and elastic forces, are involved. At longer NP separations the osmotic interaction potential (Φ_{osm}) between two NPs of size R dominates, this interaction was defined by Vincent and co-workers as:

$$\Phi_{osm} = \frac{4\pi Rk_B T}{v_{solv}} \cdot \phi^2 \cdot \left(\frac{1}{2} - \chi \right) l^2 \left(\frac{d-2R}{2l} - \frac{1}{4} - \ln \left(\frac{d-2R}{l} \right) \right) \quad \text{Equation 3-4}$$

where ϕ is the ligand surface coverage fraction on the NP surface; χ is called Flory–Huggins parameter which characterizes difference in cohesion energy between the ligand and the solvent; d is the NP core-core distance and l is the length of the stabilizing ligand. The repulsive elastic interactions dominate at very short distance, *i.e.* when the interparticle separation is less than the length of the ligand (l). The expression that describes this force was reported by Vincent and Napper^[93] as:

$$\Phi_{elas} = \frac{2\pi R k_B T l^2 \rho}{MW_2} \cdot \phi \cdot f(d - 2R, l)$$

Equation 3- 5

where ρ is the ligand density and MW_2 is the molecular weight of the ligand.

Both Equations 3-4 and 3-5 demonstrate that these interactions are dependent on the ligand coverage fraction (ϕ) which decreases with the depletion of the ligand (OA) leading to the attenuation of these repulsive forces and consequently to NP assembly. Note that in most assemblies processes the interaction potential is modulated through the osmotic interaction through the term χ which determines the sign of the interaction. So, for instance, addition of an anti-solvent can reduce the interaction or even reverse its sign. The CSD process in this regard as it relies only on depletion and ϕ .

3.3.5 Optimization of NP assembly conditions

3.3.5.1 Iron concentration

Assembly curves for iron-oxide clusters formed from γ -Fe₂O₃ NPs at different concentration of iron are shown in the Figure 3-9. ICP analysis indicates that samples have the following total initial iron concentration: 0.79 mM, 1.10 mM and 1.58 mM. In all cases an excess of oleic acid of 0.75 equivalents was used. A significant increase in the rate of NP assembly was observed with a decrease in the concentration of the primary particle. Also for more concentrated suspensions the induction time is longer. This is surprising because one would expect that with increasing NP concentration, the formation of higher amounts of NP* should be favoured so that the probability of the collision between NP* particles is higher, leading to higher assembly rates. This suggests that in the CSD process the OA depletion mechanism is crucial and dominates the kinetics.

In order to quantify the effect of the NP concentration on the assembly process, assembly curves shown in Figure 3-9 was modelled using the exponential function given by the Equation 3-1. For the first hour the data confirmed the exponential model, with R^2 values ranging from 0.98-1 as shown in Table 3-1. The parameters extracted from the fitting reveal that the NP concentration has a high impact on both the induction time (t_0) and the assembly rate (τ_{exp}^{-1}). On increasing the NP concentration, the induction time increases while the assembly rate decreases dramatically (Figure 3-10). These results show that it is possible to achieve a desired assembly rate by simply tuning the NP concentration of the suspension.

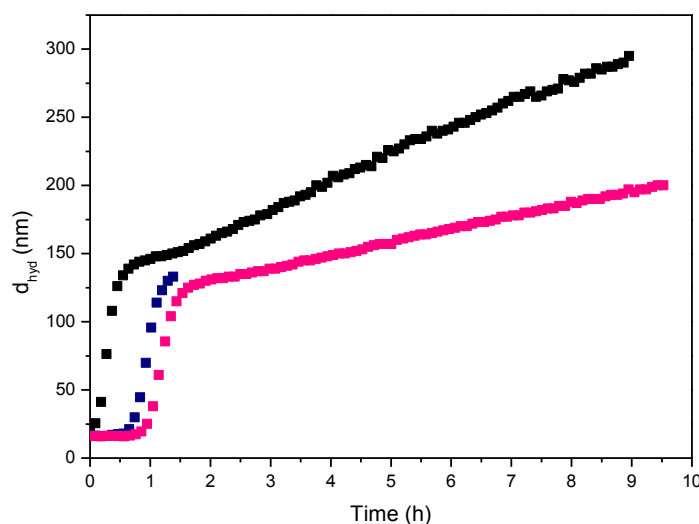


Figure 3- 9 Kinetics of particle assembly for suspensions phase transferred with 0.75 surface equivalents of oleic acid with Fe concentration of (■) 1.58, (■) 1.10, (■) 0.79 mM.

[Fe] mM	[NPs] μM	y_0 (nm)	A	Induction time, t_0 (hour)	τ_{exp} (hour/nm)	τ_{exp}^{-1} (nm/hour)
0.79	0.14	18	5.26	0.10	0.09	11.33
1.10	0.20	17	0.90	0.37	0.16	6.19
1.58	0.29	17	0.31	0.76	0.17	6.05

Table 3- 1 Parameters extracted from the exponential fitting of assemblies conducted with different NP concentration. In all the experiments, the oleic acid ratio is fixed (0.75 excess).

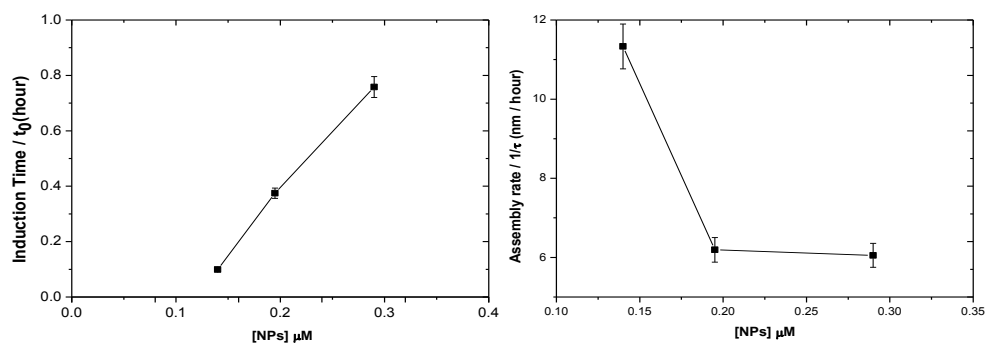


Figure 3- 10 The effect of the nanoparticle concentration on (left) the induction time and on (right) the assembly rate in the exponential phase.

3.3.5.2 Oleic acid concentration

In order to reduce as much as possible the polydispersity during the formation of FeO - CoFeO hybrid clusters, an attempt was made to match the assembly rates for each NP type (in a single component experiment) by optimizing the quantity of oleic acid on the NP surface. In the case of FeO NPs ([Fe] \sim 1.8 mM), 1.3, 1.05, 0.95 and 0.6 excesses of fatty acid were used. The assembly curves for different FeO suspensions are reported in the Figure 3-11.

In all cases the PDI value was lower than 0.112 with the exception of the assembly conducted with 1.3 equivalents of oleic acid where the PDI was in the range of 0.085-0.185. The graph demonstrates clearly that the rate of assembly is adjustable by the amount of fatty acid on the NP surface.

Similar results were achieved with CoFeO NPC assembly. In this case a fixed total metal concentration (\sim 1.86 mM) and OA excesses of 0.5, 0.6 and 0.75 have been used (Figure 3-11). The PDI values were a little higher than the previous case, in the range 0.14-0.21. The kinetics data for the experiments shown in Figure 3-11 have been fitted with the exponential function to assess the effect of the oleic acid on the assembly process. The parameters extracted are reported in Table 3-2 and Table 3-3.

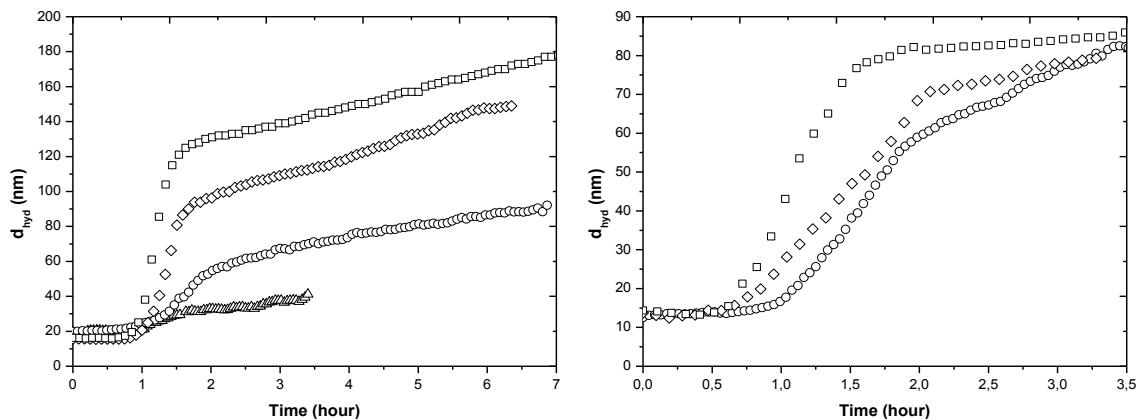


Figure 3- 11 (Left) Kinetic curves for oleic acid stabilised FeO NPs in chloroform with 0.75 (□), 0.95 (◇), 1.05 (○), 1.3 (Δ) equivalents of OA. (Right) Kinetic curves for oleic acid stabilized CoFeO NPs in chloroform with 0.5 (□), 0.6 (◇), 0.75 (○) equivalents of OA.

Oleic acid added (equiv/ug)	y_0 (nm)	t_0 (hour)	τ_{exp} (hour/nm)	τ_{exp}^{-1} (nm/hour)
0.75	19	0.75	0.22	4.61
0.95	18.7	1.00	0.32	3.10
1.05	16.2	1.09	0.44	2.26
1.30	15.7	1.11	0.59	1.70

Table 3- 2 Parameters extracted from the exponential fitting for the FeO NP assembly with different amount of OA.

Oleic acid added (equivalent)	y_0 (nm)	t_0 (hour)	τ_{exp} (hour/nm)	τ_{exp}^{-1} (nm/hour)
0.5	14.36	0.57	0.09	11.11
0.6	13.71	0.66	0.11	9.09
0.75	12.53	0.86	0.47	2.13

Table 3- 3 Parameters extracted from the exponential fitting for the CoFeO NP assembly with different concentration of OA.

It is apparent that the induction time increases on increasing the equivalents of oleic acid used. This number of equivalents is inversely correlated to the NPC assembly rate (τ_{exp}^{-1}), which demonstrates that the assembly process is faster when the NPs are loaded with low ligand coverage. Hence, the assembly can be controlled from really slow (1.70 and 2.91 nm/hr for FeO and CoFeO, respectively) to relatively fast (4.61 and 3.32 nm/hr) by varying the amount of oleic acid coupled on the NP surface while maintaining equal NP

concentration. In order to get a controlled clustering of the NPs in the co-suspensions, the assembly rates extracted from Figure 3-11 have been compared. The best match found was FeO covered with 1.05 excess (2.26 nm/hour) and CoFeO with an excess of 0.75 (2.13 nm/hr) as it is also shown in Figure 3-12. For this reason these quantities of ligand have been used in the following co-clustering experiments.

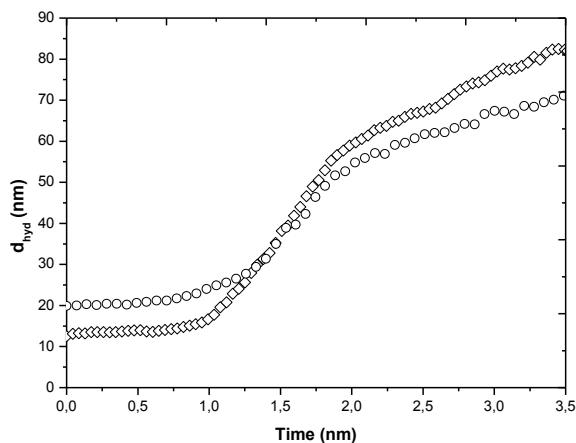


Figure 3- 12 DLS data of (○) FeO (1.05 excess OA, 18 nm) and (◇) CoFeO (0.75 excess OA, 15 nm) NP assembly. The total metal concentration used was 1.95 mM in each experiment.

3.3.6 Study of hybrid CoFeO -FeO NP assembly from mixed-metallic oxide co-suspensions

Having demonstrated that both type of NPs are stable and they assemble with good PDI values using WI-CSD, a series of experiments were performed to investigate if it is possible to create hybrid clusters. DLS data for a mixed-metal dispersion containing maghemite and cobalt ferrite NPs mixed (1:1) are shown in Figure 3-13. The overall rate assembly of the mixed-metal NP assembly curve is faster than the individual CoFeO NPs and FeO NPs dispersions. After an induction time of ~50 minutes, there is an assembly up to 4 hours and then the assembly significantly decreases. As in the case of the FeO suspension, the PDI of the co-suspension has a good PDI value (0.12) and gradually decreases to 0.09. In all cases a transition from an early rapid exponential-like assembly to a slower linear-like stage was observed.

The stability of the co-suspension without the water interface was also investigated. This was achieved by preparing a suspension of CoFeO:FeO 1:1 at the same concentration used in the assembly experiment and monitoring of the size over time by DLS. In Figure

3-13 (right) it can be seen that the NP co-suspension is stable over time in the absence of an interface, both the hydrodynamic diameter (14.5 nm) and the derived count rate are unchanged over 12.5 hours. This confirms that the water layer is necessary for assembly.

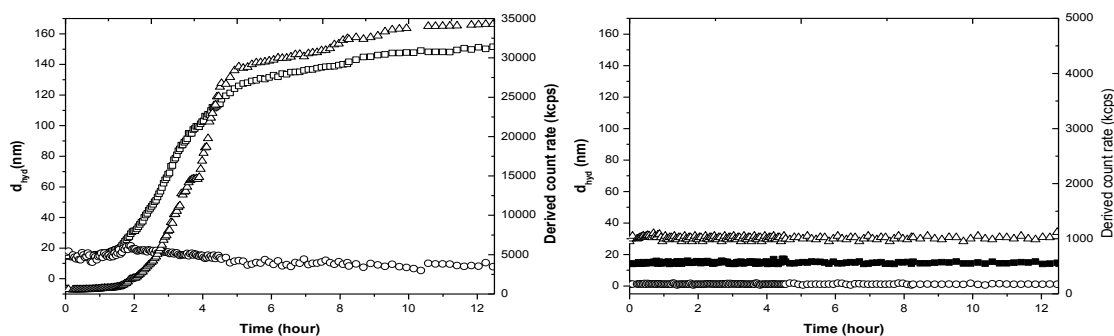


Figure 3- 13 (Left) DLS data of the co-clustering of FeO (1.05 excess OA, 17 nm) and CoFeO (0.75 excess OA, 15 nm) NPs over time by WI-CSD. (\square) d_{hyd} , (\circ) PDI*10 (left hand axes) and (\triangle) count rate (right hand axis). (Right) Monitoring of NP suspension d_{hyd} in absence of water.

The correlation function and particle size distribution by intensity of NPCs in chloroform as a function of time are shown in Figure 3-14. The primary size was not measured yet by TEM for this sample, but DLS analysis indicated a hydrodynamic diameter of 13 nm at the start of the assembly experiment. The distributions prove that there is an increase of NPC size during the assembly process.

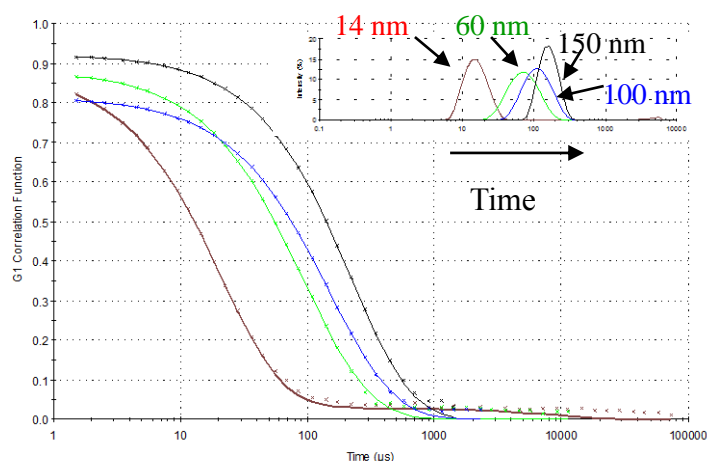


Figure 3- 14 The graph shows the intensity weighted size distribution (top right) and correlation function of the CoFeO-FeO NPs co-clustering over time. Primary NPs at $t=0$ (brown line), 60 nm NPCs (green line), 100 nm NPCs (blue line), 150 nm (black line).

3.3.7 Reproducibility of nanoparticle co-assembly

A series of reproducibility tests were performed. Suspensions of primary FeO and CoFeO NPs from different synthesis were stabilised with oleic acid, keeping the same total concentration of iron and fatty acid. These suspensions were then suspended in chloroform and assembled at the same experimental conditions. The results are shown in Figure 3-15. The difference in d_{hyd} between the two experiments is lower than 5 %, which demonstrates that both the size of the hybrid nanoclusters and the rate of assembly are reproducible up to the 250 nm size range, over a 14 hour time scale. Moreover, in both experiments the monodispersity is excellent through the whole process ($\text{PDI} < 0.15$).

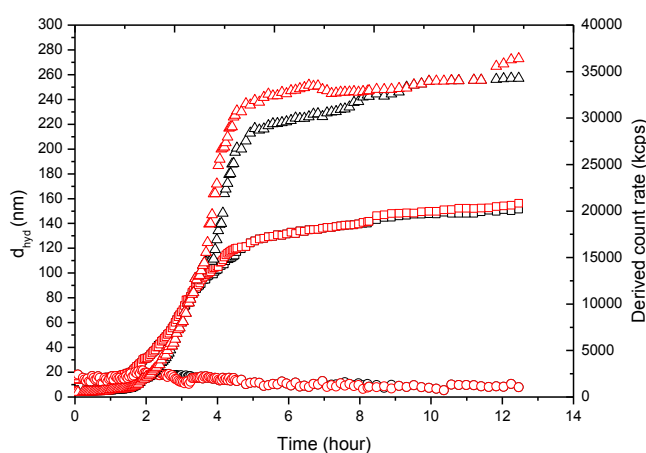


Figure 3- 15 DLS data of two different assembly experiments of CoFeO-FeO OA stabilized NPs in CHCl_3 . (\square) d_{hyd} , (\circ) $\text{PDI} \cdot 100$ (left axis); (Δ) derived count rate (right axes).

3.3.8 NP assembly using different ratios of CoFeO:FeO nanoparticles

Typical assembly data for mixed CoFeO-FeO suspensions as function of CoFeO:FeO ratio is reported in the Figure 3-16. The primary nanoparticles hydrodynamic size of CoFeO and FeO were 13 and 17 nm respectively before starting the experiment. As seen previously, there is an increase of the hydrodynamic diameter with time for the mixed NP suspensions in all cases which demonstrates the formation of clusters. The size distribution for the hybrid NPCs were unimodal during the whole assembly process and the correlograms confirmed the absence of any large aggregates. Lower assembly rates are observed at higher ratios of CoFeO to FeO NPs in the suspension. This result is not surprising because the assembly was slower for pure CoFeO suspensions. The PDI values remained lower than 0.15 for up to 1.5 hours for all the suspensions and in most cases it remained below than 0.12.

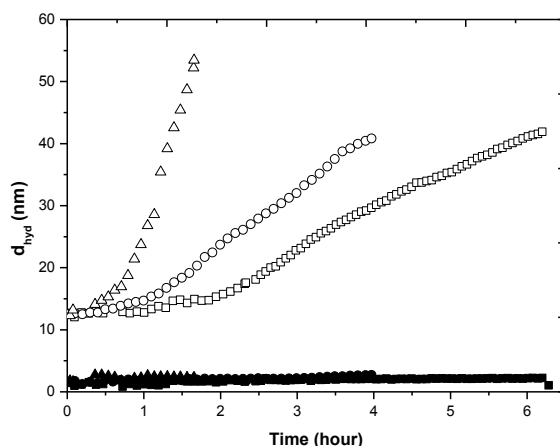


Figure 3- 16 Hydrodynamic size (d_{hyd}) and PDI*100 of hybrid CoFeO:FeO NPCs of different molar ratios. (\square) 8, (\diamond) 6, (Δ) 2.

Before any further analysis, the stability of one CoFeO:FeO NPC suspensions (1:1) was investigated. This was achieved by arresting the clustering through removal of the water layer from the suspension followed by the monitoring of d_{hyd} over time. Both size distribution graph and the correlation function graph (Figure 3-17) demonstrate that the NPCs seem to be stable over periods of days, without showing any evidence for aggregation.

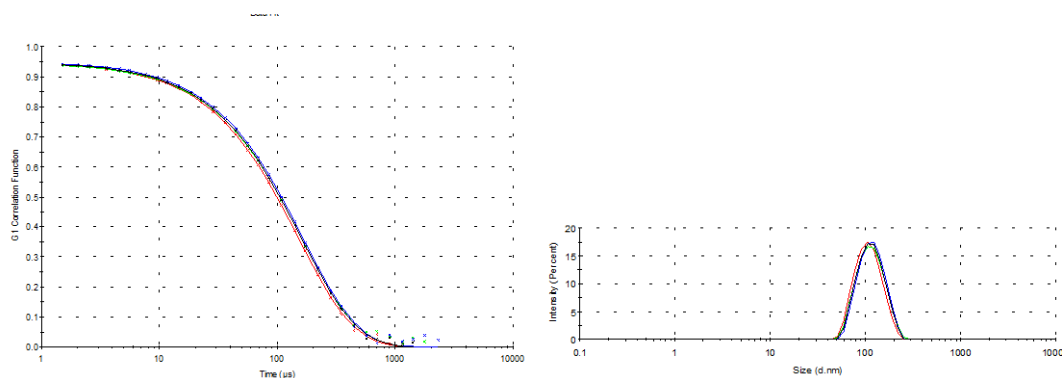


Figure 3- 17 Size distribution (right) and correlation function (left) of 107 nm CoFeO:FeO (1:1) NPCs dispersed in chloroform over time (PDI=0.07), (red line) 56 minutes, (green line) 14 months, (blue line) 5 hours, (black line) 4 days.

3.3.9 FESEM analysis of CoFeO:FeO hybrid assemblies

Further evidence for the formation of CoFeO-FeO co-clusters was provided by field emission scanning electron microscopy (FESEM) images (Figure 3-18).

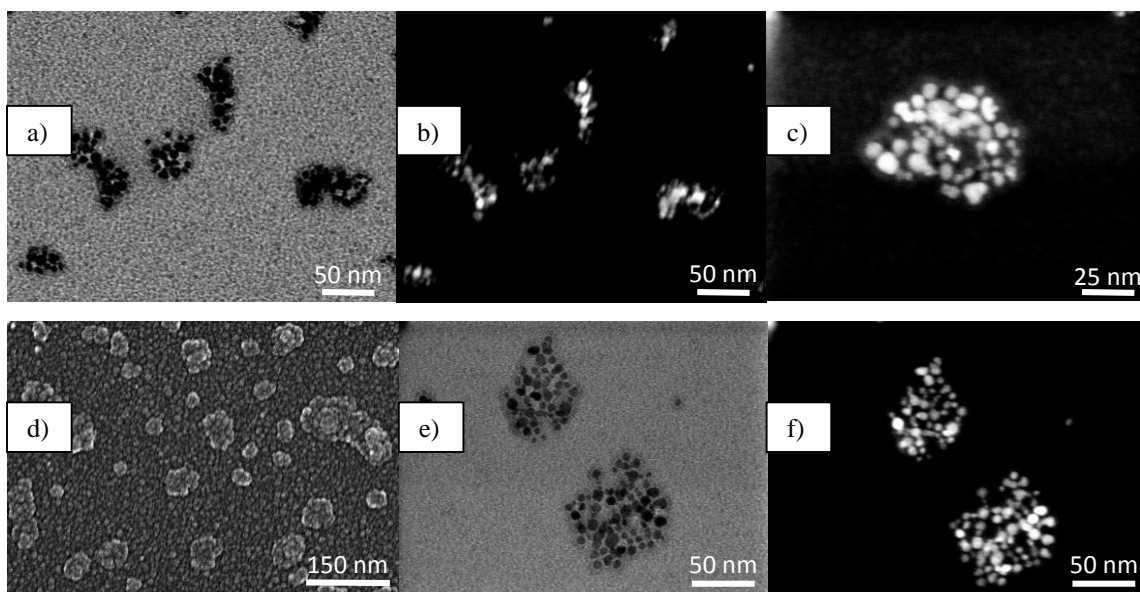


Figure 3- 18 Bright- and dark -field FSTEM images of CoFeO:FeO (1:1) NPCs ($d_{\text{hyd}} = 65$ nm, PDI = 0.11) produced by the WI-CSD method. The inset scale bar represent 300 (a, b, e,f), 25 (c) and 150 (d) nm.

In dark-field STEM mode (Figure 3-18 b,c,f), it is possible to distinguish the cobalt based NPs which generates the brighter contrast while the FeO NPs generate a darker contrast inside the clusters. We can observe the opposite situation in the case of the bright-field images (Figure 3-18 a,e) where the cobalt based nanoparticles generate a brighter contrast. It is also evident from the Figures 3-18 b, c, d, f that the CoFeO are homogeneously distributed in the clusters. The core size of these clusters is 52 nm ($\sigma = 1.5$ %) while the hydrodynamic size is 65 nm (PDI = 0.11). Even though DLS analysis shows an unimodal size distribution (PDI = 0.11), Figure 3-18b shows clusters not fully monodisperse, probably because of disaggregation/aggregation of the clusters during the deposition and drying of the sample on the grid for microscopy analysis.

3.3.10 Scale up of WI-CSD for CoFeO-FeO hybrid assemblies

Having demonstrated the successful preparation of CoFeO-FeO hybrid NPCs by microscopy, scale up experiments were performed to prepare these NPCs at large scale. The scale-up experiment was carried out in glass flat bottom vessels (Sigma Aldrich, Figure 3-19) of different capacity were used. The ratio between the volume of suspension to the interface surface area at NP concentration / surface area ratio was maintained at the same value as in the experiments conducted with the glass cuvette (~ 2 mM Fe/cm², iron to interface ratio). In the case of the larger vessel an anodized aluminum scaffold was

used added to hold up and maintain a uniform layer of the water over the suspension creating a stable interface.

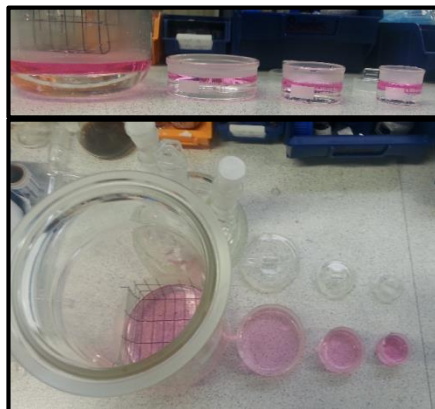


Figure 3- 19 Glass flat bottom vessels of 1 liter, 80, 30 and 15 mL capacity. The uniform water layer (pink) is place onto the chloroform (bottom) to form a stable and reproducible interface.

After careful addition of the water layer the NPC size was monitored by DLS over time by taking samples using a glass syringe with a long needle. In order to stop the assembly process, the suspension was removed from under the layer of water when the desired size was achieved. Figure 3-20 shows typical assembly data for experiments conducted with different volumes of co-suspension (1.21, 60 and 150 mL). The assembly curves have similar rates and induction times which means that it is possible to scale up the WI-CSD for binary systems maintaining low PDI values (0.075-0.11).

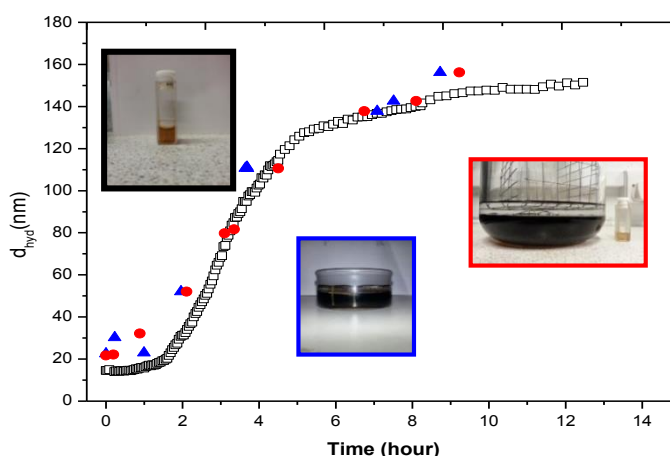


Figure 3- 20 Scale up of CSD method for CoFeO-FeO co-assembly to (□) 1.2, (▲) 60 mL and (●) 150 mL of NP co-suspension. The primary nanoparticles used have hydrodynamic diameter of 18 nm (PDI = 0.08) and 15 nm (PDI = 0.11) respectively. [M]~ 2 mM; the excess used for FeO and CoFeO NPs was 1.05 and 0.75 respectively.

The success of this approach to scaling up the WI-CSD method means that it is now possible to produce significant quantities of binary NPC chloroform suspensions, with a view to subsequently to optimizing phase transfer for biomedical applications.

3.3.11 Effect of the binary NPC composition on Nuclear Magnetic Resonance Properties

According to the data presented in the previous paragraph, it has been shown that it is possible to control the rate of the assembly process by changing the NP concentration, the ligand concentration but also by changing the fractions of the two NP types. After showing the reproducibility of the co-clustering process the next step is to investigate whether NPC composition affects the magnetic resonance properties of the resulting suspension. For these NMRD experiments, CoFeO-FeO NPCs of comparable size were prepared starting from nanoparticle dispersions of different CoFeO:FeO ratio (Table 3-4). The assembly process was then stopped by the removal of the sample from under the water layer and the chloroform NPC suspensions were then characterized by NMRD characterization.

The hydrodynamic diameter values were checked before and after the NMRD experiments to confirm the stability of the NPCs to magnetic field exposure. It is apparent from the Table 3-5 that in all cases there are no significant changes in either the d_{hyd} or PDI values.

[CoFeO:FeO] molar ratio	Before NMRD	After NMRD
	d_{hyd} (nm) [PDI]	d_{hyd} (nm) [PDI]
0	113 [0.09]	115 [0.07]
0.5	117 [0.15]	100 [0.17]
2	113 [0.18]	107 [0.11]
8	102 [0.11]	105 [0.11]

Table 3- 4 DLS data from before and after the NMRD experiment and PDI values of CoFeO-FeO clusters assembled using different CoFeO:FeO molar ratios.

In Figure 3-21 NMRD profiles of the CoFeO-FeO clusters assembled with different CoFeO:FeO ratios normalized by the total metal concentration and by the iron concentration are shown. The ^1H Larmor frequency at which the r_1 maximum occurs, ν_{max} , was unchanged in all cases at 3.5 MHz. When the normalization is per iron content there is a suppression of the $r_{1\text{max}}$ value, while when the normalization is per unit of total metal the r_1 maximum is almost constant. This interesting result suggests that the total metal content should be used and that the relaxivity at high frequencies is insensitive to the metal ion type. Moreover on increasing the ratio of CoFeO within the clusters, a gradual suppression of the r_1 maximum at high field is observed. This weak dependence of relaxivity on the field was observed also for CoFeO polystyrene-sulphonate nanocomposites [89]. Finally, the mid-frequency range longitudinal relaxivity minimum is suppressed, probably due to weak interparticle interactions within the NPCs [94]. These observations suggest that there are only NPCs in the suspensions, or at least there is a very small amount of primary NPs.

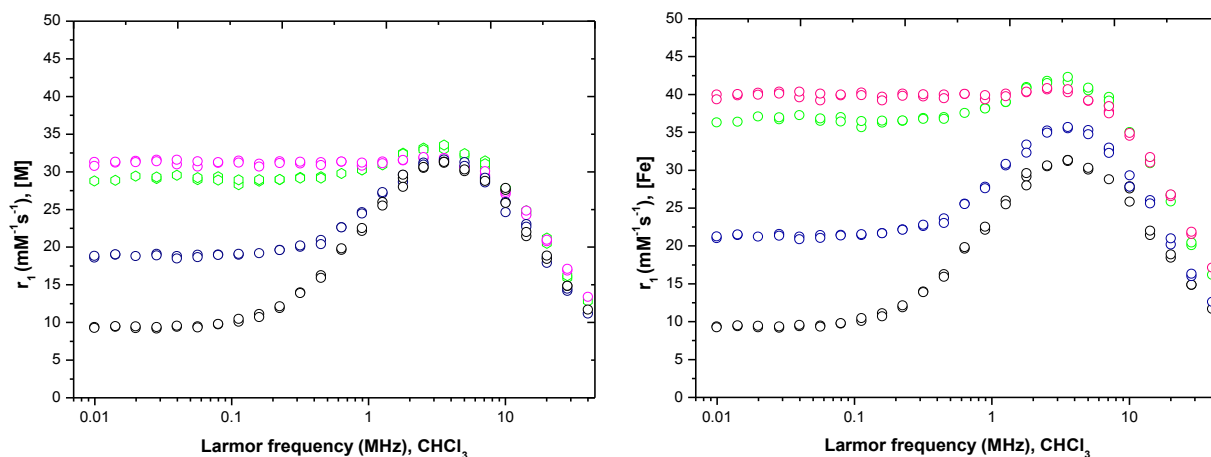


Figure 3- 21 NMRD profiles of clusters made from co-suspensions of CoFeO:FeO ratios of (○) 0 ($d_{\text{hyd}} = 113$ nm, PDI = 0.09, $[\text{Fe}] = 0.833$ mM, $[\text{M}] = 0.833$), (○) 0.5 ($d_{\text{hyd}} = 117$ nm, PDI = 0.15, $[\text{Fe}] = 0.832$ mM, $[\text{M}] = 0.938$), (○) 2 ($d_{\text{hyd}} = 113$ nm, PDI = 0.18, $[\text{Fe}] = 0.770$ mM, $[\text{M}] = 0.971$), (○) 8 ($d_{\text{hyd}} = 102$ nm, PDI = 0.11, $[\text{Fe}] = 0.826$ mM, $[\text{M}] = 0.998$). The NMRD profiles are normalized by (left) the total metal concentration and by (right) the iron concentration. The concentrations of the metals were determined by ICP-AES.

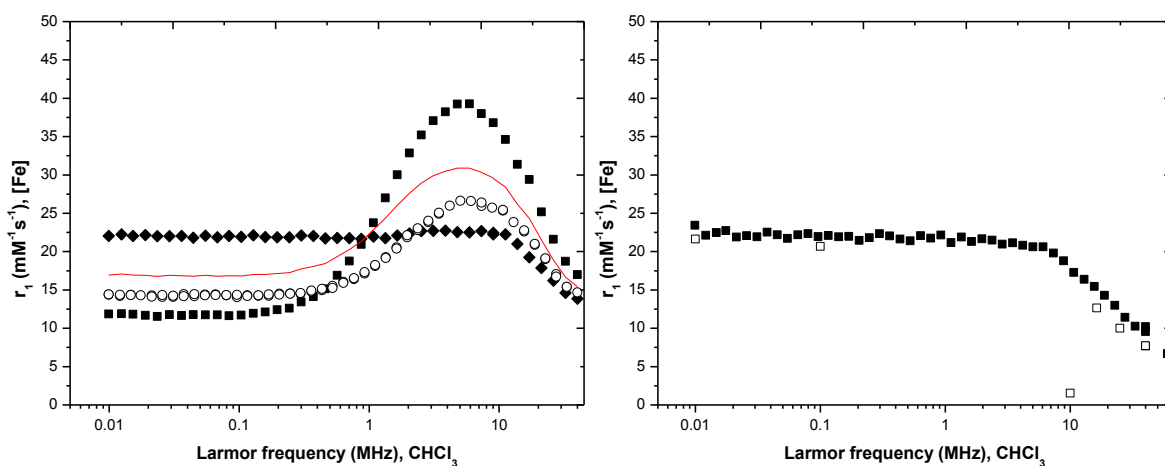


Figure 3- 22 (Left, a) NMRD profiles of (■) FeO NPCs (42 nm, PDI = 0.11), (●) CoFeO NPs (53 nm, PDI = 0.12) and CoFeO:FeO NPCs 47 nm , PDI = 0.10) in chloroform. The curves were normalized by total metal concentration. The $r_{\text{Co-NPCs}} = 0.5r_{\text{FeNPCs}} + 0.5r_{\text{CoNPCs}}$ simulation curve (red line) is also reported. (Right, b) NMRD profile of mixture of the same preformed FeO and CoFeO

Figure 3-22 (right) reports the NMRD profiles of FeO, CoFeO and CoFeO:FeO NPCs of similar sizes. The simulation curve reported in red represents the average relaxivity of single component clusters of FeO and CoFeO of similar size. As shows the red simulation curve, the CoFeO:FeO NPC longitudinal relaxivity seems to be different than the simulated average r_1 for a suspension of two single component NPCs. This confirms that CoFeO:FeO NPCs have different magnetic properties, and that the two NP types are co-assembled into mixed clusters and that single component NPCs are not formed during the assembly experiment. This result is also confirmed by the FESEM images, reported previously.

The relationship between r_1 (measured at 10, 16.3 and 61 MHz) and the CoFeO:FeO ratio used for the co-clustering is reported in the Figure 3-23 (left). It can be seen that the change in CoFeO:FeO ratio has no effect on r_1 values. For all frequencies r_1 is unchanged with CoFeO:FeO ratio.

The r_2 values for NPCs assembled with different CoFeO:FeO ratio are also reported in Figure 3-23 (right). At both frequencies the transverse relaxivity decreases with increasing the CoFeO:FeO ratio, for a given NPC size. Assuming similar packing density, this probably arise from the reduced saturation magnetization of CoFeO. Indeed the bulk saturation magnetizations of the bulk materials are 520 and 590 kA/m for CoFeO and FeO, respectively [95]. Hence it is difficult to comment on the cluster density using the

NMRD data alone. Interestingly, there is little change in the r_1 values measured, Figure 3-23, which suggests similar H₂O-NPC surface interactions in both cases.

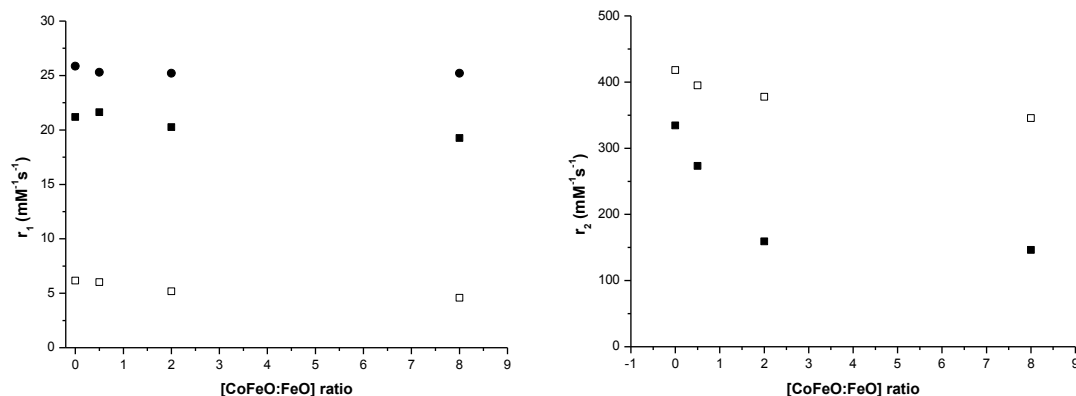


Figure 3- 23 (Left, a) r_1 values of CoFeO-FeO clusters plotted against the CoFeO:FeO ratios. The measurements have been done at two different frequencies: (●) 10 MHz, (■) 16.3 MHz, and (□) 61 MHz. (Right, b) r_2 values of CoFeO-FeO clusters plotted against the CoFeO:FeO ratios. The measurements have been done at two different frequencies: (■) 16.3 MHz and (□) 61 MHz. The relaxivity was normalized by the concentration of iron. The CoFeO:FeO ratio used for the preparation of hybrid NPCs were of 0 ($d_{\text{hyd}} = 113$ nm, PDI = 0.09, [Fe] = 0.833 mM), 0.5 ($d_{\text{hyd}} = 117$ nm, PDI = 0.15, [Fe] = 0.832 mM), 2 ($d_{\text{hyd}} = 113$ nm, PDI = 0.18, [Fe] = 0.770 mM), (○) 8 ($d_{\text{hyd}} = 102$ nm, PDI = 0.11, [Fe] = 0.826 mM).

3.4 Conclusions

Monodisperse hybrid clusters of controlled size have been successfully synthesized by the Water Interfacial Competitive Stabilizer Desorption method. This allows the selection of the magnetic properties of the resulting nanoparticle clusters. The effects of primary nanoparticle concentration and of oleic acid on the assembly rate were studied, which provided information on the kinetics of nanoparticle assembly. Electron microscopy, DLS and the NMRD technique demonstrate that there is an efficient clustering between FeO and CoFeO nanoparticles giving stable hybrid clusters with novel magnetic properties. The method is highly reproducible and can be scaled up, and so may open up new pathway to size-controlled nanocomposite materials of a wide range of composition and size.

After developing successful scale-up procedures for the production of NPCs in organic medium, the following step is to develop a phase transfer method of stabilized NPCs in water for potential biological applications. In Chapter 4 further development and optimization of the CSD process will be described. In Chapter 5 and 6 two phase transfer

methods that employ polymers/surfactants and lipids, respectively, will be described. These approaches are designed to prepare stable NPC suspensions with similar d_{hyd} to that prepared by WI-CSD in chloroform, so taking advantage of the CSD process.

Chapter 4

Competitive stabilizer desorption method development

4.1 Introduction

The control over the NPC size and their size distribution is one of the most important issues in the synthesis of clusters that have attracted considerable scientific and commercial interest.

In Chapter 3 monodisperse NPC were successfully produced by WI-CSD method and scale-up experiments were undertaken with a scaling factor of 125 (i.e. up to 150 mL). Having identified the key parameters that must be tightly controlled to enable successful CSD, in this chapter we report on the extension of the WI-CSD method as a simple and continuous synthesis of size controlled and highly monodisperse iron oxide NPCs using a flow setup. To the best of our knowledge no results have been published yet dealing with continuous synthesis of nanoparticle clusters using a flow approach. This system provides a good control over the NP assembly by taking care over reaction parameters including NP suspension concentration, OA concentration, tubing length and flow rate and clear advantages are obtained over the traditional “static” (bulk) method in terms of improved NP size distribution, reaction yields and time of reaction. It will be shown that CSD experiments where cyanopropyl-modified silica was used as the competitive substrate for the destabilizing ligands (oleic acid) will be used for the clustering of primary iron oxide NPs. The relative kinetics and the parameters involved in the assembly process in suspension are discussed.

The key experimental parameters and their influence on the resulting NPC suspensions were screened and will be reported and discussed in the following sections. The versatility of the CSD method will also be demonstrated by changing different parameters such as NP core size, mixture of NPs of different core size and type in order to obtain hybrid NPCs and finally changing competitive substrate. Larger monodisperse iron oxide NPs ($d_{\text{hyd}} > 8$ nm) were synthesized by varying the mole ratio of precursor to solvent in the modified Pinna et al. protocol ^[96] used in Chapter 3. The result of the stability and clustering of the resulting NP suspensions in chloroform will be investigated by DLS and FESEM.

Finally magnetic field induced-assembly of nanoparticles has been a subject of particular interest due to control over the NP directionality through dipolar interactions. This selectivity over the directionality has been exploited to assemble NPs (100 nm to 30 μm)

into one-dimensional structures^[97]. The use of magnetic dipolar interactions to organize primary NPs (< 100 nm) remains largely unexplored. The direct monitoring of the size distribution of organized nanostructures in suspensions is a central challenge for fundamental understanding of the assembly kinetics under application of a magnetic field. Therefore, the control and complete analysis of the average particle size and distribution is essential to study and control these processes. Herein, we report for the first time the direct monitoring of the assembly in batch of dispersed iron oxide NPCs using the previously described liquid-liquid interfacial assembly method (WI-CSD) under an applied magnetic field.

4.2 Materials and methods

4.2.1 Materials

Iron (III) acetylacetonate, Fe(III)(acac)₃ (purity ≥99.9%), benzyl alcohol, BA (≥99.0%), CHCl₃ (≥99.0%) and oleic acid, OA (≥99.0%, Sigma Aldrich) were purchased from Sigma Aldrich Ltd Ireland. Cyanopropyl modified silica particles (30-70 μm) were purchased from Alltech Associates.

4.2.2 Synthesis and stabilization of 8 nm iron oxide nanoparticles

Iron oxide NPs of core size of 8.2 nm were synthesized and functionalized with OA using the modified Pinna protocol^[96] described in Chapter 3. The synthesis was carried out under reflux conditions on a heating mantle. We will refer to these NPs as 8-NPs and to the clusters produced from these NPs as 8-NPCs.

4.2.3 SI-CSD

In a typical experiment of NP clustering by SI-CSD, oleic acid coated 8-NPs in chloroform were exposed to 52 mg of cyanopropyl-modified silica layer that allowed a continuous controlled growth of metal oxide clusters (8-NPCs) through the depletion of oleic acid from the nanoparticle surface. After the addition of 2 or 3 drops of methanol on the silica particles at the bottom of the glass cuvette, a volume of 1.2 mL of the NP suspension was added over the layer very carefully without disturbing the silica placed at the bottom. The growing of the clusters were then monitored by the DLS.

4.2.4 Synthesis and stabilization of 12.3 nm iron oxide nanoparticles

Larger NPs (core-shell NPs) were synthesized using a similar protocol similar to the one of Pinna using a microwave reactor. Briefly, 1 g of Fe(III)(acac)₃ and 20 mL of BA were mixed in a glass vial which was sealed and inserted in a microwave reactor (Anton Paar, Austria). The red solution was heated to 205 °C for 3.5 hours. The resulting black suspension was then cooled down and washed with 10 mL of fresh BA and re-dispersed using the same volume of BA. 1 g of precursor and 10 mL of BA were added to the dark solution and heated in the microwave for 3.5 hours at 205 °C. After cooling, typically 1.5 ml of the resulting NP suspension was washed twice with acetone and stabilized with a volume of OA (20-100 µL, 10 mg/mL). The stock suspension was centrifuged for 10 min at 13200 rpm before any analysis in order to get rid of eventual aggregates. We will refer to these NPs as 12-NPs and to the clusters produced from these NPs as 12-NPCs.

4.2.5 Flow assembly

In a typical flow assembly experiment, a volume (52 - 87 µL) of the stock of oleic stabilized 8-NP suspension was diluted with chloroform so that the final Fe concentration was in the range 1-2 mM. The resulting mixture was placed into 1.5 mL Eppendorf™ tubes and centrifuged for 10 minutes at 13200 rpm for removing any aggregates present. The supernatant was placed in syringe glasses (Sigma Aldrich) of 3-10 mL and pumped with distilled water through a syringe pump at different flow rates (0.4 – 1.5 mL/min). The exposure of the resulting NP suspension slugs to the interface leads to the clustering of the NP within the tubing. The final NPC size was analyzed by DLS using a Malvern™ Nano ZS.

4.2.6 Characterization

NP and NPC suspensions were characterized by DLS, NMRD and FESEM as described in Chapter 2. The total iron content was determined by AES-ICP using the procedure described in Chapter 2.

4.3 Results and discussion

4.3.1 SI-CSD method

4.3.1.1 Iron oxide NP clustering by SI-CSD

In this section chloroform suspensions of OA stabilized iron oxide NPs prepared by thermal decomposition method were exposed to cyanopropyl modified silica particles resulting in the *in situ* assembly of the NPs due to the continuous depletion of the OA from the NP surface. The assembly was monitored by DLS and reproducibility studies were undertaken. An insight into the kinetics of the process will be also presented.

DLS data of a typical assembly experiment performed by SI-CSD method is shown in Figure 4-1. The hydrodynamic diameter, PDI and the count rate are reported and plotted as a function of time. In this experiment oleic acid stabilized FeO NPs of d_{hyd} of 15 nm were used for the formation of NPCs in the size range of 20-120 nm. The NPC size distributions are unimodal throughout the whole assembly process (PDI < 0.25) and a shift of mean size distribution by intensity towards larger hydrodynamic diameters overtime is observed (Figure 4-2). The gradual increase of the intensity of the backscattered light confirms the formation of larger monodisperse NPCs in the suspension that are formed through the slow addition of primary NPs over time. The preservation of a unimodal size distribution suggests that the assembly process is controlled as a drastic increase of the PDI value is not observed [98]. As noted previously our interpretation is that the NP clustering is driven by ligand depletion and migration from the NP surface towards the silica substrate, which is activated by the methanol. More details about the role of the MeOH will be reported in the following section.

A further experiment was performed using the same experimental conditions in order to ensure the reproducibility of the method. The hydrodynamic diameters and the respective PDI values are shown in Figure 4-1. The same d_{hyd} trend (< 5% difference) was found as observed in the first experiment and also in this case the size distribution is unimodal up to 23 hours.

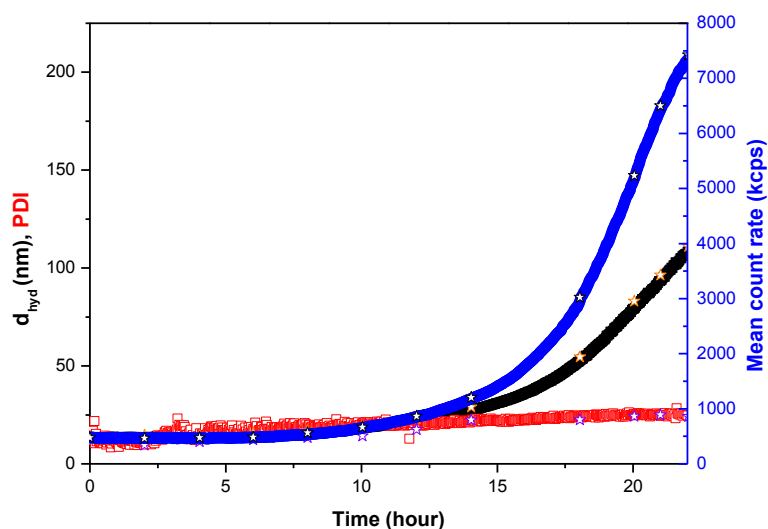


Figure 4- 1 DLS data for OA-FeO NP assembly by SI-CSD where 50 μ L of MeOH were added over silica. (■) hydrodynamic diameter (□) PDI*100 (left-hand axes), (■) count rate (right-hand axes). Reproducibility experiment at the same experimental conditions is reported. (☆) hydrodynamic diameter (☆) PDI (left-hand axes), (☆) count rate (right-hand axes).

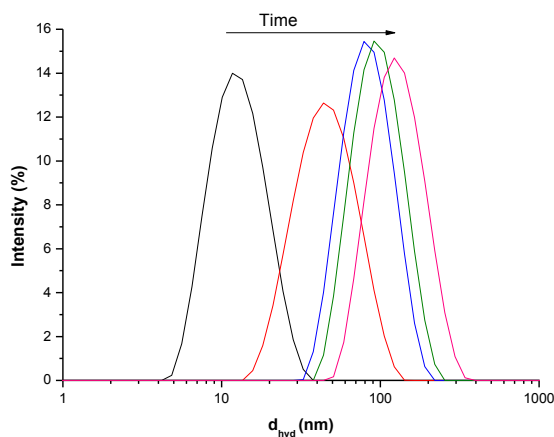


Figure 4- 2 Size distribution by intensity of clustering of FeO NPs in chloroform over CN-modified silica as a function of time.

On the basis of the results here reported and on the previous work of our group, the mechanism behind the CSD that uses silica as substrate can be described by three stages (Figure 4-3). In absence of substrate, the unbound and NP bound OA are in equilibrium. Following the exposure to silica, a gradual irreversible adsorption of the unbound OA onto silica occurs while the d_{hyd} of the suspension is unchanged for a period of time (stage I) ^[88] here called as induction time. At stage II an ongoing NP clustering occurs and the assembly rate increases gradually by addition of singular activated NPs from the organic

suspension. During stage III all the primary NPs of the suspension are assembled and further depletion of OA occurs from NPC surfaces resulting into collision among preformed clusters. At high d_{hyd} (> 200 nm) some of the larger clusters precipitate onto the silica layer resulting into the dilution of the suspension that continue over time. At this point the control over the NP clustering decreases and polydisperse agglomerates ($\text{PDI} > 0.3$) are formed. The preservation of the monodispersity of the suspension during the assembly process is related to the increased activity of the smaller NPCs in the growing size distribution, which have higher surface energy.

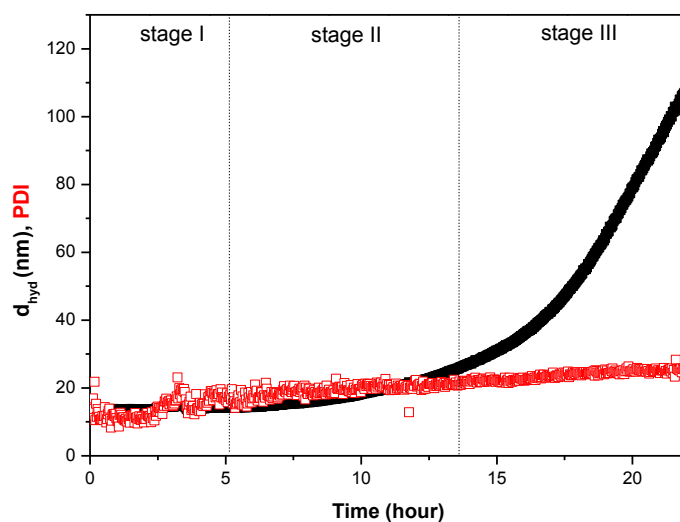


Figure 4- 1 Stages of a typical assembly experiment. DLS data of a typical NP assembly experiment monitored overtime at 1.2 mL scale in CHCl_3 . Evolution of (■) d_{hyd} following exposure to the silica substrate at $t = 0$, and (□) $\text{PDI} \times 100$ values are reported.

Microscopy analysis confirmed the formation of FeO NPCs by NP clustering through SI-CSD method. The dark-field FESEM image of a representative sample of FeO NPCs is shown in Figure 4-4. The NPCs have spherical-like shape and seem to be monodisperse since no evidence of agglomerates or of primary NPs was observed. The size of 364 NPCs was measured and the resulting was fitted to a lognormal distribution giving as a result a core NPC size of 63 ± 18 nm. The d_{STEM} obtained was in agreement with the result given by DLS analysis ($d_{\text{hyd}} = 70$ nm).

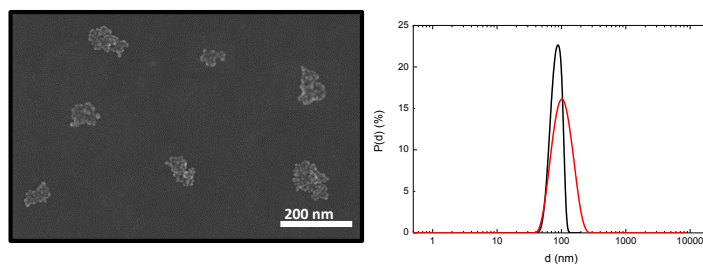


Figure 4- 2 (Left) Dark-field FESEM image of NPCs of d_{hyd} of 70 nm (PDI = 0.18). Scale bar of 200 nm. (Right) (-) d_{hyd} , (-) log-normal analysis yielding $d_{\text{STEM}} 63 \pm 18$ nm (364 clusters counted).

4.3.1.2 Effect of methanol in the clustering process

In order to investigate on the role of the methanol, clustering experiments were performed in absence and in presence of methanol, which was added at 0, 1 and 5 hours. An experiment in presence of methanol without silica is also reported for comparison. The hydrodynamic diameters plotted as function of time are reported in Figure 4-5.

In the first experiment methanol was added at the really beginning of the NP clustering ($t = 0$) and an increase of the hydrodynamic diameter started after ~ 5 hours of exposure to silica. A gradual increase of the size was observed up to 22 hours and a NPC size 115 nm was measured. By adding the MeOH at $t = 1$ hour, also in this case an induction time of 5 hours was observed but the assembly rate was slower. For instance the NPC hydrodynamic diameter after 22 hours was only 52 nm. The addition of MeOH at $t = 5$ hours decreased furthermore the assembly rate and the induction time increased to 15 hours.

In the absence of methanol, the NP d_{hyd} is unchanged (~ 14 nm) overtime even when in contact with the silica. Similar result is observed after addition of methanol in absence of the substrate. These experiments demonstrated that OA stabilized iron oxide NP were stable at a Fe mM range, and that both silica are required for their destabilization for the formation of colloidal monodisperse NPCs. Our interpretation is that MeOH activates polar adsorption sites on the surface promoting interaction of the less polar OA molecules, and ultimately desorption of bound OA from the NP surface, generating surface activated particles. We have recently published these demonstration that methanol is crucial in the assembly of NP suspensions exposed to CN-silica layer ^[98].

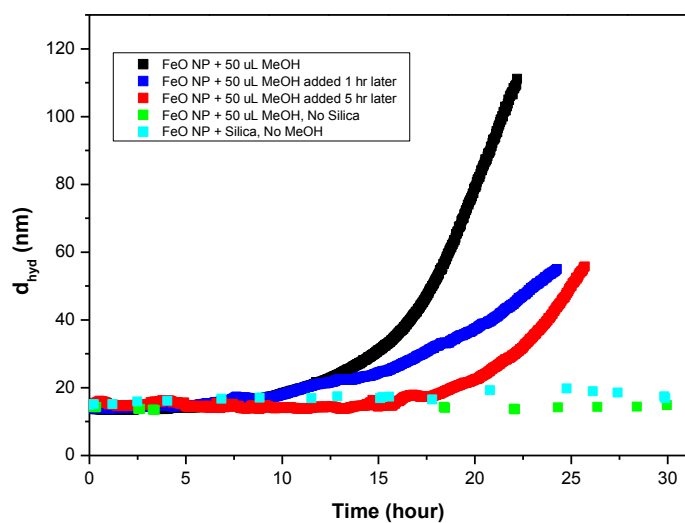


Figure 4- 3 DLS data for NPC assembly by SI-CSD at different experimental conditions; 50 μ L MeOH added at (■) $t=0$, (■) $t=1$ h; (■) $t=5$ h over silica. (■) Assembly performed in presence of 50 μ L of MeOH in absence of silica. (■) Assembly performed in presence of silica, in absence of MeOH.

4.3.1.3 NP assembly blocking in SI-CSD

In order to stop the NP clustering by SI-CSD, for instance when an optimal size had been achieved, two approaches were attempted. The first approach is based on the addition of a small excess of oleic acid (typically 5-10 μ L, 10 mg/mL) in the suspension during the clustering process. In the second approach, the NP assembly was blocked by the removal of the NPC suspension from the cuvette containing CN-silica. The concentration of Fe in the suspensions is 2.2 mM in both experiments. The hydrodynamic diameter, the PDI and the count rate were monitored overtime and are shown in Figure 4-6. The suspension was stable up to 5 weeks, without any significant change in d_{hyd} and count rate.

Following the addition of an excess of oleic acid in the NP suspension, the d_{hyd} value increased from 109 to 117 nm and then remained almost unchanged for more than 2 hours, while the count rate decreases significantly. The PDI increases from 0.17 to 0.32 and then drops rapidly to 0.18. This result suggests that the assembly in the suspension stopped completely because of full coverage of the silica layer preventing further OA desorption.

In the second approach the cuvette was removed carefully without perturbing the silica layer and placed in a 25 $^{\circ}$ C bath to main it at a constant temperature. The hydrodynamic size of the NPC in suspension was measured after a long time (37 hours) in order to make

the instrument available for other users. The d_{hyd} found was 119 nm which confirm the ending of the assembly process.

The removal of the NPC suspension from exposure to silica caused immediately a slight decrease of the count rate from 5329 to 5100 kcps while the d_{hyd} (~ 80 nm) while the PDI remained unchanged (0.16-0.18) over the course of 3 hours. The suspension like the previous case was removed from DLS machine and placed in a 25 °C bath for 11 hours. At $t = 35$ hours, the suspension was still stable and no change of the NPC hydrodynamic size was observed ($d_{hyd} = 81$ nm). Both count rate and PDI decreased slightly from 5082 to 5012 kcps and from 0.163 to 0.151 respectively.

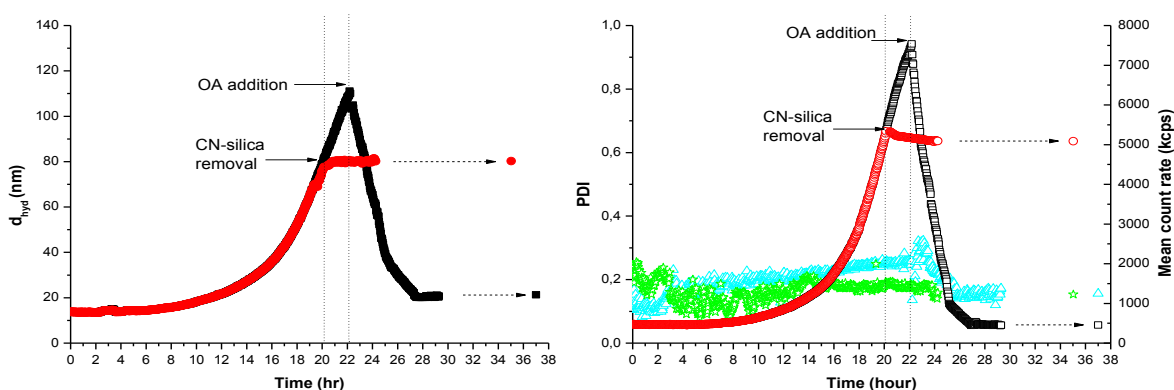


Figure 4- 4 The effect of the (i) oleic acid addition and (ii) silica removal on the NP clustering by Si-CSD method.(Left) Monitoring of the hydrodynamic diameters; (i) (■), (ii) (●). (Right) Monitoring of PDI and mean count rate over time. (Left-hand axes) PDI: (i) (Δ), (ii) (☆). (Right-hand axes) Count rate: (i) (□), (ii) (○).

The first approach confirms that when assembling NP in presence of an excess of ligand (OA) the assembly can be reversible, i.e. the NPCs can be “disaggregated”. The second approach demonstrates that it is possible to block the assembly process by the removal of the silica substrate. This is really advantageous because it permits the blockage of the assembly at any time and hence at any NPC size, which is key for biological application.

4.3.1.4 Comparison of NPC suspensions prepared with SI-CSD and WI-CSD method

The CSD method has been shown to be a controllable, reproducible and scalable using either water or silica as substrate for triggering the NP assembly. At this point we wanted to investigate whether the choice of substrate affected the kinetics of assembly or the magnetic properties of the resulting NPC suspensions.

A suspension of 14 nm of oleic acid stabilized-FeO NPs (1.98 mM, [Fe]) prepared by thermal decomposition (Chapter 3, Section 3.2.3) were assembled using SI- and WI-CSD approach. The assembly curves are shown in Figure 4-7. The early stage data were successfully fitted to a single-exponential using the previously described procedure (Chapter 3). The extracted assembly rates (τ_{exp}^{-1}) are reported in Table 4-1.

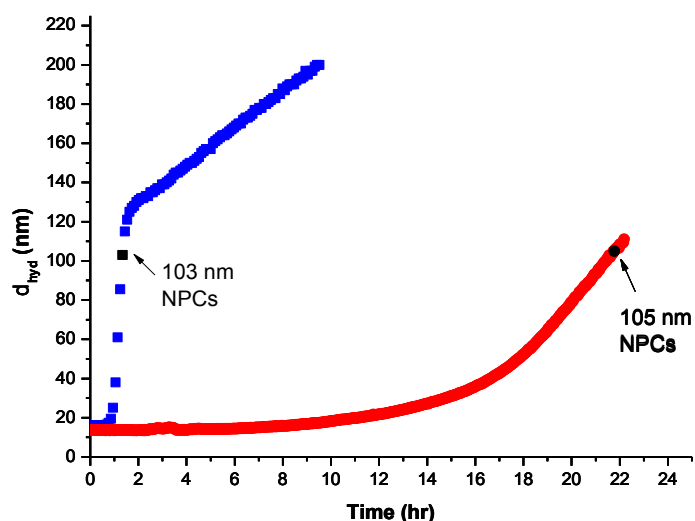


Figure 4- 5 Kinetics of particle assembly using (●) SI- and (■) WI-CSD approach for NP suspensions phase transferred with 0.75 surface equivalents of oleic acid with Fe concentration of 1.98 mM. The hydrodynamic size of NPCs used for NMRD analysis are reported in black.

In a repeat experiment the assembly process was stopped at ~100 nm by removing the interface and 500 μL of suspension were collected for further analysis by DLS and NMRD. The resulting NPC suspensions were stable and monodisperse ($\text{PDI} < 0.1$); their hydrodynamic diameter and PDI values are reported in Table 4-1.

Method	d_{NPs} (nm) [PDI]	y_0 (nm)	A	Induction time, t_0 (hr)	Assembly rate, τ_{exp}^{-1} (nm/hr)	d_{NPCs} (nm) [PDI]
SI-CSD	13 [0.07]	12	0.61	5.82	4.31	105 [0.10]
WI-CSD	15 [0.11]	17	0.31	0.76	6.05	103 [0.09]

Table 4- 1 Hydrodynamic diameter and PDI for clusters made by SI- and WI-CSD approach using iron oxide NPs (0.75 excess OA) of hydrodynamic diameter d_{NPs} . Assembly curves were fitted to an exponential growth, $y = y_0 + A \cdot \exp[-(t-t_0)/\tau_{\text{exp}}^{-1}]$.

Examining the assembly rates reported in Table 4-1, it can be seen that the change of the assembly approach used for the formation of NPCs has an effect on both the assembly rate and the induction time at a fix iron and ligand (OA) concentration. For instance, using SI-CSD approach the induction time is about 7.6 times longer than the one observed for WI-CSD experiment, while the assembly rate is ~ 0.7 times slower. Assuming there is no direct NP or NPC contact with the substrate, this is due to the time dependent (irreversible) rate of OA adsorption onto the competitor. This will be dependent on the kinetics of transport, the thermodynamic of adsorption (to a less extent) and the substrate capacity, which is clearly different (and difficult to compare) in these two experiments.

The NMRD profiles recorded at 25 °C for NPC suspensions assembled using SI- and WI-CSD approach are reported in Figure 4-8. The hydrodynamic diameter and PDI values of the NPC suspensions are reported in Table 4-2.

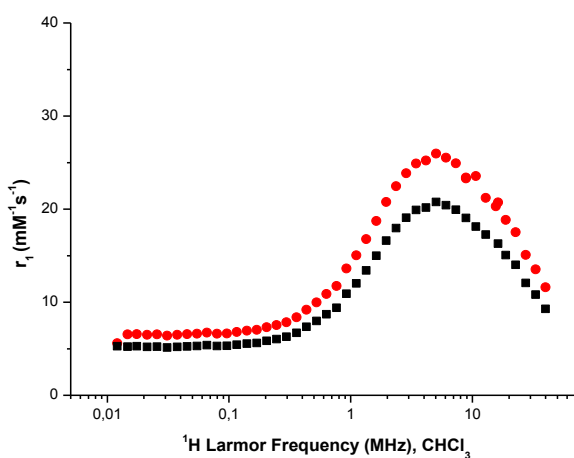


Figure 4- 6 NMRD profiles of NPC suspensions prepared with (●) SI-CSD and with (■) WI-CSD method.

Approach	d_{hyd} (nm) [PDI]	r₁ (mM⁻¹s⁻¹) @ 16.3 MHz	r₂ (mM⁻¹s⁻¹) @ 16.3 MHz
SI-CSD	105 [0.10]	20.0	195.7
WI-CSD	103 [0.09]	16.3	178.6

Table 4- 2 NMRD data of suspensions of nanoparticle clusters in chloroform prepared by WI- and SI-CSD approach. The measurements were performed at 25 °C and 16.3 MHz.

Following the NMRD measurements each sample was analyzed by DLS and in all cases no significant change in hydrodynamic size occurred demonstrating that the NPCs were stable to the applied magnetic field during the measurement. The relaxivity curves show a r_1 maximum at high fields suggesting that the clusters exhibit superparamagnetic behavior. The mid frequency minimum is suppressed following the clustering of the NPs as expected ^[59]. Indeed this result can be explained by the increase of the magneto-anisotropy which is related to the strength of the dipolar interparticle interactions following the assembly of NPs. For both NPCs produced by SI- and WI-CSD approach, with increasing of NPC size a decrease of r_1 at all frequencies is observed. This might be related to the larger number of NP within the cluster that cannot contribute to the relaxivity because of the inaccessibility of the water molecules ^[98].

Interestingly, the two samples have slightly different r_1 response with NPCs produced by more rapid assembly (WI-CSD approach in this case) showing lower relaxivity at all fields, again assuming that NP/NPC are not in contact with the substrate. If we examine the relaxivity response of the clusters at 16.3 MHz (Table 4-2), for NPCs prepared by SI-CSD (faster) the r_1 value increases by ~20% and the r_2 increases by ~11% by as compared with NPCs of similar size produced using WI-CSD (slower). Note that the PDI values are low and critically are similar for the two suspensions, so the relaxivity values can be meaningfully compared. It has been shown previously in our group ^[85] that the assembly rate can have an effect on the relaxivity; minor reductions in r_1 with increasing assembly rate (controlled through the OA content) were reported of ~11-15 %. That hint was part

of the motivation for the current investigation, which showed a much stronger and opposite effect.

The new results are difficult to explain. One could speculate that slower assembly rates might produce more densely packed NPCs and stronger interparticle interactions are generated. Hence the spin-spin relaxivity would be predicted to be higher (larger global moment). This is observed; the r_2 value is $\sim 11\%$ higher in case of NPCs produced by the SI-CSD approach (Table 4-2). However, the expectation would then be that there would be a greater number of inner NPs which would not contribute to r_1 , but this parameter is also observed to be higher. This observation suggests that the residence times of solvent in the vicinity of surface in the two cluster types may be different, altering r_1 . However, as both processes can be stopped by removing the substrate at any stage, the implication is that the surface concentrations of OA are very similar.

The limitation of these findings, as far as optimizing the magnetic resonance properties is concerned, is that were the rate to be further accelerated, *e.g.* by reducing the NP or OA concentration, then control over PDI would be lost. Nevertheless, the result demonstrates an interesting possibility for controlling the magnetic properties of the NPCs. Ideally the WI-CSD would be repeated for three concentrations (assembly rates) to confirm the observations. However the NMRD instrument is currently out of order.

4.3.2 Effect of primary NP size on assembly by WI-CSD

To further investigate over the effect of primary particle size over the assembly process using the WI-CSD approach, clustering experiments of larger NPs (> 8 nm) were undertaken varying the amount of OA through addition to the initial NP dispersion.

The FESEM image of a typical suspension of magnetic oleic acid stabilized iron oxide 12-NPs prepared by thermal decomposition is shown in Figure 4-9. The image show spherical NPs with really narrow size distribution of 12.3 nm ($\sigma = 15\%$) while the hydrodynamic diameter obtained from DLS of the same suspension was 20 nm (PDI < 0.1).

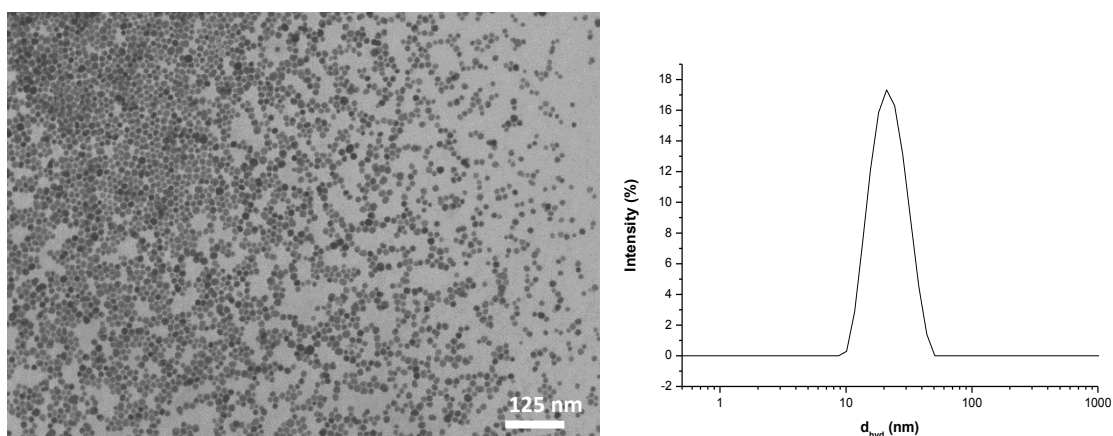


Figure 4- 7 (Left) FESEM image of iron oxide nanoparticles of $d_{STEM} = 12.3$ nm (2300 NPs counted). (Right) size distribution by intensity of FeO NPs of $d_{hyd} = 20$ nm, PDI = 0.09. Scale bar: 125 nm.

The hydrodynamic diameter, PDI values and count rate for the two repetitions of 12-NP assembly experiments performed using the same iron and OA concentration are reported in Figure 4-10. An increase of the hydrodynamic diameter and count rate was observed while the PDI decreased straight after the start of the assembly from 0.23 to 0.11 and remained almost unchanged throughout the clustering process. This confirms that it is possible to assemble NPs with hydrodynamic diameter higher than 8 nm in a controlled fashion achieving NPCs with really narrow size distribution. In this case unusually the d_{hyd} value reached a plateau of about 140 nm after only 2 hours because the assembly rate was very rapid. This is expected and can be explained with the fact that the magnetic force between the nanoparticles is really high and it is a function of both the volume and the saturation magnetization (M_s)^[99] of the particle. Hence, we observe faster clustering for these particles, confirming that the magnetic contribution to the interaction energy is high.

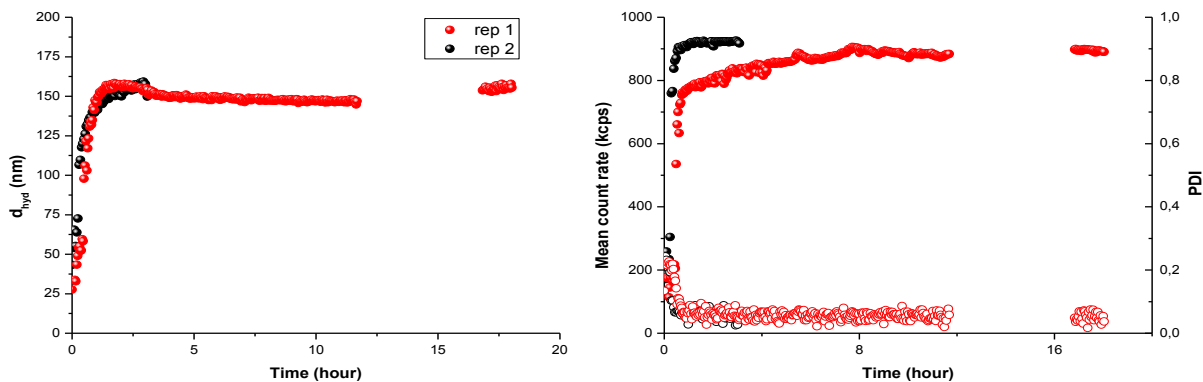


Figure 4- 8 DLS data of two repetitions of 20 nm FeO NPs (0.5 mM Fe, 0.75 equivalents of OA) clustering experiments by WI-CSD method. (Left) hydrodynamic diameter and (right) (filled circles) count rate and (open circles) PDI as function of time.

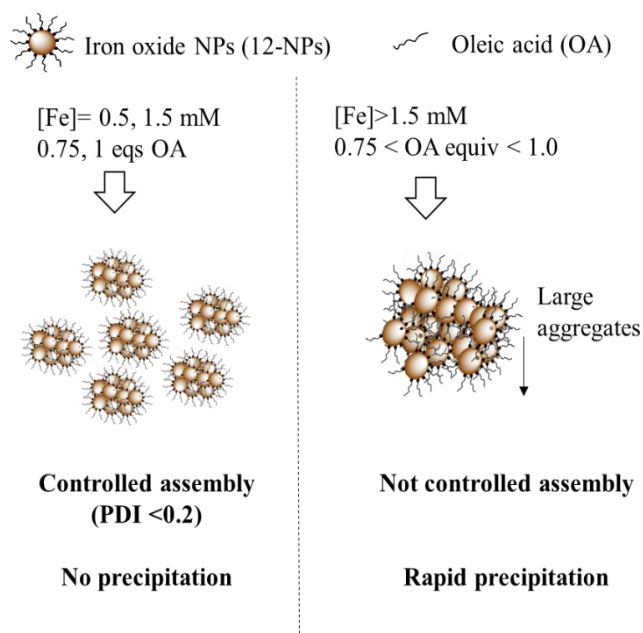


Figure 4- 9 The effect of the iron and OA content on the assembly using 12-NPs.

Good control over the assembly was obtained using suspensions of iron content of 0.5-1.5 mM and NPs stabilized with 0.75-1 equivalents of OA as shown in Figure 4-11. On increasing or decreasing these Fe and OA contents, a rapid increase of the PDI and size was observed that resulted in rapid precipitation of the material following the addition of the water layer onto the suspension.

Assembly curves for clusters from 12 nm primary iron oxide NPs in chloroform loaded with different amount of OA are shown in Figure 4-12, the quality of the data is not as good as in the case of 8-NPs. Nevertheless it was possible to extract rates as before. The

parameters extracted from the analysis of the curves are reported in Table 4-3. In most cases the PDI value was below 0.2, with the exception of the experiment where 60 μg of OA were added. A significant increase in the assembly rate was observed on decreasing in the amount of OA added from 118 to 2 nm/hr while really slow assembly was observed after addition of 100 μg of OA for up to 14 hours. The induction time increases as the amount of OA added to the NP suspension increases; this is due to the fact that at higher amounts of OA must bind to the liquid-liquid interface before the beginning of the ligand depletion from the NP surface. These results are consistent with the findings reported in Chapter 3.

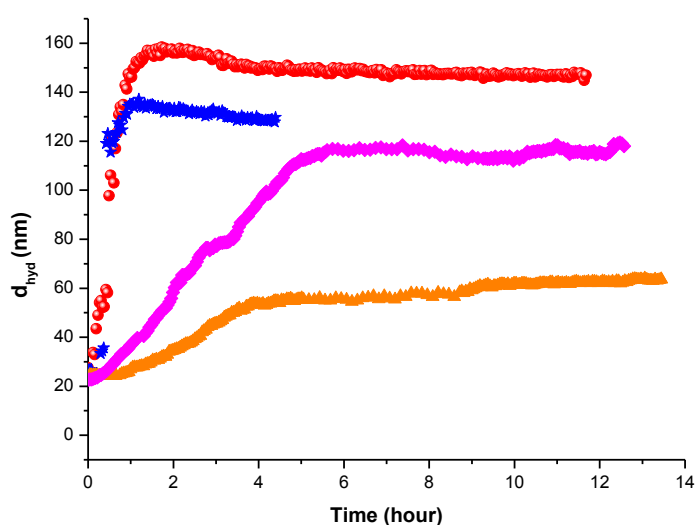


Figure 4- 12 Clustering curves of 12-NPs dispersed in chloroform (1.2 mL, 0.6 mM Fe, 0.75 equivalents of OA) with (●) 0, (★) 20, (◆) 60 and (▲) 100 μg of oleic acid added to the suspension prior the assembly experiments.

Oleic acid added (μg)	y_0 (nm)	A	Induction time, t_0 (hr)	Assembly rate, τ_{exp}^{-1} (nm/hr)
0	25.0	0.34	0.02	118.2
20	24.3	0.95	0.11	108.3
60	24.1	1.36	0.35	14.6
100	23.6	2.28	0.92	2.22

Table 4- 3 Parameters extracted from the exponential fitting of assembly experiments performed adding different amounts of oleic acid.

These experiments show that also for 12 nm NPs it is possible to control the assembly process from very fast (118 nm/hr) to very slow rates (2 nm/hr) by the amount of OA in the initial 12-NP suspension. An attempt was made by varying the concentration of NP in suspension but in this case the suspension immediately crashed out at iron concentrations higher than 1.5 mM with rapid increases of the PDI (> 0.3) observed, following the addition of the water layer onto the suspension.

These findings are quite exciting because it confirms that WI-CSD method can be applicable to different NP types and sizes and hence is suitable for the synthesis of different kind of monodispersed and size controlled-NPCs that could be used for multiple applications.

4.3.3 Flow assembly

4.3.3.1 Device development

In principle the WI-CSD process can be turned into a flow process by preparing individual slugs of NPs in CHCl_3 , separated by slugs of water, which can be set to flow along a tube, during which time they assemble, as in the batch experiment. Figure 4-13 illustrates the operation of a device used for the synthesis of 8-NPCs by flow assembly.

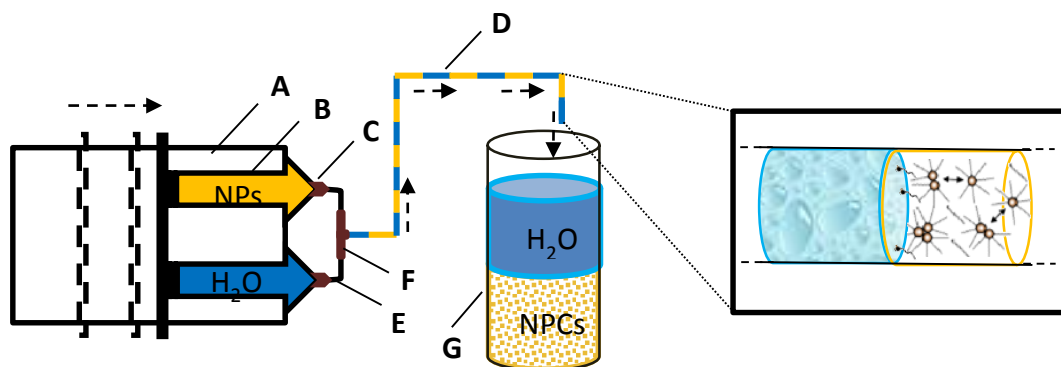


Figure 4- 13 Schematic representation of the flow assembly device. (A) Syringe pump, (B) 3-10 mL glass syringe (FORTUNA® Optima, Sigma Aldrich), (C) PTFE connector, (D) thick PTFE tube (1/8"x0.062", ID x OD), (E) thin PTFE tube (1/12"x0.062"), (F) PEEK tee. (Inset) Schematic representation of WI-CSD mechanism in the flow system.

A syringe pump injects water and oleic acid stabilized NPs along thin rigid polytetrafluoroethylene (PTFE) tubes (1/16" i.d, Kinesis Ltd, E) to a Teflon T-piece (i.d. 1/8", Kinesis Ltd, F). At this point homogeneous, monodisperse alternating slugs of water

and organic NP suspension are formed and pushed towards the end of a second PTFE tube of inner diameter of 1/8" mm (Kinesis Ltd, D). The slugs are collected in a glass vessel (G) and the relative interfacial area rapidly decreases (retarding assembly) assuming bubbles can be avoided. The NPCs were separated from the water by a needle connected to a glass syringe and placed in a glass cuvette for DLS analysis.

In initial experiments deposition of 8-NPs within the tubing was observed that lead to plugging of the tubing system. To overcome this problem two strategies were used. Firstly, three washes with chloroform and final drying with N₂ were performed at the end of each flow assembly experiment. Secondly, the flow system was used only for the production of small volumes of iron oxide NPC dispersions, i.e. less than 5 mL, and not for continuous long-time syntheses. This problem can be resolved by washing the tube, however material build up will gradually return. It is apparent that an improved inert tubing material is needed for a final process.

4.3.3.2 Reproducibility of nanoparticle assembly

To compare the size distribution of 8-NPCs obtained using different batches of oleic acid stabilized FeO NPs, three flow assembly experiments were performed at a flow rate of 1.5 mL/hr and a PTFE tube length of 40 cm. The hydrodynamic diameter and PDI values are reported in Table 4-4. In all cases NPCs with unimodal size distribution were achieved (PDI ≤ 0.11) and the hydrodynamic sizes are unchanged suggesting reproducibility of the method (Figure 4-14).

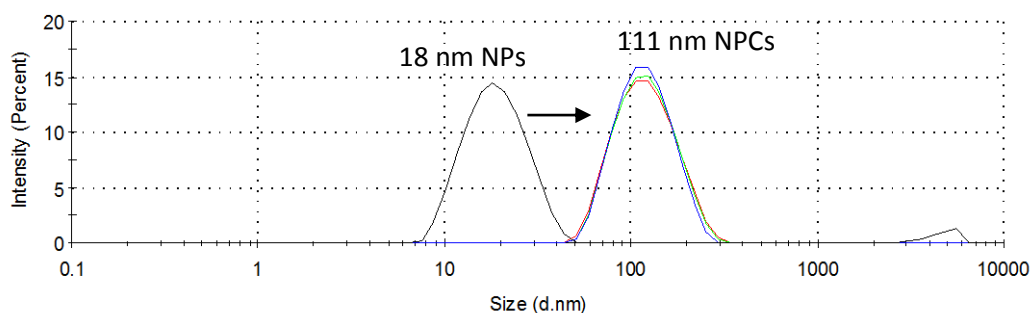


Figure 4- 14 Size distribution by intensity of FeO NPs and NPCs produced by flow assembly.

By measuring the slug length it was possible to calculate the respective slug volumes and surface areas that are shown in Table 4-4. Keeping constant the flow rate, the slugs were found to have the same length. As a result each slug of the 8-NPs suspension is exposed to a water interface of fixed and constant area for the same period of time, hence the rate of assembly is constant for each slug. Hence, there is a constant exposure factor, EF, relating the changes in NPC d_{hyd} (Δd), the time of exposure of the NP suspension slugs to the interface and the surface area/volume ratio of the slugs, which gives rise to temporal stability of the process.

exp	$d_{\text{hyd NPC}}$ (nm) [PDI]	Time, T (s)	$\Delta d_{\text{hyd NPC}}$ (nm)	Slug surface area, SA (cm^2)	Slug volume, V (cm^3)	EF = $\Delta d/t^*(V/SA)$ ($\text{nm s}^{-1} \text{cm}$)
1	110 [0.09]	20	92	0.63	0.0285	0.21
2	112 [0.11]	20	94	0.63	0.0285	0.21
3	110 [0.11]	20	92	0.63	0.0285	0.21

Table 4- 4 Reproducibility study. Primary OA FeO NPs: 18 nm, PDI = 0.200. Flow rate: 1.5 mL/min, Tube length: 40cm.

To ensure the reproducibility of the method, FeO 8-NPCs obtained starting from oleic acid stabilized FeO 8-NPs of the same batch were collected one after the other with the tubing emptied, and chloroform washed between runs during the same flow assembly experiment. The experiment was performed using a flow rate of 0.4 mL/hr and a PTFE tube length of 20 cm. The hydrodynamic diameter and PDI value of the NPC dispersion collected are reported in Table 4-5. In all cases NPCs with unimodal size distribution were achieved ($\text{PDI} \leq 0.17$) and the hydrodynamic sizes are almost unchanged confirming the reproducibility of the method (Figure 4-15). If compared to the previous experiment, the NPC formed show higher hydrodynamic sizes (~146 nm) because of the different flow rate applied (Table 4-5). For instance in this case a lower flow rate was used (0.4 ml/hr) giving a higher time of exposure of the NP suspension to the slugs of water during the assembly process.

The volume the surface area of the slugs were calculated and are shown in Table 4-5. The ratio between the difference in hydrodynamic diameter, time of exposure of the NP suspension to water and the surface area/volume ratio showed similar results to those obtained in the first reproducibility study (Table 4-4). The exposure factor (quantified as the change in sizes, per unit time exposed to the interface, per unit surface area of interface to volume, $\text{nm s}^{-1} \text{cm}$) is similar to that obtained for the reproducibility study, Table 4-4.

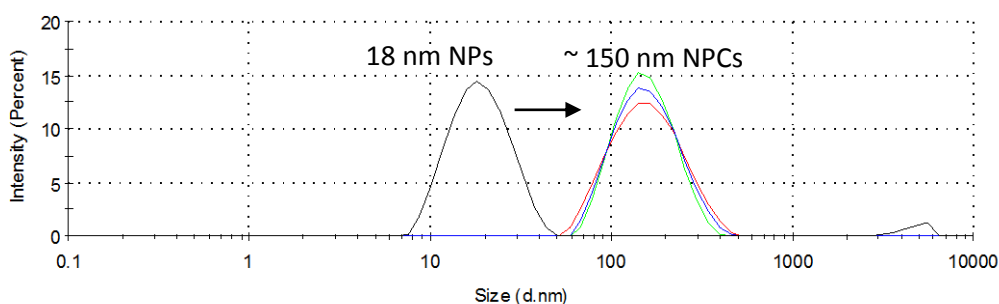


Figure 4- 15 Size distribution by intensity of different FeO NPC suspensions produced by flow assembly at similar experimental conditions.

exp	$d_{\text{hyd NPC}}$ (nm) [PDI]	Time, T (s)	$\Delta d_{\text{hyd NPC}}$ (nm)	Slug surface area, SA (cm^2)	Slug volume, V (cm^3)	EF ($\text{nm s}^{-1} \text{cm}$)
1	145 [0.17]	30	127	0.63	0.0317	0.21
2	146 [0.14]	30	128	0.63	0.0317	0.21
3	147 [0.16]	30	130	0.63	0.0317	0.22

Table 4- 5 Stability study. Primary OA FeO NPs: 18 nm, PDI = 0.200. Flow rate: 0.4 mL/min, Tube length: 20cm.

4.3.3.3 Effect of the tube length on nanoparticle assembly

In order to investigate on the dependence of the 8-NPC size distribution on the tube length, flow assembly experiments were performed using PTFE tubing of 20, 40, 57 and 70 cm at a flow rate of 1 mL/hr. Both NPC hydrodynamic diameters and PDI values rare shown in Figure 4-14. It is found that the latter remain low irrespective of the tube length. In Table 4-6 DLS data and other parameters (as above) are reported for this experiment.

A linear correlation between tube length and NPC hydrodynamic size is observed (Figure 4-16), as expected since the exposure time of the NP suspension to the interface increases. Hence the NPC size increased from 98.7 to 119 nm increasing the tube length from 20 to 70 cm keeping a unimodal size distribution in all cases (PDI 0.09-0.16). Fitting these data to a linear function the correlation coefficient R^2 of 0.973 and a slope of 0.39 nm/cm were found. The linear increase of d_{hyd} with increasing the tube length is clearly due to the time of interaction between the NP suspension and the water interface. Also in this case the exposure factor is the range 0.20-0.22 nms^{-1}cm and it is similar to the one obtained in the reproducibility studies, Table 4-6.

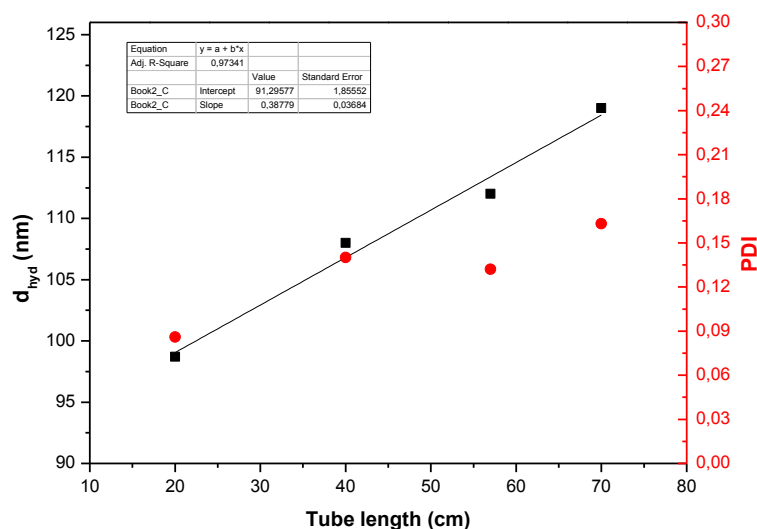


Figure 4- 16 Effect of tube length on NPC (■) hydrodynamic diameter and (●) PDI at a low rate of 1 ml/hr . (-) Linear fit $y = 91.29577 + 0.38779x$, $R^2 = 0.973$.

Tube length (cm)	d_{hyd} NPC (nm) [PDI]	Time (s)	Δd_{hyd} NPC (nm)	Surface area (cm^2)	Slug Volume (cm^3)	EF ($\text{nm s}^{-1} \text{cm}$)
20	99 [0.09]	17	128	0.63	0.0301	0.22
40	108 [0.14]	21	114	0.63	0.0301	0.20
57	112 [0.16]	23	93	0.63	0.0301	0.20
70	119 [0.13]	25	80	0.63	0.0301	0.20

Table 4- 6 Dependence of size distribution on tube length at a flow rate of 1 mL/min. Primary OA FeO NPs: 18 nm, PDI = 0.200.

4.3.3.4 Effect of flow rate on nanoparticle assembly

To study the effect of the flow rate on the NPC size distribution, flow assembly experiments were performed using rates in the range 0.4-1.5 ml/hr and a constant tube length of 20 cm. The NPC hydrodynamic diameters and PDI values are shown in Figure 4-17. Table 4-7 reports DLS data and the ratios between Δd , time of exposure and the slug surface area/ volume ratio results. The NPC size increases with increasing flow rate and the exposing factor is similar as before.

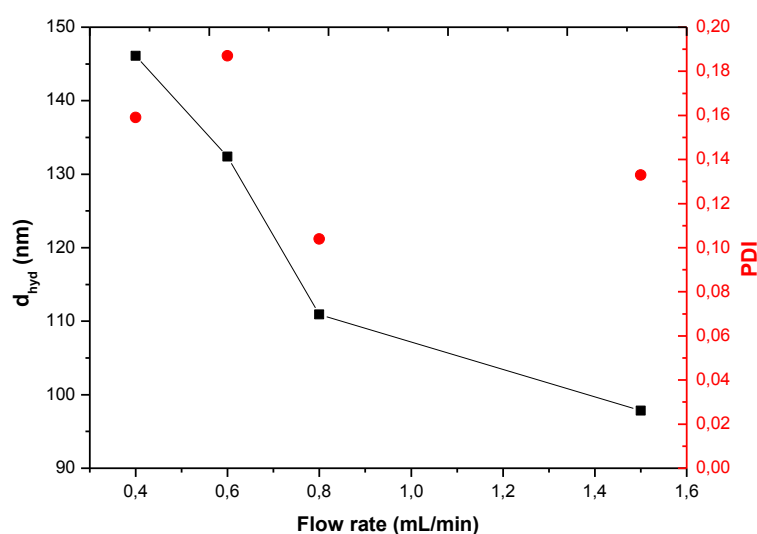


Figure 4- 17 Effect of flow rate on NPC (■) hydrodynamic diameter and (●) PDI.

Flow rate (mL/min)	d_{hyd} NPC (nm) [PDI]	Time (s)	Δd_{hyd} NPC (nm)	Slug Surface area (cm ²)	Slug Volume (cm ³)	EF (nm s ⁻¹ cm)
0.4	146 [0.16]	30	128	0.63	0.0316	0.21
0.6	132 [0.19]	24	114	0.63	0.0316	0.23
0.8	111 [0.10]	20	93	0.63	0.0285	0.21
1.5	98 [0.13]	9	80	0.63	0.0253	0.31

Table 4- 7 Dependence of size distribution on flow rate using a tube length of 20 cm. Primary OA FeO NPs: 18 nm, PDI = 0.20.

In contrast to the tube length, the NPC size is more affected by the flow rate. The mean particle diameters decreases from 146 at 0.4 ml/hr to 97.8 nm at 1.5 ml/hr and a non-linear trend is observed even though generally the higher the flow rate, the shorter is the retention time of the suspension in the flow system.

In this case the ratio between the change in d_{hyd} , the time of exposure to water and the surface area/volume ratio is the range 0.21-0.23 nms^{-1}cm up to a flow rate of 0.8 mL/min. The EF value is very similar to those obtained in the previous experiments. Hence the increased interfacial area is offset by the reduced exposure time.

Hence the flow process yielded stable NPCs of narrow size distribution and their size was controllable through the flow rate in the 0.4-0.8 mL/min range and tube lengths from 40 to 70 cm. The exposure factor changes at 1.5 mL/min; this anomaly is subject to further investigations, although there was no visual difference in the outcome of the experiment. We are also currently investigating the effect of the OA equivalent used in the CHCl_3 phase on the EF factor obtained. Finally, are also attempting further scale up. This will involve firstly the use of larger volume Duran-style mass-control pumps (peristaltic pumps were surprisingly somewhat successful, despite the inherently pulsatile nature of the flow). Secondly we are designing (with collaborators) a liquid-liquid phase separator to solve the issues of bubbling and continued assembly at the collection point.

4.3.4 Nanoparticle assembly experiments monitored with DLS Probe

4.3.4.1 Comparison of data generated by Zetasizer Nano and by DLS probe

Our collaboration with Malvern Instruments® (Worcestershire, UK) aimed to develop novel *in situ* light scattering technologies for monitoring assembly at large scale (10-200 mL scale and/or under the effect of external forces (e.g. magnetic field). This would lead to build on knowledge of nanoparticle interactions through controlled assembly under particular conditions never experienced before. To do this, we used a DLS probe system which is shown in Figure 4-18. Unlike the traditional DLS instrument described in Chapter 2, the DLS probe includes an optical temperature probe allowing the user to directly measure the sample temperature and two different lasers; a 635 nm laser for alignment purposes and an 830 nm high power laser for measurement.

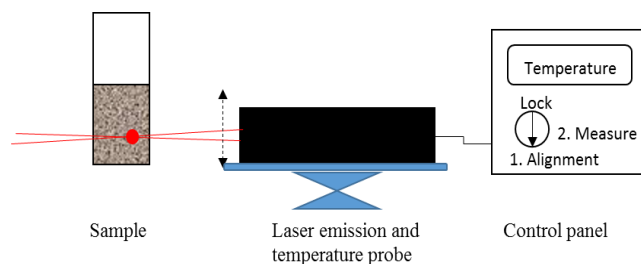


Figure 4- 18 Schematic representation of the DLS probe system (Malvern Instruments, UK). The system is formed by a laser and temperature probe block which is placed on a mobile support and a control panel.

In this section the data generated from the analysis performed with this system are compared with those obtained with the traditional DLS instrument while in the following sections studies over the special distributions of the clusters during the assembly process and the effect of an external magnetic field on the NP assembly are presented. Note that the experiments were performed at small scale (1.2 mL) in order to assess and to eventually improve the analysis by DLS probe instrument.

To optimize the DLS probe system, we first set out to verify if there was any difference with the data generated using the conventional NanoZS instrument (Malvern Instruments®). To do that the hydrodynamic size of a suspension of iron oxide NPs in chloroform was determined with both systems. The hydrodynamic diameters and size distributions by intensity achieved are shown in Figure 4-19. Higher hydrodynamic size and PDI values were observed in case of the measurement performed with the DLS probe on the same suspension. Finally, the intensity of light scattered is significantly lower than the one in the traditional DLS. This is largely because of reduced incident laser intensity and additional sources of non-backscattered light (flare).

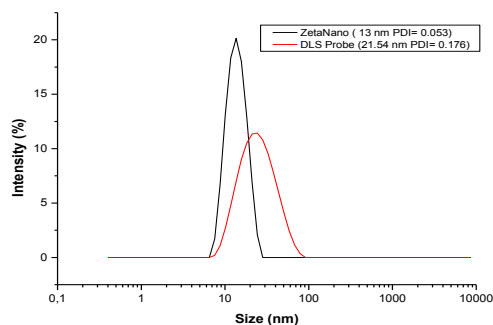


Figure 4- 19 Size distribution by intensity of measurements performed with (red line) DLS probe and (black line) Zetasizer Nano.

4.3.4.2 Investigating the spatial distribution of clusters during assembly

Taking in account the differences described above, we wanted to investigate whether the clustering of the NPs occurs homogeneously throughout the volume of the suspension by exploiting the mobility of the laser. The DLS data were collected by placing the laser at two different positions; close to the bottom of the cuvette (0.3 cm) and a second position close to the liquid-liquid interface (0.7 cm). The hydrodynamic size, count rate and PDI values were monitored over time and are shown in Figure 4-20. It has to be noted that at the beginning of the experiment, the data collected were not good because of difficulties in aligning the laser and optimizing the intensity of the light scattered. In both experiments the PDI was below 0.2 and the assembly rates were initially very similar up to ~2 hours. Transitions into the quasi-linear regime occurred at earlier times (lower d_{hyd}) further away from the interface and the rate during this stage was lower. These findings suggest that at early stage of the assembly, the clustering rate is similar at both the bottom and the top of the suspension and so the formations of NPCs occurs homogeneously throughout the suspension. At later stage (> 2 hours) the assembly rates are different; for instance the rate is faster closer to the chloroform-water interface and the count rate is higher in this case. The reasons behind this finding are still under investigation, however it does seem to coincide with the transition to a slow quasi-linear assembly. This surprising, given the fast NP and NPC diffusion and long assembly times, observation suggests improved monodispersity might be associated with reduced reaction volume.

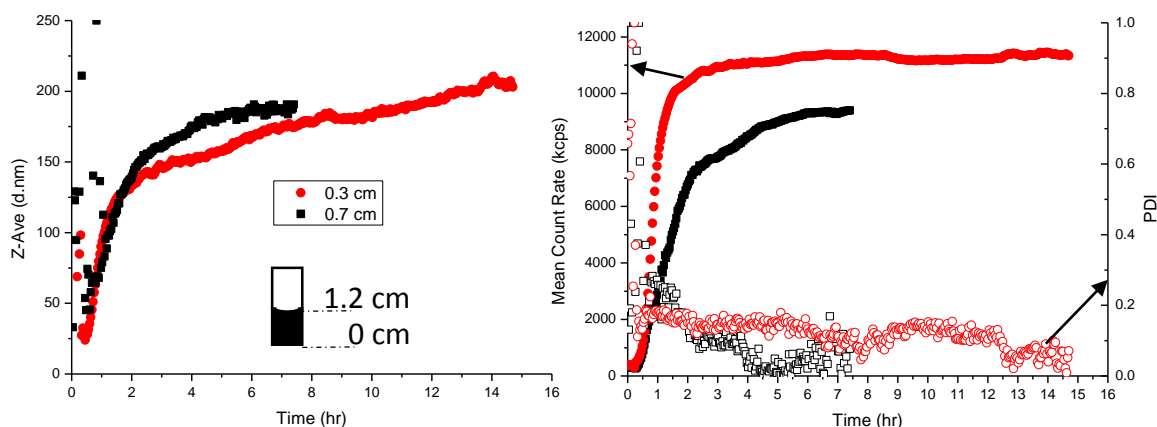


Figure 4- 20 DLS data of NP clustered with WI-CSD approach measured using two different laser positions. (Left) Monitoring of hydrodynamic diameters overtime measured at (●) 0.3 and (■) 0.7 cm. (Right) Monitoring of (solid symbols, left-hand axes) count rate and (empty filled symbols, right-hand axes) PDI over time.

4.3.4.3 Effect of magnetic field on nanoparticle assembly

In order to investigate over the effect of an external magnetic field over the assembly of 8 nm iron oxide NPs, a small round nickel plated magnet (2/10" diameter x 1/16" thick, ~0.46 T) was placed next to the cuvette and the hydrodynamic diameter was monitored over time by DLS probe. The DLS data collected is shown in Figure 4-21. In the absence of a magnet a similar response to that shown in Figure 4-20 would be expected. It has to be noted that some high PDI values (> 0.4) were observed at the beginning of the experiment. The initial iron content was ~1.5 mM in the later stages this dropped to ~0.6 mM, which is still represents a significant yield. Following the application of the magnet (i), the NP suspension was stable and the d_{hyd} was unchanged for up to ~1 hour. Hence, the NP suspension is not affected by the magnet. After 1 hour, the water layer was added onto the NP suspension and after an induction time of ~50 minutes a rapid increase of the NPC size was observed up to 300 nm. The rate of assembly in this case is higher than in, for example Figure 4-21. However, this is largely due to a lower NP concentration in this case. As a result higher sizes are observed quite rapidly, and the PDI remains below 0.2.

At ~3.5 hours (~300 nm) a significant decrease in size to about 150 nm was observed suggesting that large aggregates were caught by the magnet and just smaller clusters remained in suspension. It was indeed possible to see a pellet forming on the wall of the cuvette where the magnet was placed. The gradual deposition of larger NPCs and/or aggregates onto the cuvette wall during the experiment induces an increase in light transmission through the sample over time confirming that the decrease in d_{hyd} is not due to desegregation. The magnet was then removed (iii) and the hydrodynamic size of the NPCs in suspensions increased and gradually stopped at ~200 nm. The count rate was found to have a similar trend to d_{hyd} , while the PDI decreases from 0.26 to 0.09. The resulting NPC suspension was placed in a clean cuvette and no further change in hydrodynamic diameter, count rate and PDI was observed (iv), the suspension was stable for several weeks following the experiment.

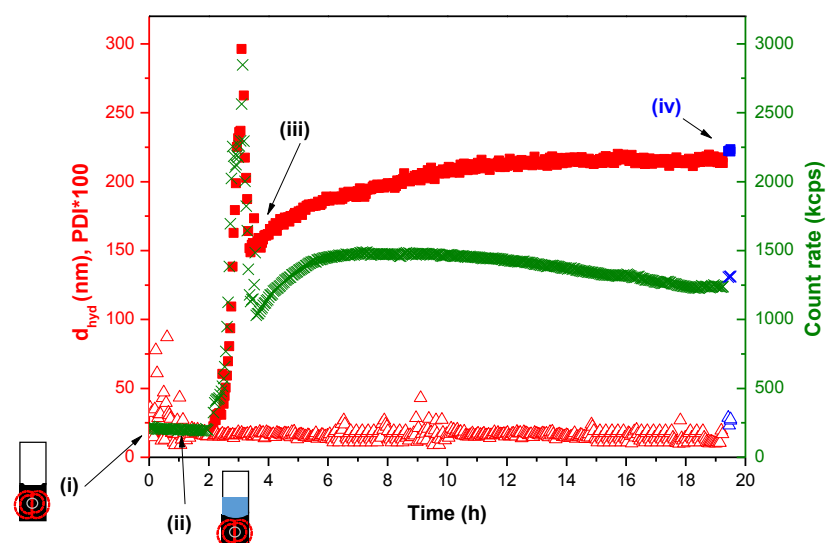


Figure 4- 21 DLS data of NP clustered with WI-CSD approach under the effect of a magnetic field. Steps performed during the experiment: (i) monitoring of the effect of the magnetic field on the d_{hyd} of the suspension (1.2 mL) for 1 hour (Left-hand axes); (ii) addition of 0.6 mL of distilled water onto the suspension;(iii) magnet removal; (iv) blocking of the assembly by the removal of the chloroform/water interface. (■) hydrodynamic diameter, (Δ) PDIx100. (Right-hand axes) (\times) Count Rate. The symbols in blue refer to the NPC suspension collected after stopping the assembly. The iron concentration of 1.1 mM and 0.75 eqs of OA were used in this experiment.

In order to investigate further the relationship between the applied field and the NP clustering process we decided to design WI-CSD experiments where magnetic field gradients of different strength were used during the assembly. The results found are reported in the following section.

4.3.4.4 Effect of attenuation of magnetic field on NP clustering by WI-CSD

The magnetic field strength was attenuated by adding round plastic spacers (0.6 cm thick) between the cuvette wall and the magnet. The magnetic field was applied 2-3 hours after adding the water layer. The hydrodynamic size was monitored over time using DLS probe, the results obtained are shown in Figure 4-22 (c-e).

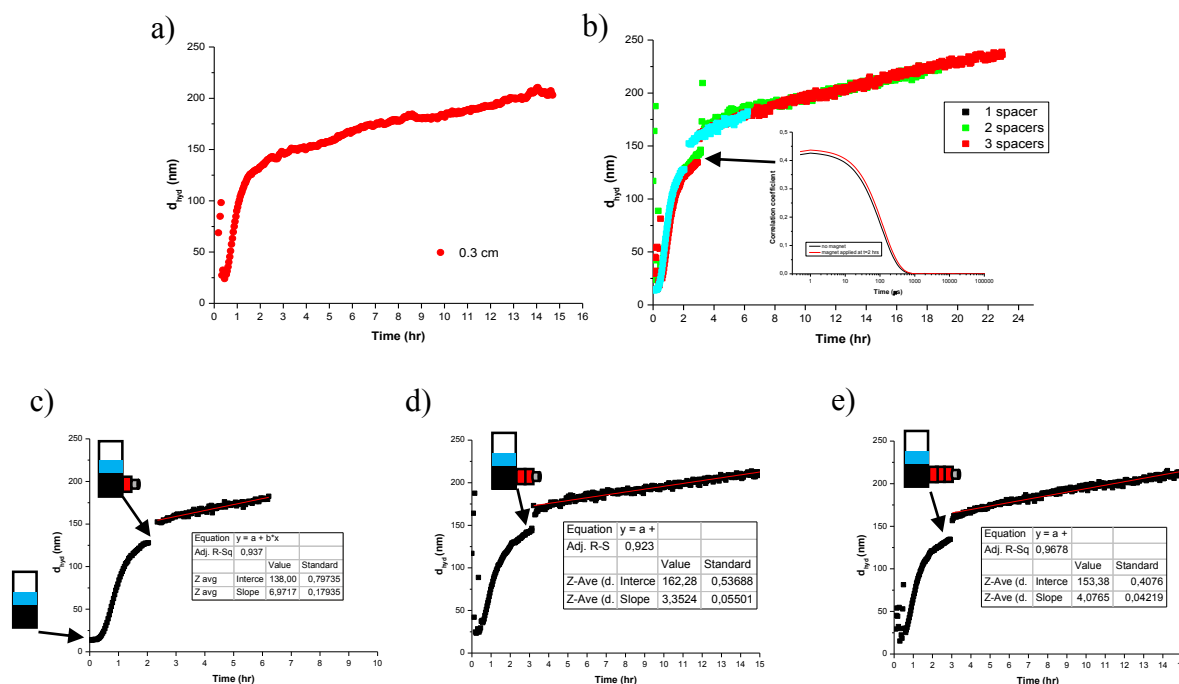


Figure 4- 22 Monitoring of hydrodynamic diameter DLS data of NP clustered with WI-CSD approach under the effect of a magnetic field of different strengths. (a) DLS data of Figure 4-19. (b) Comparison of the DLS data of Figure 4-22 c-e where (■) 1, (●) 2, (▲) 3 plastic spacers used to attenuate the magnetic field. Inset Fig.b: correlation coefficient as function of time of the suspension (black line) before and (red line) after application of the magnetic field.

In all cases a jump in d_{hyd} of ~ 20 nm was observed after the application of the magnetic field and the size continued to increase gradually for several hours. In order to investigate whether there is an effect over the assembly rate, a linear fitting of the assembly curves was undertaken. By examining the slopes obtained, it seems that altering the field gradient does not have a significant effect on the assembly. Indeed the slopes obtained from the linear fitting shown in Figure 4-20 do not present a consistent trend and indeed the general appearance of the curves are very similar. This may be due to the field strengths used not being sufficiently strong to alter the interparticle interactions; more experiments are required using higher fields and assessing the effect of key parameters involved in the assembly experiment including NP and ligand concentration. The magnetic field has little effect apart from the ~ 20 nm jump consistent with a rapid formation of larger species, presumably short chains of NPCs.

Recently Sahoo et al ^[100] reported many competing effects can influence the assembly of magnetic NPs exposed to a magnetic field including magnetic dipole-dipole and electronic polarization interactions, thermal kinetics, the particle's dipole moment to the flux directions, the solvent and ambient conditions. During the clustering process, the particles in suspension are attracted to each other by dipole interactions and they tend to align in the direction of the applied magnetic field. At some stage the growing chains spontaneously precipitate from the suspension. The sedimentation phenomenon of linear chain magnetic NPs from suspension was modeled by Zubarev ^[101] who was able to find a relationship between dipolar interparticle interactions, magnetic field strength and the critical number of NPs (called n_c) needed for the cluster sedimentation. Zubarev found that above a specific n_c value the NP chains collapse spontaneously as aggregates. It has been found that the critical number n_c increases with increasing the magnetic field strength and decreases with the energy of magnetic interaction between the NPs (ε) in the magnetic field k_0 which refers to the field in the NPC location. The dimensionless ε and k_0 are defined as follows:

$$\varepsilon = \frac{\mu_0 m^2}{2\pi d^3 KT} \quad \text{Equation 4-1}$$

$$k_0 = \frac{\mu_0 m H_0}{KT} \quad \text{Equation 4-2}$$

where μ_0 is the vacuum permeability, d is particle the hydrodynamic diameter, m the particle magnetic moment; H_0 is T is the temperature in Kelvin and K is Boltzmann constant.

Considering that larger NPCs generate higher local magnetic field k_0 than primary NPs, one would expect that with increasing the applied magnetic field strength (H_0) the interparticle interactions would increase and that would bring consecutively to higher NP assembly rates for the formations of larger NPCs in suspension. Unfortunately the experiments showed above do not confirm this. This is probably due to the fact that the strength of the magnetic fields here used were not strong enough to see an effect on the NP clustering process. The range over which we were able to attenuate the local field in the cuvette was probably sufficient to form short chains. However, despite this likelihood, the assembly process continued almost unaffected. This suggests that there is very little magnetic contribution to the interparticle interaction potential which is dominated by the gradual ongoing desorption of OA, that reduces the steric and osmotic contributions only.

Finally, according to the results presented above the NP assembly process is not affected by an external magnetic field apart from the ~20 nm jump that coincides with a fast formation of larger NPCs that form gradually larger species in a controlled fashion. Indeed the PDI was almost unchanged throughout the whole process. This is a somewhat disappointing result.

4.4 Conclusion

We have presented strategies for the development of CSD method that could pave the way towards the synthesis of water stable magnetic NPCs of controlled size and magnetic properties. The clusters were produced from the assembly of iron oxide primary NPs which were synthesized by thermal decomposition. The effect of the substrate, NP size and the presence of an external magnetic field on the assembly process was studied insights in/to the kinetics of assembly were obtained.

We have shown that the kinetics of assembly do affect the resulting magnetic properties of the NPCs. This observation may be exploited to tailor the magnetic properties of the clusters.

Preliminary assembly studies using large NPs (12 nm) demonstrated that it is possible to obtain size controlled NPCs with narrow size distribution with different NP sizes. However the experimental conditions still need further optimization before further kinetic investigations can be undertaken.

The development of a new DLS setup offers significant advantages over the traditional DLS including the possibility of monitoring the NP assembly process even using larger volumes of suspension (> 1 mL) and under a magnetic field. The results showed that the magnitude of magnetic field used in the experiments present was not sufficient to affect the assembly process. Our interpretation is that the interparticle interaction potential is mostly dominated by the gradual ongoing desorption of OA, while the magnetic contribution to the assembly process is minor.

Finally, the CSD method was extended to include the preparation of NPCs by a novel flow assembly experimental set-up which it may be useful to for a further scale up of the method for the production of volumes of NPC suspensions in the range of liters corresponding to grams of NPCs.

Chapter 5

Transfer of stabilized suspensions of magnetic nanoparticle assemblies of controlled size from an organic to aqueous medium

5.1 Introduction

Metal oxide nanoparticle made from the competitive stabiliser desorption assembly of nanoparticles synthesized by the thermal decomposition method are highly monodisperse, making them ideal candidates for many bio applications. In these syntheses surfactants, such as oleic acid (OA), mediate the dispersion of the nanoparticles and prevent agglomeration following assembly by coating the surface of the clusters, however, the coating renders the clusters insoluble in aqueous solutions. For use in biomedical applications, these clusters must first be transferred to the aqueous phase. This is a considerable problem as phase transfer often results in the formation of aggregates and/or in multiple nanoclusters or single nanoparticles being collectively coated within an envelope of coating ^[102]. However since the removal of the OA from the NPC surface would destabilize the clusters provoking their immediate aggregation, a phase transfer by the coating with a surfactant is necessary. The literature reports many studies in which lipid bilayers and amphiphilic block copolymers were used as surfactants for NP phase transfer ^[103]. However the addition of these surfactants onto the particle surface usually results in an increase of the hydrodynamic size of the particle after phase transfer. For this reason, short chain surfactants are preferred. Recently, Cao et al. ^[104] showed that DTAB provides water dispersability while maintaining a small hydrodynamic size (< 20 nm) for individual particles ^[104].

In this work the phase transfer of monodisperse, oleic-acid-coated iron oxide nanoclusters using two surfactants is reported. The surface modification of the NPCs occurs following the addition of surfactant molecules that are physisorbed onto the surface of the clusters resulting in an increase of the NPC dispersity in aqueous phase. These surfactants present different structures and the mechanism of their physisorption onto the cluster surface is described and schematically represented below. The first surfactant used is a copolymer called Pluronic P123 (M_w 5750) that has been shown to be biocompatible and studies show that its concentration in the plasma remain quite high for several hours following administration ^[105]. Pluronic co-polymers are made of two A-chains of polyethylene oxide (EO) and one B-chain of polypropylene oxide (PO) in an ABA configuration; as the molecular weight decreases, consecutively the hydrophobicity of the entire arrangement increases. P123 contains 39 EO units and 69 PO. Phase transfer using P123 is driven by hydrophobic–hydrophobic interactions between hydrocarbon tails of the oleic

acid coating on the surface of the nanoparticles and the hydrophobic PO chains of the central block (Figure 5-1).

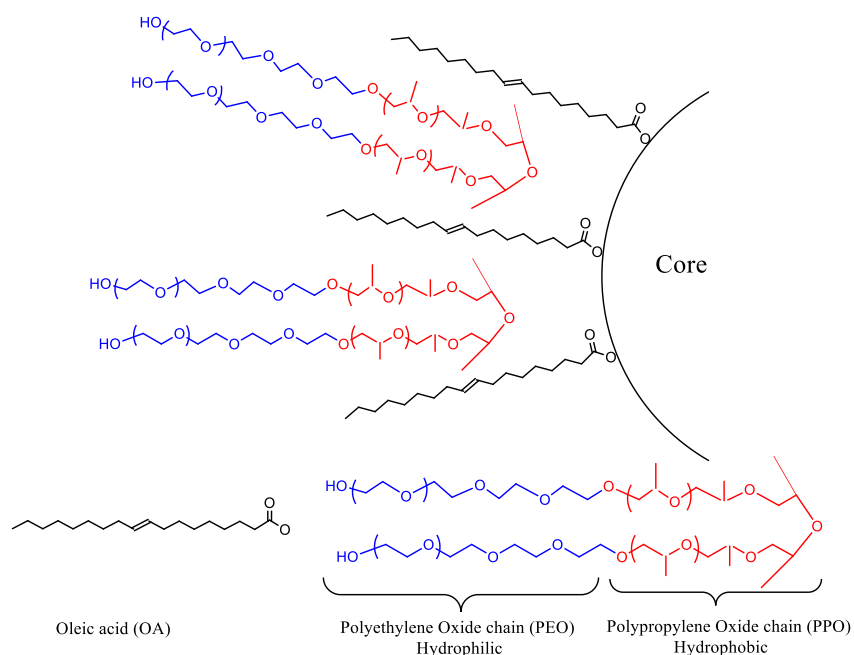


Figure 5- 1 Schematic representation of oleic acid stabilized iron oxide nanoparticle coated with P123 following phase transfer leading to steric stabilization.

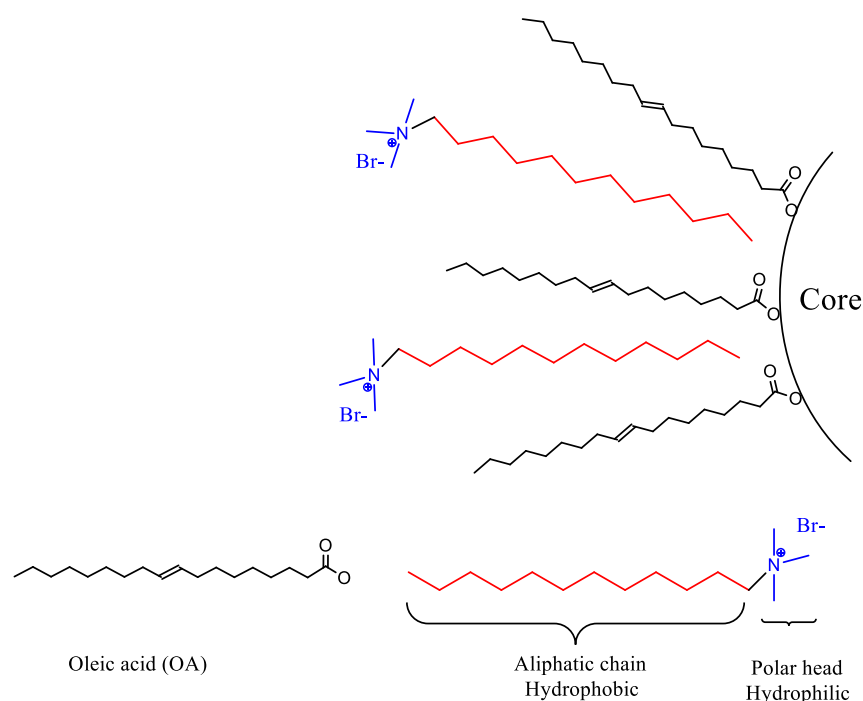


Figure 5- 2 Schematic representation of oleic acid stabilized iron oxide nanoparticle coated with DTAB following phase transfer leading to steric stabilization.

The second surfactant used is dodecyltrimethylammonium bromide (DTAB) which is a well-known surfactant and has been widely used in nanoscience. It is a quaternary ammonium salt in which four hydrocarbon chains are bound to a nitrogen atom that is thus positively charged. These salts are known as classical phase-transfer agents and are also used in colloidal science for the phase transfer of hydrophobic particles to the aqueous phase through hydrophobic adsorption of the aliphatic chain on the NP coated by hydrophobic ligands (*e.g.* fatty acids) while the ammonium moiety remains soluble into aqueous solution (Figure 5-2).

Following the phase transfer, the surface of the oleic acid stabilized iron oxide NPCs are ideally fully covered by surfactant molecules, with the polar head groups in direct contact with H₂O molecules and the tails interacting with the long C18 fatty acid chains which are bound to the NPC surface. The thermodynamic driving force for cluster stabilization with the amphiphilic surfactant is entropic in nature, arising from the reduction of solvophobic interactions. Following encapsulation, the NP bound surfactant tails interdigitate with the PPO blocks of the polymer. This reduces solvophobic interactions around the dispersed polymers (which are below the critical micelle concentration), as it releases previously ordered water molecules into the bulk, massively increasing their configurational entropy.

The conditions employed in the phase transfer have a large impact on the resulting size of the NPCs in water. Size control is typically dependent on factors such as the nature of the surfactants used, NPC:surfactant mole ratio, the pH and ionic strength of the medium. Hence the optimization of the process conditions such as the surfactant and NPC concentration was undertaken prior to scale-up.

The aims of the present work are: (i) clustering of oleic acid stabilized FeO NPs by WI-CSD and (ii) modification of these clusters with P123 and DTAB (to prepare P123-NPCs and DTAB-NPCs). The formation of modified-NPC will be assessed by DLS, FESEM and by ATR-IR. (iii) Investigation of the magnetic properties of the NPC suspensions before and after phase transfer and of the effect of NPC size on the magnetic response using the NMRD technique; (iv) evaluation of the heating properties of the aqueous suspensions of NPCs and the effect of the surfactant used in the phase transfer on the application of the cluster suspension as a mediator for magnetic fluid hyperthermia; (v) assessment of the bio-toxicity of the resulting suspensions *in vitro*.

5.2 Materials and methods

5.2.1 Materials

Iron (III) acetylacetonate (purity $\geq 99.9\%$), oleic acid ($\geq 99.0\%$), benzyl alcohol (purity $\geq 99.0\%$) and P123 were purchased from Sigma Aldrich while acetone, chloroform and THF were purchased from Labscan. De-ionised water was obtained from a Millipore MilliQ system and had a resistivity of $< 16 \text{ M}\Omega\cdot\text{cm}$ prior to use.

5.2.2 OA-NP and OA-NPC synthesis

The FeO NPs were synthesized by the thermo-decomposition protocol described previously in chapter 3 that uses 1g of precursor ($\text{FeIII}(\text{acac})_3$) dissolved in 20 mL of benzyl alcohol heated to reflux for 7 hours. The NPs were then washed with acetone twice then stabilized with Oleic acid and finally assembled with WI-CSD method described in Chapter 3.

5.2.3 Phase transfer of OA-NPCs

5.2.3.1 Preparation of P123-NPCs

An amount of NPC suspension (typically 1-2mL) in chloroform was dried in oven for 30 min at 60-70 °C for evaporating the solvent and then the clusters were dispersed in THF. The solution of P123 was previously prepared by dissolving the polymer in MilliQ water so that the final concentration of the solution was 76.5 μM . Variable volumes of the polymer solution were added to the suspension and then stirred without covering the vial to allow the THF to evaporate slowly under fume hood. After the complete THF evaporation (about 2-3 days later), the suspension was collected and the water phase with the phase transferred NPC was recovered and ready for the characterization. Typically the resulting aqueous suspension of NPCs had an iron concentration of 0.5-1.2 mM. The amounts and ratios of polymer and Fe used are reported in Table 5-1. Parameters like the Fe concentration and the surfactant concentration were optimized and will be discussed in the following sections.

P123/Fe molar ratio	Fe source used (μmol)	P123 (μmol)
0.3	2	0.6
0.5	2	1
1	2	2
2	2	4
3	2	6
4	2	8

Table 5- 1 The amount and surfactant/Fe mole ration in phase transfer with P123.

5.2.3.2 Preparation of DTAB-NPCs

DTAB coated NPCs were prepared according to a method previously used by Cao's protocol ^[104]. In brief, in a typical experiment an amount of chloroform suspension of OA-NPCs was vortexed for 2 minutes with a volume of aqueous dodecyltrimethylammonium bromide solution (DTAB, 65 mM) in a glass vial. A brown and clear aqueous suspension of DTAB coated NPCs was obtained by evaporating the chloroform under N₂ flow. The amounts and ratios of polymer and NPCs used are reported in Table 5-2. The Fe and the surfactant concentration on the phase transfer process were studied and optimized and will be discussed in the following sections. The schematic representation of the phase transfer with DTAB surfactant is shown in Figure 5-3.

DTAB/Fe molar ratio	Fe source used (μmol)	DTAB (μmol)
0.25	2	0.5
0.33	2	0.66
0.5	2	1
1	2	2
2	2	4

Table 5- 2 The amount and surfactant/Fe mole ration in phase transfer with DTAB.

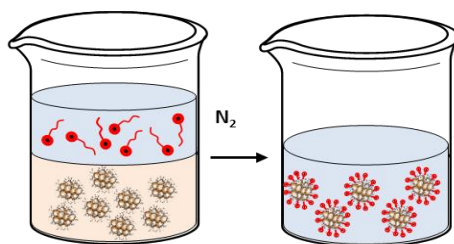


Figure 5- 3 Schematic representation of NPC phase transfer by DTAB coating.

5.2.4 Characterization

Malvern Zetasizer Nano Dynamic Light Scattering (Malvern Instrument, Worcestershire UK) machine was used to measure the NP and NPC size before and after the nanoclusters coating and for checking their colloidal stability. The effectiveness of the NPC coating by the polymer was investigated by ATR-IR and FESEM and magnetic properties of the clusters before and after phase transfer were studied by NMRD (Stelar, Italy). To prepare the sample for ATR-IR and FESEM analysis, typically 0.5 ml of sample was cleaned by typically three centrifugation cycles times (5 minute @ 5000 rpm) in order to get rid of surfactant in excess. In case of ATR-IR analysis, the sample was then freeze dried using a Freezone 4.5 freeze dryer (Labconco, USA).

Iron concentrations of phase transferred nanoparticle clusters were confirmed with Inductively Coupled Plasma-Atomic Emission Spectrophotometer (ICP-AES) using the digestion process described in Chapter 2. Finally, a magneTherm™ (nanoTherics, Newcastle UK) was used for the assessment of the heating efficiency of the NPCs in water. The experimental procedure used is identical to the one described in Chapter 2. SAR values obtained were calculated using the Equation 2-14.

5.3 Results and discussion

5.3.1 Synthesis of OA-NPCs

Iron oxide nanoparticle clusters of size in the range 48-190 nm were synthesized through WI-CSD method. The hydrodynamic diameter and PDI values of the fresh and aged

chloroform based suspensions are reported in Table 5-3. All the NPC suspensions present a unimodal size distribution ($PDI \leq 0.2$) and stable over time.

$d_{hyd, NPs}$ (nm) [PDI]	$d_{hyd, NPCs}$ (nm) [PDI]	$d_{hyd, NPCs}$ aged (nm) [PDI]	Aging days
18 [0.13]	48 [0.23]	51 [0.21]	21
14 [0.08]	79 [0.07]	76 [0.06]	24
13 [0.04]	81 [0.15]	77 [0.11]	21
15 [0.10]	126 [0.13]	124 [0.11]	22
14 [0.07]	153 [0.07]	150 [0.07]	24
13 [0.05]	190 [0.05]	200 [0.05]	24

Table 5- 3 Hydrodynamic diameter and PDI values measured at 25 °C of different batches of FeO OA-NPs, and OA-NPCs and the same OA-NPC suspensions aged in chloroform.

The OA-NPC samples will be used in the study of the phase transfer process and in the assessment of the chemical and physical properties of the NPCs in aqueous medium in the following sections.

5.3.2 Phase transfer of NPCs

5.3.2.1 Preparation of P123-NPCs

The outcome of a typical experiment of FeO NPC phase transfer from the organic to aqueous medium is shown in Figure 5-4. OA-FeO NPCs are soluble only in chloroform here their presence is observed by the brown colouring of the chloroform layer. After coating with P123 the NPCs are soluble in the aqueous phase and they do not revert to the organic phase after shaking the vial.

DLS was used to measure NP and NPC hydrodynamic diameter in both organic media and water. Figure 5-1 reports the size distributions by intensity of these suspensions used in a typical phase transfer process using P123 as co-surfactant. Starting from 13.5 nm ($PDI = 0.04$) oleic acid stabilized FeO NPs, non-aqueous NPC suspension of 152 nm ($PDI = 0.08$) were phase transferred in water. The resulting aqueous NPC suspension had d_{hyd} of 155 nm with PDI of 0.096. According to this result, no significant change in

hydrodynamic diameter occurred after coating with the polymer while the PDI improved. The surface charge found for these clusters was of -17.4 mV (Figure 5-5). The negative charge is related to the outer hydroxyl groups which are ionized in water ^[106].

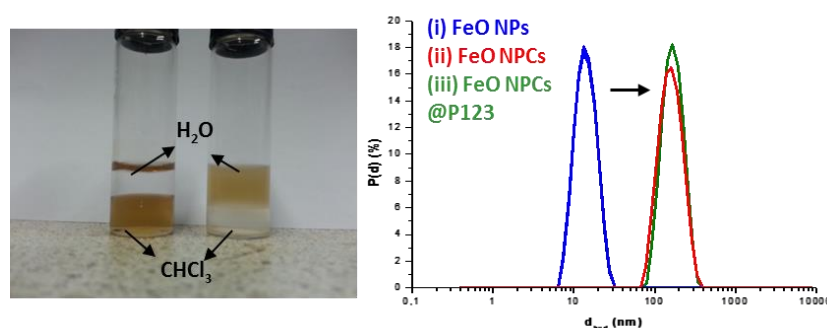


Figure 5- 4 (Left) Phase transfer of nanoparticle clusters before and after coating with F123 using 1:1 vol ratio of OA-FeO NPC:P123. Before coating the NPCs are soluble in chloroform while after coating, the NPCs becomes soluble in water. (Right) Size distribution by intensity of chloroform suspension of (-) 14 nm oleic acid stabilized OA-FeO NPs (PDI= 0.08) and (-) 152 nm OA-NPCs (PDI= 0.09). After phase transfer, (-) NPCs have a d_{hyd} of 155 nm and PDI=0.10.

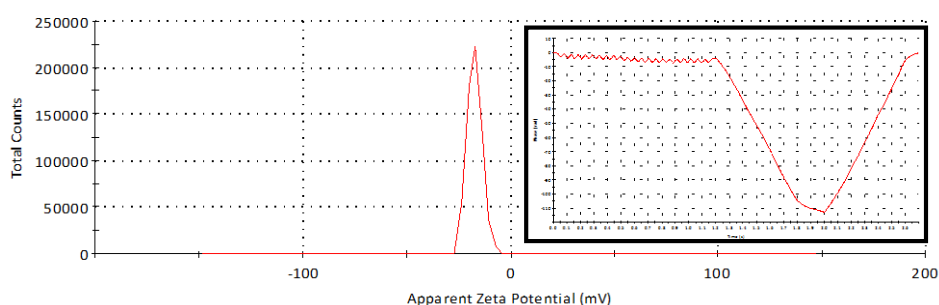


Figure 5- 5 Z-potential distribution of FeO NPCs@P123 suspension and the relative phase plot. The Z- potential for 155 nm P123-NPCs was -17.4 mV.

FESEM analysis of a typical FeO NPC@P123 suspension is dried onto a copper TEM grid shown in Figure 5-6. The NPCs show spherical-like shape and within which the NPs form densely packed compact nanostructures that are stable even after solvent evaporation process on the grid. It is also visible a thin polymer shell covers the NPC surface. The NPC@P123 average size measured for 245 NPCs from this image was of 190 nm ($\sigma = 19\%$) while the hydrodynamic diameter obtained from DLS of the same suspension was 200 nm (PDI = 0.1). Moreover there are no significant signs of formation of polymer micelles or of further NPC agglomeration, after the phase transfer process.

This confirms successful phase transfer of NPCs from chloroform to water without change in size.

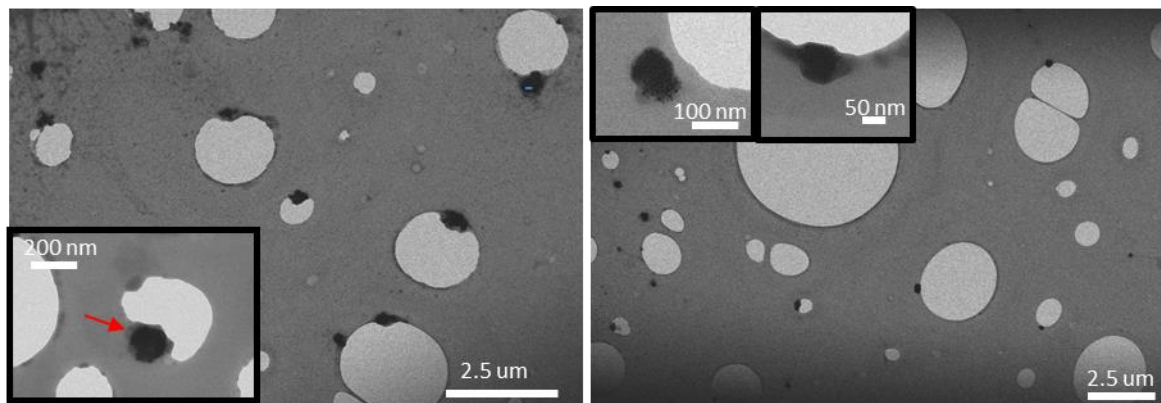


Figure 5- 6 FESEM image of a typical aqueous FeO NPC@P123 suspension ($d_{\text{FESEM}} = 190 \text{ nm}$, $\sigma = 19 \%$, 245 clusters, $d_{\text{hyd}} = 200 \text{ nm}$, PDI = 0.1). The red arrow indicates the polymeric shell that is surrounding an NPC. 245 cluster were counted for this sample.

The ATR-IR spectra of FeO NPCs before and after the coating with P123 is shown in Figure 5-7. The ATR-IR spectra of uncoated FeO NPCs, oleic acid and P123 was also recorded in order to investigate the interaction between the NPC surface and the hydrophilic polymer. Prior the analysis the NPCs were magnetically caught to remove the polymer excess and to make sure that the final sample was associated with the magnetic fraction. The IR spectra band assignments are summarized in the Table 5-4.

The IR spectrum of oleic acid shows characteristic peaks at 2893 , 2841 and 1460 cm^{-1} that are assigned to C-H asymmetric stretching, symmetric stretching and scissoring, respectively ^[64a]. At 1720 cm^{-1} a peak attributed to the C-O asymmetric stretching of the OA ligand is observed ^[107]. The characteristic bands of OA are visible in the IR spectrum of OA-FeO NPCs while the peak at 720 cm^{-1} is related to CH_2 rocking modes. Considering the IR spectra of the P123, an intense peak at 1110 cm^{-1} is observed and it is assigned to the C-O-C stretching modes characteristic of the polymeric molecule ^[64].

The spectrum of P123-NPC suspension shows all the characteristic bands of OA, OA-FeO NPCs, and mainly of P123 which give a higher contribute in the resulting IR spectra. Indeed the P123-NPC spectrum is almost identical to the IR spectra of P123 alone except for small bands at 1705 and 720 cm^{-1} that are attributed to the COO and CH_2 rocking modes of the OA attached on the NPC surface. This observation indicates the presence of

both surfactants on the cluster surface but also that P123 forms a more compact shell. Indeed, strong binding between the polymer and the clusters is needed in order to prevent exposure of OA to the aqueous media.

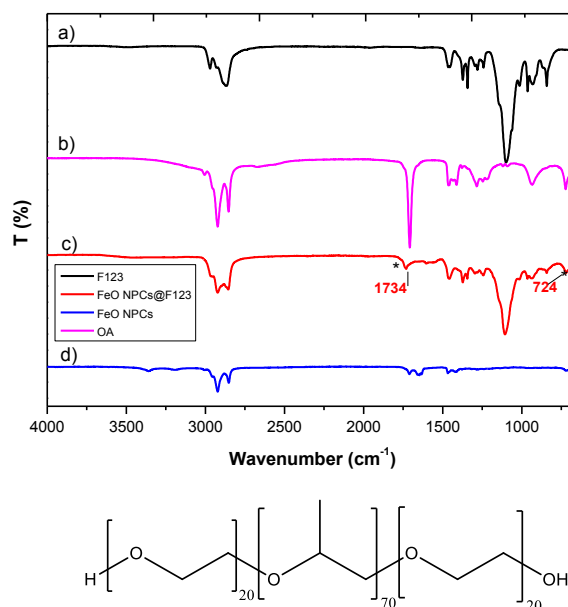


Figure 5- 7 ATR-IR spectra of (a) P123, (b) OA, (d) OA stabilized γ -Fe₂O₃ NPCs in chloroform and (c) P123-FeO NPCs in water.

OA-FeO NPCs vNPC, chloroform (cm ⁻¹)	PF123 vP123 (cm ⁻¹)	NPC@P123 vNPC, water (cm ⁻¹)	Assignment [64, 107]
2893	2923	2893	ν_a CH ₂ stretch
2841	2857	2857	ν_s CH ₂ stretch
1720	-	1720	ν_a C=O stretch
1695	-	1695	COO- rock
1460	1461	1461	ν_s CH ₂ scissor
-	1098	1098	C-O-C stretch
720	-	720	CH ₂ rocking

Table 5- 4 Infrared band assignments for oleic stabilized FeO NPCs, pure P123 polymer and P123 coated FeO NPCs.

5.3.2.2 Preparation of DTAB-NPCs

Figure 5-8 shows the size distributions by intensity of a typical NPC suspension before and after coating with DTAB. The size distribution by intensity of NPs dispersed in chloroform is also reported for comparison. DLS data showed that no significant hydrodynamic diameter changing occurred with NPC surface modification. Also the monodispersity of the NPC suspension is maintained after the phase transfer process. For instance 106 nm oleic stabilised NPC (PDI = 0.11) were transferred to water where they showed a hydrodynamic diameter of 108.6 nm and PDI of 0.08. The NPC@DTAB showed a charge of +34.3 mV (Figure 5-8).

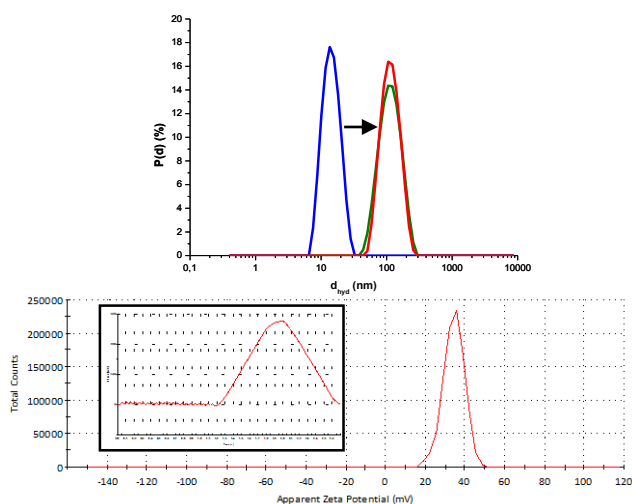


Figure 5- 8 (Top) Size distribution by intensity of chloroform suspension of (-) 14 oleic acid stabilized FeO NPs (PDI= 0.08) and (-) 106 nm NPCs (PDI= 0.11). After phase transfer, the (-) NPCs have a d_{hyd} of 108.6 nm and PDI=0.079. (Bottom) Z-potential distribution of FeO NPCs@DTAB suspension and the relative phase plot. The NPC@DTAB showed zeta potential of +34.3 mV.

FE-SEM microscopy image of a typical FeO DTAB-NPC suspension is shown in Figure 5-9. The image show quasi-spherical clusters that seems to be less densely packed than P123 coated clusters. The DTAB-NPC average size (out of 311 NPCs) measured from this image was of 192 nm ($\sigma = 21\%$) while the hydrodynamic diameter obtained from DLS of the same suspension was 200 nm. The FESEM images show that the DTAB stabilized NPCs are relatively monodisperse and have a spherical-like shape.

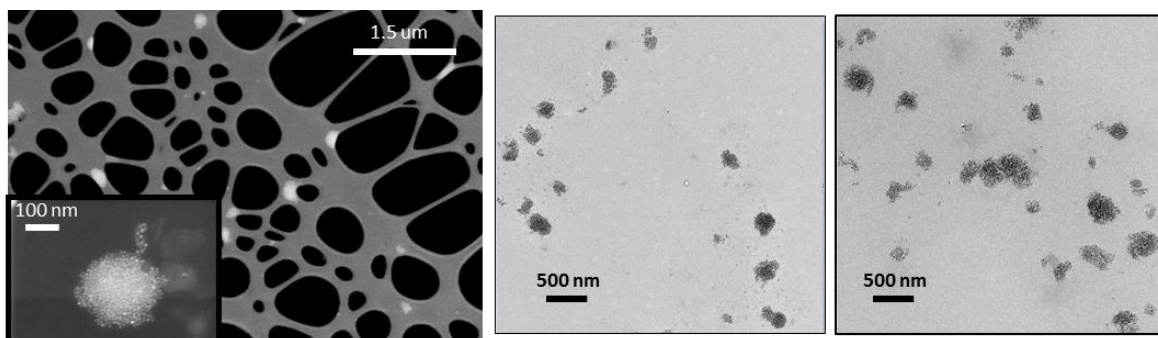


Figure 5- 9 FESEM image of a typical aqueous DTAB-NPC suspension ($d_{\text{hyd}} = 200 \text{ nm}$, PDI=0.17). N = 311 clusters were counted for this sample.

5.3.3 Reproducibility and colloidal stability

DLS data and percentage yield values of representative samples of fresh and aged suspensions of aqueous NPC suspensions prepared by coating with the two surfactants are reported in Figure 5-10. The size distribution by intensity of oleic acid NPC suspended in chloroform used are also reported for comparison. The results of DLS measurements of aged aqueous NPC suspensions prepared starting from different oleic stabilized FeO NPCs batches are reported in Table 5-5. A surfactant:NPC (DTAB or P123 to iron concentration) molar ratio of 1 was used for all aqueous suspensions. Aged samples show lower PDI values and good colloidal stability over time.

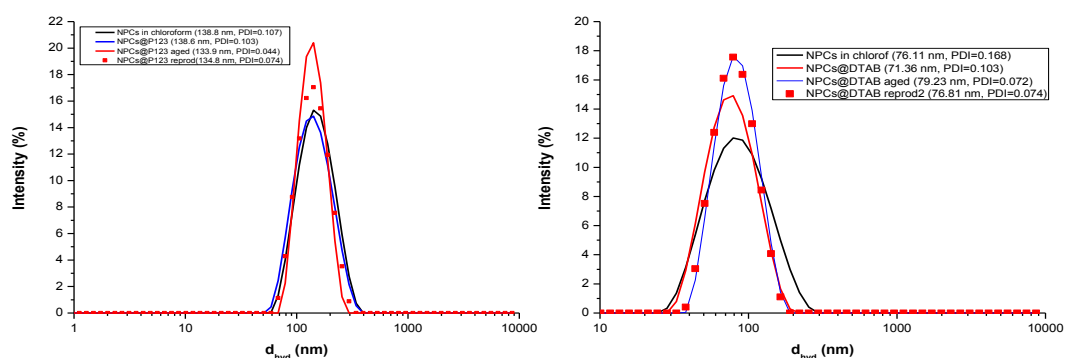


Figure 5- 10 (Left) Size distribution by intensity of suspensions of (black line) oleic acid stabilized FeO NPCs in chloroform (139 nm, PDI = 0.11); (blue line) fresh (139 nm, PDI= 0.10) and (red line) aged (134 nm, PDI= 0.04, 95 days) P123-NPCs in water. (red line) represents a new NPC@P123 (135 nm, PDI= 0.07) prepared using a different batch of OA-NPCs with same P123:NPCs: molar ratio. (Right) Size distribution by intensity of suspensions of (black line) oleic acid stabilized FeO NPCs in chloroform (76 nm, PDI = 0.17); (blue line) fresh (71 nm, PDI= 0.10) and (red line) aged (79 nm, PDI= 0.07, 42 days) DTAB-NPCs. (red line) represents a new DTAB-NPCs (77 nm, PDI= 0.07) prepared using a different batch of OA-NPCs with the same DTAB:NPCs molar ratio.

Sample	d_{hyd} (nm) [PDI]	Yield (%)	Time (day)
OA-NPCs	139 [0.11]	100	1
P123-NPCs A	142 [0.10]	35	1
P123-NPCs A	134 [0.04]	34	95
P123-NPCs B	135 [0.07]	36	223
OA-NPCs	76 [0.17]	100	1
DTAB-NPCs A	71 [0.10]	92	1
DTAB-NPCs A	79 [0.07]	92	42
DTAB-NPCs B	77 [0.08]	94	102

Table 5- 5 DLS data measured at 25 °C and % yields of fresh and aged NPCs dispersed in organic (upper) and aqueous (medium) medium. The results refers to two different preparations, A and B and same ratio was used.

DLS data demonstrates good reproducibility of the phase transfer of OA-NPCs to aqueous medium using DTAB and P123 coating without the need of any size selection. The experimental conditions used in this study were iron concentration of ~ 2 mM, 0.75 excess of OA and surfactant:P123 molar ratio of 1.

Phosphate buffered saline (PBS, 0.01 M, pH 7.3) was used as dispersant to phase transfer 77 nm OA-coated iron oxide NPCs from chloroform to aqueous medium. The results of DLS measurements carried out before and after transfer are shown in Table 5-6. P123 coated nanoclusters were monodispersed and the low PDI value indicate a unimodal size distributions. An increase of about 19 nm was observe in the hydrodynamic diameter upon phase transfer to PBS medium. In case of DTAB an increase in polydispersity was observed suggesting that aggregates were formed in the suspension following phase transfer. Finally also an increase of d_{hyd} of about 24 nm was observed after DTAB coating.

Surfactant	Dispersant	d_{hyd} (nm) [PDI]	Yield (%)
OA	CHCl ₃	77 [0.11]	100
P123@OA	PBS	96 [0.10]	54
DTAB@OA	PBS	101 [0.21]	91

Table 5- 6 Hydrodynamic diameter and polydispersity index at 25 °C of OA-, P123@OA- and DTAB@OA- stabilized FeO nanoclusters dispersed in chloroform and PBS.

For both P123- and DTAB-stabilised iron oxide NPCs it was observed that reasonable size control can be achieved on varying the surfactant and NPC concentration during the phase transfer step that are discussed more in detail in the following section. For the surfactant P123, stable and monodisperse suspensions of NPCs of hydrodynamic diameters of 80-200 nm were successfully prepared without further size selection steps, such as centrifugation or magnetic filtration. However, low yields were achieved (~ 54 %) and some of the material was visibly stuck to the vial walls after THF evaporation. For the phase transfer of OA-NPCs with d_{hyd} lower than 80 nm, an increase in size of the resulting P123-coated NPCs was observed. This might be possibly due to the formation of some aggregates of polymeric micelles. An attempt was undertaken to remove these by magnetic filtration (which is described in detail in Chapter 6) applying a magnetic field (1.41 T), but unfortunately the clusters were crushed out of suspension. For DTAB coated iron oxide NPCs a good size control was achieved by the use of surfactant/Fe molar ratio of 1 and typical hydrodynamic sizes in the range of 50-120 nm and high yield were achieved in all cases (~ 91 %). On observing the hydrodynamic size of both DTAB- and P123- coated NPCs over a period of months it was noted that P123-NPCs were significantly more stable than the others. Lastly an increase of the NPC size was observed following phase transfer to phosphate saline buffer in case of both surfactants. Although really low polydispersity was observed after coating with P123 in PBS medium.

5.3.4 Phase transfer optimization

In order to investigate the effect of the surfactant and the NPC concentration on the phase transfer process, different quantities of surfactant and NPC suspension were used. The consequence of surfactant and NPC concentration was monitored by DLS technique throughout the phase transfer process.

5.3.4.1 Effect of P123 concentration

Figure 5-11 shows the hydrodynamic size and PDI values of NPC suspension through the whole phase transfer process using different surfactant/NPC ratios keeping the concentration of oleic stabilized FeO NPCs (2 mM of Fe) fixed. Table 5-7 summarizes

the size and PDI values of the NPCs dispersed in chloroform, THF and in water for 3 days.

At a molar ratio of 4, the NPC hydrodynamic diameter almost unchanged passing from chloroform to THF (from 190 to 192) while it increases from 190 to 208 nm in water and a further increase is observed to 230 nm after 3 days. However the suspension remained stable for at least 10 days with no significant change in size. An increase of d_{hyd} from 190 to 201 nm have been observed by mixing NPCs with lower amounts of P123 (P123/NPCs ratio = 3). Using molar ratio of 1, NPC hydrodynamic diameter was almost unchanged after re-dispersion in THF (from 190 to 192 nm) and following addition of the NPC showed a d_{hyd} of 194 nm with an improvement of the PDI of the suspension.

In general, the results suggest that as the concentration of P123 is increased, the NPC hydrodynamic size in water becomes distinctly higher than the one of the initial NPC in chloroform and the PDI value becomes higher as well, indicating aggregation or formation of P123 micelles in suspension.

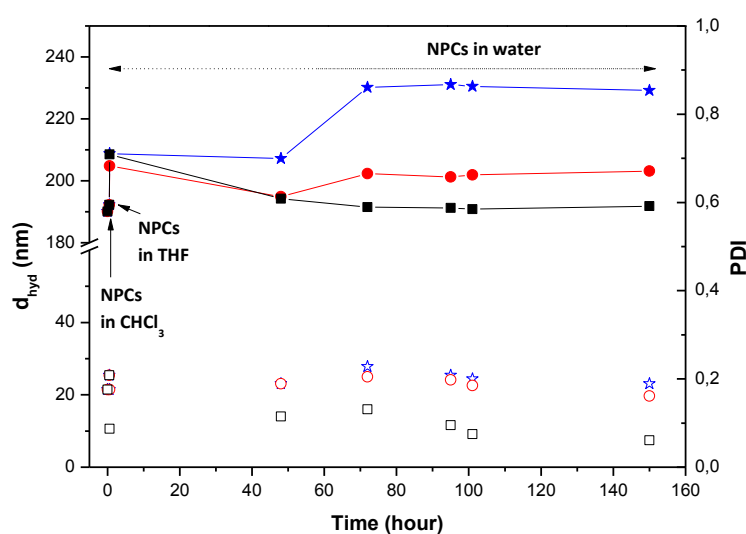


Figure 5- 11 Monitoring of the hydrodynamic size and PDI values overtime of NPC through the phase transfer process using different P123/Fe molar ratios. Filled symbols refer to d_{hyd} (left hand axes) while the unfilled ones refer to PDI values (right hand axes). The P123/Fe suspensions were prepared using (■) 1, (●) 3 and (★) 4 mL of P123 and keeping constant NPC volume (1 mL, 2 mM [Fe]).

P123/Fe molar ratio	d _{hyd} (nm) [PDI]		
	4	3	1
CHCl ₃	190 nm [0.18]		
THF	192 nm [0.21]		
P123 added			
Day 1	209 [0.18]	205 [0.18]	209 [0.09]
Day 2	207 [0.19]	195 [0.19]	194 [0.12]
Day 3	230 [0.23]	202 [0.21]	192 [0.13]
Day 10	229 [0.22]	201 [0.20]	192 [0.11]

Table 5- 7 Effect of P123/Fe molar ratio on the phase transfer process. Monitoring of the hydrodynamic size and PDI values overtime of NPC over the phase transfer process changing the concentration of P123.

In conclusion, for the NPCs coated with P123 it appears that the surfactant concentration used in the phase transfer plays an important role in determining the hydrodynamic size of the resulting NPCs in water. For instance it seems that the best P123:Fe molar ratio for the production of stable monodisperse NPC aqueous suspensions (PDI < 0.13) with unchanged size was found to be 1, using a OA-NPC suspension of 2 mM iron concentration and a P123 solution of 76.5 μ M. At higher mole ratios, NPC suspensions of larger hydrodynamic diameters and PDI values were observed.

5.3.4.2 Effect of DTAB concentration

The hydrodynamic size and PDI values through the phase transfer process of OA-FeO NPCs with changing DTAB/OA-NPCs molar ratio are shown Table 5-8.

In contrast to P123, addition of low equivalents of DTAB causes a much greater aggregation of the NPCs in the aqueous phase. Indeed for DTAB/OA-NPC molar ratio of 0.25, large NPC aggregates accumulated at the bottom of the aqueous phase, but stable NPC with uniform hydrodynamic size remain suspended in the aqueous medium when the molar ratio is increased to 1 to 2, as shown in Table 5-8. At these molar ratios, the hydrophobic interaction between OA-NPC surface and the surfactant is apparently greater so that the resulting DTAB-NPCs are more hydrophilic and they remain stably suspended in the aqueous medium.

A further experiment was undertaken to assess the DTAB-NPC robustness by collecting the NPCs through separation on magnet and dispersing them in fresh MilliQ water. The DTAB-NPC suspension was left on magnet overnight for precipitating the NPCs at the bottom of the vial and was dried in the oven for 1 h at 65 °C under vacuum. The resulting brown slurry was not completely dried and was re-suspended with fresh MilliQ water. DLS data showed that no significant change in the hydrodynamic size and PDI occurred suggesting that the DTAB-NPCs have are reasonably strong even after the drying process.

In conclusion, interestingly the increase of the DTAB onto the NPC surface was found to increase the stability of the resulting NPCs in water since a decrease of the PDI values is observed without any significant change of NPC hydrodynamic size.

DTAB/OA-NPCs molar ratio	d_{hyd} (nm) [PDI]			
	0.25	0.5	1	2
CHCl₃	78.3 [0.13]			
H₂O	101 [0.31]	89 [0.13]	81 [0.07]	81 [0.09]
re-dispersed NPCs	Visible aggregates	92 [0.15]	81 [0.08]	83 [0.11]

Table 5- 8 Monitoring of the hydrodynamic size and PDI values overtime of NPC over the phase transfer process using different DTAB:OA-NPCs molar ratios. The NPC were re-dispersed with fresh MilliQ water after decantation on magnet.

5.3.4.3 Effect of the NPC concentration on P123-NPC preparation

In this experiment three P123-NPCs suspensions were prepared by mixing a fixed amount of polymer (1 mL, 76.5 μM) and variable volumes of 2 mM (iron concentration) OA-NPC suspension (0.5-3 mL) in chloroform. The hydrodynamic size of the NPCs was monitored by DLS throughout the phase transfer process. The d_{hyd} and PDI values obtained at different P123/OA-NPC molar ratios are shown in Figure 5-12 and in Table 5-9.

For 2, 0.5 and 0.33 ratios, accumulation of aggregates at the bottom of the flask was observed following evaporation of the chloroform. However some NPCs remained suspended in the aqueous phase but with a critical increase of the hydrodynamic diameter

and PDI values of the NPCs observed. Indeed the NPC size increased from 190 nm to 301, 235, and 309 nm on mixing OA-NPC volumes of 0.33, 0.5 and 2 mL, respectively. P123-NPCs suspensions prepared using surfactant/OA-NPC ratio of 1 showed a similar size to the initial OA-NPCs size and their PDI seem to improve overtime (PDI<0.1). In conclusion we observed that the polymer coated cluster size increased with increasing NPC concentration.

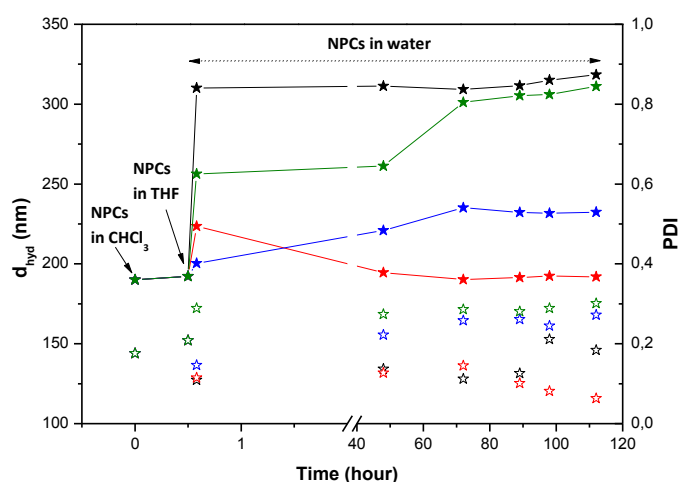


Figure 5- 12 Monitoring of the hydrodynamic size and PDI values overtime of NPC over the phase transfer process using different P123/Fe molar ratios. Filled symbols refer to d_{hyd} (left hand axes) while the unfilled ones refer to PDI values (right hand axes). P123-NPC suspensions prepared using (★) 2, (★) 1, (★) 0.5 and (★) 0.33 surfactant/NPC molar ratios.

P123/Fe molar ratio	$d_{hyd}(nm)$ [PDI]			
	2	1	0.5	0.33
CHCl ₃	190 nm [0.18]			
THF	192 [0.21]			
P123 added	256 [0.29]	224 [0.12]	200 [0.15]	310 [0.11]
Day 2	261 [0.27]	195 [0.13]	221 [0.22]	311 [0.14]
Day3	301 [0.29]	190 [0.15]	235 [0.26]	309 [0.11]

Table 5- 9 Effect of Fe concentration. Monitoring of the hydrodynamic size and PDI values overtime of NPC over the phase transfer process using different P123/Fe molar ratio.

5.3.4.4 Effect of the NPC concentration on DTAB-NPC preparation

The hydrodynamic size and PDI values of DTAB-NPCs prepared by changing DTAB/Fe molar ratio and a fix amount of DTAB (1 mL, 2 μ mol) are shown Table 5-10.

In general an increase of the hydrodynamic diameter of the initial OA-NPCs with increasing the amount of OA-NPCs added is observed. For ratios of DTAB 1 and 2 mL a marginal difference in d_{hyd} of \sim 2-7 nm was observed and the PDI found were below 0.2 in both cases.

DTAB:Fe molar ratio	d_{hyd} (nm) [PDI]			
	2	1	0.66	0.5
CHCl₃	78.3 nm [0.13]			
H₂O	81 [0.07]	83 [0.14]	96 [0.17]	95 [0.23]
re-dispersed NPCs	88 [0.08]	85 [0.20]	98 [0.20]	105 [0.29]

Table 5- 10 Monitoring of the hydrodynamic size and PDI values overtime of NPC over the phase transfer process using different DTAB:Fe molar ratios.

In general, for the preparation of OA-FeO coated with DTAB, it appears that, keeping the amount of DTAB constant, the Fe concentration used in the phase transfer plays an important role in determining the resulting hydrodynamic size of the resulting NPCs in water. The results found suggest that a surfactant/OA-NPCs molar ratio of 1 was the most optimum for the phase transfer as the hydrodynamic diameter of the NPC remained almost unchanged and the clusters had narrow size distribution. For ratios lower and higher of 1, the resulting aqueous suspension show higher both d_{hyd} and PDI values. This may be due to the aggregation or desegregation of the clusters forming polydisperse suspensions.

Finally it was observed for both the synthesis of P123- and DTAB- coated oleic acid stabilized-iron oxide NPCs that parameters such as the surfactant and cluster concentration has a crucial effect on the NPC phase transfer to water. It was found that with increasing the P123 concentration, the resulting NPC size increases while an opposite effect was observed in case of the DTAB surfactant. It was also observed that

the NPC size in water showed higher hydrodynamic size with increasing of the NPC concentration for both surfactants.

5.3.5 Scale up

After demonstrating the stability of aqueous FeO NPC suspensions and the reproducibility of the phase transfer methods, scale up experiments were performed for the synthesis of large volumes of NPC suspensions in water under the optimized conditions. A suspension of 60 mL of oleic stabilized Fe NPCs was phase transferred to water phase through P123 and DTAB coating in Duran glass bottles (Sigma Aldrich). DLS data of aqueous NPC suspensions at large (60 mL) and small (2 mL) scale were measured at room temperature after 50 hours from the preparation and are compared in Table 5-11. Both hydrodynamic diameter and PDI value were measured after 45 days in order to investigate on the stability of the suspensions. Comparing the results achieved at small and large scale, the NPC size is unchanged and slight improvement of the PDI value is observed after covering with both P123 and DTAB. This result shows that it is possible to phase transfer monodisperse NPCs from the organic phase to water at large scale. The hydrodynamic size and PDI values were unchanged for more than one month following the preparation of the NPC aqueous suspensions (Table 5-11).

Final NPC volume (mL)	1		60	
	d_{hyd} 50 hours (nm) [PDI]	d_{hyd} , aged (nm) [PDI]	d_{hyd} , 50 hours (nm) [PDI]	d_{hyd} , aged (nm) [PDI]
NPCs@P123	150.3 [0.08]	153.6 [0.07]	159.6[0.07]	166.4 [0.09]
NPCs@DTAB	61 [0.13]	56.5 [0.16]	58 [0.10]	69.5 [0.09]

Table 5- 11 Phase transfer scale up experiment. In case of the P123 coating experiment, a suspensions of oleic acid stabilized NPCs in chloroform of d_{hyd} of 147 nm (PDI= 0.09) were used ([Fe] = 2.12). The P123:Fe molar ratio of 1 was used. For DTAB coating experiment, OA-NPCs of 57 nm (PDI= 0.18) were phase transferred to aqueous medium ([Fe] = 2.35). A DTAB:Fe molar ratio of 2 was used. An excess of OA of 0.75 was used in both experiments.

5.3.6 Effect of nanoparticle cluster encapsulation on Nuclear Magnetic Resonance Properties

In order to evaluate the potential contrast of the NPC transferred in water and to investigate over their magnetic properties before and after phase transfer, NMRD experiments for NPC dispersed in chloroform and in water were performed and are reported in the following sections.

5.3.6.1 Relaxometric properties of P123-NPC suspensions

The spin-lattice relaxivity as function of ^1H Larmor Frequency for samples of OA-NPC and P123-NPC of similar size are reported in Figure 5-13. The NMRD profile of OA-NPs are also reported for comparison. Table 5-12 reports the spin-lattice and spin-spin relaxivity for OA-NPs, OA-NPCs and P123-NPCs at 16.3 MHz.

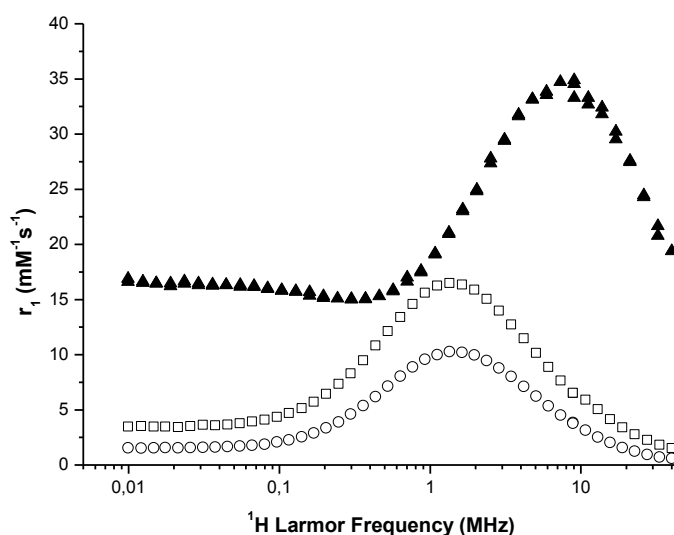


Figure 5- 13 NMRD profile of (\blacktriangle) OA-NPs ($d_{\text{hyd}}= 13$ nm, PDI = 0.052) and (\square) OA-NPCs ($d_{\text{hyd}}= 111$ nm, PDI = 0.113) in chloroform, (\circ) P123-NPCs ($d_{\text{hyd}}= 120$ nm, PDI = 0.105) in water. Measurements performed at 25 °C.

Sample	d_{hyd} (nm) [PDI]	r_1 ($\text{mM}^{-1}\text{s}^{-1}$)	r_2 ($\text{mM}^{-1}\text{s}^{-1}$)
OA-NPs	13 [0.05]	31.0	72.0
NPCs@OA	111 [0.11]	8.4	180.1
NPCs@P123	120 [0.11]	3.6	173.6

Table 5- 12 Hydrodynamic diameter, PDI, spin-lattice and spin-spin relaxivity at 16.3 MHz, 25 °C.

Comparing the NMRD profiles of the NPCs with that of OA-NPs three observations can be pointed out. Firstly, both NMRD profiles of P123 and OA-NPCs show an intense peak at high fields which is characteristic of superparamagnetic NPs. The shape of the relaxivity curves is consistent with SPM theory^[108] discussed in Chapter 1 (section 1.6). Secondly, a shift of r_1 to lower frequency is observed for NPCs because of the greater size of the clusters, as confirmed by DLS. Finally, OA-NPC and P123-NPC profiles show a suppression of r_1 at lower fields and do not show a mid-frequency minimum as in case of primary NPs^[59]. This last observation is due to the strong dipolar interparticle interactions within the clusters in chloroform and in water, and suggests that few primary NPs are present following assembly and phase transfer.

Comparing the P123-NPCs and OA-NPCs NMRD profiles; the shape of the profile is largely unchanged while a suppression of r_1 peak is observed (~38 %) after phase transfer of the NPCs. This observation may be due to the limited diffusion of molecules of water towards the cluster surface which is fully covered by the polymer shell and also due to the difference in ^1H content in CHCl_3 solvent. The key point is that the shape is unchanged demonstrating that the internal magnetic organization of the clusters is unchanged suggesting that no difference in order or density of the NPCs following phase transfer to water. The assembly of the NPs results in a significant increase in the r_2 values from $72 \text{ mM}^{-1}\text{s}^{-1}$ for OA-NPs, to $180 \text{ mM}^{-1}\text{s}^{-1}$ for 111 nm OA-NPCs, to $173.6 \text{ mM}^{-1}\text{s}^{-1}$ for P123-NPCs at 16.3 MHz (Table 5-12). According to SPM theory, the r_2 value is predicted to increase with the cluster size because of the increase of the magnetization of the system. This is consistent for clusters dispersed both in chloroform and in water. Following assembly r_1 value decreases from 31 to 8.4 to $3.4 \text{ mM}^{-1}\text{s}^{-1}$ for OA-NPs, OA-NPCs and P123-NPCs respectively at 16.3 MHz. This result is expected because, following the particle assembly the NPC itself can be considered a large magnetized sphere where interparticle interactions produce a high magnetic field gradient and consequently a dominant r_2 effect^[108]. It is interesting that the r_2 value is found to be independent of the coating but the r_1 value is 2.3 times higher for oleic acid stabilised NPCs than for P123 coated NPCs. According to Qin and co-workers^[64b], the coating of iron oxide core with Pluronic molecules provokes a dual effect that are the maintenance of the spin-spin relaxation rate (r_2) and the decrease of the spin-lattice relaxation rate (r_1). The decrease of r_1 can be explained as following. The subsequent coating with P123 polymer further increases the thickness of the hydrophobic layer all around the cluster that obstruct the

water molecules from contact with the magnetic core, which result in a decreasing of the r_1 value for P123-NPCs.

Figure 5-14 shows the NMRD profiles of aqueous suspensions of P123-NPCs of different size. The NMRD profile of an aqueous suspension of DTAB-NPs is also reported for comparison. The suspensions show a superparamagnetic behaviour because of the intense r_1 peak at high fields while the r_1 minimum in the mid-frequency range is absent again suggesting that few nanoparticles are present in suspension. As the NPC size increases the r_1 maximum shifts to lower frequencies as expected, while the r_1 value decreases at all fields. This behaviour is explained by the fact that at higher NPC sizes the diffusion of water is limited to the surface of the NPs towards the centre of the cluster contribute less to the resulting lattice relaxivity^[59] and this effect is exaggerated for larger sizes.

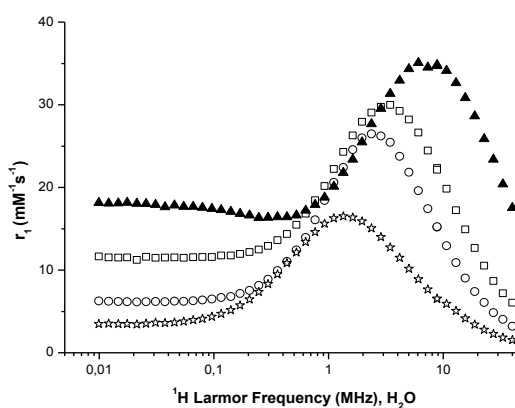


Figure 5- 14 NMRD profiles of P123-NPCs of different sizes; (□) 50, (○) 70 and (☆) 120 nm. (▲) 14 nm DTAB-NPs.

Figure 5-15 reports the plot of r_1 , r_2 and r_2/r_1 ratio as function of P123-NPCs. It can be seen that r_1 decreases slightly with increasing NPC size as noted above, r_2 shows the opposite trend which can be attributed to the larger magnetic moment of larger NPCs. The r_2/r_1 ratio increases with increasing NPC size as expected, given by the significant change in r_2 . The same trend was observed by Berret et al^[109] for iron oxide NPCs coated with poly(trimethylammonium ethylacrylate methyl sulfate)-b-poly-(acrylamide). Ai and co-workers^[110] have also obtained similar results for magnetic nanoparticles encapsulated into the hydrophobic cores of 20-100 nm polymeric micelles.

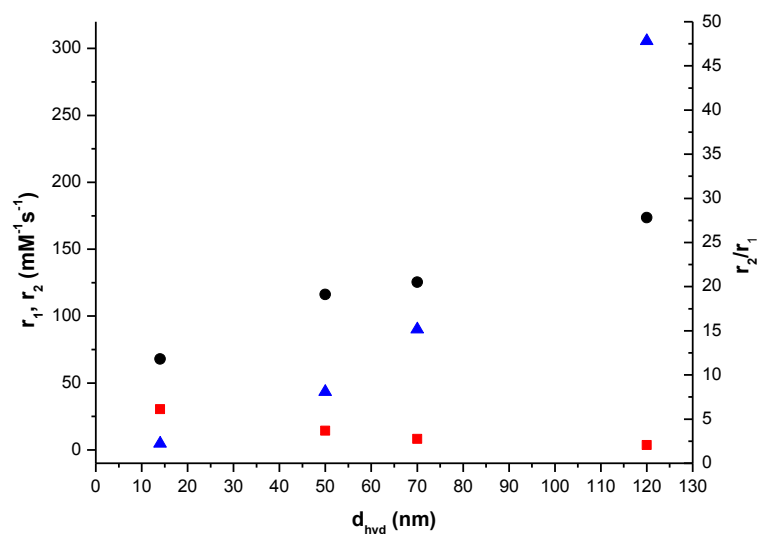


Figure 5- 15 (Left hand axes) (■) r_1 and (●) r_2 and (right hand axes) (▲) r_2/r_1 ratio as function of P123-NPCs size at 16.3 MHz, 25 °C.

5.3.6.2 Relaxometric properties of DTAB-NPC suspensions

The spin-lattice relaxivity as a function of 1H Larmor frequency for samples of OA-NPCs and DTAB-NPCs of similar size is reported in Figure 5-16. The NMRD profile of OA-NPs are also reported for comparison. Table 5-13 reports the spin-lattice and spin-spin relaxivity for OA-NPs and NPC before and after phase transfer through DTAB coating at 16.3 MHz (25 °C).

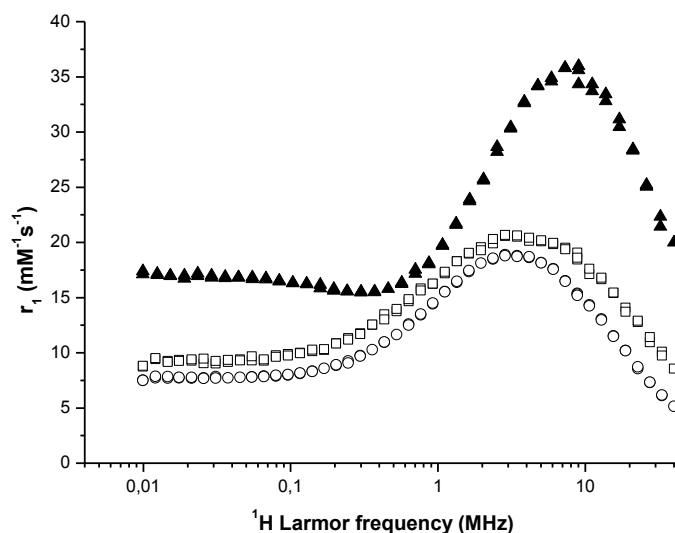


Figure 5- 16 NMRD profile of (▲) OA-NPs (d_{hyd} = 13 nm, PDI = 0.05), (□) OA-NPCs (d_{hyd} = 151 nm, PDI = 0.10), (○) P123-NPCs (d_{hyd} = 157 nm, PDI = 0.10).

Sample	d_{hyd} (nm) [PDI]	r_1 ($\text{mM}^{-1}\text{s}^{-1}$)	r_2 ($\text{mM}^{-1}\text{s}^{-1}$)
OA-NPs	13 [0.05]	31.0	72.0
NPCs@OA	151 [0.10]	16.0	201.9
NPCs@DTAB	157 [0.10]	14.3	191.8

Table 5- 13 Hydrodynamic diameter, PDI, spin-lattice and spin-spin relaxivity @ 16.3 MHz, 25 °C.

Both the NMRD profiles of NPCs before and after phase transfer show characteristic features of superparamagnetic behaviour and no r_1 minimum is observed in the mid-frequency range, the reasons were mentioned previously. Also in this case, a shift of r_1 peak is observed towards lower frequencies confirming the formation of larger clusters with no evident presence of primary NPs in suspension because of the absence of the minimum in the mid- range frequencies as previously stated. Even after coating with DTAB the NPC show the same NMRD profile shape as in the chloroform suspension with a slight suppression of the r_1 value at all fields. The assembly of the OA-NPs results in a significant increase in the r_2 values from 72 $\text{mM}^{-1}\text{s}^{-1}$ for OA-NPs, to 201 $\text{mM}^{-1}\text{s}^{-1}$ for 151 nm OA-NPCs, to 191.8 $\text{mM}^{-1}\text{s}^{-1}$ for DTAB-NPCs at 16.3 MHz. There is little change of r_2 with this surfactant/cluster combination, as was the case for the P123 coating.

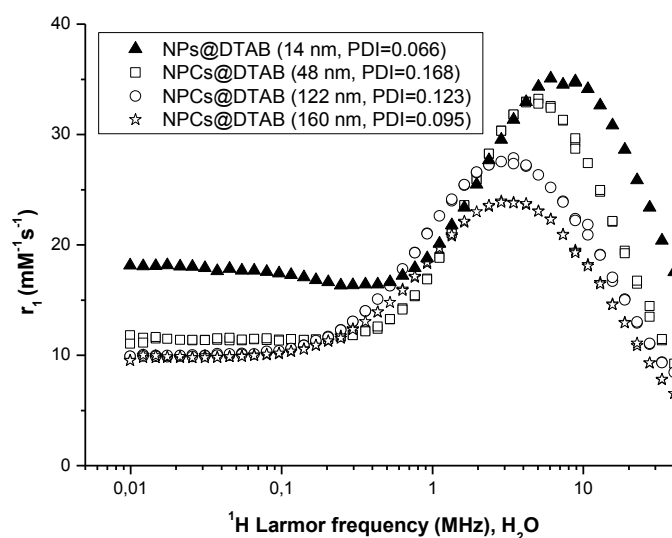


Figure 5- 17 NMRD profiles of P123 NPCs of different sizes; (\square) 49, (\circ) 70 and (\star) 120 nm. (\blacktriangle) 14 nm DTAB-NPs.

Figure 5-17 shows the NMRD profiles of different sized DTAB-NPCs suspended in water. The NMRD profile of an aqueous suspension of DTAB-NPs is also reported for comparison. The profiles of the NPC suspension do not show an r_1 minimum in the mid-frequency range and they exhibit superparamagnetic properties. Additionally as the NPC size increases the r_1 maximum shifts significantly to lower frequencies while the r_1 value decreases at all fields. This observation can again be attributed to the increased diffusional correlation time for the larger clusters diffusion of water which is limited to the surface of the NPs assembled and densely packed.

The r_1 , r_2 and r_2/r_1 ratio of DTAB-NPC suspensions as a function of size are shown Figure 5-18. A similar trend to that observed for P123-NPCs was observed for aqueous DTAB-NPC suspensions. It can be seen that r_1 decreases with increasing NPC size while r_2 and the r_2/r_1 ratio increase. As before these effects are because of surface limitations, total magnetization per cluster, for r_1 and r_2 respectively and because the latter dominates the values of the ratio.

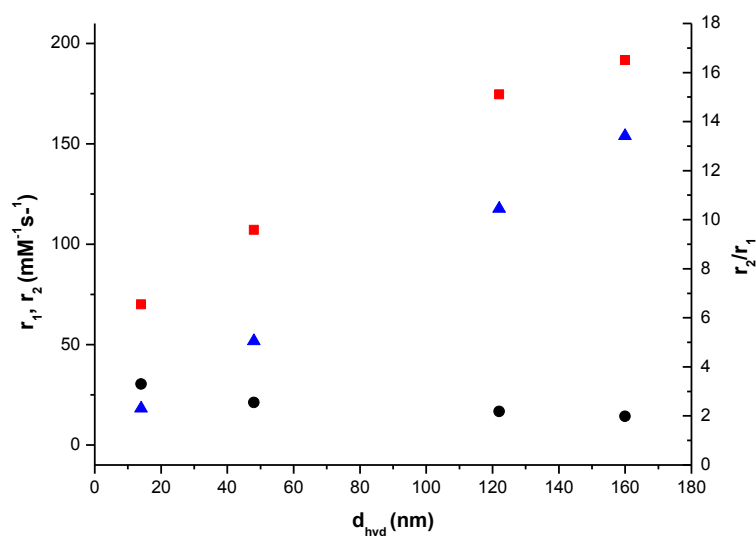


Figure 5- 18 (Left hand axes) (●) r_1 and (■) r_2 and (right hand axes) (▲) r_2/r_1 ratio as function of DTAB-NPCs size at 16.3 MHz, 25 °C.

5.3.6.3 Comparison of P123-NPC and DTAB-NPC magnetic properties

The relaxivity values measured at 16.3 MHz for clusters coated with P123 and DTAB of similar hydrodynamic size are briefly summarised in Table 5-14. If compared, both P123-NPCs and DTAB-NPCs show a decrease of the spin-lattice relaxivity (r_1) with increasing

of the cluster diameter as expected. This is because just the NPs of the outer layer of the cluster contribute to the relaxation of the diffusing molecules of the water. In case of P123-NPCs a more accentuated decrease of r_1 is observed (~ 75 %) and this may be attributed to greater thickness of the polymer shell formed around the cluster (as also suggested by FESEM analysis) that limits the interaction between the cluster surface and the water molecules.

The two cluster types are in agreement in the trend of r_2 with the changing of hydrodynamic diameter. Indeed both NPC types show a significant increase of the spin-spin relaxation rate (r_2) with increasing of the cluster size as the magnetic moment of larger NPCs is higher.

In case of r_2/r_1 ratio the NPC types show an opposite trend as a result of the r_1 and r_2 trend.

Surfactant	$d_{\text{hyd, NPCs}}$ (nm)	r_1	r_2	r_2/r_1
P123	50	14.4	116.1	8.1
DTAB	48	21.2	107.2	5.1
P123	120	3.6	173.6	47.8
DTAB	122	16.7	174.6	10.5

Table 5- 14 Summary of the r_1 , r_2 and r_2/r_1 ratios of the NPCs coated by P123 and DTAB at 16.3 MHz.

5.3.7 Magnetic fluid hyperthermia

In order to assess the heating efficiency of the NPCs in aqueous medium, MFH experiments were performed on P123- and DTAB- coated clusters of different hydrodynamic diameters which were compared to aqueous suspensions of 14 nm DTAB-NPs. Hyperthermia experiments were carried out in triplicate using three different samples which were exposed to AC-magnetic field of intensity 15.9 kA/m with a frequency of 527 kHz. The iron concentrations were determined in triplicate by ICP-AES and the mean values were used to calculate SAR values from the initial slope at the time dependent temperature curves, using the approach reported in Chapter 2 (Equation 2.14).

Temperature-time curves for both P123- and DTAB- coated NPC suspensions are reported in Figure 5-19.

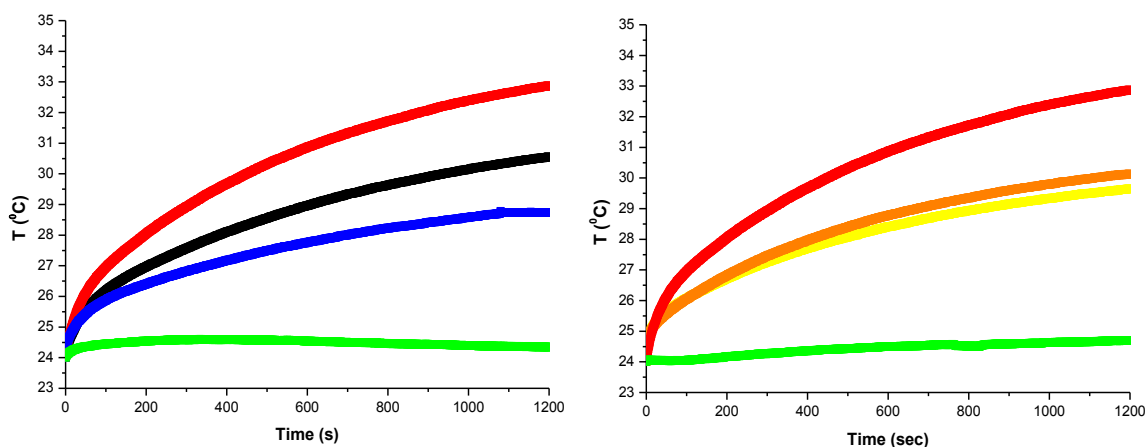


Figure 5- 19 Temperature–time curves of suspensions of different NPC sizes of (left) P123-NPCs and (right) DTAB-NPCs in water under the AC magnetic field (527 KHz, 15.9 KA/m). (Left) (red) 120, (black)70 and 50 nm P123-NPCs, (green) DTAB-NPCs. (Right) (red) 122, (orange) 85 and (yellow) 55 nm DTAB-NPCs; (green) 14 nm DTAB-NPCs.

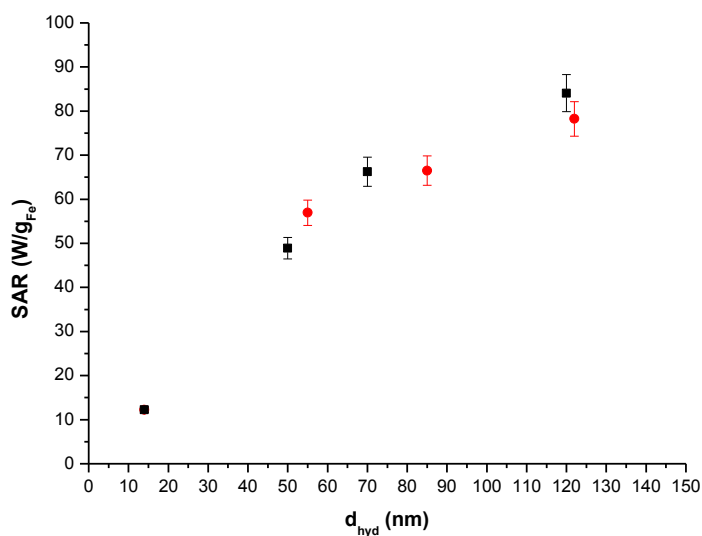


Figure 5- 20 SAR values of suspensions of (■) P123-NPCs and (●) DTAB-NPCs as function of cluster size. The error bars refer to standard deviation of three measurements performed using three different samples.

The SAR values of P123-NPCs were evaluated using coated clusters of hydrodynamic size of 49, 70 and 120 nm and the iron concentration of the samples was in the range of 0.85-1.1 mM. The plot of the SARs obtained in function of P123-NPC size is shown in Figure 5-20. Apparently, the heating efficiency of the aqueous suspensions increases on

forming NPCs and on increasing NPC size. Indeed the average SAR values for samples of P123-NPCs of 50, 70 and 120 nm were 44, 73.4 and 91.8 W/g_{Fe} respectively while for the sample of dispersed DTAB-NPs the SAR was 12 W/g_{Fe}.

The SAR values for DTAB-NPCs suspensions of hydrodynamic diameter of 55, 85 and 122 nm (2.5 – 3 mM, Fe) are also shown in Figure 5-19. As in the previous case an increase of the SAR values with increasing NPC size was observed. The SAR increased from 57 to 81 W/g_{Fe} increasing the DTAB-NPCs size from 55 to 122 nm. These findings are in agreement with the results observed for self-assembled iron oxide nanocubes^[111] confirming that NP separation and so dipolar interactions are strictly correlated to the resulting SAR. The physical reason for the increase of SAR with increasing of the NPC size could be explained by considering the magnetic properties of the NPs and the particle-particle dipolar interaction within the clusters. The dipole-dipole particle energy for spherical interacting particles can be described by the Equation 5-1, reported by Grzybowski and co-workers^[112]:

$$\Phi_{magn}(d) = \frac{m_1 m_2}{4\pi\mu_0 d^3} \quad \text{Equation 5-1}$$

where m_1 and m_2 are the magnetic moments of two neighboring NPs and d is the distance between their centers. Increasing the NPC size increase the number of NPs per cluster and, as shown by NMRD, increases the effective magnetocrystalline anisotropy energy thorough increased dipolar coupling. Assuming that the SAR is largely determined by hysteresis losses^[113] the transition towards ferromagnetism should result in increased squareness of the magnetometry response. Indeed the internal area of this curve is related to the magnetic energy that can be stored in the system, and that is indirectly related to the hyperthermic efficiency. Confirmation of this hypothesis could be obtained by magnetometry analysis, however this is not currently available to us.

In general, aqueous suspensions of FeO NPCs showed higher SAR values compared to primary NPs dispersed in water independently of the surfactant applied. The highest SAR values obtained were 92 and 81 for 120 nm P123-NPCs and 122 nm DTAB-NPCs respectively. These values are higher or comparable to the ones found in literature for

similar NPC size and type [113-114]. For example, Dutz and co-workers [113] reported SAR value of 60 W/g for 158 nm carboxymethyl dextran stabilized iron oxide NPCs. Nevertheless, the difference in SAR between the two surfactants used in the phase transfer is small therefore we can conclude that the nature of the surfactant does not have a significant effect on the heating efficiency of the clusters.

5.3.8 Biotesting

A preliminary screening of the toxicity of the aqueous suspension of clusters of different sizes coated with both DTAB and P123 was undertaken in collaboration with Dr. Andrew Kellett (Dublin City University). DTAB-NPCs samples of 53 and 122 nm and P123-NPCs of 57 and 116 nm were prepared and tested using two human cell lines, leukemic monocyte (THP-1) and liver carcinoma cells (HepG2). The cell viability results after different periods of incubation and different iron concentrations are shown in Figure 5-21. Samples of aqueous NPC suspensions with an iron concentration ranging from 0.1 to 100 μM were incubated with THP-1 and HepG2 cell lines for 24 and 72 hours.

The results showed increased toxicity is shown for clusters coated by DTAB at all concentrations in both cell lines. The reason can be attributed to the nature of the surfactant. In case of P123 coated NPCs some toxicity is observed at high concentrations for 116 nm NPCs. The reason for this is currently under investigation.

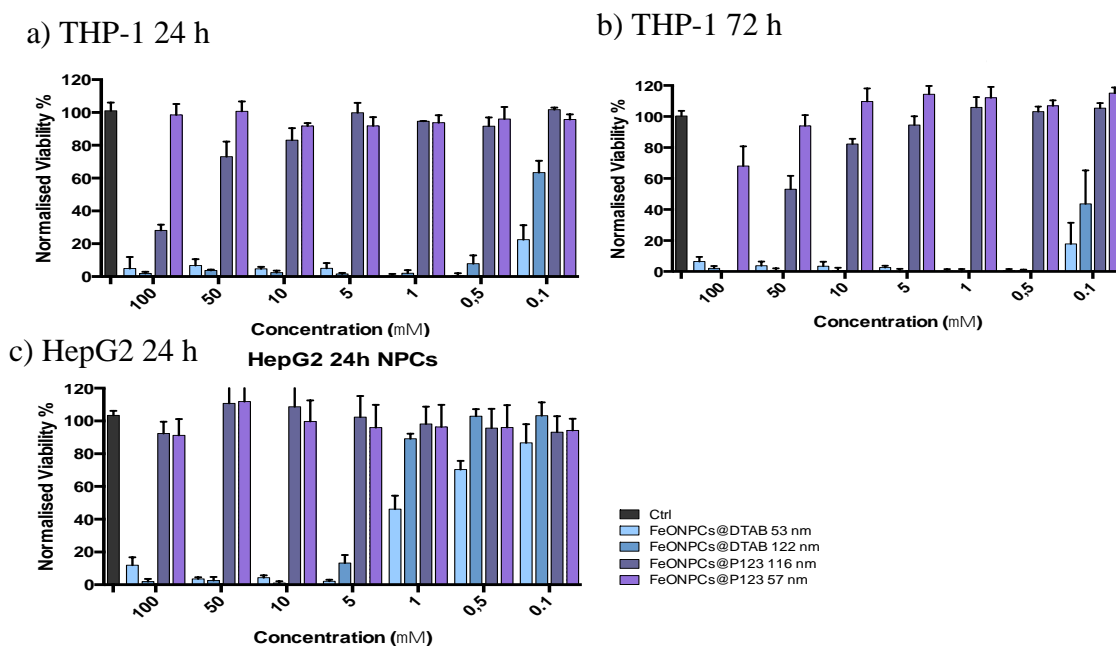


Figure 5- 21 Cell viability of (a,b) THP-1 and (c) HepG2 cells after 24 and 72 hour incubation with P123-NPCs and DTAB-NPCs at various iron concentrations.

5.4 Conclusions

In summary, we have reported two reproducible and up-scalable methods for the phase transfer of pre-formed oleic acid stabilized NPCs (produced by WI-CSD approach) to aqueous medium by coating with partially hydrophilic surfactants.

The resulting aqueous suspensions were characterized and compared by dynamic light scattering, infrared spectroscopy, microscopy, magnetic fluid hyperthermia and relaxivity measurements. ATR-IR, DLS and FESEM analysis confirmed the monodispersity, stability and the conservation of the size in most cases of the NPCs in water following phase transfer. The surface charge found for P123 coated clusters was of -17.4 mV while the NPC@DTAB showed zeta potential of +34.3 mV. ATR-IR analysis indicates the presence of both surfactants on the cluster surface but also that P123 forms a more compact shell than DTAB coated NPCs which seem to have a more loose NP packing. Low polydispersity was observed after coating with P123 and DTAB in PBS medium but and high yield were achieved only in case of DTAB coated NPCs (~ 91 %) while for P123 stabilized NPC the yield was lower (~ 54 %).

For the NPCs coated with P123 it appears that the surfactant and NPC concentration used in the phase transfer affects the hydrodynamic size of the resulting NPCs in water. The best P123:Fe molar ratio for the production of stable monodisperse NPC aqueous suspensions (PDI < 0.13) with unchanged size was found to be 1, using a OA-NPC suspension of 2 mM iron concentration and a P123 solution of 76.5 μ M. At higher mole ratios, NPC suspensions of larger hydrodynamic diameters and PDI values were observed. Interestingly increasing DTAB content was found to increase the stability of the resulting NPCs in water, since a decrease of the PDI values is observed without significant change of NPC hydrodynamic size. The best DTAB:Fe molar ratio for the production of stable monodisperse NPC aqueous suspensions (PDI < 0.13) with unchanged size was found to be 1 and 2. Moreover, we also observed that the size of the resulting nanostructures was increased with increasing NPC concentration in the phase transfer step. This effect was stronger for P123 stabilized NPCs. Scale up experiments have shown that it is possible to phase transfer monodisperse NPCs from the organic phase to water using up to 60 mL of NP suspension.

According to NMRD data, the clusters maintain their superparamagnetic behaviors even after their phase transfer to water. Both P123-NPCs and DTAB-NPCs show a decrease

of the spin-lattice relaxivity (r_1) with increasing of the cluster diameter as expected. This is because only the NPs of the outer layer of the cluster contribute to the relaxation of the diffusing water. In case of P123-NPCs a more pronounced decrease of r_1 is observed (~ 75 %) and this may be attributed to greater thickness of the polymer shell formed around the cluster that restricts the interaction between the cluster surface and the water. The two cluster types show the same trend of increasing in r_2 with the increasing hydrodynamic diameter arising from increased cluster magnetic moment. The highest values of r_2 obtained were 173.6 and 191.8 $\text{mM}^{-1}\text{s}^{-1}$ for 120 nm P123-NPCs and 157 nm DTAB-NPCs, respectively. Berret and co-workers^[109] obtained similar results ($162 \pm 4 \text{ mM}^{-1}\text{s}^{-1}$) for 170 ± 20 nm iron oxide NPCs coated with poly(trimethylammonium ethylacrylate methyl sulfate)-b-poly-(acrylamide). Hence the response of these materials is in the expected range.

NPCs coated by P123 and DTAB showed higher heating efficiency than primary NPs and comparable SAR values to the ones reported in literature^{[115] [113]}. For example, Dutz and co-workers^[113] reported SAR value of 60 W/g for 158 nm carboxymethyl dextran stabilized iron oxide NPCs. The highest SAR values obtained were 92 and 81 for 120 nm P123-NPCs and 122 nm DTAB-NPCs, respectively. The SAR values were found to increase with increasing NPC size. This was attributed to increased average inter-particle dipolar interactions within the larger clusters. The SAR values were found to be independent of the surfactant used.

P123-NPCs showed lower cytotoxicity (particularly at 0.1 – 5 μM of iron) than that showed by DTAB-NPCs which were really toxic even at lower iron concentrations. Nevertheless, we believe that it is possible to utilize a wide variety of surfactants of low molecular weight with different functionally terminated groups, which can be used to improve biocompatibility and to enable further functionalization with drugs for example. An example of other surfactants that could be used would be low molecular weight hydrophilic ligand including folic acid (~ 441 g/mol), PEG 600 (~ 570 - 630 g/mol) (coupled or singularly) which according to previous studies^[114, 116] exhibits high biocompatibility and eventually would not change the final size of the NPCs in water.

The phase transfer protocols described here could also be applied to binary NPCs, as shown in Chapter 3, or other hydrophobic nanoassemblies.

Chapter 6
**Preparation and characterization of size
controlled lipid stabilized magnetic nanoparticle
and nanoparticle clusters**

6.1 Introduction

Since their discovery in 1965 by A. Bangham^[117], liposomes were studied in detail over the last decades because of their biocompatibility, long blood circulation half-life and permeability. Great interest was addressed towards magnetoliposomes^[118] which are lipidic vesicles that can incorporate magnetic NPs and can have many advantages. By encapsulating magnetic NPs they can provide good magnetic properties so that they can be applied as contrast agents in MRI. Secondly, they can retain the advantages of conventional liposomes is that encapsulate a large variety of hydrophilic and hydrophobic drugs and finally they can be functionalized with ligands for targeting. The most studied magnetoliposomes are the FeO NP based ones which are largely used in pre-clinical setting for the development of magnetic hyperthermia because their metabolic pathway is well known and their low toxicity^[119]. The current challenges for MFH applications are the development of stable nanostructures with long blood half-life that accumulate specifically in the tumorous cells. For instance iron FeO NPs encapsulated within PEG grafted vesicles have been reported to be highly efficient MRI contrast agent^[119b]. The modification of the liposome surface with PEG reduces the opsonization of the liposome extending its circulation half-life^[120]. The physiological factors that largely define the magnetoliposome efficiency for application are their size and formulation, factors that determine circulation time, permeability, encapsulation volume and biological fate.

Solid lipid nanoparticles (SLN) were introduced for the first time at the beginning of the 1990s as an alternative carrier system to liposomes and polymeric NPs by Muller^[121] and Gasco^[122] in Turin. SLNs consist of biodegradable physiological lipids which are solid at room and physiological temperature. The solid state of these particles is of prime importance, as it reduces the mobility of the eventual incorporated drug/NPs and thus prevents leakage from the carrier. Compared to the traditional liposomes and other nanocarrier systems, SLNs present several advantages including lower cytotoxicity, longer physical stability and a relative cost-effective scale-up synthesis. A potential problem of SLNs in drug delivery application is that their lipid molecules can crystallize forming compact 'brick molecules' that give rise to inefficient and inconsistent the drug release from the SLN structure. This issue can be solved by blending different lipid molecules to form nanostructured lipid carriers (NLC) that have imperfections to accommodate the drug. Recently it has been demonstrated that the inclusion of iron oxide NPs within lipid-based matrix can report interesting benefits for hyperthermia against colon cancer^[123] and introduces several advantages including the prevention of

agglomeration *in vitro* and *in vivo* and possibility to include further therapeutic functionalities^[124]. Such lipid stabilized NPs have been reported to be biodegradable, and well tolerated materials^[125] that can find promising applications as carriers in the drug delivery^[126] and as contrast agents in MRI^[127]. Therefore, lipid stabilized magnetic nanoparticle or nanoparticle clusters remain a strong research focus both in industry and in academia because of the clinical success of a range of delivery vehicles arising from their relative biocompatibility. However, as mentioned before the challenge of producing formulations which are applicable for multiple therapeutic molecules and which are colloiddally and chemically stable remains. The aim of this work is to develop biocompatible size-controlled lipidic nanostructures starting from a single magnetic iron-oxide nanoparticle or from nanoparticle clusters. It must be emphasized that in these materials there is no aqueous lumen. Hence the application are as MRI-tunable agents for delivery of hydrophobic moieties. Particularly we are using the three approaches reported in Figure 6-1.



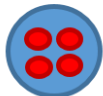
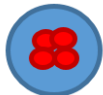
	Name	d_{hyd} (nm)	Application
	Solid Lipid Nanoparticle (SLN)	> 20	Delivery formulations
	Lipidic- NP (LNP)	< 30	T ₁ -wighted MRI agent Drug delivery
	Lipidic-NPC Aggregate (LNPA)	> 60	T ₂ -wighted MRI agent Drug delivery
	Lipidic-NPC (LNPC)	> 60	T ₂ -wighted MRI agent Drug delivery

Figure 6- 1 Schematic representation of solid lipid nanoparticle (SLN) and biocompatible magnetoliposomes and their potential applications.

The first approach used was for the preparation of lipid stabilized dispersed magnetic nanoparticles (LNPs) which are formed from a single magnetic core and a thin layer of lipids. If they maintain full dispersion, such liposomes can find applicability as T₁-agents for MRI and drug delivery carriers.

The second approach used was for the preparation of lipid stabilized dispersed magnetic nanoparticle clusters of controlled size and controlled internal architecture. Two types of lipid stabilized magnetic clusters were investigated: clusters of LNPs (LNPA) which were formed from the aggregation of dispersions of lipid stabilized nanoparticles and lipid

encapsulated nanoparticle clusters (LNPCs) produced by the lipid stabilization of pre-formed clusters of controlled size. These lipid based structures could find application in MRI as T₂- contrast agents and for drug loading. The oleic acid stabilized iron oxide NPCs used for lipid encapsulation were synthesized by the competitive stabilizer desorption method (CSD) which offers significant advantages over other methods that can be found in literature for the formation of size-controlled clusters. Firstly, the size dispersity of the original NP suspension remain unaltered throughout the whole clustering process. Secondly, as shown in Chapter 3 the process can be blocked at any NPC size in the range 40-500 nm.

The formulation of the lipidic component used for lipidic nanostructure synthesis is based on mixture of cholesterol esters (CLABP), phosphatidylcholine (PC, surfactant), bile salts (Na-taurocholate) and polyethylene glycol (PEG, co-surfactant). These “ingredients” were chosen because they never have been studied before for NP encapsulation and because of their favorable temperature profile and the broad range of compositions possible which facilitates optimization for particle dispersion, high monodispersity and good stability over time and in physiological buffers. Cholesterol-like lipids have been also chosen in order to reduce the crystallization of the solid lipidic matrix which as mentioned above could cause difficulties in triggered drug release.

We aimed then to load LNP with an anti-inflammatory and immunosuppressive drug in order to evaluate LNPs as potential drug carriers. Dexamethasone acetate (DxAc) was chosen because of its favorable hydrophobicity [128]. The aim was to test whether enhancement of the temperature obtained by applying a magnetic field can affect the drug release profile. To assess the DxAc-LNPs as drug platforms, drug released studies were performed by alternate magnetic fields (Figure 6-2).

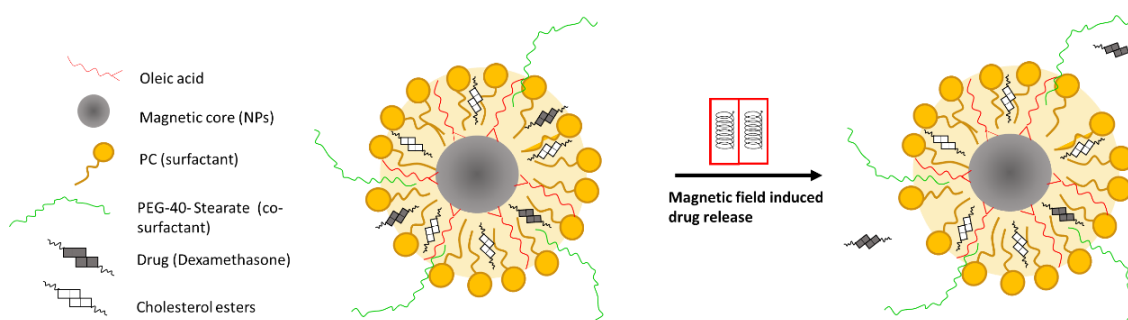


Figure 6- 2 Schematic representation of LNP structure and drug release after magnetic field application.

In this work a novel preparation of lipid stabilized magnetic nanoparticles (LNPs) and nanoparticle clusters (LNPCs) of controlled size with optimized internal structure will be presented. In the first part of the chapter, the lipidic nanostructure suspensions will be characterized by infrared spectroscopy, DLS, the magnetic resonance properties will be assessed using NMRD before and after magnetic chromatography. In the second part of the chapter the lipidic nanostructure heating efficiency and drug release studies through MFH will be assessed. Finally, a preliminary assessment of toxicity and cellular uptake of optimized magnetolipidic nanomaterials will be included.

6.2 Materials and methods

6.2.1 Materials

Iron (III) acetylacetonate, Fe(III)(acac)_3 (purity $\geq 99.9\%$), benzyl alcohol (BA $\geq 99.0\%$), CHCl_3 ($\geq 99.0\%$), oleic acid (OA, $\geq 99.0\%$) were purchased from Sigma Aldrich Ltd Ireland; soy phosphatidylcholine (PC, purity 92% Epikuron200) and 1-butanol were purchased from A.C.E.F. s.p.a. Italy; cholesterol esters (Acetate and palmitate CE, purity 95%) 2-phenylethanol, PEG 40 Stearate were purchased from Sigma Aldrich s.r.l. Italy; cholesteryl butyrate was purchased from Zentek srl Italy and sodium taurocholate was purchased from P.C.A. s.p.a. Italy.

6.2.2 Synthesis of iron oxide nanoparticle

Oleic acid stabilized iron oxide nanoparticles were synthesized using the Pinna method already reported in Chapter 3.

6.2.3 Synthesis of iron oxide nanoparticle clusters

Iron oxide nanoparticle clusters were produced by the WI-CSD method reported in Chapter 3. Suspensions of NPCs in chloroform of iron content of 2-5 mM and volumes of typically 40-60 mL were produced for each NPC size and used for lipid encapsulation.

6.2.4 Lipid encapsulation of magnetic nanoparticles and nanoparticle clusters

NP and NPC encapsulation in a lipidic matrix was performed by Nanovector srl (Turin, Italy). The procedure used will be outlined in short in the following sections.

6.2.4.1 Preparation of aqueous suspensions of LNPs

In a typical synthesis 22.5 mg of phosphatidylcholine (PC), 9 mg of cholesterol esters (CE, cholesteryl acetate, butyrate, palmitate weight ratio 1:1:1:1), and 8 ml of CHCl_3 suspension of oleic acid stabilised NPs (116 mM) in were mixed into a 2-neck round bottom flask then the CHCl_3 was evaporated by N_2 flow at 65 °C by a rotavapor until a brown slurry is formed. While keeping the temperature at 65 °C, 58.35 mg of 1-butanol and 4.08 mg of 2-phenylethanol were added to the vial and the resulting mixture was vortexed. Simultaneously 8 mg of sodium taurocholate, 25 mg PEG-40 stearate were dissolved in 1 ml of MES buffer (2-(N-morpholino)ethanesulfonic acid, 50 mM) which was previously degassed by N_2 flow. The aqueous suspension was brought at 65 °C and then added to the iron oxide-lipid mixture and the final microemulsion was vortexed and kept at 65 °C. The micro-emulsion was dispersed in 10 ml MilliQ water at 4 °C and mechanically stirred. The resulting aqueous LNP suspension is usually filtered at 0.7 μm then washed 3 times by tangential ultra-filtration device, with 100 KDa cut off regenerated cellulose membrane, and finally filtered (pore size of 0.2 μm). Formulation can be concentrated (by tangential filtration) to obtain specific higher level of iron. Size exclusion chromatography was applied to determine size and excipients/iron distribution.

6.2.4.2 Preparation of aqueous suspensions of LNPA

Unlike LNP suspension preparation, LNPA micro-emulsions were dispersed in warm MilliQ water (~65 °C) while the rest of the synthetic procedure for magnetic core encapsulation is unchanged.

6.2.4.3 Formation of aqueous suspensions of LNPC

LNPC suspensions were prepared using typically 25 mL NPCs of 8 mM of iron content. The procedure for NPC encapsulation with lipids is similar to the one used for the preparation of LNP suspensions with the only difference that the suspensions was kept at

28 °C during the evaporation of chloroform at the rotavapor, as temperature in presence of used surfactants caused disruption of clusters into single NPs. (Micro)emulsion is obtained after adding usual external water phase, same as previously described, taking advantage of solvents at 28°C (avoiding lipid melting): it is then dispersed into water at 15°C, where lipid layers form for solvent diffusion.

6.2.5 LNP drug loading

The loading of model drug dexamethasone acetate (purchased from Sigma Aldrich srl Italy) in lipid layer was carried out by simple adding drug into hydrophobic phase in process. In a typical LNP-DxAc preparation, 3.6 mg of dexamethasone acetate was added iron oxide and cholesterol esters mixture at 65 °C. DxAc-LNPs filtered at 0.7 µm showed 97% recovery of DxAc (versus theoretical), while applying TFF three times at 100 kDa the recovery was only of 37%; this is probably due to reduced volume of lipid layer. By filtering with pore size of 0.2 µm, an 83% recovery of DxAc was obtained recovery versus previous filtration. For further concentration by TFF (100 kDa membrane), a reduction of volume (3,2 to 1) showed a DxAc recovery of 72% (vs filtrated at 0.2 µm) and the final DxAc concentration was 0.194 mg/mL while the final iron concentration was 7.54 mg/mL (total iron recovery 88% versus theoretical).

Typically 50 µl of the stock suspension of LNP-DxAc was first diluted with MilliQ water, analyzed by the DLS and then the magnetic properties were investigated by NMRD technique. Normally 1 mL of the stock suspension was used for drug delivery study.

6.2.6 Magnetic chromatography

The experimental set up used for magnetic chromatography is shown in Figure 6-3. A peristaltic pump with variable flow rates and a 1/8 inch inner diameter tubing packed with ~50 mg of steel wool was placed in the middle of electromagnet poles. The liposome suspensions were injected in the tubing at a fixed flow rate of 8 mL/Hour at a field of 61 MHz (1.41 T) and all the magnetic material was retained on the magnetized steel wool (retentate) while the lipidic diamagnetic material was washed off through the tubing (fraction). The electromagnet was then switched off and the retentate was collected by pumping fresh MilliQ water through the system to re-disperse the magnetic material at the same fixed flow rate. The final retentate was collected for further analysis.

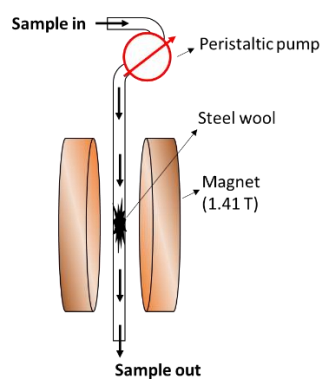


Figure 6- 3 Schematic representation of the experimental set up of magnetic chromatography.

6.2.7 Characterization

The liposomes were characterized by DLS and NMRD as described in Chapter 2.

Total iron content was determined by ICP-AES as described in Chapter 2. To prepare the samples for analysis, we used the procedure described in Chapter 2.

Attenuated total reflectance infrared (ATR-IR) spectra were recorded on a Spectrum GX FT-IR System (Perkin Elmer; Norwalk, CT, USA). The SLN suspensions were first dried by freeze drier (Millrock, Kingston, NY, USA) and then placed on the face of a diamond crystal. An average of twelve scans were recorded over a 650-4000 cm^{-1} spectral range for each sample.

Magnetic fluid hyperthermia (MFH) studies were performed on a magneTherm™ system (Nanotherics, Newcastle, UK). In a typical MFH experiment, a volume (0.5-1 mL) of SLN suspension was analyzed using the procedure described in Chapter 2 (section 2.6.2).

6.3 Results and discussion

6.3.1 Primary characterization of LNP suspensions

Figure 6-4 reports the ATR-IR spectra of oleic acid stabilized FeO NPs before and after the coating with a lipid layer made of a mixture of phosphatidylcholine/cholesterol esters. IR spectra of SLN (unloaded lipid particle) were also recorded. All the IR spectra band assignments are summarized in the Table 6-1. Starting with the uncoated FeO NP spectrum, two bands are visible at 3435 and 713 cm^{-1} ; the first it is attributed to O-H stretching modes related mainly to residues of water contained in the sample while the

second one is related to Fe–OH stretching modes. The wide bands correlated to O–H are visible also in unloaded SLN and LNP spectra at 3388 and 3387 cm^{-1} respectively. The signals in the range of 3002–2850 cm^{-1} and at 1412 cm^{-1} are related to asymmetric, symmetric and scissoring C–H modes due to the PC attached at the NP surface.

Considering the unloaded SLN spectra, the broad band related to O–H stretching appears at 3388 cm^{-1} while the ones related to C–H vibrational modes are visible in the range 3008–2853 cm^{-1} and at 1464 cm^{-1} . The signals at 1241 and 1062 cm^{-1} are ascribed to antisymmetric and symmetric PO^{2-} stretching respectively of the phospholipid headgroup and that at 1637 cm^{-1} to C=O stretching.

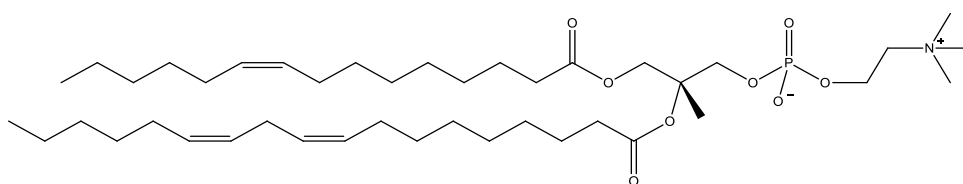
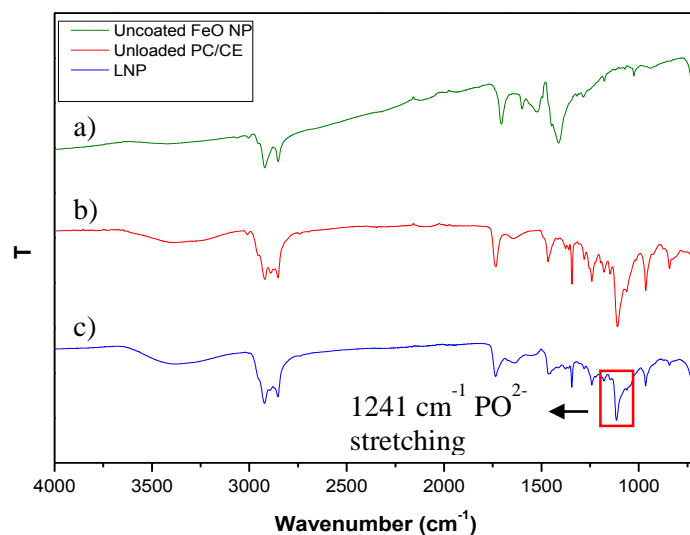


Figure 6- 4 ATR-IR spectra of (c) LNP, (a) uncoated OA@ γ - Fe_2O_3 NPs and (b) unloaded SLN. (Bottom) The molecular structure of phosphatidylcholin (PC).

The LNP IR spectrum shows most of the characteristic bands of both FeO NPs and unloaded SLN but two differences are apparent. Firstly, the band at 713 cm^{-1} characteristic of Fe–OH stretching is not visible in LNP spectra, which suggests that FeO NP are fully coated with lipids all over their surface. Secondly, unlike FeO NPs LNP spectrum shows an additional band at 1241 cm^{-1} , which we assign to PO^{2-} antisymmetric vibrational modes. These two bands suggest that both PO^{2-} and –OH groups are directly involved in the NP–lipid layer bound in LNP suspensions. Figure 6-5 shows the proposed NP–lipid

interaction in a typical PC based magnetoliposome suspension, suggesting chemisorption of the lipid and at least partial replacement of OA.

Uncoated FeO NPs	Unloaded SLN	LNPs	Assignment
$\nu_{\text{FeO}} (\text{cm}^{-1})$	$\nu_{\text{PCs}} (\text{cm}^{-1})$	$\nu_{\text{LNPs}} (\text{cm}^{-1})$	[129]
3435	3388	3387	OH stretch
3002	3008	3008	sp^2 CH stretch
2911	2917	2922	ν_a CH ₂ stretch
2850	2853	2853	ν_s CH ₂ stretch
1706	1736	1735	C=O stretch
1600	1637	1637	COO ⁻
1412	1464	1464	ν_s CH ₂ scissor
-	1240	1241	ν_a PO ²⁻ stretch
-	1062	-	ν_s PO ²⁻ stretch
713	-	-	Fe-OH stretch

Table 6- 1 Infrared band assignments for uncoated FeO NPs, unloaded SLN and LNPs.

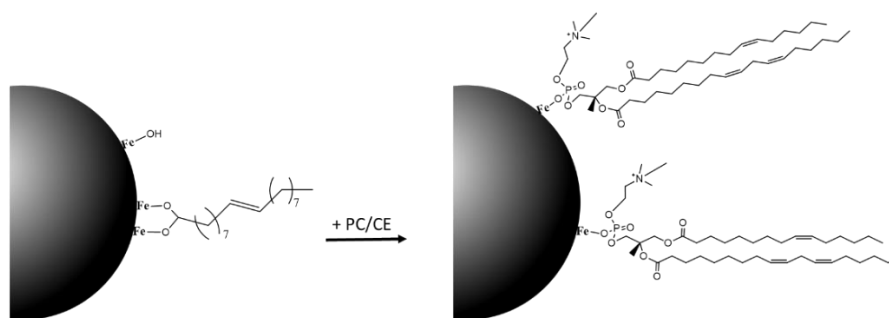


Figure 6- 5 Schematic representation of the (left) oleic stabilised FeO NPs and the (right) possible FeO-PC interaction following the encapsulation of the NPS with lipids.

Confirmation of the chemisorption of the lipids onto the NP surface could be provided by TGA analysis. This work is ongoing.

DLS results of fresh LNP suspensions are reported in Table 6-2 yields. In all cases the PDI values are lower than 0.3 suggesting that all suspensions contain relatively monodisperse particles. The hydrodynamic diameter of the preparations is in the range of

23-44 nm before any size selection step. The variability of the average size, improved as the process was optimized and finally we demonstrated good reproducibility of the method of preparation. Figure 6-6 shows the size distribution by intensity of a typical suspensions of 13 nm oleic acid stabilized FeO NPs in organic phase and 24 nm LNPs in water for comparison.

Sample	$d_{\text{hyd, chlor}}$ (nm)	$d_{\text{hyd, water}}$ (nm)	Fe, Yield (%)
	[PDI]	[PDI]	
LNP 1	17 [0.16]	44 [0.25]	85
LNP 2	13 [0.05]	24 [0.07]	92
LNP 3	13 [0.05]	30 [0.15]	91
LNP 4	13 [0.05]	32 [0.08]	89
LNP 5	14 [0.09]	30 [0.09]	95

Table 6- 2 DLS data at 25 °C of LNP suspensions prepared with different formulations.

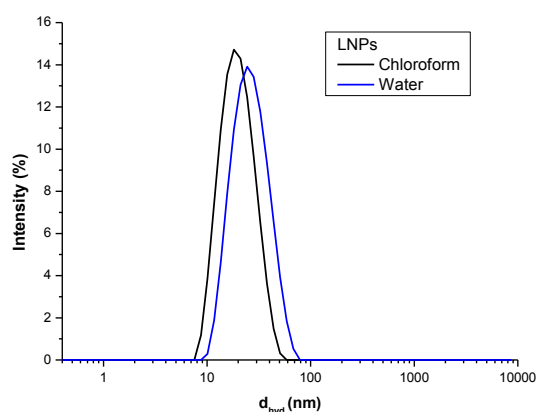


Figure 6- 6 Size distribution by intensity of (black line) oleic acid stabilized FeO NPs dispersed in chloroform (13 nm, PDI=0.05) and (blue line) lipid coated NPs (24 nm, PDI=0.07) dispersed in water.

FESEM analysis of a representative LNP suspension dried onto a copper TEM grid is shown in Figure 6-7. The LNPs show spherical-like shape and well dispersed particles with approximate diameter of 22 nm. The average hydrodynamic diameter (d_{hyd}) of these magnetoliposome suspensions was 30 nm. In the secondary electron images the lipid layer that fully covers each NPs, while the magnetic core is visible in the STEM image (insets of Figure 6-7). Finally, no significant signs of formation of lipid aggregates nor of further FeO NPs agglomeration were observed in the sample analyzed.

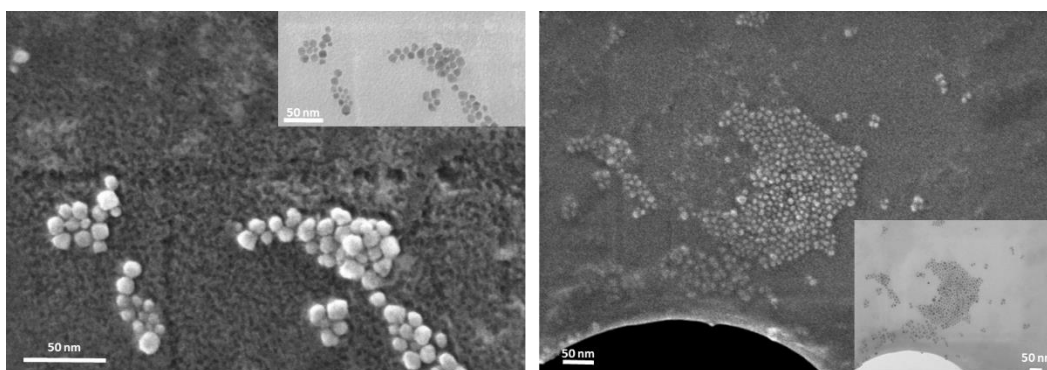


Figure 6- 7 FESEM images of a typical aqueous FeO LNP suspension ($d_{\text{hyd}} = 30 \text{ nm}$, PDI= 0.08) Insets) STEM images. The scale bar for all images is 50 nm.

6.3.2 Primary characterization of LNPA suspensions

In Figure 6-8 ATR-IR spectrum of a typical suspension of LNPAs is compared to the spectra of uncoated FeO NPs, unloaded SLN and LNPs which were already reported in the section above. The band assignments of these spectra are summarized in Table 6-3. The LNPA spectrum shows the characteristic peaks of both unloaded SLNs and LNPs, which means that the FeO NPs are effectively coated by lipid layer confirming the presence of chemical interaction between PC and NP interface in the LNPA suspension.

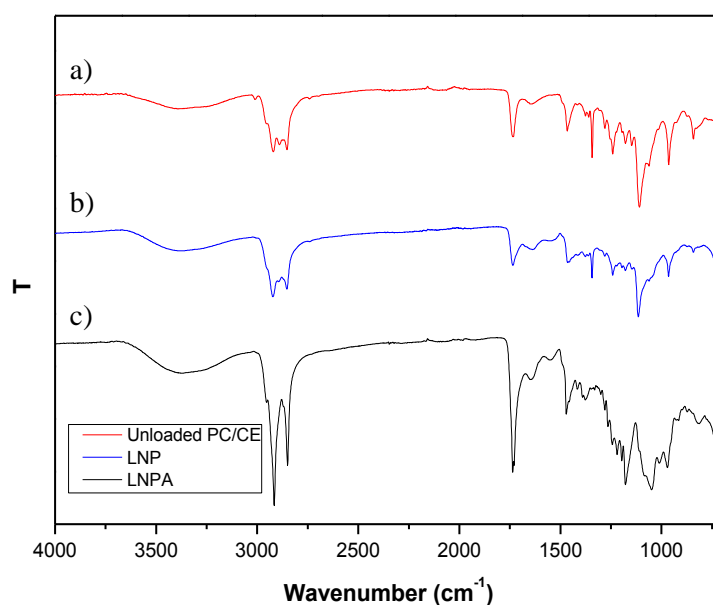


Figure 6- 8 Comparison of the ATR-IR spectra of (a) unloaded SLNs, (b) LNPs and (c) LNPAs.

Really small differences exist between the spectra of LNPAs and LNPs so in conclusion ATR-IR analysis alone cannot distinguish between LNPs and LNPAs.

Unloaded SLNs $\nu_{\text{SLN}} (\text{cm}^{-1})$	LNPAs $\nu_{\text{LNPA}} (\text{cm}^{-1})$	Assignment [129]
3388	3376	OH stretch
3008	3008	sp^2 CH stretch
2917	2964	ν_{a} CH ₂ stretch
2853	2849	ν_{s} CH ₂ stretch
1736	1738	C=O stretch
1637	1637	COO ⁻
1464	1473	ν_{s} CH ₂ scissor
1240	1240	ν_{a} PO ²⁻ stretch
1062	1052	ν_{s} PO ²⁻ stretch

Table 6- 3 Infrared band assignments for unloaded SLNs and LNPAs.

Sample	$d_{\text{hyd,water}}$ (nm) [PDI]	Fe Yield (%)
LNPA 1	220 [0.21]	88
LNPA 2	187 [0.12]	87
LNPA 3	194 [0.13]	88
LNPA 4	146 [0.15]	85
LNPA 5	172 [0.20]	82
LNPA 6	127 [0.22]	79

Table 6- 4 DLS data at 25 °C of LNPA suspensions in water prepared with different formulations. The initial OA-NPs in chloroform have d_{hyd} of 17 nm, PDI<0.2, 1.05 excess of OA and the iron concentration of ~109 mM.

Table 6-4 reports both hydrodynamic diameter and PDI values of LNPA samples prepared starting from different batches of FeO NPs. According to the data all samples present a unimodal size distribution (PDI<0.22) and it is possible to form stable and monodisperse LNPA of size in the range of 127 to 238 nm. The stability of these

suspensions will be shown below. Figure 6-9 shows the size distribution by intensity of the NPs before and after their encapsulation with lipids and their aggregation to form LNPA structures. In both cases the size distribution observed was unimodal.

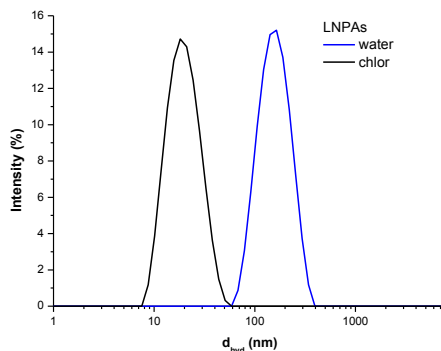


Figure 6 - 9 Size distribution by intensity of (black line) oleic acid stabilized FeO NPs in chloroform (13 nm, PDI=0.05) and (blue line) LNPA structures (141 nm, PDI=0.14) in water.

6.3.3 Primary characterization of LNPA suspensions

ATR-IR spectra of a typical suspension of LNPA is shown in Figure 6-10. The band assignment is summarized in Table 6-5 IR spectra of uncoated FeO NPs and unloaded SLN are also reported for comparison. All peaks observed in FeO NP spectrum are observed in uncoated FeO NP and unloaded SLN spectra. No remarkable differences were observed between LNPA and LNPA suspensions through ATR-IR analysis alone.

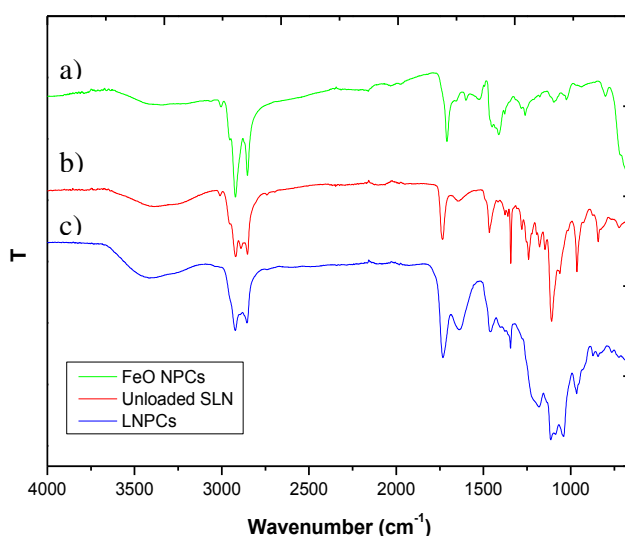


Figure 6- 10 ATR-IR spectra of freeze dried suspensions of (a) uncoated γ -Fe₂O₃ NPs (51 nm PDI=0.21); (b) unloaded SLN (13 nm, PDI=0.09) and (c) LNPA (112 nm PDI=0.07).

Uncoated NPCs $\nu_{\text{NPC}} (\text{cm}^{-1})$	LNPCs $\nu_{\text{LNPC}} (\text{cm}^{-1})$	Assignment [129]
3435	3399	OH stretch
3002	-	sp^2 CH stretch
2911	2926	ν_a CH ₂ stretch
2850	2857	ν_s CH ₂ stretch
1706	1734	C=O stretch
1600	1610	COO ⁻
1412	1412	ν_s CH ₂ scissor
-	1264	ν_a PO ²⁻ stretch
-	1052	ν_s PO ²⁻ stretch

Table 6- 5 Infrared band assignments for uncoated NPCs and LNPCs.

DLS analysis were performed for fresh LNPC suspensions prepared starting from different NPC batches in chloroform. The hydrodynamic diameter and PDI values of the NPCs before and after lipid coating are reported in Table 6-6. Representative size distributions by intensity of the NPCs in both organic and aqueous media are shown in Figure 6-11.

Sample	$d_{\text{hyd, chlor}}$ (nm) [PDI]	$d_{\text{hyd, water}}$ (nm) [PDI]	$ \Delta d_{\text{hyd}} $ (nm) (% change)
LNPC 1	75 [0.17]	98 [0.19]	23 (31)
LNPC 2	70 [0.15]	92 [0.20]	22 (31)
LNPC 3	120 [0.10]	106 [0.17]	14 (-12)
LNPC 4	132 [0.09]	125 [0.12]	7 (-5)
LNPC 5	147 [0.08]	131 [0.12]	16 (-10)
LNPC 6	215 [0.10]	156 [0.11]	59 (-27)

Table 6- 6 DLS data at 25 °C of LNPC suspensions prepared with different formulations.

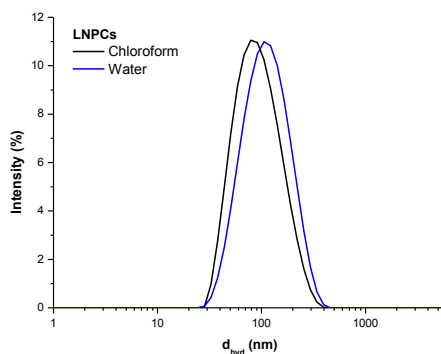


Figure 6- 11 Size distribution by intensity of (black line) oleic acid stabilized FeO NPC in chloroform (75 nm, PDI=0.17) and (blue line) lipid coated NPCs (98 nm, PDI=0.19) dispersed in water.

The DLS data reported in Table 6-6, suggests that all NPC suspensions of NPC have a relatively good monodispersity ($PDI \leq 0.2$) before and after the coating with lipids. According to these DLS results it seems that 70 and 75 nm clusters dispersed in chloroform show higher hydrodynamic diameters after lipid covering and dispersion in water. An opposite effect it is observed at NPC size higher than 120 nm in fact the NPC size is higher in water. In the first case the increase of the NPC size a lower hydrodynamic diameters can be due to the thickness of the lipid layer on the NPC surface. In the second case it is possible that NPC disaggregation occurs. Finally DLS data suggests that it is possible to get reasonably similar hydrodynamic size of the clusters even after encapsulation with lipids for the 100-140 nm size range.

Collectively, the IR and DLS data shown above demonstrates successful encapsulation of NPs and NPCs with lipids and reasonable reproducibility and particle dispersity ($PDI < 0.25$) for all type of magnetoliposomes. Low PDI values and smaller change in hydrodynamic size was to be found for NPC size of 100-140 nm otherwise an unpredictable change in size was observed upon phase transfer. It has to be noted that it was not possible to image both LNPA and LNPC suspensions by FESEM because these clusters are not stable to drying on the copper grid. Confirmation of the morphology of these magnetoliposomes might be possible from cryo-TEM, however this technique is not currently available to us.

6.3.4 Magnetoliposome stability

In order to assess the colloidal stability, the hydrodynamic size of NP and NPC based magnetoliposomes was monitored over time. Both hydrodynamic diameter and PDI values are reported in Table 6-7 while the relative size distributions by intensity are showed in Figure 6-12.

The LNP size and PDI was almost unchanged for up to 53 days for suspensions stored at 4 °C, while the PDI was identical. Also in the case of LNPA suspension the hydrodynamic diameter was relatively unchanged (< 5% d_{hyd} increase) for up to 26 days for samples stored. In this case the LNPA size decreased from 142 to 141 nm and the PDI value was unchanged. Considering the LNPC suspensions, both size and PDI value were unchanged increasing from 111 to 112 nm and 0.09 to 0.11 respectively in 86 days. The samples showed good colloidal stability also in PBS media with no significant increase of hydrodynamic diameter and PDI (PDI < 0.2) (Table 6-7).

Collectively, all these aqueous magnetoliposome suspensions showed good colloidal stability overtime and a unimodal polydispersity (PDI<0.2) in water and PBS buffer at 4 °C.

Sample	Time (day)	$d_{\text{hyd, H}_2\text{O}}$ (nm)	$d_{\text{hyd, PBS}}$ (nm)
		[PDI]	[PDI]
LNPs	0	23 [0.16]	30 [0.19]
	21	25 [0.13]	32 [0.14]
	53	29 [0.12]	35 [0.15]
LNPA	0	142 [0.16]	150 [0.17]
	5	141 [0.14]	144 [0.16]
	26	141 [0.16]	141 [0.12]
LNPCs	0	111 [0.09]	111 [0.11]
	45	110 [0.10]	110 [0.18]
	86	112 [0.11]	111 [0.08]

Table 6- 7 Overtime monitoring of hydrodynamic diameter and polydispersity index of LNP, LNPA and LNPC suspensions in water and PBS. The samples were stored at + 4 °C while DLS measurements were performed at 25°C.

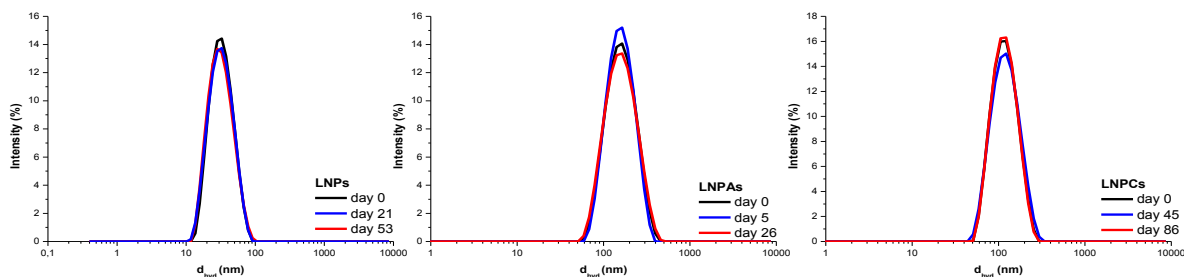


Figure 6- 12 Colloidal stability study by DLS in water. Size distribution by intensity overtime of representative suspensions (Table 6-7) of (left) LNPs, (middle) LNPAs, and (left) LNPCs.

6.3.5 Nuclear magnetic resonance relaxometry

After confirming the colloidal stability of the magnetoliposomes in water, an investigation over the SLN magnetic properties through NMRD technique was performed. NMRD measurements were recorded at 25 °C and in all cases the proton magnetization recovery curves were mono-exponential and the fitting errors were below 1%.

The relaxivity profile for a representative sample of LNPs is shown in Figure 6-13. The NMRD curve of primary DTAB-stabilized iron oxide NPs in water prepared by thermal decomposition as described in Chapter 5, are reported for comparison. The hydrodynamic size, PDI, r_1 and r_2 values measured at 1.41 T for the suspensions are reported in Table 6-8. The NMRD profiles exhibit the features of dispersed superparamagnetic particles, for instance a plateau at low frequencies, a maximum at high frequencies and a rapid decrease toward zero at high frequencies are observed. The shape of the profiles is consistent for both samples with a slight shift of r_1 maximum towards lower frequencies for lipid encapsulated NPs. This is a result of the higher hydrodynamic diameter of LNPs. In addition in the mid-frequency range a minimum is distinguishable and that is characteristic of small particles (< 20 nm)^[130] which confirms full particle dispersion and the absence of any aggregates, which is critical for T_1 -weighted MRI applications. According to Table 6-8, the r_1 at 1.41 T is lower for LNPs as expected while r_2 is comparable for both DTAB and lipid stabilized NPs.

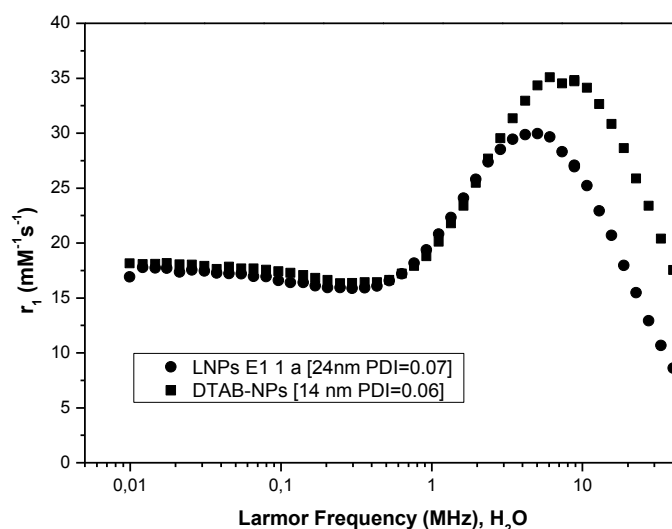


Figure 6- 13 NMRD profiles of (●) LNP and (■) DTAB-NPs in water. The measurements were performed at 25 °C.

Sample	$d_{\text{hyd, fresh}}$ (nm)	r_1 ($\text{mM}^{-1}\text{s}^{-1}$)	r_2 ($\text{mM}^{-1}\text{s}^{-1}$)
	[PDI]	@ 1.41 T	@ 1.41 T
DTAB-NPs	14 [0.06]	16.58	60.15
LNPs	24 [0.07]	4.08	73.78

Table 6- 8 The hydrodynamic diameters, PDI and relaxivity values of fresh aqueous suspensions of DTAB-NPs and LNPs. The DLS and NMR measurements were performed at 25°C.

Figure 6-14 shows the NMRD profiles of fresh and aged suspensions of LNPA and LNPs while Table 6-9 reports the r_1 and r_2 values of the same suspensions in water measured at 1.41 T compared to those of DTAB-NP suspensions. As in the case of LNP suspensions, LNPA and LNPs NMRD profiles show a r_1 maximum at high fields and a plateau at low frequencies, however the absence of the minimum in the mid-range frequencies suggests an increase in the magnetocrystalline anisotropy energy due to the interparticle interactions that arise only for the clusters. Another difference compared with LNPs is that multi core magnetoliposome assemblies samples show lower relaxivity at all fields. The reasons are discussed below. Moreover, it can be seen from Figure 6-14 that LNPA shows lower relaxivity than LNPs presumably because of their higher d_{hyd} . Hence, predictively r_1 decreases with increasing of the magnetoliposome size (Table 6-9). The opposite effect was observed for r_2 . This is due to the increase of the global magnetic moment.

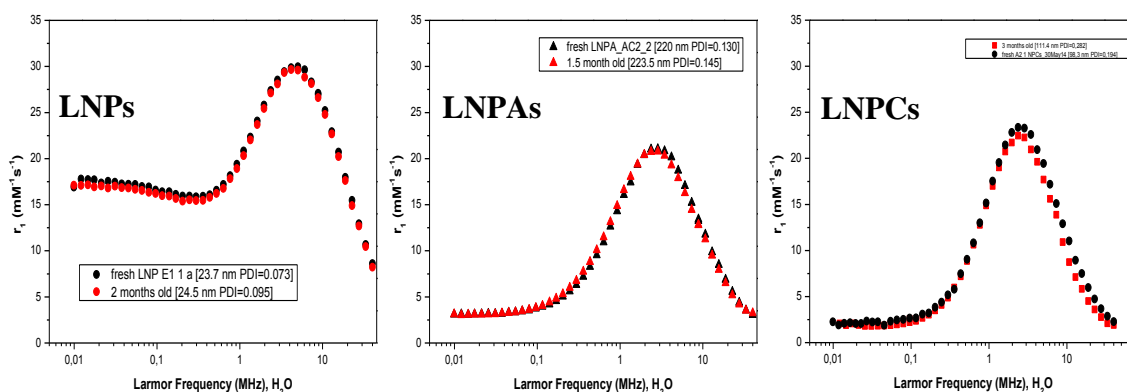


Figure 6- 14 NMRD Profiles at 25 °C of (left) a typical (●) fresh ($d_{\text{hyd}} = 24 \text{ nm}$ PDI = 0.073) and (●) aged (61 days, $d_{\text{hyd}} = 25 \text{ nm}$ PDI = 0.10) suspension of LNP in water; (middle) (▲) fresh ($d_{\text{hyd}} = 220 \text{ nm}$ PDI = 0.13) and (▲) aged (45 days, $d_{\text{hyd}} = 224 \text{ nm}$ PDI = 0.15) aqueous suspension of LNPA; (right) (●) fresh ($d_{\text{hyd}} = 111 \text{ nm}$ PDI = 0.28) and (■) aged ($d_{\text{hyd}} = 98 \text{ nm}$ PDI = 0.19) aqueous suspension of LNPCs.

Sample	$d_{\text{hyd, fresh}}$ (nm) [PDI]	r_1 ($\text{mM}^{-1}\text{s}^{-1}$)	r_2 ($\text{mM}^{-1}\text{s}^{-1}$)
		@1.41 T	@1.41 T
LNPA	220 [0.13]	0.36	108.51
LNPC	111 [0.28]	1.45	422.50

Table 6- 9 The hydrodynamic diameters, PDI and relaxivity values of fresh aqueous suspensions of LNPA and LNPC. The DLS and NMR measurements were performed at 25 °C.

Figure 6-14 shows the functional stability of the LNP, LNPA and LNPC suspensions over time and with exposure to magnetic fields. Comparison of the properties are included below. For the LNP sample both hydrodynamic diameter and PDI are basically unchanged for 2 months; also the relaxivity response seems to be stable. In case of LNPA the hydrodynamic diameter is unchanged while the PDI is also slightly increased from 0.13 to 0.15; the r_1 response of the fresh suspension is almost identical to the one of the same aged sample at all frequencies. Considering LNPC suspensions, a slight decrease of the hydrodynamic diameter is observed from 111 to 98 nm while the PDI is improved (from 0.28 to 0.2). However the r_1 response of the aged suspension differs only slightly (<5 % decrease) from that of the fresh suspension.

Having confirmed the stability of the lipidic magneto-structure suspensions with a wide hydrodynamic size range (24-250 nm), size selection by magnetic chromatography on the magnetic resonance properties was investigated.

6.3.6 Magnetic chromatography of lipidic magnetic nanostructure suspensions

Magnetic chromatography was undertaken as a means of selective cluster size control^[131], as it separates particles based on the strength of their interaction with an externally applied magnetic field. A second goal was to separate the magnetic material from any diamagnetic (lipidic) components. The result of magnetic chromatography is lipidic magnetocomposite fractions, here called retentates, for which the hydrodynamic diameter can be controlled. For our purposes the aim was to improve the suspension monodispersity. In the following sections studies into the effect of magnetic chromatography on the lipidic nanocomposite suspensions by DLS and NMRD technique will be presented and discussed.

6.3.6.1 Magnetic chromatography of LNP suspensions

Size selection by magnetic chromatography was carried out using the procedure described in the Materials and Methods section. In the case of LNP, samples of initial size of 25, 29, 59 and 74 nm were used. DLS was used for characterizing the LNP retentate after size selection process. Table 6-10 reports the hydrodynamic diameter and PDI values of the retentates collected after chromatography at a magnetic field of 1.41 T and flow rate of 8 mL/hr. A slight increase of LNP hydrodynamic diameter a significant improvement of PDI values were observed especially for 51 and 74 nm LNP suspensions. Unfortunately the iron recovery after chromatography was low (24-43 %) and that can be a limiting factor.

Sample	Magnetic field (T)	Flow rate (mL/hr)	Initial sample d_{hyd} (nm) [PDI]	Retentate d_{hyd} (nm) [PDI]	Yield Fe (%)
LNP 1	1.41	8	24 [0.15]	29 [0.11]	32
LNP 2			29 [0.13]	31 [0.15]	24
LNP 3			51 [0.43]	57 [0.23]	41
LNP 4			74 [0.45]	80 [0.16]	43

Table 6- 10 DLS data of suspensions of LNPs before and after magnetic chromatography at 8 mL/hr, 1.41 T and at 25°C. The % recovery of Fe after magnetic chromatography is also reported.

Magnetic chromatography was found to be a better approach to improve the size distribution of LNPs than other size selection techniques such as centrifugation or magnetic decantation. These approaches resulted in the formation of large aggregates as indicated by an increase in the PDI value. The low yields could be addressed by increasing the external magnetic field strength which could allow a more effective fractionation of magnetic particles from empty liposomes. However, it was not possible to increase further the magnetic field using the available electromagnet (maximum $B_0 = 1.5$ T).

The catching of the magnetic particles by the steel wool is due to two forces opposite in direction, the magnetic force and the viscous drag force generated by the fluid flow ^[132]. The magnetic force (F_m) on a spherical magnetic particle is proportional to the particle volume and magnetization saturation (M_s) as described by the Equation 6-1.

$$F_m = \frac{4}{3}\pi r^3 M_s B \quad \text{Equation 6- 1}$$

This suggests that LNPs are small to be effectively caught resulting in a low amount of magnetic material deposited on the steel wool and low yields are obtained.

6.3.6.2 Magnetic chromatography of LNPA suspensions

In case of aqueous LNPA suspensions size selection by magnetic chromatography was performed to prepare samples of hydrodynamic diameters in the range 125-240 nm with PDI values < 0.21 in all cases. Hydrodynamic diameter and PDI values of the LNP suspensions before and after magnetic chromatography at 1.41 T and 25 °C are reported in Table 6-11. According to this DLS data, an improvement of the PDI values in most cases was observed in all cases, with a slight but unpredictable change of the hydrodynamic diameter. A different behavior was observed for the sample in which case d_{hyd} and PDI changed from 125 nm and 0.21, to 131 nm and 0.24 respectively. For LNPA samples the Fe recovery is in the range of 30 up to 46 %. The suspensions were stable for up to 16 weeks at 4 °C.

Sample	Magnetic field (T)	Flow rate (mL/hr)	Initial sample d_{hyd} (nm) [PDI]	Retentate d_{hyd} (nm) [PDI]	Yield Fe (%)
LNPA 1	1.41	8	125 [0.21]	131 [0.17]	30
LNPA 4			189 [0.12]	192 [0.11]	44
LNPA 3			220 [0.13]	215 [0.19]	43
LNPA 5			230 [0.13]	223 [0.10]	35
LNPA 7			240 [0.20]	249 [0.16]	42

Table 6- 11 DLS data of suspensions of LNPAs before and after magnetic chromatography at 8 mL/hr, 1.41 T and at 25°C. The Fe % recovery is also reported.

A slight change in hydrodynamic diameter for LNPAs and an improvement of the PDI was observed for all the samples studied. This indicates that presumably both LNPA core and morphology are preserved upon exposure to an external magnetic field and at a relatively low flow rate suggesting that LNPAs have a robust structure and are resistant to the field applied.

6.3.6.3 Magnetic chromatography of LNPC suspensions

Table 6-12 reports DLS data for LNPC suspensions before after magnetic chromatography experiments conducted at 1.41 T and the flow rate used was also in this case 8 mL/hr.

In all cases, the magnetic chromatography promoted a slight improvement of PDI values except in case of sample LNPC4, for which both size and PDI increased from 98 to 111 nm and 0.19 to 0.28 respectively. Higher Fe recovery was observed, in the range of 49 to 61 %. This result suggests that most of the NP cluster liposomes of the suspensions have a high magnetization and they are more easily caught by the magnetic field as compared with LNP, and even LNPA samples of similar size. The resulting suspensions were monitored over time by DLS and they showed unchanged hydrodynamic size for more than 20 weeks at 4 °C.

Sample	Magnetic field (T)	Flow rate (mL/hr)	Initial sample d_{hyd} (nm) [PDI]	Retentate d_{hyd} (nm) [PDI]	Yield Fe (%)
LNPC 1	1.41	8	110 [0.08]	117 [0.06]	61
LNPC 2			131 [0.12]	128 [0.10]	56
LNPC 3			156 [0.11]	152 [0.09]	58
LNPC 4			98 [0.19]	111 [0.28]	49
LNPC 5			106 [0.17]	107 [0.11]	51

Table 6- 12 DLS data of suspensions of LNPs before and after magnetic chromatography at 8 mL/hr, 1.41 T and at 25°C. The % recovery of Fe is also reported.

6.3.7 Effect of magnetic chromatography on lipidic magnetic nanostructure magnetic properties

In the following sections the DLS and NMRD results of the investigation over the effect of the size selection by magnetic chromatography on the lipidic nanostructure magnetic properties will be presented and discussed.

6.3.7.1 Effect of magnetic chromatography on LNP magnetic properties

The magnetic field dependence of the spin-lattice relaxivity, r_1 , over the range 0.25 mT- 1 T for typical LNP suspensions before and after magnetic chromatography are shown in Figure 6-15. Magnetic chromatography experiments were performed at 1.41 T and the flow rate used was 8 mL/hr. In Table 6-13 the r_1 , r_2 and the r_1/r_2 ratios recorded at 0.4 are shown along with the equivalent size change due to application of a magnetic field.

According to the DLS data, the initial LNP sizes were 25, 52 and 98 nm and all suspensions seemed to be stable while the size distribution was broader for the 98 nm LNP sample (PDI = 0.38) as reported in Table 6-13. It has to be noted that the 52 and 98 nm LNPs are too large to be considered as single LNPs; these suspensions might be mainly formed by aggregates of LNPs, and hence are effectively LNPA suspensions so here will be called LNPs*. An improvement of the PDI values after chromatography is observed, while hydrodynamic diameters are, interestingly, almost unchanged. According to the NMRD profiles (Figure 6-15), all the suspensions show a superparamagnetic behavior since they have an intense peak centered at high fields. The comparison of the NMRD profiles of the initial samples and the retentates reveals that the

relaxivity of the samples is unchanged for LNPs but increases both at low and at high fields after the magnetic chromatography in case of 51 and 98 nm LNPs*, as does r_2 without significant increase in d_{hyd} and that this effect is stronger for the LNPs* samples (LNP* 1 and LNP* 2). This behavior will be discussed below. In case of this hypothesis one would expect a higher difference in r_1 . However a shift of the r_1 maximum toward lower frequencies is observed for 98 nm LNP* sample because of an increase of d_{hyd} to 111 nm following magnetic chromatography while the PDI value decreases from 0.38 to 0.25 (Table 6-13).

Sample	Initial sample, 16.3 MHz (0.4 T)				After m.c., 16.3 MHz (0.4 T)				
	d_{hyd} (nm) [PDI]	r_1 ($\text{mM}^{-1}\text{s}^{-1}$)	r_2 ($\text{mM}^{-1}\text{s}^{-1}$)	r_2/r_1	d_{hyd} (nm) [PDI]	Yield Fe (%)	r_1 ($\text{mM}^{-1}\text{s}^{-1}$)	r_2 ($\text{mM}^{-1}\text{s}^{-1}$)	r_2/r_1
LNP	25 [0.18]	15.48	48.52	3.14	28 [0.11]	30	13.56	105.54	7.78
LNP* 1	52 [0.25]	26.94	138.46	5.14	54 [0.24]	41	13.51	101.45	7.51
LNP* 2	98 [0.38]	10.25	40.69	3.96	111 [0.25]	58	11.60	92.60	7.97

Table 6- 13 DLS and NMRD data of aqueous LNP suspensions before and after magnetic chromatography performed at room temperature, 16.3 MHz (0.4 T) and at a flow rate of 8 mL/hr.

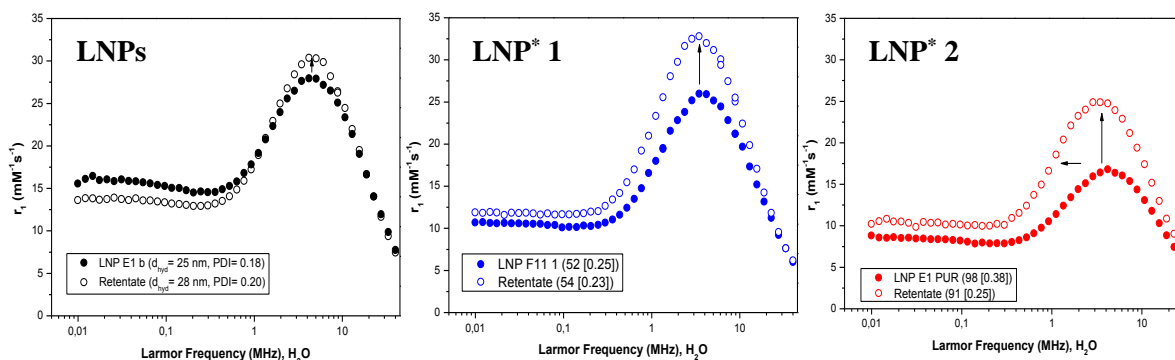


Figure 6- 15 NMRD profiles recorded at 25 °C of aqueous suspensions of LNP and LNPA suspensions before and after magnetic filtration at 65 MHz and a flow rate of 8 mL/hr. Closed marks refer to the initial sample while the open marks refer to the retentates. (Left) (●) 25 nm, PDI= 0.18; (□) 28 nm, PDI= 0.2. (Middle) (●) 52 nm, PDI= 0.25; (○) 54 nm, PDI= 0.24. (Right) (●) 98 nm, PDI= 0.38; (○) 91 nm, PDI= 0.25.

Collectively, for samples of hydrodynamic size in the range 25-98 nm we found that the r_2 values are always significantly higher than the r_1 values and that in most cases r_2 increased significantly after magnetic chromatography at both 0.4 and 1.41T (except for

52 nm sample). Interestingly, the r_2 value for the sample LNP* 1 is notably higher than expected for small dispersed superparamagnetic NPs. This suggests that this sample could contain aggregates which might contribute to the spin-spin relaxivity and which were removed by the magnetic chromatography. In case of LNP* 2 suspension the r_2 value is similar to the one obtained for 25 nm LNPs even though one would expect higher values because of its larger d_{hyd} ; this finding is currently not fully understood. Finally, the r_2/r_1 ratios of all samples measured at 1.41 T (Table 6-14) are comparable or higher than those observed for the current generation of negative contrast agents of d_{hyd} of 15-60 nm, such as Feridex[®] (d_{hyd} = 18-24 nm, $r_2/r_1 = 17$), Sinerem (d_{hyd} = 17-20 nm, $r_2/r_1 = 6.6$)^[133].

6.3.7.2 Effect of magnetic chromatography on LNPA magnetic properties

DLS and NMRD results before after magnetic chromatography are reported in Table 6-14 while Figure 6-16 shows the comparison between the NMRD profiles of the initial LNPA samples and the respective retentates. No significant increase of the d_{hyd} after magnetic chromatography was observed, while an improvement of the PDI occurred in all cases.

Sample	Initial sample, 16.3 MHz (0.4 T)			After filtration, 16.3 MHz (0.4 T)			
	d_{hyd} (nm) [PDI]	r_1 ($mM^{-1}s^{-1}$)	r_2 ($mM^{-1}s^{-1}$)	d_{hyd} (nm) [PDI]	Yield Fe (%)	r_1 ($mM^{-1}s^{-1}$)	r_2 ($mM^{-1}s^{-1}$)
LNPA 1	125 [0.21]	8.61	163.08	131 [0.24]	27	8.05	240.95
LNPA 2	220 [0.13]	3.71	367.56	215 [0.19]	39	2.87	126.63
LNPA 3	234 [0.17]	3.45	710.13	240 [0.14]	41	1.39	205.32

Table 6- 14 DLS data of suspensions of LNPAs before and after magnetic chromatography performed at 8 mL/hr, 0.4 T and at 25°C. The % recovery of Fe is also reported.

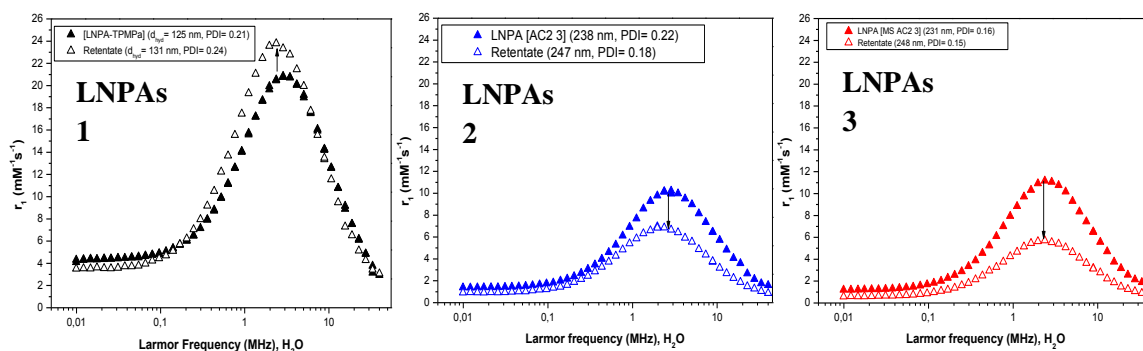


Figure 6- 16 NMRD profiles recorded at 25 °C of aqueous suspensions of LNPA suspensions before and after magnetic filtration at 65 MHz and a flow rate of 8 mL/hr. Closed marks refer to the initial sample while the open ones refer to the retentates. (Left) (\blacktriangle) 125 nm, PDI= 0.21; (\triangle) 131 nm, PDI= 0.24. (Middle) (\blacktriangle) 220 nm, PDI= 0.25; (\triangle) 215 nm, PDI= 0.19. (Right) (\blacktriangle) 234 nm, PDI= 0.17; (\triangle) 240 nm, PDI= 0.14.

The comparison of the NMRD profiles of the initial samples and retentates shows interesting features. Firstly, both initial and filtrated samples show superparamagnetic properties as they all present an intense r_1 peak at high fields the absence of any r_1 minimum in the mid-frequency range suggests that the particles are well packed giving rise to dipolar interactions within the clusters. Secondly the r_1 response seem to be suppressed after chromatography of LNPA of hydrodynamic diameters of 220 and 234 nm. Indeed the spin-lattice relaxation rate decreases at both low and high fields and a remarkable decrease of the r_1 peak is observed. Interestingly, for 125 nm LNPA the r_1 increased, as was the case for 52 nm and 98 nm LNP* which suggests that the assemblies of $d_{\text{hyd}} \leq 200$ nm are very similar.

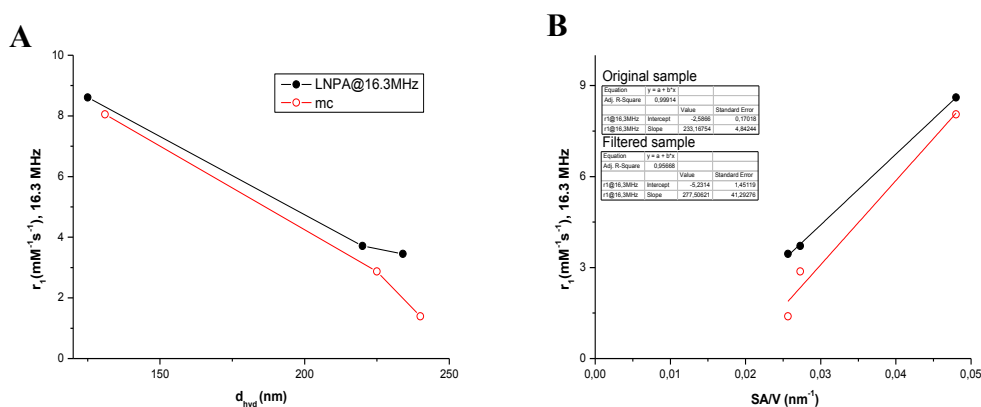


Figure 6- 17 Spin-lattice relaxivity values, r_1 as function of (a) hydrodynamic size and (b) surface area-to-volume ratio (SA/V) ratios of (closed marks) initial and (open marks) filtered LNPA samples in water. The measurements were performed at 16.3 MHz, 25 °C. (b) the solid lines are linear fits with equations (black) $y=233.17x-2.57$, $R^2=0.999$; (red) $y=277.5x-5.23$, $R^2=0.957$.

Figure 6-17 (a) shows the r_1 for LNPA samples as a function of hydrodynamic size. It is clear that as the size increased, the longitudinal proton relaxation rate r_1 decreases; this effect is slightly higher for the initial sample. The linear dependence of the relaxivity can be explained by considering the surface area effects, for the larger clusters fewer NPs interact with the external water (as they are embedded).

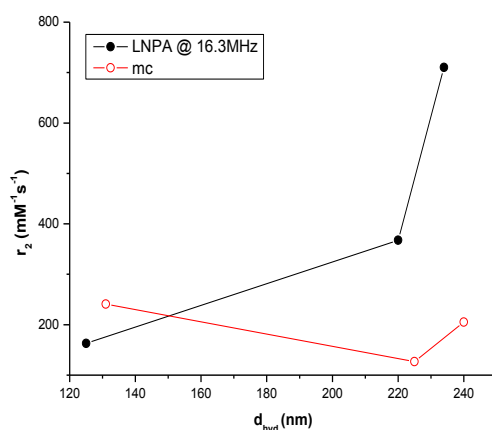


Figure 6- 18 Spin-spin relaxivity values, r_2 as function of hydrodynamic size of (closed marks) initial and (open marks) filtered LNPA samples in water. The measurements were performed at 16.3 MHz, 25 °C.

Figure 6-18 shows the r_2 values for LNPA suspensions as a function of the hydrodynamic size. For all the samples it was found that the r_2 values to be always significantly higher than the r_1 values before and after magnetic chromatography. An increase of r_2 with increasing LNPA size was observed just for initial samples; the values of r_2 increased from 163 to 710 $\text{mM}^{-1}\text{s}^{-1}$ as the lipidic composites size increased from 131 to 240 nm. Nevertheless it was found that for filtered samples of 215 and 240 nm r_2 values were lower than expected given their larger size. However, it should be mentioned that when the LNP aggregate size of the suspensions of 131 nm is filtered, the r_2 values increased from 163 to 241 $\text{mM}^{-1}\text{s}^{-1}$ resulting in an increase in r_2 relaxivity of about 48 % with only a slight change in d_{hyd} . For larger LNPA's r_2 decreases without significant change in size. This effect is reproducible (Table 6-15). The cause of this behavior is not clear. The r_2 value is largely determining by the cluster magnetization. For r_2 to change without change in size suggests that the packing density increases for smaller LNPA's and decreases for larger LNPA's. This is hard to understand. It should be noted that the NMR effects reflects number averages, *i.e.* are the volume whereas the DLS response is strongly weighted to the larger scatterers in any given sample. One alternative is that chromatography removes

a small fraction of primary NPs; however this would reduce r_1 and increase r_2 . Such behavior is only seen for the smaller clusters, so for now the expectation remains elusive.

Sample	$d_{\text{hyd,initial}}$ (nm) [PDI]	Initial sample r_2 ($\text{mM}^{-1}\text{s}^{-1}$)	After magnetic chromatography r_2 ($\text{mM}^{-1}\text{s}^{-1}$)
LNPAs 4	135 [0.11]	170.93	251.35
LNPAs 5	241 [0.22]	736.51	243.78

Table 6- 15 DLS data of suspensions of LNPAs before and after magnetic chromatography performed at 8 mL/hr, 0.4 T and at 25°C. The % recovery of Fe is also reported. The r_2 values were recorded at 16.3 MHz.

It has been reported that in nanoparticle assemblies, interparticle exchange interactions between neighboring particles can also result in magnetic moment reorientation^[134]. Nanoparticle magnetic moment transitions induced by an external magnetic field and inter-nanoparticle exchange were observed for the first time by Mukherjee et al^[135] for γ - Fe_2O_3 NPs dispersed in a silica glass matrix. If the interparticle exchange occurs, it would mean that the NPs are close within the lipid matrix within the LNPA structure and that might be separated by thin lipid layer that allows interparticle interactions. Nonetheless the results showed above demonstrate that the relaxivity can be controlled by changing the LNPA size and using magnetic chromatography in some cases.

6.3.7.3 Effect of magnetic chromatography on LNPC magnetic properties

Table 6-16 reports the hydrodynamic diameter, PDI values, relaxivities (r_1 and r_2) before and after magnetic chromatography and the yield of iron recovered. Figure 6-19 shows the NMRD profiles for suspensions of LNPCs in the size range 98-152 nm and the respective retentates.

Sample	Initial sample, 16.3 MHz (0.4 T)			After filtration, 16.3 MHz (0.4 T)			
	d_{hyd} (nm) [PDI]	r_1 ($\text{mM}^{-1}\text{s}^{-1}$)	r_2 ($\text{mM}^{-1}\text{s}^{-1}$)	d_{hyd} (nm) [PDI]	Yield Fe (%)	r_1 ($\text{mM}^{-1}\text{s}^{-1}$)	r_2 ($\text{mM}^{-1}\text{s}^{-1}$)
LNPC 2	110 [0.08]	9.55	156.02	117 [0.06]	59	5.03	220.59
LNPC 3	123 [0.11]	2.92	184.92	122 [0.11]	53	3.96	268.93
LNPC 4	152 [0.09]	4.73	331.08	149 [0.09]	55	5.35	389.10

Table 6- 16 DLS data of suspensions of LNPCs before and after magnetic chromatography performed at 8 mL/hr, 1.41 T and at 25°C. The % recovery of Fe is also reported.

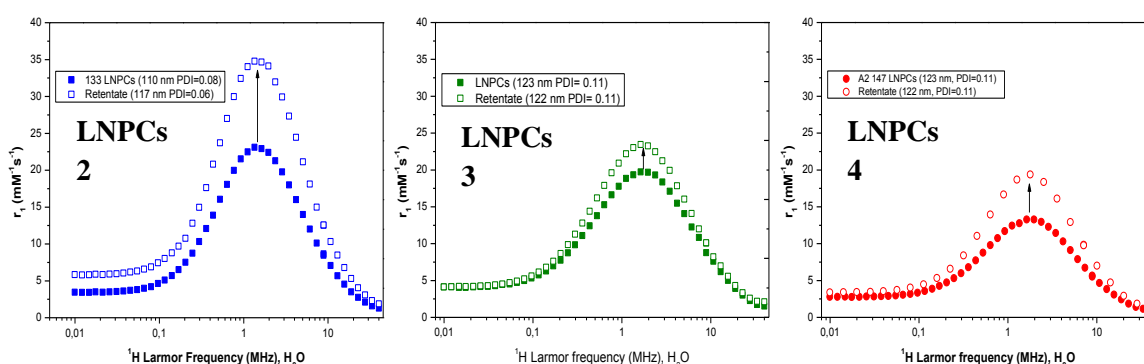


Figure 6- 19 NMRD profiles recorded at 25 °C of aqueous suspensions of LNPC suspensions before and after magnetic filtration at 0.4 T and a flow rate of 8 mL/hr. Closed marks refer to the initial sample while the open ones refer to the retentates. A) (■) 110 nm, PDI= 0.08; (□) 117 nm, PDI= 0.06. B) (■) 123 nm, PDI= 0.11; (□) 122 nm, PDI= 0.11. C) (■) 152 nm, PDI= 0.09; (□) 149 nm, PDI= 0.11.

The NMRD response shown in Figure 6-19 suggests that all lipid stabilized clusters present superparamagnetic properties since the profiles show an intense r_1 peak at high fields. Comparison of the NMRD profiles of the initial samples with the retentate NMRD ones (Figure 6-19) reveals that the relaxivity of the samples increases after magnetic chromatography especially in the mid frequency range 0.1-10 MHz without any increase in d_{hyd} or change in PDI (Table 6-16). These suspensions are far more stable to magnetic chromatography than the other LNP* or LNPA suspensions. This behavior suggests that preformed clusters are more robust. The r_1 effect is interesting but the r_2 is more relevant for application as T_2 agents.

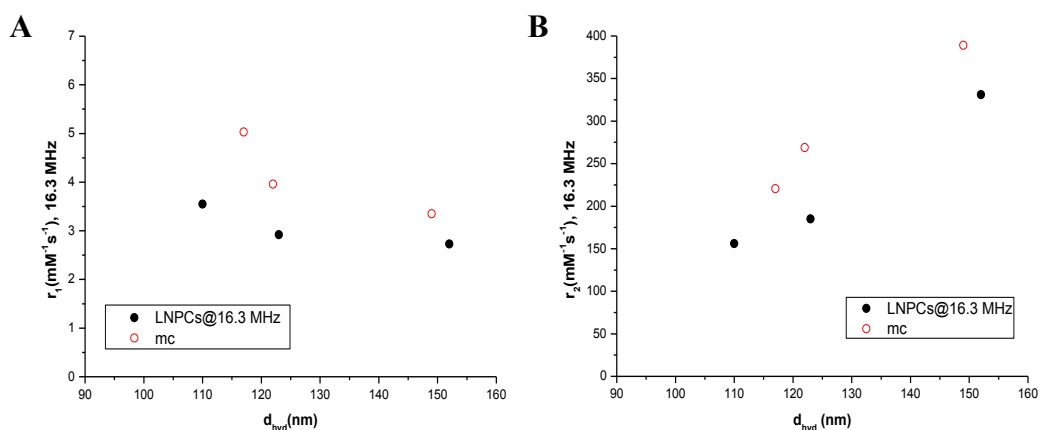


Figure 6- 20 (a) Spin-lattice relaxivity values, r_1 and (b) spin-spin relaxivity values, r_2 as function of hydrodynamic size of (closed marks) initial and (open marks) filtered LNPC samples in water. The measurements were performed at 16.3 MHz, 25 °C.

The r_1 and r_2 values for the initial and filtered LNPC samples as a function of the hydrodynamic size are shown in Figure 6-20. As it can be seen from Figure 6-20 (a), the r_1 decreases with increasing of the LNPC size; the differences between the samples with respect to the longitudinal relaxation rate were small ranging from 3.55 to 2.73 $mM^{-1}s^{-1}$ and from 5.03 to 3.35 $mM^{-1}s^{-1}$ for initial and filtered samples respectively with increasing LNPC size. As in the case of LNPA the decrease of the relaxivity suggests that with the increasing of the NPC size, the number of NPs that cannot contribute to the relaxation of the water molecules. Surprisingly, the relaxivity response was higher for all filtered suspensions, again this is not fully understood yet.

As in the case of LNPA, an opposite trend was found for r_2 that increases with increasing of LNPC size (Figure 6-20 (b)). The r_2 effect is more pronounced for the LNPCs filtered with magnetic chromatography. The r_2 values increases from 156 to 331 $mM^{-1}s^{-1}$ and from 221 to 389 $mM^{-1}s^{-1}$ for initial and filtered samples respectively with increasing LNPC size. For LNPCs repeat experiments have yet have to be performed. However it was not possible to produce LNPCs in the 200 nm size range so we cannot see if the effects observed for larger LNPA also occur for LNPCs.

6.3.7.4 Comparison of the magnetic properties of initial and filtered lipidic nanostructures

A comparison of the magnetic properties (r_1 and r_2) of initial and filtered LNPA and LNPCs of different size is shown in Figure 6-21 and reported in Table 6-17.

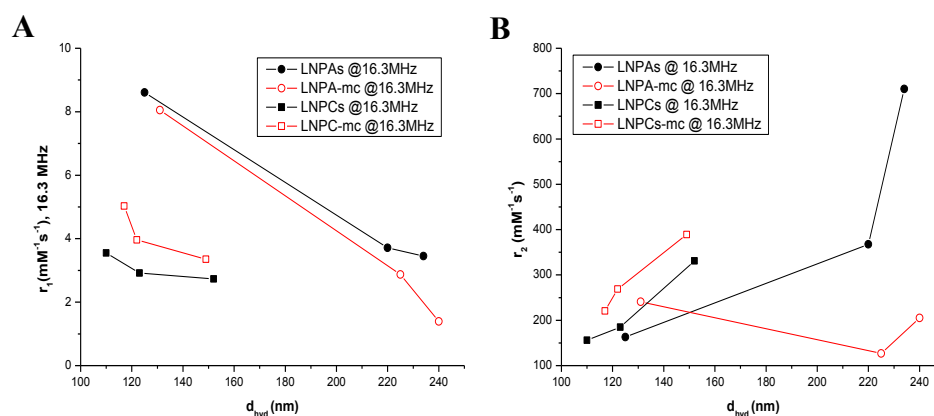


Figure 6- 21 (Left) Spin-lattice relaxivity values, r_1 and (right) spin-spin relaxivity values, r_2 as function of hydrodynamic size of (closed marks) initial and (open marks) filtered (circles) LNPA and (squares) LNPC samples in water. The measurements were performed at 16.3 MHz, 25 °C.

Sample	Initial sample		After magnetic chromatography		r_2 trend
	d_{hyd} (nm) [PDI]	r_2 ($\text{mM}^{-1}\text{s}^{-1}$)	Yield Fe (%)	r_2 ($\text{mM}^{-1}\text{s}^{-1}$)	
LNPs	25 [0.18]	48.52	30	105.54	↑
LNPA	125 [0.21]	163.08	27	240.95	↑
	220 [0.13]	367.56	39	126.63	↓
	234 [0.17]	710.13	41	205.32	↓
LNPCs	110 [0.08]	56.02	59	220.59	↑
	123 [0.11]	184.92	53	268.93	↑
	149 [0.09]	331.00	55	389.10	↑

Table 6- 17 DLS and r_2 values of suspensions of lipidic constructs before and after magnetic chromatography performed at 8 mL/hr, 0.4 T and at 25°C.

The trend of r_1 as function of the size is similar for both lipidic magnetic nanostructures but in case of LNPA samples higher r_1 values were observed at comparable sizes. This suggests that the single NPs are not clustered within the LNPA lipidic structure and that more NPs can contribute to the relaxation process thus higher is the relaxivity. This

behavior is observed for both initial and filtered LNPA samples. Collectively initial and filtered LNPs show higher transversal relaxivity response at similar d_{hyd} values as expected. This behavior can be related to the higher magnetic moment due to the assembled NP within the lipidic nanostructure. The r_2 effect is enhanced in case of filtered LNPs.

In conclusion, the NMRD results reported so far for LNP, LNPA and LNP suspensions are quite interesting, as they suggest that the relaxivity of the magnetoliposomes can be controlled over a wide range of frequencies by changing the internal architecture of the magnetic core and by using magnetic filtrations in some cases. Given the importance of the lipids in biomedical purposes as drug carriers, these findings may be interesting for nanotechnology and MRI application.

6.3.8 Magnetic Fluid Hyperthermia

To assess the effectiveness of the lipidic nanocomposite suspensions as potential agents for magnetic fluid hyperthermia, their heating efficiencies were measured. The evolution of the suspension temperature as a function of time was recorded during irradiation at three AC-frequencies. It has to be noted that the suspensions analyzed were not processed with magnetic chromatography and that an adiabatic condition was maintained during each experiment for minimizing the initial heat loss by placing the suspensions within a polystyrene tube. A typical temperature-time curve recorded at 523 kHz and 13.5 kA/m is shown in Figure 6-22. Under the AC-field, the heating curves were linear at early stage and after for few minutes (~ 200 s) they tend to saturate at a certain temperature depending on the nature of the suspension and of iron content. The heating efficiency was determined from the initial slope of the temperature-time curve (first 200 s) and was adjusted for the iron content.

The relationship between specific absorption rate (SAR) and the AC-field frequency (335-995 kHz) for magnetoliposome suspensions is also shown in Figure 6-22. The SAR values of 14 nm DTAB stabilized NPs in water are reported for comparison.

The SAR values obtained for LNP suspension are broadly comparable to the ones achieved for aqueous suspension of DTAB stabilized NPs. Indeed, it is found that the SAR values of LNPs are very similar irrespective of the surface chemistry, which might

be as expected. This is further confirmation of the full dispersion of the LNP samples with hydrodynamic diameter of 20-30 nm.

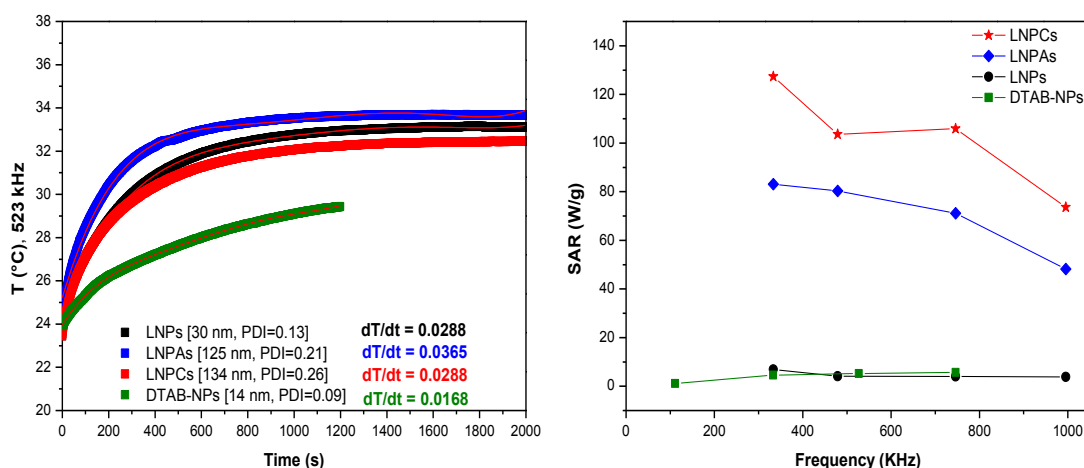


Figure 6- 22 (Left) Temperature as a function of time and (Right) SAR values in function of frequency of suspensions of (green) DTAB stabilized FeO NPs (14 nm, PDI=0.095); (black) LNPs (30 nm, PDI=0.128, 0.4 mg/mL Fe), (blue) LNPA (125 nm, PDI= 0.21, 0.14 mg/mL Fe) and (red)LNPC (134 nm, PDI=0.26, 0.045 mg/mL Fe). The measurements were performed at fixed field strength of 15.9 kA/m.

According to Figure 6-22 (right) the specific absorption rate of both LNPC and LNPA samples of size 125-134 nm decreases with increasing the AC-field frequency. This trend is opposite to the theoretical and experimental results reported by Wang^[136] and Rosensweig^[137] that showed that SAR response of magnetite particles increases with increasing of the AC-field frequency according to a power equation. This behavior suggests that in our study the relaxation mechanisms dominant in the heat release is different to those in Wang's study (Brownian and Neel relaxation mechanisms) suggesting that hysteresis losses are responsible for the heat release. The LNPC heating efficiencies were generally higher than those showed by LNPA and LNP suspensions at all frequencies, particularly at 333 kHz. These different magnetic hyperthermia heating behaviors can be related to the difference in terms of configuration, interparticle spacing and physical confinement of the NPs within the lipidic matrix. In case of LNPCs (Figure 6-23 (c)) the assembled NPs can be described as a single-domain material that act as a giant magnet of large magnetic moment that generates heat through hysteresis losses that overcome the Néel relaxation process^[138]. This is related to the existence of stronger dipolar interactions interactions between the NPs^[138-139] within the LNPC nanostructure.

LNPAs dissipate a reduced amount of heat probably because of the randomly orientation of magnetic NPs (Figure 6-23 (b)) and differences in interparticle separation within the nanostructure which leads to weaker dipole-dipole interactions thus lower SAR values [140]. The SAR values obtained for LNPAs and LNPCs at 333 kHz compare well with literature values for similar NP assemblies^[113, 119a]. For example, Dutz et al. reported SAR values between 60 and 300 W/g_{Fe} for iron oxide NPCs of hydrodynamic diameter of 158 nm at 400 kHz (10 kA/m).

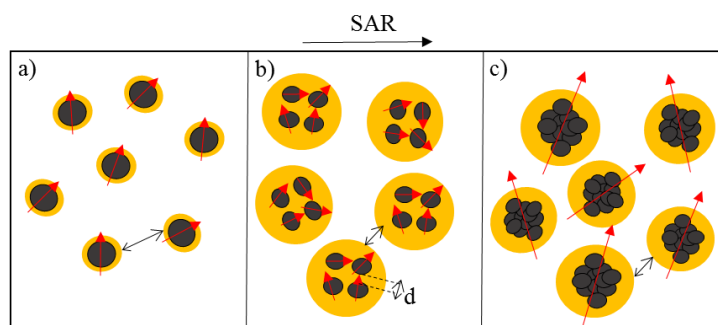


Figure 6- 23 Schematic representation of the nanoparticle magnetic moments in a) LNP, b) LNPA and c) LNPC suspensions. The SAR of the suspensions increases as following: LNPs<LNPA<LNPCs.

Figure 6-23 shows schematically represents the magnetic moments of the lipidic constructs. The fact that LNPCs and LNPAs exhibit SAR values an order of magnitude higher than LNPs suggests that the hysteresis losses mechanism are much more efficient in the ferromagnetic region ($> 13 \text{ nm}$)^[141]. However, magnetometry measurements (not currently available) would provide data for a fully understanding of the reason behind this behavior. However the optimum field parameters found are 335 kHz (15.9 kA/m) for 125 nm LNPAs and 134 nm LNPCs. Collectively, these results demonstrate that suspensions of LNPA and LNPC could be more efficient for magnetic fluid hyperthermia therapy than LNPs.

6.3.9 Drug loading and release experiments

To investigate on the effectiveness of LNP magnetoliposome suspension as carriers for drug delivery, drug loading and MFH release experiments were performed. In the following sections results of the studies on DxAc-LNP stability and drug delivery by MFH technique will be presented and discussed. The drug loading experiments were

completed at Nanovector s.r.l (Turin, Italy), using the method described in the experimental section.

6.3.9.1 Stability of drug loaded LNPs

LNPs functionalized with DxAc (dexamethasone) were first analyzed by DLS to evaluate their size and stability. Figure 6-24 reports the size distributions by intensity of the suspensions. The stability of the suspensions overtime, the LNP size was confirmed by DLS (Table 6-18). Collectively the drug loading leads to an increase of the hydrodynamic size and PDI values of the lipidic nanostructures. It has to be noted that the PDI was particularly high in case of LNPs (PDI > 0.4). However all the lipidic nanocomposite suspensions analyzed were stable over time at 4 °C and both PDI and d_{hyd} values remained unchanged up to 50 days in case of LNPs-DxAc.

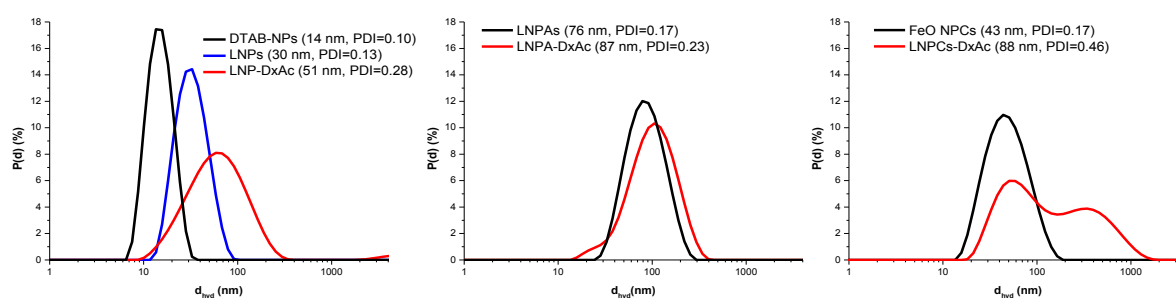


Figure 6- 24 Typical size distributions by intensity of suspensions of (left) (black line) FeO NPs, 14 nm PDI= 0.10; (blue line) LNPs, 30 nm PDI=0,13; (red line) LNP-DxAc, 51 nm PDI=0.27. (Middle) (black line) LNPA NPs, 76 nm PDI= 0.17; (red line) LNPA-DxAc, 87 nm PDI=0.23. (Right) (black line) FeO NPCs, 43 nm PDI= 0.17; (red line) LNPs-DxAc, 88 nm PDI=0.46.

Sample	Time (day)	d_{hyd} (nm) [PDI]
LNP-DxAc	0	51 [0.27]
	50	51 [0.25]
LNPA-DxAc	0	87 [0.23]
	35	86 [0.22]
LNPC-DxAc	0	88 [0.46]
	22	85[0.42]

Table 6- 18 Stability of the same suspensions were investigated by DLS overtime. DLS measurements were performed at 25 °C.

6.3.9.2 Device development and drug release experiments

After proving the stability of the lipid magnetic nanostructure loaded with DxAc, drug release studies were performed in DCU to assess these suspensions as potential drug devices for medical treatments. The device used for these experiments is shown in Figure 6-25 and it is formed by a 20 kDa dialysis membrane (Sigma Aldrich) and a PE centrifuge tube. All experiments were conducted at room temperature without stirring.

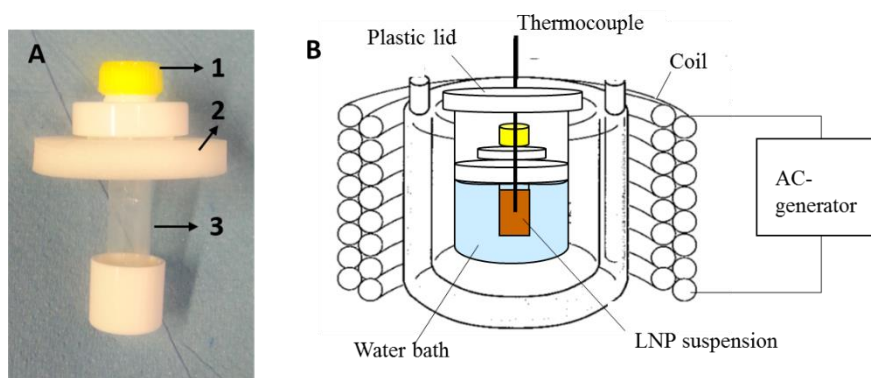


Figure 6- 25 Structure of the device used in drug delivery studies. (A) The device is formed by different components: a floating (3) 20kDa dialysis membrane which floats thanks to (2) polystyrene ring, and a 110 mL PE centrifuge tube. The sample is introduced in the membrane through the plastic lid (1). (B) Components assembled and placed inside the magnetotherm instrument.

Typically 1 mL of lipid magnetic nanostructure suspension (0.2 mg/mL) was introduced in the dialysis membrane and then the floating system was immersed in a water bath of 50 mL contained in the outer tube to provide sink conditions. The device was then inserted in magnetotherm coil and aliquots of samples were collected from the dialysis membrane at fixed times (0, 4, 24 and 29 hours). The experiments were performed by irradiating at 335 KHz, 17 kAm^{-1} and in absence of any AC-field under the same experimental conditions. After each set of experiments the magnetolipidic suspensions were separated through centrifugation and the supernatant analyzed for the drug quantification by HPLC. There was no measurable bulk temperature change, probably due to the fact that any eventual heating generated by the magnetic material was removed by the water bath (the effective iron concentration is very low).

Figure 6-26 shows the drug release percentage overtime. Data show 47 % of DxAc release after 4h with and without the presence of magnetic field, while a slight difference is observed later at 24 and 29 hours. Overall it seems that the applications of RF doesn't

affect remarkably the release of the drug overtime under the conditions used. However, almost 80% of the drug was released in less than 30 h at 25 °C in each case.

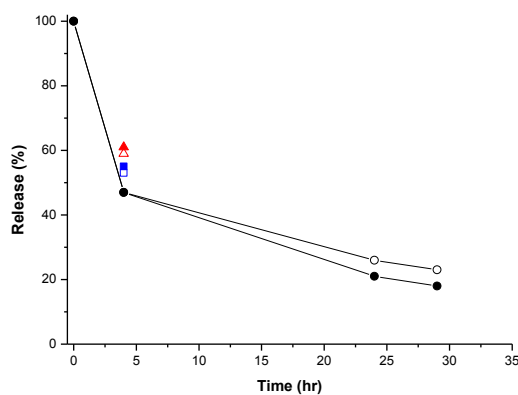


Figure 6- 26 Drug release results from LNP-DxAc suspension (63 nm, PDI=0.26) in (closed marks) presence and in (open marks) absence of a magnetic field. The experimental conditions used were 335 KHz (17 mT) at 25 °C, without stirring. Three repetitions for experiment with (●, ▲, ■) and without (○, △, □) RF (were made at t = 4 hrs and the same experimental conditions and the same sample were used).

In conclusion, no control over the release of the drug was achieved under the application of RF pulses. Future work needs to be focused on doing drug delivery studies using LNPA and LNPC liposomes which showed higher heating efficiency. These results suggest that it may not be possible to combine T₁-weighting with stimulated drug release.

6.3.10 Biotesting

A preliminary screening of the toxicity of the aqueous suspension of lipidic nanocomposites of similar sizes loaded with drug (dexamethasone) and/or dye (DiO, 3,3-dioctadecyloxacarbocyanine perchlorate) was undertaken in collaboration with Dr. Andrew Kellett (Dublin City University). LNPs samples of 48-57 nm, LNPC sample of 50 nm and LNPA sample of 84 nm were prepared and tested using two human cell lines, leukemic monocyte (THP-1) and liver carcinoma cells (HepG2). The hydrodynamic diameters, PDIs, iron concentration, dye and drug concentrations of the initial samples are summarized in Table 6-19. Samples of aqueous LNP, LNPA and LNPC suspensions with an iron concentration ranging from 0.1 to 100 μM were incubated with THP-1 and HepG2 cell lines for 24 and 72 hours. The viability of the cell lines was evaluated by

MTS (3-(4,5-dimethylthiazol-2-yl)-5-(3-carboxymethoxyphenyl)-2-(4-sulfophenyl) 2Htetrazolium) assay and the results are shown in Figure 6-27 and 6-28.

The results showed no significant cytotoxicity for all samples at all concentrations for either cell lines.

Sample	dhyd (nm) [PDI]	[Fe] (mg/mL)	DxAc (mg/mL)	DiO (µg/mL)
LNPs	48 [0.17]	1.87	-	-
LNP-DiO	57 [0.26]	1.87	-	10.6
LNP-DxAc-DiO	50 [0.34]	1.87	0.037	5.93
LNPA-DxAc	84 [0.25]	0.84	0.068	-
LNPC-DxAc	50 [0.21]	0.49	0.041	-

Table 6- 19 DLS data, iron, dye and drug content in the lipidic nanocomposite suspensions used in biotesting experiments.

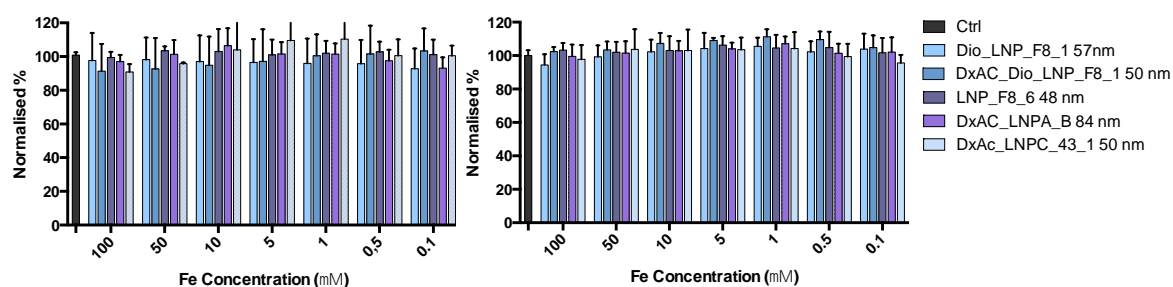


Figure 6- 27 Cell viability of THP-1 cells after 24 and 72 hour incubation with lipidic nanocomposite of similar size loaded with dexamethasone and/or DiO dye.

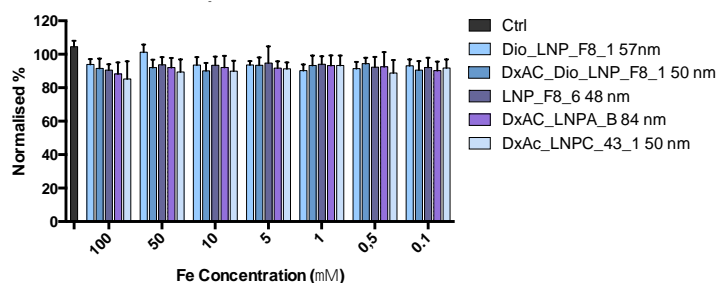


Figure 6- 28 Cell viability of HepG2 cells after 24 hour incubation with magnetoliposomes of similar size loaded with dexamethasone and/or DiO dye.

6.4 Conclusion

- In this work lipidic nanocomposites of different internal architecture and relatively narrow size distributions were successfully prepared through the encapsulation of primary NPs and NPCs prepared by the CSD method.
- The encapsulation of NPs and NPCs was supported by infrared spectroscopy, DLS data; unfortunately it was only possible to image LNPs by FESEM microscopy, because of the instability of LNPA and LNPC following evaporation of the solvent on the TEM grid.
- The magnetoliposome suspensions were compared and evaluated in terms of physical and magnetic properties. The difference in the NMRD response demonstrated that LNPCs (preformed clusters) and LNPA (NPs encapsulated in lipid matrix) have different internal order. The magnetoliposomes showed high relaxivity values that are higher or comparable to commercially available FeO T₂ based contrast agents including Ferridex and Sinerem.
- An improvement in size distribution and most importantly r₂ response was observed following magnetic chromatography for all LNPC samples analyzed and at LNPA sizes (< 200 nm). The higher r₂ response for initial and filtered LNPC samples can be related to the higher magnetic moment due to the assembled NP within the lipidic nanostructure. The potential to tune the relaxivity by changing the internal architecture of the liposome and by magnetic chromatography is an interesting finding considering the importance of the liposomes in biotechnology.
- We have shown magnetic fluid hyperthermia results and the highest heating efficiency response found was obtained with LNPA and LNPC suspensions. We believe that the heating loss might be related to the dipolar interparticle interactions. This finding is quite interesting because it suggests that is possible to control the heating release by changing the particle architecture and interparticle interactions within these nanostructures. The highest SAR value found was 104 W/g_{Fe} for 134 nm LNPCs at 335 kHz (13.5 kA/m)
- Finally we have shown that it is possible to load the LNPs with a low molecular weight drug (dexamethasone) but unfortunately it was not possible to control the drug release through radiofrequencies pulses. The same surface chemistry could in principle be used for LNPCs. The increased SAR of these constructs would render them useful as delivery vehicles that would be traceable under T₂-weighted

MRI. The downside is the reduced loading iron/drug inevitable with increased surface area.

Thesis conclusions

In this work size controlled hybrid magnetic clusters were produced in organic medium through the assembly of oleic acid stabilized cobalt ferrite and iron oxide nanoparticle by WI-CSD method. It was found that the kinetics of the assembly process can be controlled by optimizing some parameters, including the oleic acid concentration, nanoparticle concentration and the CoFeO:FeO molar ratio. ¹H-NMRD data have shown that magnetic properties of the resulting hybrid clusters were found to be different than the single component assemblies. The resulting magnetic properties were successfully tailored by changing the composition of the starting mixed NP suspensions.

Having identified the key parameters that must be tightly controlled to enable successful CSD, a further improvement of the assembly of nanoparticles into monodisperse nanoparticle clusters of controlled size by the CSD method was undertaken. The versatility of the CSD method was demonstrated by changing different parameters such as NP core size, mixture of NPs of different core size and type and finally changing competitive substrate. In the latter case it was observed that the nature of the substrate affects the assembly rate and the resulting magnetic properties of the assemblies presumably because of the difference in ligand density on the cluster surface that is responsible of local magnetic field inhomogeneities around the cluster. Moreover we reported a method as a simple and continuous synthesis of size controlled and highly monodisperse iron oxide assemblies using a flow setup based on the CSD approach. Through control over the reaction parameters including the tube length and the flow assembly used, the kinetics of the assembly can be modified allowing the synthesis of stable clusters of desired size. Finally the monitoring of the nanoparticle assembly under the effect of an external magnetic field through DLS demonstrated that the kinetics of the assembly is not particularly affected and that the assembly process is completely dominated by the gradual ongoing desorption of OA

For their applicability in biomedicine, it was necessary to give hydrophilic character to the clusters by coating them with a second layer using low molecular weight surfactants. The role of the surfactant in determining the magnetic properties of the assemblies in

aqueous medium was investigated. It was found that the inclusion of hydrophilic surfactants on the clusters surface reduced the r_1 values while still enhancing r_2 values resulting in higher r_2/r_1 ratios for both P23- and DTAB-coated clusters. This is caused by the partial inaccessibility of the water through the magnetic cluster. Moreover hyperthermia studies have shown that the heating efficiency increases with increasing of the cluster size suggesting that the heating response of the NPCs may be associated with the NP dipolar interactions within the clusters. In general the SAR values found were comparable or in certain cases higher to those previously published of comparable materials. Finally bio-testing studies have shown that P123 coated NPCs present lower cytotoxicity, particularly at low iron concentrations while DTAB stabilized NPCs seem to be highly toxic even at low concentrations. However, these results are encouraging as they provide a guide for the identification and use of other suitable low weight biocompatible surfactants for the phase transfer of NPCs to water. This work is on-going within the group.

Finally the role of the internal architecture in determining the magnetic properties of aqueous suspensions magnetoliposomes produced by lipid encapsulation of iron oxide NPs and NPCs produced by CSD has been investigated. It was found that the internal magnetoliposome structure have a large influence in determining the resulting magnetic properties and heating capacity in water. An increase of the r_1 and r_2 values cluster based magnetoliposomes was observed following magnetic filtration. It is suggested that the enhancement of the transversal relaxivity is related to a magnetic field induced reorientation of the magnetic moments of the NPs of the assemblies. NPCs and NP aggregates based magnetoliposomes have shown higher heating efficiencies presumably because of the NP dipolar interactions that lead to an enhancement of the hysteresis losses mechanism. Finally the magnetoliposomes have shown high biocompatibility; this is an encouraging result considering the importance of the liposomes in biotechnology.

As already mentioned, good results in scale-up experiments up to 150 mL of NPC suspension were achieved; the key process parameter was found to be the ratio of the concentration of the NP to the liquid-liquid interfacial area. In order to increase the volumes of NPCs, a new experimental flow set up system was built this should in

principle remove all barriers to up-scaling. So far the results are encouraging and stable and monodisperse FeO NPCs were obtained. However three main practical limitations can be found including, the formation of water bubbles that cause the continuation of the assembly in the final NPC suspension losing the control over the NPC size; difficulty in separation between the organic and aqueous phase and waste of the solvent (water). Another issue in the system used is the sedimentation of the material in the tubing during the assembly experiment that leads to lower yields. These issues could be addressed using different setups for the separation of the NPC suspension from the water that we are currently designing in collaboration with Dr. Steven Ferguson (University College Dublin). These systems would lead to 100 % yields as material is not wasted while starting up and shutting down and in addition the water can be recycled so that the overall solvent consumption is low at industrial level. The assessment of these systems are currently under development.

References

- [1] Z. Lu, Y. Yin, *Chemical Society reviews* **2012**, *41*, 6874-6887.
- [2] K. Ariga, Q. Ji, J. P. Hill, N. Kawazoe, G. Chen, *Expert Opin Biol Ther* **2009**, *9*, 307-320.
- [3] Z. Nie, A. Petukhova, E. Kumacheva, *Nature nanotechnology* **2010**, *5*, 15-25.
- [4] G. C. D. Cullity B. D., *Introduction to Magnetic Materials* 2nd ed., Wiley-IEEE Press, **2008**.
- [5] G. C. Chikazumi S *Physics of Ferromagnetism*, Oxford University Press, **2009**.
- [6] L. Duo, Marco Finazzi, Franco Ciccacci, *Magnetic Properties of Antiferromagnetic Oxide Materials*, **2010**.
- [7] R. M. a. S. Cornell, U., *The Iron Oxides: Structure, Properties, Reactions, Occurrences and Uses*, Weinheim: Wiley-VCH,.
- [8] R. A. F. a. P. K. Trojan, *Engineering Materials and Their Applications*, 4th ed., **1990**.
- [9] D. L. a. R. Leslie-Pelecky, R.D., *Chem. Mater.* **1996**, *8*, 1770-1783.
- [10] S. Laurent, D. Forge, M. Port, A. Roch, C. Robic, L. V. Elst, R. N. Muller, *Chem Rev* **2008**, *108*, 2064-2110.
- [11] X. Chen, S. S. Gambhir, J. Cheon, *Accounts of chemical research* **2011**, *44*, 841.
- [12] Y. Huang, S. He, W. Cao, K. Cai, X. J. Liang, *Nanoscale* **2012**, *4*, 6135-6149.
- [13] C. Sun, J. S. Lee, M. Zhang, *Advanced drug delivery reviews* **2008**, *60*, 1252-1265.
- [14] H. Otsuka, Y. Nagasaki, K. Kataoka, *Advanced drug delivery reviews* **2003**, *55*, 403-419.
- [15] N. Nasongkla, E. Bey, J. Ren, H. Ai, C. Khemtong, J. S. Guthi, S. F. Chin, A. D. Sherry, D. A. Boothman, J. Gao, *Nano letters* **2006**, *6*, 2427-2430.
- [16] R. Cavaliere, E. C. Ciocatto, B. C. Giovanella, C. Heidelberger, R. O. Johnson, M. Margottini, B. Mondovi, G. Moricca, A. Rossi-Fanelli, *Cancer* **1967**, *20*, 1351-1381.
- [17] D. Yoo, J. H. Lee, T. H. Shin, J. Cheon, *Accounts of chemical research* **2011**, *44*, 863-874.
- [18] R. E. Rosensweig, *J Chem Phys* **2004**, *121*, 1228-1242.
- [19] J. H. C. Silvio Dutz, Dietmar Eberbeck, Thorsten Gelbrich, Rudolf Hergt, Robert Müller, Jana Wotschadlo, Matthias Zeisberger, *J Magn Magn Mater* **2009**, *321*, 1501-1504.
- [20] S. Mornet, Vasseur, S., Grasset, F. and Duguet, E., *J Mater Chem* **2004**, *14*, 2161-2175.
- [21] A. B. K. Salunkhe, V.M.; Pawar, S.H., *Current Topics in Medicinal Chemistry* **2014**, *14*, 572-594(523).
- [22] P. Guardia, R. Di Corato, L. Lartigue, C. Wilhelm, A. Espinosa, M. Garcia-Hernandez, F. Gazeau, L. Manna, T. Pellegrino, *ACS nano* **2012**, *6*, 3080-3091.
- [23] R. H. Rudolf Hergt, Matthias Zeisberger, Dirk Schüler, Udo Heyen, Ingrid Hilger, Werner A. Kaiser, *293*, 80-86.
- [24] A. M. B. Mehdaouia, L.-M. Lacroixa, J. Carreya, S. Lachaizea, M. Gougeonc, M. Respauda, B. Chaudretd, **2010**, *322*, L49-L52.
- [25] M. L. P. Hugounenq, D. Alloyeau, L. Lartigue, E. Dubois, V. Cabuil, C. Ricolleau, S. Roux, C. Wilhelm, F. Gazeau, and R. Bazzi, *J. Phys. Chem. C* **2012**, *116*, 15702-15712.
- [26] J. P. Fortin, F. Gazeau, C. Wilhelm, *European biophysics journal : EBJ* **2008**, *37*, 223-228.

- [27] M. G. Harisinghani, J. Barentsz, P. F. Hahn, W. M. Deserno, S. Tabatabaei, C. H. van de Kaa, J. de la Rosette, R. Weissleder, *N Engl J Med* **2003**, *348*, 2491-2499.
- [28] R. Weissleder, K. Poss, R. Wilkinson, C. Zhou, A. Bogdanov, Jr., *Antimicrobial agents and chemotherapy* **1995**, *39*, 839-845.
- [29] J. Park, K. An, Y. Hwang, J. G. Park, H. J. Noh, J. Y. Kim, J. H. Park, N. M. Hwang, T. Hyeon, *Nature materials* **2004**, *3*, 891-895.
- [30] Y. W. Jun, Y. M. Huh, J. S. Choi, J. H. Lee, H. T. Song, S. Kim, S. Yoon, K. S. Kim, J. S. Shin, J. S. Suh, J. Cheon, *Journal of the American Chemical Society* **2005**, *127*, 5732-5733.
- [31] R. Reszka, P. Beck, I. Fichtner, M. Hentschel, J. Richter, J. Kreuter, *The Journal of pharmacology and experimental therapeutics* **1997**, *280*, 232-237.
- [32] C. Khemtong, O. Togao, J. Ren, C. W. Kessinger, M. Takahashi, A. D. Sherry, J. Gao, *Journal of magnetic resonance* **2011**, *209*, 53-60.
- [33] D. Kim, N. Lee, M. Park, B. H. Kim, K. An, T. Hyeon, *Journal of the American Chemical Society* **2009**, *131*, 454-455.
- [34] R. N. M. a. P. G. Alain Roch, *J. Chem. Phys.* **1999**, *110*, 5403
- [35] A. Roch, Y. Gossuin, R. N. Muller, P. Gillis, *J Magn Magn Mater* **2005**, *293*, 532-539.
- [36] A. Roch, R. N. Muller, P. Gillis, *J Chem Phys* **1999**, *110*, 5403-5411.
- [37] A. Roch, Gossuin, Y., Muller, R.N. and Gillis, P., *J Magn Magn Mater* **2005**, *293*, 532-539.
- [38] C. Meledandri, PhD Thesis thesis, Dublin City University. **2009**.
- [39] J. K. Stolarczyk, A. Deak, D. F. Brougham, *Adv Mater* **2016**, *28*, 5400-5424.
- [40] D. J. Norris, A. Sacra, C. B. Murray, M. G. Bawendi, *Physical review letters* **1994**, *72*, 2612-2615.
- [41] S. K. Sarita Kango, Annamaria Celli, James Njuguna, Youssef Habibi, Rajesh Kumar, *Progress in Polymer Science* **2013**, *38*, 1232-1261.
- [42] Y. Yin, A. P. Alivisatos, *Nature* **2005**, *437*, 664-670.
- [43] aB. Luo, S. Xu, A. Luo, W. R. Wang, S. L. Wang, J. Guo, Y. Lin, D. Y. Zhao, C. C. Wang, *ACS nano* **2011**, *5*, 1428-1435; bB. Luo, X. J. Song, F. Zhang, A. Xia, W. L. Yang, J. H. Hu, C. C. Wang, *Langmuir : the ACS journal of surfaces and colloids* **2010**, *26*, 1674-1679.
- [44] J. Ge, Y. Hu, M. Biasini, W. P. Beyermann, Y. Yin, *Angewandte Chemie* **2007**, *46*, 4342-4345.
- [45] J. H. Park, G. von Maltzahn, L. Zhang, M. P. Schwartz, E. Ruoslahti, S. N. Bhatia, M. J. Sailor, *Adv Mater* **2008**, *20*, 1630-1635.
- [46] M. Yoon, Y. Kim, J. Cho, *ACS nano* **2011**, *5*, 5417-5426.
- [47] Y. Lin, H. Skaff, T. Emrick, A. D. Dinsmore, T. P. Russell, *Science* **2003**, *299*, 226-229.
- [48] E. Poselt, S. Fischer, S. Foerster, H. Weller, *Langmuir : the ACS journal of surfaces and colloids* **2009**, *25*, 13906-13913.
- [49] Y. Xia, T. D. Nguyen, M. Yang, B. Lee, A. Santos, P. Podsiadlo, Z. Tang, S. C. Glotzer, N. A. Kotov, *Nature nanotechnology* **2012**, *7*, 479.
- [50] D. Grosso, Cagnol, F., Soler-Illia, G. J. de A. A., Crepaldi, E. L. Amenitsch, H., Brunet-Bruneau, A., Bourgeois, A. and Sanchez C. , *Adv Funct Mater* **2004**, *14*, 309-322.
- [51] J. Bahadur, Sena, D., Mazumder, S., Bhaskar Paul, S., Arshad Khan and G. Ghosh, **2010**, *351*, 357-364.
- [52] D. S. W. F. Bai, Z. Y. Huo, W. Chen, L. P. Liu, X. Liang, C. Chen, X. Wang, Q. Peng and Y. D. Li, *Angew. Chem., Int. Ed.* **2007**, *46*, 6650.

- [53] S. K. S. T. Isojima, J. B. V. Sande and T. A. Hatton, *Langmuir : the ACS journal of surfaces and colloids* **2009**, *25*, 8292.
- [54] A. Ahniyaz, Y. Sakamoto, L. Bergstrom, *Proceedings of the National Academy of Sciences of the United States of America* **2007**, *104*, 17570-17574.
- [55] F. Caruso, R. A. Caruso, H. Mohwald, *Science* **1998**, *282*, 1111-1114.
- [56] F. Caruso, H. Lichtenfeld, M. Giersig, H. Mohwald, *Journal of the American Chemical Society* **1998**, *120*, 8523-8524.
- [57] aF. Caruso, R. A. Caruso, H. Mohwald, *Science* **1998**, *282*, 1111-1114; bF. Caruso, A. S. Susha, M. Giersig, H. Mohwald, *Advanced Materials* **1999**, *11*, 950-+; cF. Caruso, M. Spasova, A. Susha, M. Giersig, R. A. Caruso, *Chem Mater* **2001**, *13*, 109-116.
- [58] C. J. Meledandri, J. K. Stolarczyk, D. F. Brougham, *ACS nano* **2011**, *5*, 1747-1755.
- [59] J. K. Stolarczyk, S. Ghosh, D. F. Brougham, *Angewandte Chemie* **2009**, *48*, 175-178.
- [60] T. Pellegrino, L. Manna, S. Kudera, T. Liedl, D. Koktysh, A. L. Rogach, S. Keller, J. Radler, G. Natile, W. J. Parak, *Nano letters* **2004**, *4*, 703-707.
- [61] D. I. Gittins, F. Caruso, *Angewandte Chemie* **2001**, *40*, 3001-3004.
- [62] Y. Wang, J. F. Wong, X. W. Teng, X. Z. Lin, H. Yang, *Nano letters* **2003**, *3*, 1555-1559.
- [63] A. Swami, A. Kumar, M. Sastry, *Langmuir : the ACS journal of surfaces and colloids* **2003**, *19*, 1168-1172.
- [64] aK. M. K. Marcela Gonzales, *J Magn Magn Mater* **2007**, *311*, 59-62; bS. L. Jian Qin, Yun Suk Jo, Alain Roch, Maria Mikhaylova, Zaver M. Bhujwalla, Robert N. Muller, and Mamoun Muhammed, *Advanced Materials* **2007**, *19*, 1874-1878.
- [65] D. E. Koppel, *Journal of Chemical Physics Letters* **1972**, 4814-4820.
- [66] S. Twomey, *Dover Publications* **1997**, 237.
- [67] I. S. I. International Organization for Standardization (ISO), **1996**.
- [68] C. L. a. H. Lawson, R.J. , *SIAM Society for Industrial & Applied Mathematics* **1995**, 350.
- [69] C. I. Europe.
- [70] *Vol. 1.1*, University of Cambridge, **2004**, p. 15.12.
- [71] M. Kazuba, Malvern Lecture Series, **2010**.
- [72] M. Instruments.
- [73] R. Kimmich, E. Anoardo, *Prog Nucl Mag Res Sp* **2004**, *44*, 257-320.
- [74] G. G. E. Anoardo, G. Ferrante, *Applied Magnetic Resonance* **2001**, *20*, 365-404.
- [75] C. J. Meledandri, J. K. Stolarczyk, S. Ghosh, D. F. Brougham, *Langmuir : the ACS journal of surfaces and colloids* **2008**, *24*, 14159-14165.
- [76] H. R. Kohl, Ludwig, *Transmission electron microscopy: physics of image formation*, Springer-Verlag New York, New York, NY, **2008**.
- [77] D. M. K. L. Bunker, K. A. Allison, K. Wagner, K. Rickabaugh, A. M. Levine, B. R. Strohmeier, and R. J. Lee *Microscopy and Microanalysis* **2008**, *14*, 580-581.
- [78] G. Zeiss, Zeiss, Germany.
- [79] SIGMA, **2012**, p. 33.
- [80] I. M. Obaidat, B. Issa, Y. Haik, *Nanomaterials-Basel* **2015**, *5*, 63-89.
- [81] B. Thiesen, A. Jordan, *International journal of hyperthermia : the official journal of European Society for Hyperthermic Oncology, North American Hyperthermia Group* **2008**, *24*, 467-474.
- [82] I. M. Obaidat, Issa, B. and Haik, Y., *Nanomaterials-Basel* **2015**, *5*, 63-89.
- [83] U. P. a. G. Fringeli, H.H., *E. Gell, Ed., New York* **1981**, 270-332.
- [84] B. H. Stuart, *Chichester: John Wiley and Sons Inc.* **2004**, 242.

- [85] E. Fox, PhD thesis thesis, Dublin City University **2014**.
- [86] K. S. Lee, R. M. Anisur, K. W. Kim, W. S. Kim, T. J. Park, E. J. Kang, I. S. Lee, *Chem Mater* **2012**, *24*, 682-687.
- [87] F. X. Redl, K. S. Cho, C. B. Murray, S. O'Brien, *Nature* **2003**, *423*, 968-971.
- [88] C. J. Meledandri, J. K. Stolarczyk, D. F. Brougham, *ACS nano* **2011**, *5*, 1747-1755.
- [89] G. L. Davies, S. A. Corr, C. J. Meledandri, L. Briode, D. F. Brougham, Y. K. Gun'ko, *Chemphyschem* **2011**, *12*, 772-776.
- [90] aC. Cannas, A. Ardu, A. Musinu, D. Peddis, G. Piccaluga, *Chem Mater* **2008**, *20*, 6364-6371; bC. Cannas, A. Ardu, A. Musinu, L. Suber, G. Ciasca, H. Amenitsch, G. Campi, *ACS nano* **2015**, *9*, 7277-7286.
- [91] M. Niederberger, N. Pinna, *Eng Mater Process* **2009**, 205-209.
- [92] K. D. a. K. P. A. Danov, *Colloid J+* **2012**, *74*, 172-185.
- [93] R. E. a. D. H. Napper, *J. Chem. Soc. Faraday Trans. 1* **1977**, *73*, 1377-1385.
- [94] J. K. Stolarczyk, S. Ghosh, D. F. Brougham, *Angew Chem Int Edit* **2009**, *48*, 175-178.
- [95] J. A. Schwarz, Contescu, C.I. and Putyera, K. Dekker in *Encyclopedia of Nanoscience and Nanotechnology* (Ed.: C. Press), **2004**, p. 3200.
- [96] N. Pinna, M. Niederberger, *Angewandte Chemie* **2008**, *47*, 5292-5304.
- [97] H. Singh, P. E. Laibinis, T. A. Hatton, *Langmuir : the ACS journal of surfaces and colloids* **2005**, *21*, 11500-11509.
- [98] T. Ninjbadgar, E. K. Fox, J. Hierrezuelo, F. El Haddassi, D. F. Brougham, *J Mater Chem B* **2015**, *3*, 8638-8643.
- [99] Y. Min, M. Akbulut, K. Kristiansen, Y. Golan, J. Israelachvili, *Nature materials* **2008**, *7*, 527-538.
- [100] Y. Sahoo, M. Cheon, S. Wang, H. Luo, E. P. Furlani, P. N. Prasad, *Journal of Physical Chemistry B* **2004**, *108*, 3380-3383.
- [101] A. Y. Zubarev, L. Y. Iskakova, *Colloid J+* **2003**, *65*, 703-710.
- [102] R. A. Sperling, W. J. Parak, *Philosophical Transactions of the Royal Society a-Mathematical Physical and Engineering Sciences* **2010**, *368*, 1333-1383.
- [103] aB. S. Kim, J. M. Qiu, J. P. Wang, T. A. Taton, *Nano letters* **2005**, *5*, 1987-1991; bB. A. M. Benjamin W. Muir, Peter Harbour, Greg Coia, Guoliang Zhen, Lynne Waddington, Judith Scoble, Daniel Kraus, San H. Thang, Yen K. Chong, Paul Mulvaney and Patrick Hartley, *J. Phys. Chem. C*, **2009**, *113*, 16615-16624; cA. Prakash, H. Zhu, C. J. Jones, D. N. Benoit, A. Z. Ellsworth, E. L. Bryant, V. L. Colvin, *ACS nano* **2009**, *3*, 2139-2146.
- [104] J. Zhuang, H. Wu, Y. Yang, Y. C. Cao, *Journal of the American Chemical Society* **2007**, *129*, 14166-14167.
- [105] V. Y. Kabanov, *High Energy Chemistry* **2000**, *34*, 203-211.
- [106] H. R. Lin, P. C. Chang, *Journal of biomedical materials research. Part B, Applied biomaterials* **2013**, *101*, 689-699.
- [107] T. K. Jain, M. A. Morales, S. K. Sahoo, D. L. Leslie-Pelecky, V. Labhsetwar, *Molecular pharmaceuticals* **2005**, *2*, 194-205.
- [108] P. Gillis, A. Roch, R. A. Brooks, *Journal of magnetic resonance* **1999**, *137*, 402-407.
- [109] J. F. Berret, N. Schonbeck, F. Gazeau, D. El Kharrat, O. Sandre, A. Vacher, M. Airiau, *Journal of the American Chemical Society* **2006**, *128*, 1755-1761.
- [110] C. F. H. Ai, B. Weinberg, X.-T. Shuai, M. D. Pagel, D. Farrell, J. Duerk, J. Gao, *Advanced materials* **2005**, *17*, 1949-1952.

- [111] C. Martinez-Boubeta, K. Simeonidis, A. Makridis, M. Angelakeris, O. Iglesias, P. Guardia, A. Cabot, L. Yedra, S. Estrade, F. Peiro, Z. Saghi, P. A. Midgley, I. Conde-Leboran, D. Serantes, D. Baldomir, *Scientific reports* **2013**, *3*, 1652.
- [112] K. J. M. Bishop, C. E. Wilmer, S. Soh, B. A. Grzybowski, *Small* **2009**, *5*, 1600-1630.
- [113] S. Dutz, Clement, J. H., Eberbeck, D., Gelbrich, T., Hergt, R., Muller, R., Wotschadlo, J., Zeisberger, M., *J Magn Magn Mater* **2009**, *321*, 1501–1504.
- [114] K. Hayashi, M. Nakamura, W. Sakamoto, T. Yogo, H. Miki, S. Ozaki, M. Abe, T. Matsumoto, K. Ishimura, *Theranostics* **2013**, *3*, 366-376.
- [115] R. Ludwig, M. Stapf, S. Dutz, R. Muller, U. Teichgraber, I. Hilger, *Nanoscale research letters* **2014**, *9*, 602.
- [116] aJ. J. Lin, J. S. Chen, S. J. Huang, J. H. Ko, Y. M. Wang, T. L. Chen, L. F. Wang, *Biomaterials* **2009**, *30*, 5114-5124; bB. Stella, S. Arpicco, M. T. Peracchia, D. Desmaele, J. Hoebeke, M. Renoir, J. D'Angelo, L. Cattel, P. Couvreur, *Journal of pharmaceutical sciences* **2000**, *89*, 1452-1464.
- [117] M. S. a. J. W. AD Bangham, *Journal of molecular biology* **1965**, *13*, 238.
- [118] E. Reimhult, *New biotechnology* **2015**, *32*, 665-672.
- [119] aJ. Alonso, Khurshid, H., Devkota, J., Nemati, Z., Khadka, N.K., Srikanth, H., Pan, J. and Phan, M. H., *J Appl Phys* **2016**, *119*, 083904; bM. S. Martina, J. P. Fortin, C. Menager, O. Clement, G. Barratt, C. Grabielle-Madelmont, F. Gazeau, V. Cabuil, S. Lesieur, *Journal of the American Chemical Society* **2005**, *127*, 10676-10685.
- [120] J. W. Bulte, M. de Cuyper, D. Despres, J. A. Frank, *Journal of magnetic resonance imaging : JMRI* **1999**, *9*, 329-335.
- [121] J. S. L. R.H. Muller, in *European Patent, Vol. No. 0605497* (Ed.: E. Patent), **1996**.
- [122] M. R. Gasco, in *US Patent, Vol. 5 250 236* (Ed.: U. Patent), **1993**.
- [123] M. Munoz de Escalona, E. Saez-Fernandez, J. C. Prados, C. Melguizo, J. L. Arias, *International journal of pharmaceutics* **2016**, *504*, 11-19.
- [124] E. Rostami, Kashanian, S., Azandaryani, A.H., Faramarzi, H., Dolatabadi, J.E. and Omidfar, K., *Chem. Phys. Lipids* **2014**, *181*, 56–61.
- [125] S. Doktorovova, Souto, E.B. and Silva, A.M., *Eur. J. Pharm. Biopharm.* **2014**, *87*, 1–18.
- [126] S. Zhao, Zhang, Y., Han, Y., Wang, J. and Yang, J.,, *Pharm. Res.* **2015**, *32*, 482–491.
- [127] E. Peira, Marzola, P., Podio, V., Aime, S., Sbarbati, A. and Gasco, M.R., *J. Drug Target.* **2003**, *11*, 19–24.
- [128] X. M. Liu, L. D. Quan, J. Tian, F. C. Laquer, P. Ciborowski, D. Wang, *Biomacromolecules* **2010**, *11*, 2621-2628.
- [129] M. Cagnasso, V. Boero, M. A. Franchini, J. Chorover, *Colloids and surfaces. B, Biointerfaces* **2010**, *76*, 456-467.
- [130] A. Roch, Muller, R. and Gillis, P., *J Chem Phys* **1999**, *110*,, 5403-5411.
- [131] C. J. N. Meledandri, T. and Brougham D. F., *J. Mater. Chem.* **2011**, *21*, 214-222.
- [132] X. P. Y Bi, L Chen, QH Wan, *Journal of Chromatography A* **2011**, *1218*, 3908–3914.
- [133] aT. Allkemper, C. Bremer, L. Matuszewski, W. Ebert, P. Reimer, *Radiology* **2002**, *223*, 432-438; bL. Xiao, J. Li, D. F. Brougham, E. K. Fox, N. Feliu, A. Bushmelev, A. Schmidt, N. Mertens, F. Kiessling, M. Valldor, B. Fadeel, S. Mathur, *ACS nano* **2011**, *5*, 6315-6324.
- [134] C. Frandsen, S. Morup, *Physical review letters* **2005**, *94*, 027202.
- [135] S. Mukherjee, Kumar Pal, A, Bhattacharya , S and Chattopadhyay S, *Journal of Physics: Condensed Matter* **2008**, *20*, 055204.

- [136] X. Wang, Gu, H., and Yang, Z., *J Magn Magn Mater* **2005**, 293, 334–340.
- [137] R. E. Rosensweig, *J Magn Magn Mater* **2002**, 252, 370–374.
- [138] V. a. B. V. Singh, *J Appl Phys* **2012**, 112, 114912.
- [139] aM. Jeun, Bae, S., Tomitaka, A., Takemura, Y., Park, K. H., Paek, S. H. and Chung K. W., *Applied Physics Letters* **2009**, 95, 082501 ; bT. Maehara, Konishi, K., Kamimori, T., Aono, H., Hirazawa, H., Naohara, T., Nomura, S., Kikkawa, H., Watanabe, Y. and Kawachi, K. , 2005. *J. Mater. Sci.* **2005**, 40, 135 - 138.
- [140] D. F. Coral, P. M. Zelis, M. Marciello, P. Morales Mdel, A. Craievich, F. H. Sanchez, M. B. van Raap, *Langmuir : the ACS journal of surfaces and colloids* **2016**, 32, 1201-1213.
- [141] K. S. K. D. Bakoglidis, D. Sakellari, G. Stefanou, and M. Angelakeris, *Ieee T Magn*, 48, 1320-1323.

Appendix

Published work

A.1 List of papers

1. T. Ninjbadgar, E. K. Fox, J. M. Hierrezuelo, **F. El Haddassi** and D. F. Brougham, “Monodisperse magnetic nanoparticle assemblies prepared at scale by competitive stabiliser desorption”, *Journal of Materials Chemistry B*, **2015**, 3, 8638-8643. DOI: 10.1039/C5TB01573A.
2. T. Borase, E. K. Fox, **F. El Haddassi**, S. A. Cryan, D. F. Brougham and A. Heise, “Glyco-copolyptide grafted magnetic nanoparticles: the interplay between particle dispersion and RNA loading“, *Polymer Chemistry*, **2016**, 7, 3221-3224. DOI: 10.1039/C6PY00250A.

Contribution of the Author:

1. Synthesis, characterization and assembly of oleic acid stabilized iron oxide nanoparticles. Recording of the Fast Field Cycling NMR measurement of samples and ICP-AES analysis.
2. Recording of the Fast Field Cycling NMR measurement of samples and ICP-AES analysis.

A.2 Conference Proceedings

- Poster presentation: “Preparation of stable suspensions of magnetic nanoparticle clusters of controlled size by competitive stabiliser desorption method to a liquid interface” by F. El Haddassi, E. K. Fox, J. M. Hierrezuelo and D. F. Brougham. RSC Faraday Discussion 181: Nanoparticle synthesis and assembly”, Chicago (USA), April 20th-22nd 2015.
- Oral presentation: “Synthesis and characterization of size-controlled hybrid nanoparticle clusters for biomedical applications” F. El Haddassi and D. F. Brougham. European Materials Research Society, Warsaw (Poland), September 15th-18th 2015.